Ph.D. Program in Civil, Chemical and Environmental Engineering
Curriculum in Fluid Dynamics and Environmental Engineering

Department of Civil, Chemical and Environmental Engineering
Polytechnic School, University of Genoa, Italy.

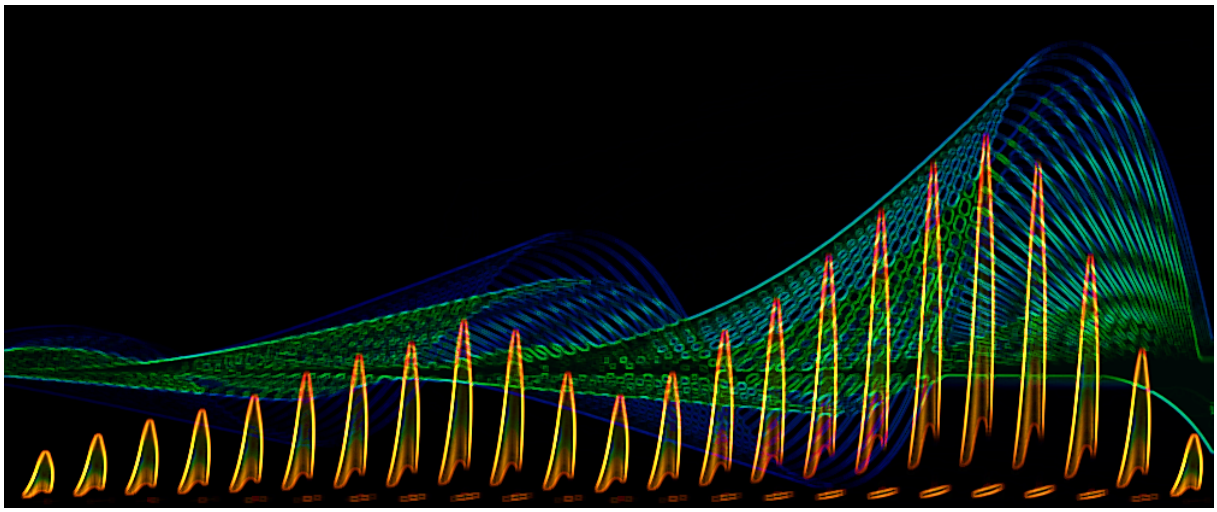

Forward and Inverse Modelling in Thermoacoustics

Jiasen Wei

FORWARD AND INVERSE MODELLING

IN THERMOACOUSTICS

BY

JIASEN WEI

Dissertation discussed in partial fulfillment of
the requirements for the Degree of

DOCTOR OF PHILOSOPHY

Civil, Chemical and Environmental Engineering
curriculum in Fluid Dynamics and Environmental Engineering,
Department of Civil, Chemical and Environmental Engineering, University of Genoa, Italy

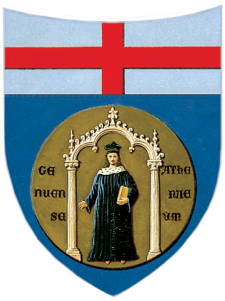

March, 2025

Advisers:
Prof. Alessandro Bottaro - DICCA, Università degli Studi di Genova
Prof. Jan O. Pralits - DICCA, Università degli Studi di Genova

External Reviewers:
Prof. Luca Magri - Department of Aeronautics, Imperial College London; DIMEAS, Politecnico di Torino
Prof. Susann Boij - Department of Engineering Mechanics, Kungliga Tekniska Högskolan (KTH)

Examination Committee:
Prof. Nicoletta Tambroni - DICCA, Università degli Studi di Genova
Prof. Alessandro Orchini - Chair of Nonlinear Thermo-Fluid Mechanics, Technische Universität Berlin
Prof. Davide Laera - Department of Mechanics, Mathematics & Management, Politecnico di Bari; CERFACS

Ph.D. program in Civil, Chemical and Environmental Engineering
Curriculum in Fluid Dynamics and Environmental Engineering
Cycle XXXVI

ACKNOWLEDGMENTS

First and foremost, I am deeply grateful to my parents for giving me the freedom to focus entirely on my studies.

To HongPeng, thank you for the countless night bus rides over the past four years and for being by my side through both the toughest and the most joyful moments.

The deepest gratitude goes to my supervisors, Prof. Alessandro Bottaro and Prof. Jan O. Pralits, for your invaluable patience and guidance despite my "slowly-growing nonlinear progress". Your support, in every possible way, has made this path smoother and far more enriching than I could have imagined.

To my amazing colleagues and friends at UniGe, thank you for all the coffee time, lunch breaks, hikes, aperitivi, and all the great times we shared together.

Special thanks to Prof. Maria Heckl, Jemma Sharrock, and Sadaf Arabi for making my secondment at Keele University truly enjoyable and fruitful and for an unforgettable British Christmas. I also extend my sincere gratitude to Prof. Susann Boij and Charitha Vaddamani, for your warm hospitality during my short stay at KTH during a snowy week in April. To all the POLKA members, fellows and mentors, thank you for the fun time together and inspiring discussions during every workshop.

I also extend my thanks to Prof. Francisco J. Valdés-Parada and Prof. Didier Lasseux for their comprehensive and insightful introduction to the world of upscaling techniques, which has deepened my understanding of the field. My sincere appreciation also goes to Dr. Giuseppe Antonio Zampogna for his sharp mathematical insight and indispensable contributions to the homogenization theory.

To my dearest friends—Dili, WangYuan, Joy, MoRan, ShuXuan, and HanYu—your friendship has been a source of strength, keeping me moving forward.

Last but not least, my appreciation reaches Mother Nature for moments of joy and tranquillity—for the breathtaking coastlines of Liguria, the calming respiration of the Mediterranean Sea, the mesmerizing sunsets, and for keeping my little balcony garden thriving.

This thesis is part of the Marie Skłodowska-Curie Innovative Training Network ***Pol****lution* ***K****now-How and* ***A****batement* (POLKA). I gratefully acknowledge the financial support from the European Union's Horizon 2020 research and innovation program under the Marie Skłodowska-Curie grant agreement No. 813367.

ABSTRACT

Thermoacoustic instabilities are self-sustained oscillations that arise in combustion systems such as domestic boilers, gas turbines, and rocket engines. These instabilities result from the feedback between unsteady combustion, unsteady flow, and the structural dynamics of the system, leading to undesirable vibrations that range from irritating noise to severe oscillations capable of causing structural damage and safety risks. Due to the complexity of the underlying physics, the accurate prediction, prevention, and mitigation of thermoacoustic instabilities remain a challenge in the combustion industry.

This research work addresses this problem from three key perspectives: (1) the modelling and prediction of thermoacoustic instabilities, (2) the impact of mean-flow uncertainties and feedback forcings on a thermoacoustic system, and (3) the acoustic properties of passive control devices such as porous materials and acoustic liners. For the first two perspectives, we demonstrate the application of adjoint approaches for stability analysis and sensitivity analysis in thermoacoustics. In the last part, we show the application of the homogenization approach in acoustic modelling.

First, a theoretical framework based on the adjoint Green's function (AGF) is developed to predict thermoacoustic instabilities in systems with mean flow. The adjoint method aids in determining the AGF system of non-self-adjoint systems. This approach converts the acoustic analogy equation with convection into an integral equation, yielding sensitivity functions that quantify the system's response to initial conditions, boundary conditions, and external forcings. The framework is applied to two types of resonators with different boundary conditions: a Rijke tube and a matrix burner, where control parameters include heat source position, heater power, and tube length. The results demonstrate the model's ability to capture key nonlinear behaviours observed in experiments, including limit cycles, triggering phenomena, hysteresis, and Hopf bifurcations. The analysis further reveals that mean flow velocity plays a crucial role in stabilizing the system and alteration of bistability. Additionally, the AGF framework is extended to thermoacoustic systems with non-uniform temperature fields and stochastic forcing. The study highlights the influence of mean temperature differences on system stability and examines the effects of white noise and pink noise. The impact of noise on the transient phase of the instability, before saturation is reached, is examined, and noise-induced triggering phenomena are found near stability margins. Pink noise is found to be more effective than white noise in triggering instabilities, while the presence of mean flow exhibits a hindering effect.

Second, a comprehensive adjoint-based sensitivity analysis framework is demonstrated for a low-order lumped model of a gas turbine combustor. Three types of sensitivity analyses are carried out. The base-state sensitivity reveals how uncertainties in base flow properties, such as the density of cold gas in the premixer, significantly impact the growth rates of the eigenmodes. The structural sensitivity to steady feedback forcings uncovers steady control strategies such as local mass suction and heating as effective stabilizing mechanisms. Furthermore, the structural perturbation sensitivity examines the effect of localized feedback forcings on the perturbation flow. The results identify Helmholtz resonators as effective stabilizers and pinpoint their optimal placement. These insights broaden the scope of uncertainty quantification and control strategies for premixed combustion systems.

Finally, the acoustic properties of passive control devices, such as porous materials and acoustic liners with periodic microstructures, are examined. While classical homogenization

methods effectively describe wave refraction inside the bulk region of porous media, they fail to capture the reflection of acoustic waves coming from the free field at material surface faces. To address this limitation, a homogenization approach combined with asymptotic matching is employed, yielding an effective interface jump condition for acoustic propagation in porous materials with rigid scatterers. The results show that this interface condition effectively models the reflection of the acoustic waves at the free-field-porous material interface for porous materials of porosity $\phi \geq 0.8$. In another case, a homogenized model is developed to describe acoustic propagation through a single array of rigid cylinders. The model introduces an effective domain represented as a slab of specified thickness. Reflection and transmission coefficients are computed using the upscaled model and compared with direct numerical results and experimental measurements. The results demonstrate good agreement at lower frequencies, while discrepancies increase at higher frequencies due to the decreasing wavelength, which affects the validity of the length scale separation assumption.

INDEX

List of Figures

List of Tables

判天地之美，析万物之理，察古人之全。

——《庄子·天下》

"To see the sublime in nature;
To trace the patterns of things;
To embrace the wisdom of seers."

INTRODUCTION

This chapter provides an overview of the background of thermoacoustic instabilities and adjoint methods, and a summary of selected existing literature on these subjects. Additionally, the structure of the thesis is outlined.

1.1. THERMOACOUSTIC INSTABILITIES

Thermoacoustic instability is self-excited large-amplitude pressure oscillations in the combustors of aero-engines (Eckstein and Sattelmayer, 2006), rocket engines (Summerfield, 1951; Crocco and Cheng, 1956), gas turbines (Lieuwen, 1999), and boilers (Zhou and Meng, 2019). It is triggered by combustion in an enclosed volume and can be across a broad range of frequencies. Therefore, it is also often referred to as combustion instabilities. Since the increasing use of carbon-free fuels, such as hydrogen and ammonia, and the use of premixed combustors for the reduction of NOx emissions, it appears that these attempts increase the propensity of the combustion system to thermoacoustic instabilities. Thermoacoustic instability is caused by interactions between acoustic waves, combustion, and hydrodynamics, as shown in the feedback loop depicted in Fig. 1.1. This sequence begins when the flow of the gaseous fuel mixture is disturbed. The unsteady flow induces disturbances in the flame and unsteady heat release. These heat release fluctuations generate sound waves, which in turn perturb the flow, thus closing the feedback loop. If the acoustic oscillation resonates with the natural frequency of the enclosed volume, it could lead to unfavourable operational issues, catastrophic structural damage, and equipment failure (Lieuwen and Yang, 2005).

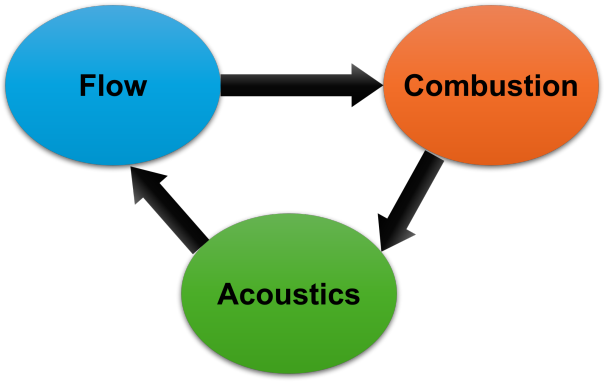

Figure 1.1: Interacting feedback loop giving rise to thermoacoustic instabilities.

In this section, the mechanism of thermoacoustic instability is described first. Then, thermoacoustic modelling approaches in existing literature are summarized. In the end, the control devices for suppressing and mitigating thermoacoustic instabilities are introduced.

1.1.1. Rayleigh criterion

In one of Lord Rayleigh's early works (Rayleigh, 1878), he described a heat-driven oscillation phenomenon and the condition of heat as a motive power to generate or sustain acoustic waves:

> "If heat be given to the air at the moment of greatest condensation, or taken from it at the moment of greatest rarefaction, the vibration is encouraged. On the other hand, if heat be given at the moment of greatest rarefaction, or abstracted at the moment of greatest condensation, the vibration is discouraged."

This is the well-known Rayleigh criterion. This is a necessary but not sufficient condition for instability to occur in a thermoacoustic system. Putnam and Dennis (1954) gave a preliminary mathematical representation of this condition. In later works, Chu (1956) and Culick (1987) provided explicit formulations of Rayleigh's criterion based on the definition of acoustic energy, applicable to a general analysis of thermoacoustic instabilities in arbitrary combustor geometries. The mathematical formalization of the Rayleigh criterion is expressed as,

$$\int_{\mathcal{V}} \int_0^T p\,\dot{Q}\,\mathrm{d}t\,\mathrm{d}V \geq \int_{\mathcal{V}} \int_0^T \sum L_i\,\mathrm{d}t\,\mathrm{d}V, \tag{1.1}$$

where $\sum L_i$ is the sum of all the loss mechanisms in the system, T is the oscillation period, and $\mathcal{V}$ is the volume of the system. The integral on the left-hand side is called the Rayleigh integral, and it states that the energy increases in the system when the acoustic pressure p and the unsteady heat release rate $\dot{Q}$ oscillate in phase. If the above inequality is satisfied, i.e., the energy added to the system by pressure-heat feedback exceeds the sum of all energy losses in the system, such as boundary radiation and viscous dissipation, instability is generated. The amplitude of a small disturbance will keep growing until it reaches saturation due to nonlinear effects, where the equality in Eq. (1.1) holds. The Rayleigh criterion has been used to diagnose local acoustic wave amplification due to the heat-addition process (Lieuwen and Yang, 2005).

The energy norms are very important for the quantification of disturbance mechanisms, analysing the growth and decay of the energy in small disturbances in a fluid system. Chu (1956) proposed the Chu-norm, a positive definite energy norm for characterizing the level of energy disturbance. In the absence of heat transfer at the boundaries, work done by boundary or body forces, heat, and material sources of energy, this norm is a monotone, non-increasing function of time. It is well-suited for analysing stability and energy transfer in compressible, viscous, and heat-conductive flows. Joseph George and Sujith (2011) demonstrated that it ensures self-adjointness of the linearized operator and avoids spurious transient energy growth, making it suitable for analyzing thermoacoustic instability.

1.1.2. Thermoacoustic modelling

In combustion systems, the time and length scales vary in a large range. The chemical reaction in the combustion process usually happens fast, and the flame front wrinkling is tiny, while the

acoustic waves are typically of low frequency and have long wavelengths. Hence, the prediction of thermoacoustic instability using only computational techniques is a real challenge and expensive. A typical methodology is to separate the flame dynamics and the acoustic field. The flame is considered to be infinitesimally short compared to the acoustic wavelength. The fast combustion process is studied by experiments or numerical simulations. The flame dynamics are described by the gain and phase differences between the unsteady heat release rate and the upstream flow disturbances. Acoustic physics is usually treated with analytical models. The flame models and the acoustic models used in thermoacoustic analysis are introduced in this section.

Flame models

Flame transfer function

In the field of thermoacoustic instability analysis, the concept of the transfer function can be traced back to Merk (1957), where the general transfer function of the heat source as a function of frequency was given. The flame transfer function (FTF) has been widely used to model flame dynamics in both analytical and practical applications because it is easy to measure by experiments, convenient to use in analytical models, and can be combined with numerical tools.

In linear models, the acoustic fluctuations are assumed to be small compared to the mean value. For premixed systems at constant equivalence ratio (the ratio of the actual fuel/air ratio to the stoichiometric fuel/air ratio), the flame dynamics is described by a flame transfer function (FTF) as follows,

$$\mathcal{F}(\omega) = G(\omega)\mathrm{e}^{\mathrm{i}\omega\varphi} = \frac{\hat{\dot{Q}}(\omega)/\bar{\dot{Q}}}{\hat{u}(\omega)/\bar{u}}, \tag{1.2}$$

where ω is the frequency of the perturbation, $\dot{Q}$ is the heat release rate, and u is the acoustic velocity fluctuation corresponding to different modes in the combustor. The $\hat{}$ denotes the Fourier transform of fluctuations, and $\bar{}$ denotes the mean values. The gain of the FTF, $G(\omega)$, represents the amplification effect of the flame on the incident acoustic flow perturbations, showing the property as a low-pass filter (Noiray, 2007). φ is the phase lag for the unsteady heat release rate responding to the upstream acoustic velocity. The FTF only depends on frequency and links the ratio between the Fourier transforms of the unsteady heat release rate fluctuations and acoustic velocity fluctuations.

The FTF is usually implemented within acoustic models as a heat release model. Summerfield (1951) first raised the hypothesis in the modelling of a liquid fuel rocket engine that the rate of evolution of combustion at a given instant is related to the upstream flow rate at some time τ earlier. This time-lag τ is a crucial parameter that characterises the gas convection effect in a system. A commonly used $n-\tau$ heat release law was introduced by Crocco (1951, 1952). The heat release rate fluctuation is related to the upstream acoustic velocity perturbations, with the following form in the time domain:

$$\dot{Q}'(t) = nu'(t-\tau), \tag{1.3}$$

where n is the coupling coefficient and $'$ denotes the time-domain fluctuations. The $n-\tau$ heat release model has been used in numerous studies on fundamental aspects of combustion instabilities. n and τ can be constants or vary in space (Crocco and Cheng, 1956; Nicoud et al., 2007). There are variants of $n-\tau$ heat release model that relate the unsteady heat release rate with acoustic pressure, upstream mass flow rate disturbances (Peracchio and Proscia, 1998; Dowling and Stow, 2003), or equivalence ratio perturbations (Lieuwen and Zinn, 1998).

A multi-time-lag model described in Polifke (2020), also known as the distributed-time-delay (DTD) model, provided a new perspective to examine the flame dynamics in the time domain. The response of the heat release rate, instead of happening instantly at a certain time lag after the velocity perturbation is imposed, is spread out over an interval of time. It is defined as the unit impulse response to the incoming velocity perturbations. The flame response can be described as a superposition of distributions or in terms of the histogram. Gopinathan et al. (2018) introduced a generalized coupling function that depends on the time lags to represent the distribution of time lags causing delayed heat release rate fluctuations. DTD models capture all key features of a typical FTF: a gain of unity at zero frequency, excess gain at low frequencies, and low-pass filter behaviour. Compared with the $n-\tau$ model, the DTD model can better reflect the flame dynamics in the system (Æsøy et al., 2020) and gives better prediction in stability (Bigongiari and Heckl, 2018).

Flame describing function

The describing function is a term used in control theory to represent nonlinear systems by making use of a family of transfer functions depending on the amplitude of the input. This concept is also adopted for nonlinear analysis in thermoacoustic systems. The flame describing function (FDF) is basically a family of FTFs evaluated repeatedly for increasing forcing levels. The FTF is only applicable when the initial disturbances are small. When the system experiences a large amplitude disturbance, nonlinear effects are profound, and the amplitude effect in flame dynamics has to be taken into account, as

$$\mathcal{F}(\omega, A) = \frac{\hat{\dot{Q}}(\omega, A)/\bar{\dot{Q}}}{\hat{u}(\omega, A)/\bar{u}}, \tag{1.4}$$

where A is the amplitude of acoustic velocity. In combination with an acoustic analysis, it allowed predictions of limit cycle amplitudes, resonant frequency shifting, mode switching, instability triggering, and hysteresis behaviour. Dowling (1999) developed a kinetic model for the flame response to flow disturbance and its amplitude. It is found that for nonlinearity in the heat release rate, the describing function analysis can give a good estimation of the limit-cycle frequency and amplitude. Noiray et al. (2008) measured the FDF of a matrix burner, and by combining it with an acoustic model, nonlinear dynamics observed in experiments were predicted. Durox et al. (2009) measured the FDF of the flame of different shapes: a single conical flame, a "V"-shaped flame, an "M"-shaped flame, and a group of conical flames stabilized on a perforated plate. It was shown that the gain and phase of the FDF greatly depend on the steady-state configurations. Bourgouin et al. (2015) measured FDF in an annular combustor with multiple matrix injectors and investigated the oscillations and limit cycles. FDF is also extended to not only accounting for the perturbation amplitude dependence but also the fluctu-

ations in equivalence ratio (Birbaud et al., 2008; Schuller et al., 2020).

Acoustic models

The acoustics are usually considered linear and can be modelled with analytical techniques. Analytical approaches can provide crucial physical insights and capture significant phenomena with a modest computational effort. The starting point for the acoustic analysis is usually the linearized Euler equations for compressible flow, neglecting viscous and thermal dissipation (Dowling and Stow, 2003; Rienstra and Hirschberg, 2004):

$$\frac{\mathrm{D}\rho'}{\mathrm{D}t} + \bar{\rho}\frac{\partial u_i'}{\partial x_i} = 0, \tag{1.5a}$$

$$\frac{\mathrm{D}u_i'}{\mathrm{D}t} + \frac{1}{\bar{\rho}}\frac{\partial p'}{\partial x_i} = 0, \tag{1.5b}$$

$$\frac{\mathrm{D}p'}{\mathrm{D}t} + \gamma\bar{p}\frac{\partial u_i'}{\partial x_i} = (\gamma - 1)q', \tag{1.5c}$$

where $\dfrac{\mathrm{D}}{\mathrm{D}t} = \dfrac{\partial}{\partial t} + \bar{u}_j\dfrac{\partial}{\partial x_j}$, γ is the specific heat ratio, and q' is the heat release rate per unit volume. Sometimes, an alternative form of the above equations (1.5), an inhomogeneous wave equation, is used to solve for acoustic disturbances,

$$\frac{1}{\bar{c}^2}\frac{\mathrm{D}^2p'}{\mathrm{D}t^2} - \frac{\partial^2 p'}{\partial x_i^2} = \frac{\gamma - 1}{\bar{c}^2}\frac{\mathrm{D}^2q'}{\mathrm{D}t^2}, \tag{1.6}$$

with $\bar{c}$ the speed of sound. A brief overview of the approaches in the existing literature to solving the above governing equations is given below.

The travelling wave-based approach

The travelling wave-based approach is initially reported in Rayleigh (1896). In a one-dimensional system, the Riemann invariants are exploited to decompose the flow fluctuations into upstream- and downstream-travelling components. Crocco and Cheng (1956) demonstrate a wave-based approach to analyse the high-frequency oscillations in a rocket combustion chamber. This method was later extended to full acoustic networks by Dowling (1995). With the network modelling approach, the geometry, boundary conditions, and heat-release source of the combustion system are modelled as individual elements, each described by a linear transfer function, connected by jump conditions. Evesque and Polifke (2002) applied the wave-based modelling approach to a generic annular combustor and investigated the effect of non-identical burners as a means of passive control. The method was also adapted by Schaefer and Polifke (2019) to treat systems with duct elements of varying cross-sectional area and arbitrary mean temperature profiles. Ghirardo et al. (2019) focused on low-frequency acoustic modes in a can-annular combustor, showing that the connection between neighbouring cans may trigger azimuthally-travelling unstable modes.

The Galerkin technique

One of the earliest applications of the Galerkin technique is reported in Zinn and Lores (1971) to analyse nonlinear axial combustion instabilities in a liquid-fuel rocket engine. The flow disturbance variables (usually pressure or acoustic velocity oscillations) are projected onto a set of basis functions satisfying the boundary conditions. The system can then be formulated as an eigenvalue problem. Solving the eigenvalue problem gives the complex eigenvalues containing the linear stability information and the eigenvectors containing the amplitude information of each mode. Balasubramanian and Sujith (2008b) used the Galerkin technique to analyse the acoustic pressure oscillations and ensuing nonlinear dynamics in a Rijke tube. Sayadi et al. (2014) used the Galerkin methods to approximate both the linear and nonlinear behaviour of a Rijke tube system, providing a numerical solution for the damped system and demonstrating phenomena such as mean-flow modulation and frequency switching. Kashinath et al. (2013) implemented a numerically computed FDF of premixed flame in a model of an open pipe, with damping included. They examined the fundamental acoustic mode and found the phase speed of velocity perturbations strongly affects the nonlinear thermoacoustic behaviour of ducted premixed flames. A drawback of the Galerkin approach is that, in practice, the solutions of acoustic flow variables are truncated and this might lead to significant errors (Dowling, 1995).

The Helmholtz solver framework

Nicoud et al. (2007) developed a numerical framework to solve Eq. (1.6) in the frequency domain, the inhomogeneous Helmholtz equation, neglecting the mean flow. A nonlinear eigenvalue problem can be formed from the discretized thermoacoustic system and an iterative method is used to solve the eigenvalues and eigenvectors. Unlike the linear Galerkin approach (Culick, 1988), the Helmholtz solver framework is not limited to particular choices of boundary impedance and the assumption that the flame only slightly perturbs the acoustic modes. Silva et al. (2013) combined the FDF with a linear Helmholtz solver and estimated the growth rate and limit cycle amplitude of the acoustic perturbations in a swirled combustor. Selle et al. (2006) combined the large-eddy simulation with the Helmholtz solver and investigated the rotating modes in an industrial swirled combustor. They found that the transverse acoustic modes in the combustion chamber could create a rotating motion of the flame, which leads to a self-sustained turning mode whose features resembled hydrodynamic swirled flow.

The Green's function approach

The Green's function technique, originally developed by George Green to tackle electrostatic problems (Green, 1828), has been widely used in various fields of physics and engineering, especially in the study of wave propagation. Lighthill's acoustic analogy benefits from the application of the Green's function technique (Lighthill, 1952). The Green's function is a powerful tool due to its computational efficiency and versatility. With the help of the Green's function, the acoustic disturbances can be expressed in the form of an integral equation. In unbounded space, the Green's function is called the free-space Green's function, and the analytical solution is known. In a confined system, the Green's function satisfying certain boundary conditions is called exact Green's function or tailored Green's function (Morse and Feshbach, 1953). Yang and Morgans (2016, 2017) developed a semi-analytical model based on Green's function for

a short circular hole with through flow to study the vortex-sound interactions. The Green's function was in terms of stagnation enthalpy fluctuations. Hegde et al. (1988) established a theoretical model based on Green's function to study the sound field of a V-shaped flame in a rectangular duct. Heckl et al. (2022) gave a summary of the tailored Green's function framework applications in the study of aerodynamic and thermoacoustic instabilities. Arabi and Heckl (2025) used the tailored Green's function approach to examine noise-induced nonlinear effects on thermoacoustic instabilities in a combustion chamber prototype.

1.1.3. Control of thermoacoustic instabilities

There are mainly two ways to prevent thermoacoustic instabilities: (1) through the equipment design, to avoid such instabilities in the designing stage. It is conducted through shape optimization, prediction of safe operation conditions, and design of certain crucial components, such as flame stabilizers. (2) For an existing combustor experiencing such instabilities, one can pursue feedback control strategies or acoustic liners that increase acoustic energy dissipation in the engine so that the unwanted noise and vibration can be mitigated. A thorough review by Zhao and Li (2015) described the use and effectiveness of various acoustic dampers such as Helmholtz resonators, perforated liners, baffles, half- and quarter-wave tubes in aerospace combustors.

Existing feedback control techniques and devices have been extensively studied. Raghu and Sreenivasan (1987) examined a set of active control methods, including heat addition, force addition, and periodic mass addition, for the suppression of pressure oscillations in a laboratory scale pipe flow and demonstrated that the combination of mesh screens and heating coils applied to a large combustion set-up successfully eliminated undesired pressure oscillations. Dowling and Morgans (2005) summarized the application of feedback control to mitigate thermoacoustic instabilities, including the development of control strategies and controller design. They also demonstrated a case of feedback control on a full-scale combustion system. Zhao and Morgans (2009) used Helmholtz resonators with tuned geometry to stabilize combustion systems with multiple unstable modes, validated through numerical simulations and experiments on a Rijke tube. Zhao and Li (2012) developed a Helmholtz resonator with oscillating volume that is more robust and capable of stabilizing the combustion system at a faster rate than that of a conventional Helmholtz resonator. Bellucci et al. (2005) applied a Helmholtz damper with cooling flow entering the resonator volume to a gas turbine combustor for noise reduction.

Porous materials and micro-perforated plates are often used as noise-control devices. Gullaud and Nicoud (2012) studied the impact of multiperforated plates on acoustic modes in aeronautical gas turbine combustion chambers with a 3D Helmholtz solver and revealed that the damping effect of the perforated plate varies with mode structure and bias flow speed. Another investigation by Bellucci et al. (2004) assessed the impedance of perforated plates with a low-Mach number bias flow over a range of plate thicknesses, orifice size, and bias flow velocities. Conventional porous acoustic absorbers use viscous dissipation and heat conduction at the fluid-solid interface to reduce the acoustic energy of noise. Some specially designed acoustic metamaterials (Yang and Sheng, 2017), consist of microstructures that effectively damp acoustic waves, such as micro honeycomb structures and inner Helmholtz resonators (Boutin,

2013). Modelling methods of porous materials can be found in Allard and Atalla (2009). One of the widely used approaches is to obtain an effective medium description of porous media and micro-perforated panels as effective sound absorbers, via upscaling methods. Olny and Boutin (2003) used the homogenization method to analyse acoustic wave propagation in rigid double-porosity media saturated with fluid, revealing that macroscopic flow behaviour depends on the permeability contrast, with low contrast leading to a generalized Darcy's law and high contrast causing pressure diffusion effects in micro-pores that influence material dissipation and dynamic bulk modulus. Marigo and Maurel (2017) developed a homogenization method to determine the effective behaviour of a periodically stratified block, incorporating discontinuity conditions, or jump conditions, for the displacement and for the normal stress at the boundaries of the slab.

1.2. ADJOINT METHODS

Adjoint equations are a powerful mathematical and computational tool widely used in physics, engineering, and optimization problems. The origin of the adjoint equation traces back to de Lagrange (1763), who introduced them as a technique for reducing the order of linear differential equations and applying them to problems such as fluid motion and vibrations. Over time, adjoint methods have gained prominence, particularly due to their efficiency in reducing computational costs, especially when dealing with systems with a small number of outputs for a large range of input variables. This property makes them particularly valuable in optimization problems, where a single objective function—often dependent on many input parameters—must be minimized or maximized.

The adjoint equations are for systems with linear operators and can be derived in two ways: either using the Lagrange-Green identity or using a Lagrange multiplier approach. For a system with a linear operator $\mathbf{A}$, its adjoint linear operator $\mathbf{A}^*$ satisfy the following identity,

$$\langle \mathbf{v}, \mathbf{A}\mathbf{u} \rangle = \langle \mathbf{A}^* \mathbf{v}, \mathbf{u} \rangle, \tag{1.7}$$

where $\langle \, , \, \rangle$ denotes an inner product. The adjoint operator doesn't have any physical meaning. If the operator of the adjoint equation is identical to the operator of the direct system, i.e., $\mathbf{A} = \mathbf{A}^*$, this is a self-adjoint system. Otherwise, it is a non-self-adjoint system.

Within the context of constrained optimization, for a system governed by the state equation

$$\mathbf{F}(\mathbf{u}, \mathbf{g}) = 0, \tag{1.8}$$

with $\mathbf{u}$ the state vector. To find the control vector $\mathbf{g}$ that minimizes the cost function $J(\mathbf{u}, \mathbf{g})$, The Lagrangian is defined as

$$\mathcal{L} = J(\mathbf{u}, \mathbf{g}) - \mathbf{v} \cdot \mathbf{F}(\mathbf{u}, \mathbf{g}) \tag{1.9}$$

with $\mathbf{v}$ the vector of Lagrange multipliers. Setting the variation of the Lagrangian with respect

to the independent variables $\mathbf{u}$, $\mathbf{g}$, and $\mathbf{v}$ respectively to zeros, this gives rise to

$$\frac{\partial \mathcal{L}}{\partial \mathbf{u}} = 0 \quad \rightarrow \quad \left[\frac{\partial \mathbf{F}}{\partial \mathbf{u}}\right]^{\intercal} \mathbf{v} = \frac{\partial J}{\partial \mathbf{u}}, \tag{1.10a}$$

$$\frac{\partial \mathcal{L}}{\partial \mathbf{g}} = 0 \quad \rightarrow \quad \left[\frac{\partial \mathbf{F}}{\partial \mathbf{g}}\right]^{\intercal} \mathbf{v} = \frac{\partial J}{\partial \mathbf{g}}, \tag{1.10b}$$

$$\frac{\partial \mathcal{L}}{\partial \mathbf{v}} = 0 \quad \rightarrow \quad \mathbf{F}(\mathbf{u}, \mathbf{g}) = 0. \tag{1.10c}$$

The above derivation yields the adjoint equations (1.10a), the gradient expression that defines the optimality condition (1.10b), and (1.10c) recovers the state equation (1.8). By solving the adjoint equation for $\mathbf{v}$, one can obtain the gradient information at once for all control variables in the vector g. This makes the adjoint equation a powerful and efficient tool for gradient computation.

The adjoint equations can also be obtained using the identity (1.7), as follows

$$\langle \mathbf{v}, \frac{\partial \mathbf{F}}{\partial \mathbf{u}} \delta \mathbf{u} \rangle = \langle \left[\frac{\partial \mathbf{F}}{\partial \mathbf{u}}\right]^{\intercal} \mathbf{v}, \delta \mathbf{u} \rangle, \tag{1.11}$$

with the inner product defined as $\langle \mathbf{a}, \mathbf{b} \rangle = \mathbf{a}^{\intercal}\mathbf{b}$.

A review of the application of adjoint equations in fluid mechanics problems is reported by Luchini and Bottaro (2014), with supplementary material which provides a detailed introduction to the mathematical background of adjoint methods. In this section, some applications of adjoint methods on stability and sensitivity analysis are reviewed.

1.2.1. Adjoint methods in stability analysis

One of the first reported works using the adjoint equation to solve PDE is by Green (1828), who used Green's function of the Poisson equation to solve electromagnetic wave fields. The unknown function in the adjoint equation is called Green's function in many applications. Greenberg (1978) showed how to define the boundary conditions and the forcing term of the adjoint system as a Dirac delta function to evaluate the value of interested variables at a target location. Hill (1995) presented the adjoint equations for the linearized Navier-Stokes equations for incompressible boundary layers and demonstrated that unsteady forcing near the critical layer induces the strongest response, while boundary motion is most effective in the normal direction, with results validated against previous analytical and numerical findings. Similarly, for compressible flows, Pralits et al. (2000) analysed the sensitivity of disturbances in a compressible boundary layer to wall and momentum forcing using adjoint parabolized stability equations. Their findings highlighted that for compressible flow, the three-dimensional disturbances are the most sensitive to wall forcings. Luchini and Bottaro (1998) defined the receptivity of the Görtler instability with the aid of Green's function. The numerical solution of Green's function is obtained from an adjoint problem via a backward-in-time technique. The receptivity provides the amplitude of the nonlinear saturation stage efficiently, without repetitive computations for every new initial disturbance.

1.2.2. Adjoint methods in sensitivity analysis

The adjoint method is a powerful tool for optimization and control problems in complex systems, with extensive applications in hydrodynamics stability (Pralits et al., 2002; Luchini and Bottaro, 2014; Schmid and Brandt, 2014). Compared with the traditional finite-difference approach, the adjoint method is more cost-effective in the analysis of systems that depend on many parameters. Previous adjoint-sensitivity work can be broadly subdivided into three types of analysis:

- To evaluate eigenvalue variations due to generic base-state modifications δU, possibly related to uncertainties in the measurement or in the calculation of the base state. Bottaro et al. (2003) first applied the *base-state sensitivity analysis* to examine the eigenvalues of the Orr-Sommerfeld operator. They found variations (of given amplitude) of the basic flow with the most destabilizing effect on the eigenvalues for the case of the plane Couette flow and introduced the concept of the δU-pseudospectrum. Brandt et al. (2011) calculated the sensitivity to base-flow modifications for a flat-plate boundary layer, demonstrating that Tollmien-Schlichting waves are highly sensitive to such changes, whereas streamwise streak amplification remains robust due to the differing spatial structures of optimal forcing and response.

- To find the eigenvalue changes due to feedback sources in the flow disturbances. This is often referred to as *structural sensitivity analysis*. Giannetti and Luchini (2007) conducted such an analysis for the case of the flow around a cylinder and identified regions in which variations, for instance, due to truncation of the domain or grid resolution, cause the largest eigenvalue drift.

- To evaluate the sensitivity of source terms acting on the steady equations of the base flow in order to stabilize unstable eigenmodes. Marquet et al. (2008) calculated the *sensitivity to a steady force* and gave predictions of possible passive control methods to suppress the vortex shedding in the wake of a cylinder. Pralits et al. (2010) introduced the idea of *structural sensitivity to base-flow modifications* and showed successful examples of its application. Other steady source terms can easily be envisaged for the mass and/or energy conservation equations. Luchini et al. (2008) conducted a structural sensitivity analysis for finite-amplitude global modes on a periodic base flow and showed good comparison with experiments on the flow control in the cylinder wake.

Existing literature reflects substantial endeavours towards uncertainty quantification and sensitivity analysis in thermoacoustic systems (Orchini and Juniper, 2016; Juniper and Sujith, 2018), as well as shape optimization of thermoacoustic systems such as the Rijke tube, in swirl combustors (Falco and Juniper, 2021), also using low-order models (Aguilar and Juniper, 2018). A comprehensive review of the applications of adjoints to thermoacoustic problems has been published by Magri (2019). Mensah and Moeck (2017) applied the adjoint perturbation theory to a generic annular combustor model and found the optimal damper arrangements and the impedance design to mitigate instabilities. Magri et al. (2020) extended the original Rayleigh criterion to arbitrary time intervals and interpreted it in the frequency domain. An adjoint Rayleigh criterion was also derived, which was able to provide the sensitivity information

of stability to perturbations of the heat source. Schäfer et al. (2022) developed a hybrid adjoint approach, exploiting the self-adjointness of duct elements and simplifying the derivation of the adjoint system for sensitivity analysis of thermoacoustic network models. By computing the feedback sensitivity and base-state sensitivity of an annular combustor network model, they tuned a Helmholtz resonator to achieve passive control. Juniper (2018) applied adjoint methods to a thermoacoustic Helmholtz solver and calculated receptivity, feedback sensitivity, and base-state sensitivity for a Rijke tube and a rocket engine combustor. Base-state sensitivities were calculated to evaluate the effect of base-state variables such as time delay in the heat release model, boundary conditions, and heat release distribution. He revised the Rayleigh criterion for linear analysis of thermoacoustic oscillations, showing that in non-self-adjoint systems, the rate of change of energy is the integral of the injected heat-release rate multiplied by the adjoint pressure instead of the physical pressure. Aguilar et al. (2017) calculated feedback sensitivity and base-state sensitivities of a 1D two-segment thermoacoustic system. The base-state sensitivity of reflection coefficients, time delay, and interaction index of the heat release model. In a later study, Aguilar and Juniper (2020) optimized the combustor geometry based on the sensitivity analysis of a longitudinal bluff-body combustor. They examined the eigenvalue variation due to the steady base flow alteration by changing the combustor geometry. This is similar to the third type of sensitivity analysis but not quite the same, because there is no steady force introduced into the system.

The conventional adjoint sensitivity analysis is based on the direct system, i.e., the governing equations. In recent work, Ozan and Magri (2024) developed a data-driven computational strategy using a parameter-aware echo-state network to infer adjoint sensitivities without requiring explicit governing equations, demonstrating its application in thermoacoustics by accurately predicting parameter and initial condition sensitivities, handling noisy data, and enabling instability suppression through gradient-based optimization.

1.3. THESIS STRUCTURE

The primary motivation of this work is to explore the application of adjoint methods in various aspects of thermoacoustic studies. This gives rise to three distinct research projects, each addressed in a separate chapter. The structure of this research work is shown in Fig. 1.2.

In Chapter 2, the adjoint Green's function approach is developed for the purpose of modelling thermoacoustic systems incorporated with the mean flow and predicting the nonlinear dynamics. The following research questions are answered:

- ***How can the Green's function framework be extended to accurately model non-self-adjoint thermoacoustic systems that include the effects of mean flow?***
- ***What is the influence of mean flow velocity on the onset and nonlinear behaviour of thermoacoustic instabilities?***

Chapter 3 shows a framework of adjoint-based sensitivity analysis, which is employed to derive gradient information that can be used to evaluate uncertainties within thermoacoustic systems and to inform strategies for their stabilization. In this chapter, the following questions are answered:

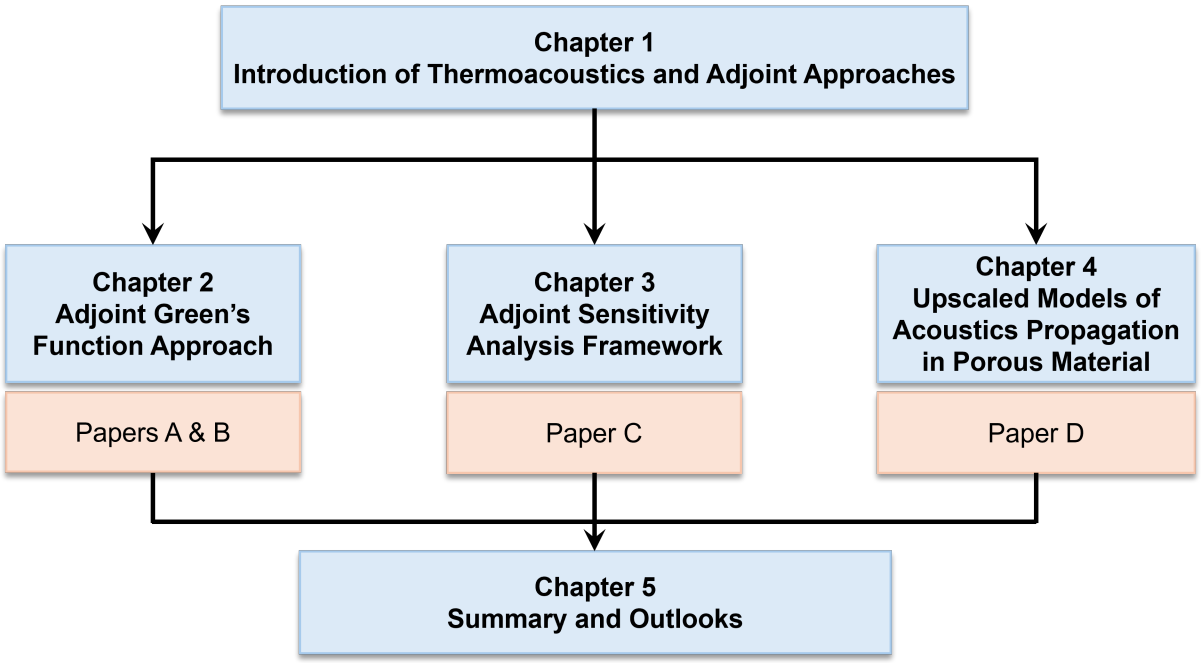

Figure 1.2: The structure of the thesis and the published/ongoing articles based on this work. Paper A: Wei et al. (2024), Paper B:Wei and Arabi (2025) under review, Paper C: Wei et al. (2025), Paper D:Wei and Bottaro (2025) ongoing.

- ***How can adjoint sensitivity analysis quantify the effects of base-flow uncertainties and steady/unsteady feedback on thermoacoustic instability to inform control strategies?***
- ***How does the critical geometry parameter (premixer length) influence the effectiveness of the above mechanisms?***

In Chapter 4, the homogenization approach is applied to model the acoustic propagation properties of porous material with micro-periodic structures, which play a crucial role in mitigating thermoacoustic instabilities. The focus is on the development of effective jump conditions for acoustic wave propagation across a heterogeneous thin region consisting of air and porous material. The following questions are answered in this chapter:

- ***How can homogenization theory be applied to develop accurate models of acoustic wave reflection and transmission at heterogeneous interfaces? What are the limits of validity for these models?***

In the end, Chapter 5 presents the summary of the findings from these investigations and gives some outlooks of research in this field.

物无非彼，物无非是。自彼则不见，自知则知之。

——《庄子·齐物论》

"All is perspective: Outward gaze obscures, inward sight reveals."

THE ADJOINT GREEN'S FUNCTION APPROACH

This chapter introduces a fundamental framework for modelling thermoacoustic instabilities in systems with a mean flow, based on the definition of the adjoint Green's function (AGF). The presence of the mean flow makes the acoustic analogy equation become a non-self-adjoint system, where the tailored Green's function approach fails. The AGF approach transforms the acoustic analogy equation into an integral equation, enabling a direct calculation of the system's response to various external forcing terms. A simple one-dimensional system is examined, consisting of a steady mean flow and a nonlinear heat source with an amplitude-dependent time-delay heat release model. The adjoint Green's problem gives receptivity information that quantifies the system's response to initial, boundary, or other forcing terms. While both adjoint-based sensitivity analysis and the AGF approach rely on adjoint equations, the former is typically used to optimize system design and control strategies, whereas the latter provides insights into how disturbances propagate and interact within the system. The versatility of this framework is demonstrated by applying it to two resonators with different boundary conditions, two configurations (flow duct with and without a uniform temperature field), and systems with different forcings. Additionally, the role of the Dirac delta function in capturing local receptivity is highlighted, showing the effectiveness of the AGF in the prediction of thermoacoustic instabilities.

The structure of this chapter is as follows: Section 2.1. gives a brief introduction to the bifurcation theory and a summary of mean flow effects and noise-induced dynamics in thermoacoustic systems. Section 2.2. provides full details of the theoretical, highlighting the reciprocity property between the direct and the adjoint Green's functions in both the time and the frequency domain. The theory is developed based on the tube configuration with uniform temperature flow. Section 2.3. shows the application of theory for a Rijke tube case, focusing on the bifurcation and hysteresis behaviour by varying the position of the heat source, the tube length, and the heater power. In section 2.4., the theory is applied to an experimental matrix burner setup, and the prediction results are compared with experiment results. Then, the theory is extended to the flow duct with a non-uniform temperature field, of which the details are provided in section 2.5.. Furthermore, in section 2.6., we investigated the noise-induced phenomenon by introducing different external coloured noises into the thermoacoustic system. The conclusions and outlook of this study are given in section 2.7..

2.1. BACKGROUND

2.1.1. Bifurcation theory

In dynamical systems theory, a bifurcation refers to a sudden qualitative change in a nonlinear system's behaviour due to an infinitesimal variation in control parameters. When this transition

shifts the system from a stable steady state to an oscillatory state, it is specifically known as a Hopf bifurcation (Strogatz, 2018). There are two types of Hopf bifurcation, supercritical and subcritical, of which the diagrams are depicted in Fig. 2.1.

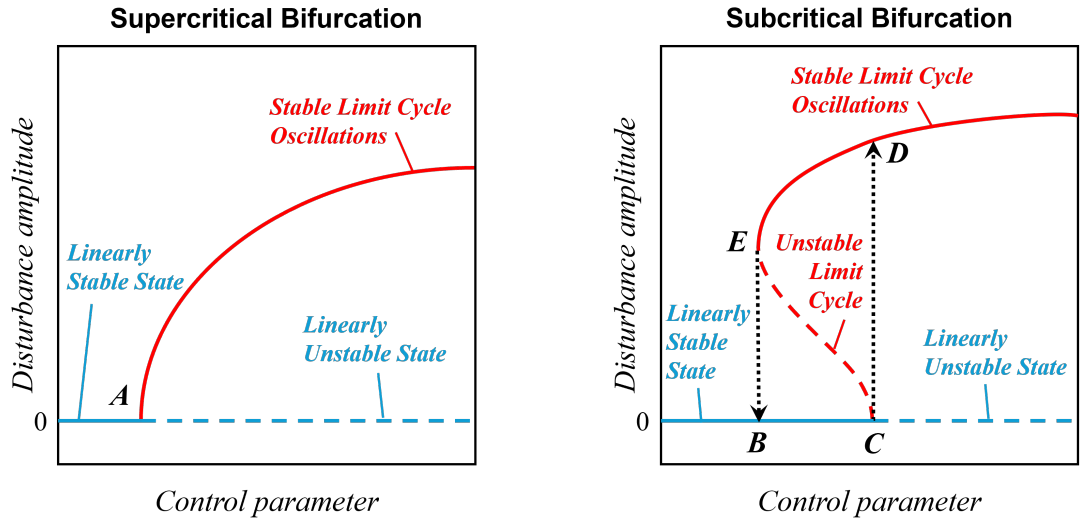

Figure 2.1: Diagrams of Hopf bifurcations: supercritical bifurcation (left) and subcritical bifurcation (right).

For a supercritical Hopf bifurcation, the system remains stable in a non-oscillatory state until the control parameter reaches a critical threshold. When this threshold is exceeded, the non-oscillatory state loses stability, causing the system to transition into an oscillatory state characterized by a stable, low-amplitude limit cycle. The parameter value at which this loss of stability occurs is referred to as the Hopf point (point A in Fig. 2.1).

For a subcritical Hopf bifurcation, the system jumps into large amplitude oscillations immediately when the control parameter reaches the critical value of Hopf bifurcation point C. Moreover, when returning to the non-oscillatory state, the control parameter must be reduced well beyond the critical threshold. The point at which stability is regained during this reversal process, point E in Fig. 2.1, is known as the fold point. When the value of the control parameter lies in the range between a fold point and a Hopf bifurcation point, the system exhibits bistability, meaning it can settle into either an oscillatory or a non-oscillatory state depending on initial conditions. In this range, if the oscillation amplitude of the system is forced to be large enough, the stable state can jump to an unstable state. This phenomenon is known as triggering. The unstable limit cycle marks the stability margin for the initial excitations as well as the triggering amplitude. The path for the system to go from a stable state to an unstable state and the path that the system returns to a stable state from an unstable state are different. This is known as the hysteresis phenomenon. The region formed by points $B \rightarrow C \rightarrow D \rightarrow E$ is called the hysteresis region.

2.1.2. Rijke tube

The Rijke tube is the simplest thermoacoustic system, consisting of a vertical tube with both ends open and a heated wire mesh at a quarter to the bottom end, as shown in Fig. 2.2(a). Once the wire mesh is heated, it causes contraction and expansion of air and consequently leads to unsteady flow in the tube and generation of acoustic waves. The acoustic waves resonate with the tube, and sound is generated. The Rijke tube is very useful for the investigation of elementary mechanisms of thermoacoustic instability and its dynamics. Experiments and theory have shown that such a thermoacoustic system exhibits bifurcations and hysteresis.

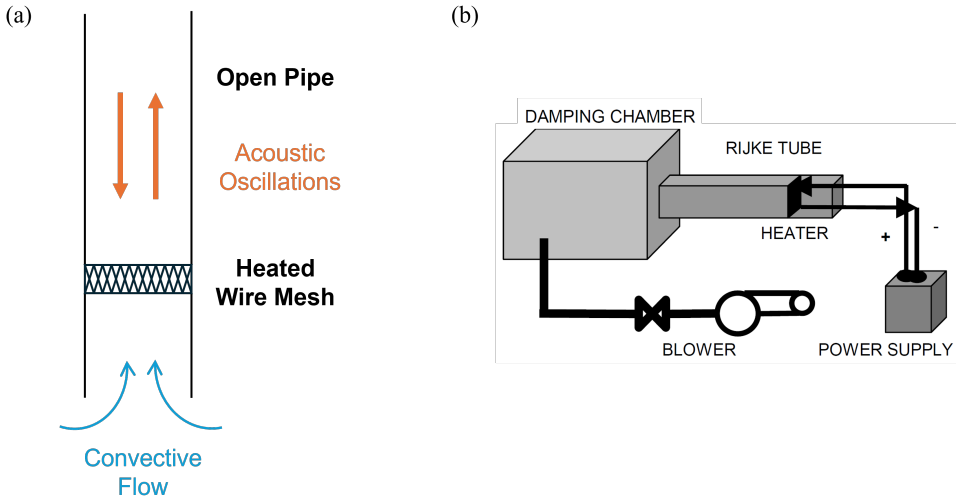

Figure 2.2: (a) Sketch of a Rijke tube. (b) Experimental setup of horizontal electric Rijke tube with a forced mean flow, taken from Matveev (2003b).

An early review of the studies on the Rijke tube can be found in Raun et al. (1993). The horizontal Rijke tube setup was devised by Heckl (1988, 1990) to decouple the variation of mean flow and the heat release rate fluctuations of the electrical-heated source placed within the tube. It has been widely used for laboratory-scale experiments to study the dynamics of thermoacoustic instabilities, as shown in Fig. 2.2(b). Matveev and Culick (2003a) (cf. also refs. Matveev (2003a,b)) investigated the nonlinear effects in a non-uniform temperature Rijke tube and the balance between thermoacoustic energy and acoustic losses. Gopalakrishnan and Sujith (2014) observed hysteresis and subcritical bifurcations in a horizontal Rijke tube setup by varying the heater power, the mass flow rate, and the heat source position.

2.1.3. The mean flow contribution

Existing investigations on acoustics in a confined geometry using (tailored) Green's function approach have consistently adopted the zero-Mach-number assumption, thus neglecting the mean flow. Mean flow can, however, be important, and several analytical methods exist which allow

for its inclusion. It was argued by Nicoud and Wieczorek (2009) that not only the heat source but also the mean flow could enhance the non-normality of the system, favouring the possibility of transient growth of instabilities. Stow and Dowling (2001), Orchini et al. (2022), and Polifke et al. (2001) have used a wave-based network model by describing the acoustic field in various combustion systems in terms of Riemann invariants, with forward- and backward-travelling waves displaying different transport speeds.

2.1.4. The noise effects

A comprehensive summary of noise-induced dynamics in thermoacoustic systems is provided by Kabiraj et al. (2020). Jegadeesan and Sujith (2013) conducted experiments in a ducted non-premixed flame system and observed noise-induced triggering phenomena: when a stable system is subject to a low amplitude noise, it evolves transiently towards an unstable limit cycle state. It is well-established that the linearised equations describing thermoacoustic systems are non-normal (Balasubramanian and Sujith, 2008b,a), meaning transient growth plays a significant role in amplifying small perturbations and thus triggering instabilities under noise. Waugh and Juniper (2011) and Waugh et al. (2011) investigated the effect of different coloured noise on triggering thermoacoustic instabilities in a Rijke tube model. Their findings showed that pink noise (with higher power at low frequencies) is more effective at inducing high-amplitude oscillations than white noise (with power equally distributed across all frequencies). Blue noise (with higher power at high frequencies) was found to be the least effective. Kabiraj et al. (2015) experimentally investigated the noise-induced dynamics of a thermoacoustic system undergoing a subcritical Hopf bifurcation and found that as the system approaches the bistable region, the noise level required to achieve an optimal coherent response decreases, suggesting that this behaviour could serve as a precursor to Hopf bifurcations. Additionally, Gopalakrishnan and Sujith (2015) examined the influence of external noise on hysteresis characteristics in a horizontal Rijke tube. Their results showed that increasing noise intensity reduces the width of the hysteresis zone, while high-intensity noise can suppress both subcritical transitions and hysteresis. Noise-induced transition can also happen between multiple oscillatory states. Bonciolini et al. (2017) applied system identification to a thermoacoustic system modelled by a Van-der-Pol oscillator. The nonlinear system is driven by coloured noise mimicking stochastic forcing by turbulence. Noiray and Schuermans (2013) performed measurements on the dynamics of azimuthal thermoacoustic modes in gas turbine annular combustion chambers and developed a theoretical framework through system identification. Their analysis revealed that the modes intermittently switch between standing and rotating waves due to stochastic perturbations arising from highly turbulent, reactive flows. To the authors' knowledge, existing models for the prediction of noise-induced dynamics in thermoacoustic systems neglect the effects of mean flow.

2.2. THEORETICAL FRAMEWORK

The theoretical framework is developed for a uniform temperature flow-duct. The configuration studied is described in section 2.2.1. The governing equations are given in section 2.2.2. and solved for the case without forcing in section 2.2.3. The full governing equations can be solved with minimal effort if they are converted into an integral equation. To this end, the direct Green's function is introduced in section 2.2.4. The adjoint Green's function is introduced in Section 2.2.5. and calculated in section 2.2.6. Its relationship with the direct Green's function is given in section 2.2.7.. The final result for the integral governing equation is shown in section 2.2.8. A by-product of the integral equation is an algebraic equation for the complex frequencies of the thermoacoustic modes; this equation is derived in section 2.2.9.

2.2.1. The configuration considered

Our configuration is shown in Fig. 2.3. It is a one-dimensional resonator, i.e., a straight tube of length L. The upstream end at $x = 0$ is described by the reflection coefficient R_0, and its downstream end at $x = L$ is described by R_L. We do not limit ourselves to idealized boundary conditions but, in principle, allow the reflection coefficients to be complex functions of frequency.

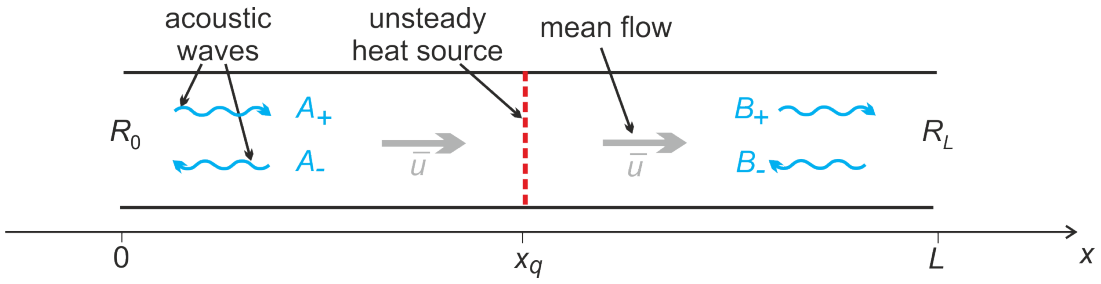

Figure 2.3: Schematic illustration of a flow duct with mean velocity $\bar{u}$, an unsteady heat source at x_q, acoustic waves with amplitudes A_+, A_-, B_+, B_- and reflection coefficients R_0 and R_L.

A steady uniform flow with speed $\bar{u}$ passes through the tube and the Mach number, $M = \bar{u}/c$, is assumed to be smaller than 1. The mean values of temperature ($\bar{T}$), density ($\bar{\rho}$), and speed of sound (c) are also uniform along the tube. We also neglect viscous and thermal dissipation. Since there is neither a temperature gradient nor a sudden area change in the present simplified setting, the generation of entropy waves is not considered (Marble and Candel, 1977; De Domenico et al., 2021).

An unsteady heat source is located at the axial position x_q. This source is assumed to be compact and described in terms of the delta function by

$$q(x,t) = q(t)\delta(x - x_q); \tag{2.1}$$

$q(x,t)$ is the rate of heat release per unit mass (local heat release rate). The time-dependent

part, $q(t)$, is closely related to the global heat release rate, $Q(t)$, by

$$Q(t) = S\bar{\rho}q(t), \tag{2.2}$$

where S is the cross-sectional area of the tube. The rate of heat release is not independent but coupled with the acoustic field. A generalised n-τ heat release law developed by Heckl (2015) is used to describe this coupling,

$$q(t) = K\left[n_1 u_q(t-\tau) - n_0 u_q(t)\right], \tag{2.3}$$

where u_q is the acoustic velocity at the heat source. Our assumption that the mean temperature is uniform implies that we neglect the mean heat release rate from the heat source and only consider the fluctuating part. In this context, the parameter K is a measure of the coupling between the heat release rate and the acoustic field. We call K the "heater power" with units of J kg^{-1}. The three parameters τ (time-lag), n_0 and n_1 (coupling coefficients) are assumed to depend on the non-dimensional acoustic velocity amplitude at the heat source, $\epsilon = A/\bar{u}$, with $\bar{u}$ denoting the mean flow velocity and A the amplitude of $u_q(t)$, by the following expressions,

$$\tau = \tau_0 + \tau_2\epsilon^2, \tag{2.4a}$$

$$n_0 = \frac{1}{2}(g_0 - g_1\epsilon - 1), \tag{2.4b}$$

$$n_1 = \frac{1}{2}(g_0 - g_1\epsilon + 1). \tag{2.4c}$$

The quantities $\tau_0,\ \tau_2,\ n_0,\ n_1$, in Eqs. (2.4) are constants. g_0 and g_1 are the parameters obtained by fitting a flame describing function (Heckl, 2015). Eq. (2.3) represents a nonlinear heat release rate law due to the amplitude dependence of its parameters.

2.2.2. Governing equations for the acoustic field

The acoustic field resulting from the unsteady heat source in the presence of a mean flow can be described by an acoustic analogy equation in terms of acoustic velocity potential, similar to Eq. (1.6),

$$\frac{\partial^2\phi}{\partial t^2} + 2\bar{u}\frac{\partial^2\phi}{\partial t\partial x} - (c^2 - \bar{u}^2)\frac{\partial^2\phi}{\partial x^2} = -(\gamma-1)q(x,t). \tag{2.5}$$

This is a PDE for the acoustic velocity potential $\phi(x,t)$; the heat release rate appears in the forcing term on the right-hand side. The initial conditions represent the excitation of the heat source acting only at the point x_q, and they are given by

$$\phi(x,t)\Big|_{t=0} = \varphi_0\delta(x - x_q), \tag{2.6}$$

$$\left[\frac{\partial\phi}{\partial t} + \bar{u}\frac{\partial\phi}{\partial x}\right]_{t=0} = \varphi_0'\delta(x - x_q), \tag{2.7}$$

where φ_0 and φ_0' have prescribed values.

The boundary conditions at $x = 0$ and $x = L$ are given in the frequency-domain by the reflection coefficients $R_0(\omega)$ and $R_L(\omega)$.

2.2.3. Natural frequencies of the unforced uniform-temperature system

The unforced version of the PDE (2.5) governs the propagation of acoustic waves up and down the flow duct on either side of x_q, where $q(x,t) = 0$. We transform this into the frequency domain (assuming the time dependence $\mathrm{e}^{-\mathrm{i}\omega t}$) in order to determine the wave numbers of these waves. This gives

$$\omega^2\hat{\phi} + 2\bar{u}(\mathrm{i}\omega)\frac{\partial\hat{\phi}}{\partial x} + (c^2 - \bar{u}^2)\frac{\partial^2\hat{\phi}}{\partial x^2} = 0, \tag{2.8}$$

where $\hat{\phi}(x,\omega)$ is the frequency-domain equivalent of $\phi(x,t)$. Eq. (2.8) is readily solved when $\hat{\phi}$ is assumed to behave in space as $\mathrm{e}^{\mathrm{i}kx}$. Two wave numbers are obtained, of the waves travelling with and against the flow, respectively:

$$k_+ = \frac{\omega}{c+\bar{u}}, \qquad \text{and} \qquad k_- = \frac{\omega}{c-\bar{u}}. \tag{2.9}$$

The acoustic velocity potential can then be written as a superposition of forward and backward travelling waves:

$$\hat{\phi}(x,\omega) = \begin{cases} A_+\mathrm{e}^{\mathrm{i}k_+x} + A_-\mathrm{e}^{-\mathrm{i}k_-x} & \text{for} \quad 0 < x < x_q \\ B_+\mathrm{e}^{\mathrm{i}k_+(x-L)} + B_-\mathrm{e}^{-\mathrm{i}k_-(x-L)} & \text{for} \quad x_q < x < L, \end{cases} \tag{2.10}$$

where A_+, A_-, B_+ and B_- are (generally complex) amplitudes of the velocity potential, see Fig. 2.3.

The reflection coefficients R_0 and R_L are used to define the boundary conditions. At $x = 0$ there is

$$R_0 = \left.\frac{A_+\mathrm{e}^{\mathrm{i}k_+x}}{A_-\mathrm{e}^{-\mathrm{i}k_-x}}\right|_{x=0}, \quad \text{giving} \quad A_+ = A_-R_0, \tag{2.11}$$

and likewise at $x = L$,

$$R_L = \left.\frac{B_-\mathrm{e}^{-\mathrm{i}k_-(x-L)}}{B_+\mathrm{e}^{\mathrm{i}k_+(x-L)}}\right|_{x=L}, \quad \text{giving} \quad B_- = B_+R_L. \tag{2.12}$$

This reduces the number of unknown amplitudes to two, and Eq. (2.10) becomes

$$\hat{\phi}(x,\omega) = \begin{cases} A_-(R_0\mathrm{e}^{\mathrm{i}k_+x} + \mathrm{e}^{-\mathrm{i}k_-x}) & \text{for} \quad 0 < x < x_q \\ B_+(\mathrm{e}^{\mathrm{i}k_+(x-L)} + R_L\mathrm{e}^{-\mathrm{i}k_-(x-L)}) & \text{for} \quad x_q < x < L. \end{cases} \tag{2.13}$$

The natural frequencies ω_n of the tube as an acoustic resonator, are obtained by considering the case without the heat source, where the sound field in the tube is given by

$$\hat{\phi}(x,\omega) = A_+\mathrm{e}^{\mathrm{i}k_+x} + A_-\mathrm{e}^{-\mathrm{i}k_-x} \quad \text{for} \quad 0 < x < L. \tag{2.14}$$

The boundary conditions given above in terms of R_0 and R_L have to be satisfied, and this leads to two homogeneous equations for A_+ and A_- and subsequently to the characteristic equation

$$-1 + R_0R_L\mathrm{e}^{\mathrm{i}(k_+ + k_-)L} = 0. \tag{2.15}$$

The left-hand side of the above equation is a function of ω. Thus Eq. (2.15) can be written as

$$F(\omega) = 0, \quad \text{with} \quad F(\omega) = -1 + R_0 R_L \mathrm{e}^{\mathrm{i}\omega \frac{2cL}{c^2 - \bar{u}^2}}. \tag{2.16}$$

The solution of Eq. (2.16) gives the natural frequencies ω_n of the uniform-temperature duct for monde $n = 1, 2, 3...$

We note here that our acoustic field variable is the *velocity potential* ϕ and that in our notation, R_0 and R_L are the reflection coefficients of ϕ. It is more common to work with the reflection coefficients of the *acoustic pressure* p; these are closely related to those of the velocity potential. The linearized momentum equation in the form

$$p' = -\bar{\rho}\left(\frac{\partial \phi}{\partial t} + \bar{u}\frac{\partial \phi}{\partial x}\right) \tag{2.17}$$

allows us to express the pressure field in terms of its forward and backward travelling waves. The result for the upstream side is

$$\hat{p}(x, \omega) = A_+(\mathrm{i}\omega - \bar{u}\mathrm{i}k_+)\mathrm{e}^{\mathrm{i}k_+ x} + A_-(\mathrm{i}\omega - \bar{u}\mathrm{i}k_-)\mathrm{e}^{-\mathrm{i}k_- x}. \tag{2.18}$$

This gives the pressure reflection coefficient as

$$R_0^{(p)} = \frac{A_+}{A_-}\frac{\omega - \bar{u}k_+}{\omega + \bar{u}k_-} = R_0\frac{1 - M}{1 + M}. \tag{2.19}$$

An analogous derivation can be performed for the downstream side, and this leads to

$$R_L^{(p)} = \frac{B_-}{B_+}\frac{\omega + \bar{u}k_+}{\omega - \bar{u}k_-} = R_L\frac{1 + M}{1 - M}. \tag{2.20}$$

For mean flows with low Mach number M, the numerical values of R_0 and $R_0^{(p)}$, as well as R_L and $R_L^{(p)}$, are very similar.

2.2.4. The direct Green's function

The direct Green's function is a mathematical concept with a clear physical meaning. If an impulse is emitted at time t' from a hypothetical point source at position x' in the tube, a sound field is generated in the tube. This sound field is called the impulse response and is described mathematically by the function $g(x, x', t, t')$. The variable x denotes the position of an observer, and the variable t denotes the observer's time. The measured sound field does not depend on t or t' individually, but on the time elapsed since the impulse, $t - t'$. Here, we call g the *direct Green's function* to distinguish from the tailored Green's function for a self-adjoint system.

In line with its physical meaning, the direct Green's function is defined by the following governing equations. The PDE

$$\frac{\partial^2 g}{\partial t^2} + 2\bar{u}\frac{\partial^2 g}{\partial t \partial x} - (c^2 - \bar{u}^2)\frac{\partial^2 g}{\partial x^2} = \delta(x - x')\delta(t - t') \tag{2.21}$$

describes the sound field generated in the tube (of unspecified end conditions). The causality conditions

$$g(x, x', t - t') = 0 \quad \text{for} \quad t < t' \tag{2.22}$$

$$\frac{\partial g}{\partial t} + \bar{u}\frac{\partial g}{\partial x} = 0 \quad \text{for} \quad t < t' \tag{2.23}$$

guarantee that no sound field is generated before the source has emitted its impulse.

We also require the direct Green's function to be "tailored" to the tube boundaries, which are described by the reflection coefficients R_0 and R_L; however, these are given in the frequency domain.

The Fourier transform of $g(x, x', t - t')$ is $\hat{g}(x, x', \omega)$, given by

$$\hat{g}(x, x', \omega) = \int_{t=-\infty}^{\infty} g(x, x', t - t')\mathrm{e}^{\mathrm{i}\omega(t-t')}\mathrm{d}t. \tag{2.24}$$

Its governing equation is the Fourier transform of Eq. (2.21), i.e.

$$\omega^2\hat{g}(x, x', \omega) + 2\bar{u}\mathrm{i}\omega\frac{\partial \hat{g}}{\partial x} + (c^2 - \bar{u}^2)\frac{\partial^2 \hat{g}}{\partial x^2} = -\delta(x - x'). \tag{2.25}$$

In analogy to Eq. (2.13), we can write down solutions for $\hat{g}(x, x', \omega)$ on either side of the heat source

$$\hat{g}(x, x', \omega) = \begin{cases} A_-(x', \omega)[R_0\,\mathrm{e}^{\frac{\mathrm{i}\omega}{c+\bar{u}}x} + \mathrm{e}^{-\frac{\mathrm{i}\omega}{c-\bar{u}}x}] & \text{for} \quad 0 < x < x' \\ \\ B_+(x', \omega)[\mathrm{e}^{\frac{\mathrm{i}\omega}{c+\bar{u}}(x-L)} + R_L\mathrm{e}^{-\frac{\mathrm{i}\omega}{c-\bar{u}}(x-L)}] & \text{for} \quad x' < x < L \end{cases} \tag{2.26}$$

This satisfies the required boundary conditions.

Equations (2.25) and (2.26) form the governing equations for $\hat{g}(x, x', \omega)$. The latter contains the two functions $A_-(x', \omega)$ and $B_+(x', \omega)$, which have yet to be determined. This can be done with a generalized function approach (see Appendix A.1.1.). The result is

$$\hat{g}(x, x', \omega) = \begin{cases} \dfrac{1}{2c(\mathrm{i}\omega)F(\omega)}\mathrm{e}^{-\mathrm{i}(k_+ - k_-)x'}\mathrm{e}^{\mathrm{i}k_+ L}b(x', \omega)a(x, \omega) & \text{for} \quad 0 < x < x' \\ \\ \dfrac{1}{2c(\mathrm{i}\omega)F(\omega)}\mathrm{e}^{-\mathrm{i}(k_+ - k_-)x'}\mathrm{e}^{\mathrm{i}k_+ L}a(x', \omega)b(x, \omega) & \text{for} \quad x' < x < L \end{cases} \tag{2.27}$$

where $F(\omega)$ is given by Eq. (2.16), and

$$a(x, \omega) = R_0\mathrm{e}^{\mathrm{i}k_+ x} + \mathrm{e}^{-\mathrm{i}k_- x}, \tag{2.28}$$

$$b(x, \omega) = \mathrm{e}^{\mathrm{i}k_+(x-L)} + R_L\mathrm{e}^{-\mathrm{i}k_-(x-L)}. \tag{2.29}$$

The time-domain function, $g(x, x', t - t')$, is then obtained by inverse Fourier transform of $\hat{g}(x, x', \omega)$. This requires integration in the complex ω-plane and application of the residue theorem (see Appendix A.1.2.). The result is

$$g(x, x', t - t') = H(t - t')\sum_{n=1}^{\infty}\Re\left[\frac{g_n(x, x', \omega_n)}{\omega_n F'(\omega_n)}\mathrm{e}^{-\mathrm{i}\omega_n(t-t')}\right]. \tag{2.30}$$

$F'(\omega)$ in Eq. (2.30) denotes the derivative of the function $F(\omega)$ (given by Eq. (2.16)) with respect to ω. The other quantities in Eq. (2.30) are

$$g_n(x,x',\omega_n) = \begin{cases} \psi(x',\omega_n)b(x',\omega_n)a(x,\omega_n) & \text{for} \quad 0 < x < x' \\ \\ \psi(x',\omega_n)a(x',\omega_n)b(x,\omega_n) & \text{for} \quad x' < x < L \end{cases} \tag{2.31}$$

with the functions a and b given by Eq. (2.28) and Eq. (2.29), and ψ by

$$\psi(x,\omega) = -\frac{1}{c}\mathrm{e}^{\frac{2\mathrm{i}\omega\bar{u}}{c^2-\bar{u}^2}x}\mathrm{e}^{-\frac{\mathrm{i}\omega}{c+\bar{u}}L}. \tag{2.32}$$

The expression for $g(x,x',t-t')$ in Eq. (2.30) features all the physical properties one would expect from the acoustic response to an impulsive point source in a resonator. Eq. (2.30) describes a superposition of modes; n is the node number, ω_n is the (generally complex) frequency of mode n, and $\dfrac{g_n(x,x',\omega_n)}{\omega_n F'(\omega_n)}$ is the corresponding mode amplitude. The Heaviside $H(t-t')$ function expresses the *causality* of the direct Green's function:

$$H(t-t') = \begin{cases} 0 & \text{for} \quad t < t', \quad \text{i.e. before the impulse,} \\ 1 & \text{for} \quad t > t', \quad \text{i.e. after the impulse.} \end{cases} \tag{2.33}$$

2.2.5. The adjoint Green's function

The full governing equations in section 2.2.2. cannot be solved analytically because they involve a PDE with a forcing term that is coupled nonlinearly to the acoustic field. To systematically assess the effect of forcing terms on the acoustic field, the PDE of the direct system has to be solved repetitively for various boundary conditions and the initial conditions, and for a variety of heat release rates, Eq. (2.1). Motivated by the tailored Green's function approach of Heckl and collaborators (Heckl and Howe, 2007; Heckl, 2013; Bigongiari and Heckl, 2016) for the case without mean flow and Luchini and Bottaro (1998), our aim is to derive an integral governing equation for the non-self-adjoint thermoacoustic system.

To this end, we perform a series of mathematical operations on Eq. (2.5):

- write it in terms of the new variables x', t' (instead of x, t);
- multiply it by a test function $G(x', x, t', t)$ (yet to be defined);
- integrate the result with respect to t' from the initial time 0 to a "terminal time" T_t (yet to be defined);
- integrate with respect to x' over the whole length of the tube;
- shift the derivatives from ϕ to G by repeated use of integration by parts.

This leads to (for mathematical steps, see Appendix A.2.1.)

$$\int_{t'=0}^{T_t}\int_{x'=0}^{L}\left[\frac{\partial^2 G}{\partial t'^2}+2\bar{u}\frac{\partial^2 G}{\partial t'\partial x'}-(c^2-\bar{u}^2)\frac{\partial^2 G}{\partial x'^2}\right]\phi(x',t')\mathrm{d}x'\mathrm{d}t'+BT1+BT2= \\ =-(\gamma-1)\int_{t'=0}^{T_t}G(x_q,x,t',t)q(t')\mathrm{d}t', \tag{2.34}$$

with

$$BT1=\int_{x'=0}^{L}\left[G(\frac{\partial\phi}{\partial t'}+\bar{u}\frac{\partial\phi}{\partial x'})-\phi(\frac{\partial G}{\partial t'}+\bar{u}\frac{\partial G}{\partial x'})\right]_{t'=0}^{T_t}\mathrm{d}x', \tag{2.35}$$

$$BT2=\int_{t'=0}^{T_t}\left[\bar{u}(G\frac{\partial\phi}{\partial t'}-\phi\frac{\partial G}{\partial t'})-(c^2-\bar{u}^2)(G\frac{\partial\phi}{\partial x'}-\phi\frac{\partial G}{\partial x'})\right]_{x'=0}^{L}\mathrm{d}t'. \tag{2.36}$$

The terms $BT1$ and $BT2$ in Eq. (2.35) and Eq. (2.36) are "boundary terms". The aim is now to define the test function $G(x',x,t',t)$ in such a way that Eq. (2.34) yields an integral equation for the acoustic field, $\phi(x,t)$, as simple as possible, without unwelcome boundary terms.

The first term on the left-hand-side of Eq. (2.34) inspired us to define $G(x',x,t',t)$ to satisfy the PDE

$$\frac{\partial^2 G}{\partial t'^2}+2\bar{u}\frac{\partial^2 G}{\partial t'\partial x'}-(c^2-\bar{u}^2)\frac{\partial^2 G}{\partial x'^2}=\delta(x'-x)\delta(t'-t), \tag{2.37}$$

then the double integral in Eq. (2.34) reduces to $\phi(x,t)$. If we further impose the terminal conditions

$$G(x',x,t',t)=0 \quad \text{at} \quad t'=T_t, \tag{2.38}$$

$$\frac{\partial G}{\partial t'}+\bar{u}\frac{\partial G}{\partial x'}=0 \quad \text{at} \quad t'=T_t, \tag{2.39}$$

then the terms at $t'=T_t$ in the boundary term $BT1$ of Eq. (2.34) vanish. The terms at $t'=0$ can be rewritten with the initial conditions Eq. (2.6) and Eq. (2.7). Hence, integral of Eq. (2.35) becomes

$$BT1=-\left[\varphi_0' G(x',x,t',t)-\varphi_0(\frac{\partial G}{\partial t'}+\bar{u}\frac{\partial G}{\partial x'})\right]_{\substack{x'=x_q\\ t'=0}}. \tag{2.40}$$

The boundary term $BT2$, given by Eq. (2.36), involves the time integral $\int_{t'=0}^{T_t}...\mathrm{d}t'$. Here, we are faced with the fact that the integrand contains boundary expressions at $x=0$ and $x=L$, which are given in the *frequency* (and not in the *time*) domain. The acoustic field is not defined for times before the initial conditions act, so there is

$$\phi(x',t')=0 \quad \text{for} \quad t'<0. \tag{2.41}$$

Similarly, $G(x',x,t',t)$ is not defined for times beyond the terminal time T_t, so there is

$$G(x',x,t',t)=0 \quad \text{for} \quad t'>T_t. \tag{2.42}$$

This allows us to extend the integration limits in Eq. (2.36) from $\int_{t'=0}^{T_t}$ to $\int_{t'=-\infty}^{\infty}$ and subsequently use Fourier transforms. Appendix A.3. shows the detailed calculation which leads to

$$BT2 = 0. \tag{2.43}$$

Using Eqs. (2.37)-(2.40) and (2.43), Eq. (2.34) becomes:

$$\begin{aligned}\phi(x,t) = &-(\gamma-1)\int_{t'=0}^{T_t} G(x_q,x,t',t)q(t')\mathrm{d}t' + \\ &\left[\varphi_0' G(x',x,t',t) - \varphi_0(\frac{\partial G}{\partial t'} + \bar{u}\frac{\partial G}{\partial x'})\right]_{\substack{x'=x_q \\ t'=0}}.\end{aligned} \tag{2.44}$$

In section 7.5 of Morse and Feshbach (1953), $G(x',x,t',t)$ is referred to as the "Green's function of the adjoint operator". In the present work, we call $G(x',x,t',t)$ the *adjoint Green's function (AGF)*. The AGF governed by Eq. (2.37) is the adjoint field of the direct system, with an impulse source term. Note that we choose to show the derivation of the adjoint system following a continuous approach since we believe that it is more pedagogical, and it elucidates the rationale behind the selection of terminal and boundary conditions in the next subsection. The equivalent discrete adjoint approach would be feasible but requires a discretization in both spatial and temporal domains before using Green's identity (cf. the Supplementary Material of Luchini and Bottaro (2014)).

2.2.6. The AGF in the frequency- and time-domain

The boundary conditions of the AGF are given in the frequency domain, so we focus for now on the adjoint of $\hat{g}(x,x',\omega)$. This adjoint function is determined by performing a series of mathematical operations on the PDE, Eq. (2.25) for $\hat{g}(x,x',\omega)$; these are shown in Appendix A.2.2. The adjoint PDE turns out to be

$$\omega^2\hat{G}(x,x',\omega) - 2\bar{u}\mathrm{i}\omega\frac{\partial\hat{G}}{\partial x} + (c^2-\bar{u}^2)\frac{\partial^2\hat{G}}{\partial x^2} = -\delta(x-x'). \tag{2.45}$$

Comparison of Eq. (2.45) with Eq. (2.25) reveals that $\hat{g}$ and $\hat{G}$ satisfy very similar PDEs: they only differ by the sign of the mean velocity $\bar{u}$. The functional dependence of $\hat{G}(x,x',\omega)$ is also determined in Appendix A.2.2.; the result is

$$\hat{G}(x,x',\omega) = \begin{cases} \tilde{A}_-(x',\omega)[R_0\,\mathrm{e}^{\frac{\mathrm{i}\omega}{c-\bar{u}}x} + \mathrm{e}^{-\frac{\mathrm{i}\omega}{c+\bar{u}}x}] & \text{for} \quad 0<x<x' \\ \\ \tilde{B}_+(x',\omega)[\mathrm{e}^{\frac{\mathrm{i}\omega}{c-\bar{u}}(x-L)} + R_L\,\mathrm{e}^{-\frac{\mathrm{i}\omega}{c+\bar{u}}(x-L)}] & \text{for} \quad x'<x<L \end{cases} \tag{2.46}$$

The functions $\tilde{A}_-(x',\omega)$ and $\tilde{B}_+(x',\omega)$ are analogous to $A_-(x',\omega)$ and $B_+(x',\omega)$ in Eq. (2.26), and they are undetermined at this stage. $\hat{G}(x,x',\omega)$ satisfies Eq. (2.45), while $G(x',x,t',t)$ satisfies Eq. (2.37). These two functions form a Fourier transform pair, i.e.

$$G(x',x,t',t) = \frac{1}{2\pi}\int_{\omega=-\infty}^{\infty}\hat{G}(x',x,\omega)\mathrm{e}^{-\mathrm{i}\omega(t-t')}\mathrm{d}\omega, \tag{2.47}$$

(for details see Appendix A.4.).

2.2.7. Relationship between the adjoint and the direct Green's function

In order to determine the formulation of the AGF, $G(x', x, t', t)$, from the solution of direct Green's function $g(x, x', t - t')$, obtained in Section 2.2.4., we need to find the relationship between $G(x', x, t', t)$ and $g(x, x', t - t')$. The detailed derivation steps are shown in Appendix A.2.3. The result is

$$G(x', x, t', t) = g(x, x', t, t'). \tag{2.48}$$

This result expresses the reciprocity between the direct and adjoint Green's function (Morse and Feshbach, 1953). It is also called the symmetry property of Green's functions (Greenberg, 1978). Mathematically, it demonstrates that the systems of $g(x, x', t - t')$ and $G(x, x', t - t')$ are adjoint system of each other. It also notes that neither G, nor g, are self-adjoint, i.e.

$$g(x, x', t - t') \neq g(x', x, t' - t), \tag{2.49}$$

$$G(x, x', t - t') \neq G(x', x, t' - t), \tag{2.50}$$

This is a key difference to the case of a tube without mean flow. With the presence of the convection term, the problem is no longer self-adjoint.

With the reciprocity theorem given by Eq. (2.48), and the functional dependence of $g(x, x', t-t')$ given by Eq. (2.30), the AGF $G(x, x', t - t')$ is obtained simply by swapping the source position and the observer position in Eq. (2.30), as well as the source time and observer time.

The function g and G are both solutions to the same source problem, but they differ in terms of causality. The direct Green's function describes the evolution as time increases, starting with the initial impulse and ending with the acoustic field measured by the observer. The AGF describes the same process in reverse time, beginning with the acoustic field measured by the observer and going backward in time to the initial impulse (Morse and Feshbach (1953), section 7.4). Given that the direct Green's function is causal, we call the AGF *causal in reverse time*. These properties are expressed in terms of the following equations:

$$g(x, x', t - t') = 0 \quad \text{for} \quad t < t' \qquad \text{(causality of the direct Green's function)} \tag{2.51}$$

$$G(x', x, t' - t) = 0 \quad \text{for} \quad t > t' \qquad \text{(causality in reverse time of the AGF)} \tag{2.52}$$

2.2.8. Integral equation for the acoustic field

It remains to fix the terminal time T_t. According to Eq. (2.52), $G = 0$ for all times $t > t'$. Therefore the integrand in Eq. (2.44) is zero in the range $t' = t, ...T_t$. This suggests that the

upper integration boundary in Eq. (2.44) should be changed from T_t to t. The final version of the integral equation for ϕ is

$$\begin{aligned}\phi(x,t) = &-(\gamma-1)\int_{t'=0}^{t} G(x_q,x,t',t)q(t')\mathrm{d}t' \\ &+\left[\varphi_0' G(x',x,t',t) - \varphi_0(\frac{\partial G}{\partial t'} + \bar{u}\frac{\partial G}{\partial x'})\right]_{\substack{x'=x_q \\ t'=0}}.\end{aligned} \tag{2.53}$$

The velocity at the heat source is given by $u_q(t) = \left.\dfrac{\partial \phi(x,t)}{\partial x}\right|_{x=x_q}$, and this allows us to turn Eq. (2.53) into an integral equation for the velocity $u_q(t)$,

$$\begin{aligned}u_q(t) = &-(\gamma-1)\int_{t'=0}^{t} \left.\frac{\partial G(x',x,t',t)}{\partial x}\right|_{x=x_q,\ x'=x_q} q(t')\mathrm{d}t' + \\ &\left[\varphi_0'\frac{\partial G(x',x,t',t)}{\partial x} - \varphi_0(\frac{\partial^2 G}{\partial x \partial t'} + \bar{u}\frac{\partial^2 G}{\partial x \partial x'})\right]_{\substack{x'=x_q \\ t'=0 \\ x=x_q}}.\end{aligned} \tag{2.54}$$

The heat release rate $q(t')$ is given in terms of u_q by Eq. (2.3), so Eq. (2.54) represents an integral equation (Volterra type) for $u_q(t)$. It can be solved with a straightforward iteration process, stepping forward in time. The strength of the approach outlined, related to the role of $G(x',x,t',t)$ as evaluation of receptivity, emerges clearly from Eqs. (2.53) and (2.54): knowledge of the unique AGF (and its derivatives) is sufficient to map immediately the output, i.e. $\phi(x,t)$ or $u_q(t)$, to whatever input, represented here by $q(t)$, φ_0 and φ_0'.

2.2.9. Modal analysis

Numerical solution of the integral equation Eq. (2.54) gives the time history of $u_q(t)$. Eq. (2.54) also allows an analytical approach, which will give the frequencies of the acoustic modes driven by the thermoacoustic feedback.

Motivated by the observation that the frequency spectrum of a thermoacoustic oscillation has discrete peaks, we express the acoustic velocity as a sum of modes with complex frequencies Ω_m and complex amplitudes u_m,

$$u_q(t) = \sum_{m=1}^{\infty}\left(u_m \mathrm{e}^{-\mathrm{i}\Omega_m t} + u_m^* \mathrm{e}^{-\mathrm{i}\Omega_m^* t}\right). \tag{2.55}$$

At this stage, Ω_m and u_m are unknown; their complex conjugate is denoted by $*$. It is possible to determine them from a series of mathematical manipulations, which are described in Appendix A of Bigongiari and Heckl (2016). The resulting equation for Ω_m (for m = 1, 2 ...) is

$$(n_0 - n_1 \mathrm{e}^{\mathrm{i}\Omega_m \tau})\sum_{n=1}^{\infty}\left[\frac{\Gamma_n}{\mathrm{i}(\omega_n - \Omega_m)} - \frac{\Gamma_n^*}{\mathrm{i}(\omega_n^* + \Omega_m)}\right] = \frac{2}{(\gamma-1)K} \tag{2.56}$$

where

$$\Gamma_n = \left. \frac{\partial \hat{g}_n(x, x', \omega)}{\partial x} \right|_{\substack{x=x_q \\ x'=x_q}} . \tag{2.57}$$

The real part of Ω_m gives the circular frequency of mode m, while the imaginary part represents the growth rate, revealing whether mode m is stable or not.

2.3. A RIJKE TUBE CASE

The stability behavior of the first thermoacoustic eigenmode in a horizontal Rijke tube with uniform temperature is investigated. We focus on the first mode because the flame model is valid mainly in the low-frequency range (Heckl, 2015); as such, the results for the higher order modes would be less reliable, and this will be shown in a later section of this chapter. The parameters in the model are chosen from the work by Bigongiari and Heckl (2016), with a steady mean flow included, and choose the following three control parameters: heat source position, x_q, tube length, L, and heater power, K. The values of the model parameters and ranges of the control parameters are given in Table 2.1.

Table 2.1: Model parameters of the horizontal Rijke tube

Parameters	Symbol	Value	Unit
Mean temperature	$\bar{T}$	304	K
Sound speed	c	350	m s^{-1}
Reflection coefficient (upstream end)	R_0	-1	
Reflection coefficient (downstream end)	R_L	-1	
	g_0	1.4	
Fitting parameters	g_1	0.3	
of nonlinear heat release model	τ_0	5×10^{-3}	s
	τ_2	4.4×10^{-3}	s
Mach number	M	0, 0.1, 0.3, 0.5	
Tube length	L	0.4 ... 2	m
Heat source position	x_q	0 ... L	m
Heater power	K	0 ... 4×10^6	J kg^{-1}

Stability maps are created by numerically solving Eq. (2.56), which contains implicitly the parameter $\epsilon = A/\bar{u}$. In order to avoid numerical problems for the case without mean flow ($\bar{u} = 0$), we put $\bar{u} = 1$ m s^{-1} if $M = 0$. Our stability maps show unstable regions, where $\Im(\Omega_1) > 0$, and stable regions, where $\Im(\Omega_1) < 0$. Stable regions are depicted in blue shading, and unstable regions are displayed in red shading, with the growth rates indicated by colour bars. The maps highlight the dependence of the stability behaviour on the control parameter and the dimensionless acoustic velocity fluctuation amplitude at the source, ϵ.

2.3.1. Dependence on the position of the heat source

The stability maps based on the control parameter x_q for different mean flow velocities through the tube are shown in Fig. 2.4. The tube length is fixed at $L = 2$ m and the heater power is maintained at $K = 3 \times 10^5$ J kg^{-1}. For purely illustrative purposes, the plots display the growth rate with ϵ up to the rather large value of 1.5.

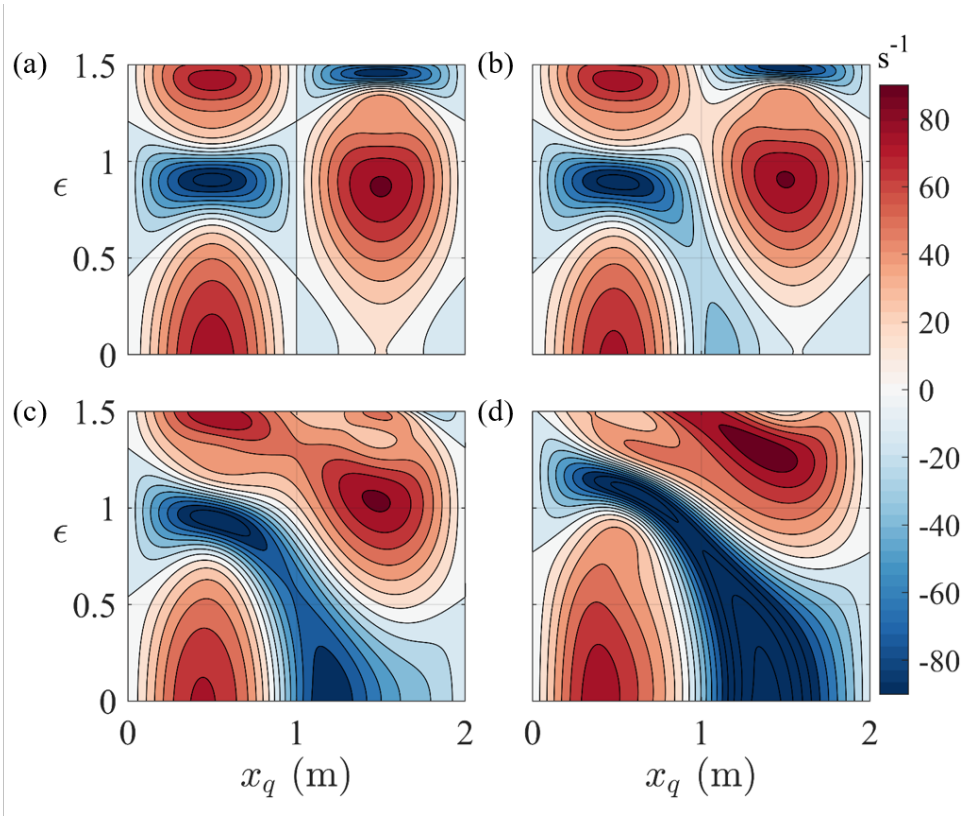

Figure 2.4: Stability maps of a horizontal Rijke tube; the coloured shading indicates the growth rates given on the colour bar on the right. The control parameter is x_q, the position of the heat source; $L = 2$ m, $K = 3 \times 10^5$ J kg^{-1}. (a) Mean flow is absent; (b) M = 0.1; (c) M = 0.3; (d) M = 0.5.

For the case $M = 0$, shown in Fig. 2.4(a), the system is linearly unstable if x_q is anywhere within the upstream half of the tube (0 m $< x_q <$ 1 m), and again in the range between 1.25 m and 1.75 m within the downstream half. The points (x_q, ϵ)=(1.25 m, 0) and (1.75 m, 0) are subcritical Hopf bifurcation points. For the case $M = 0.1$, shown in Fig. 2.4(b), these two points have moved close together, reducing the linearly stable range along the x_q-axis. For the cases $M = 0.3$ and $M = 0.5$, shown in Figs. 2.4(c) and 2.4(d), respectively, the Hopf bifurcation points have disappeared and there is linear stability for any position x_q in the downstream half. For such positions, a non-zero initial amplitude is required to trigger instability. This triggering amplitude becomes progressively larger as M increases. Thus, the presence of a mean flow generally stabilizes the system. This observation qualitatively agrees with the experimental finding by Gopalakrishnan and Sujith (2014) that, at a higher mass flow rate, no instability

occurred when $x_q > L/2$. On the other hand, when the heat source is in the upstream half of the duct ($x_q < 1$ m), the stretching of the unstable region towards higher values of ϵ when M increases results in enhanced limit cycle amplitudes.

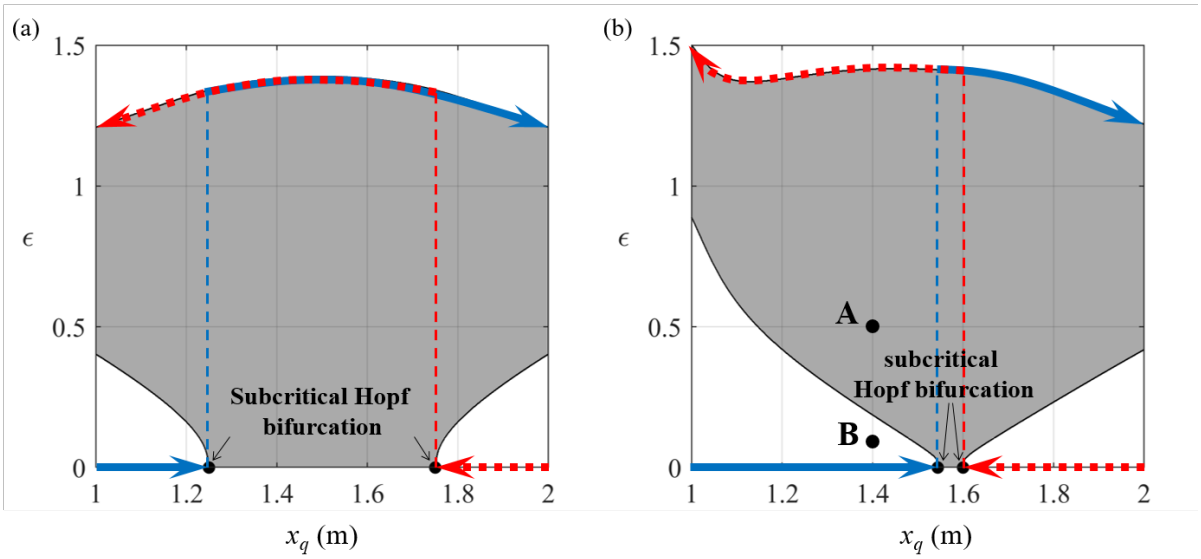

Figure 2.5: Hysteresis effect and bistable regions in a horizontal Rijke tube with changing heat source position $1 < x_q < 2$ m, $L = 2$ m, $K = 3 \times 10^5$ J kg^{-1}. The white part indicates the stable region and the grey part indicates the unstable region. The blue solid arrows denote the forward bifurcation path when the system is switched on with a small perturbation when $x_q = 1$ m and the heat source is moved downstream. The red dashed arrows denote the backward path when the system is switched on with a small perturbation when $x_q = 2$ m and the heat source is moved upstream. Bistability occurs for x_q on the left (right) of the blue (red) dashed line. (a) Mean flow is absent; (b) M = 0.1.

Figure 2.5 shows the same results for two values of M (M = 0 and M = 0.1), focusing on the range 1 m $< x_q <$ 2 m, to highlight the presence of bistable regions and the occurrence of hysteresis. Again, stable regions are marked in white, while unstable regions are shown in grey (without the growth rate contours). Bistability is the phenomenon where the solution can be either steady or oscillatory, depending on the initial condition. As Fig. 2.5(a) shows for $M = 0$, there is a bistable region for x_q between 1 m and 1.25 m, and another one between 1.75 m and 2 m. Let's, for example, consider the position x_q =1.1 m, which is in the bistable region. If the initial amplitude is small enough to be in the white region, the system will oscillate with a decaying amplitude and approach a linearly stable state. Conversely, if the initial amplitude is large enough to be in the grey region, the oscillation amplitude will grow. It will reach a limit at the upper edge of the grey region, and the system will subsequently oscillate in a stable limit cycle. Fig. 2.5(b) gives equivalent results for $M = 0.1$. It is evident that the stability boundaries have changed and that the bistable regions have become much larger. For example, the bistable region now includes the point $x_q = 1.4$ m, which was outside the bistable region for $M = 0$. This prediction is consistent with papers in the literature (Matveev, 2003b; Gopalakrishnan and Sujith, 2014; Mariappan et al., 2011), which report that a decrease in mass flow rate in a Rijke tube reduces the width of bistable regions. The results in Fig. 2.5 also highlight the incorrect

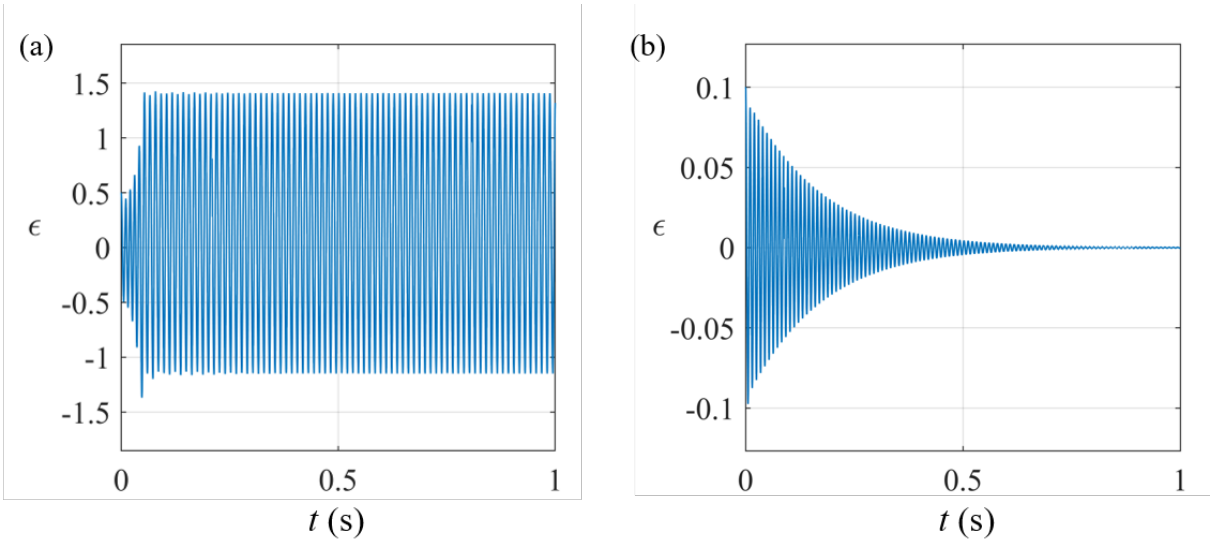

Figure 2.6: Time histories starting from points A and B as initial conditions, cf. Figure 2.5(b), computed iterating in time Eq. (2.54). Mean flow with $M = 0.1$: (a) Point A: $x_q = 1.4$ m, $\epsilon = 0.5$; (b) Point B: $x_q = 1.4$ m, $\epsilon = 0.1$.

conclusions one could draw when assuming zero Mach number when, in fact, the Mach number is small but non-zero.

The presence of bistable regions is an indicator that hysteresis occurs if the control parameter is first increased, and then decreased again. This is also illustrated in Fig. 2.5. The solid blue curves represent the forward path, with x_q increasing, and the dashed red curves represent the backward path, with x_q decreasing. In Fig. 2.5(a), in the absence of mean flow, the forward path starts at $x_q = 1$ m and zero initial amplitude. As the heat source is moved downstream, this stable state persists until the position $x_q = 1.25$ m (a subcritical Hopf bifurcation), where a sudden transition occurs: an oscillation with growing amplitude sets in until a limit cycle is reached. As x_q is increased beyond this point, the system follows the blue path along the top edge of the grey region. The backward path in Fig. 2.5(a) starts at the downstream end, $x_q = 2$ m, and zero amplitude. The system is stable until the position $x_q = 1.75$ m is reached. Another sudden transition occurs there through a subcritical Hopf bifurcation. A limit cycle ensues, and as x_q is decreased further, the limit cycle persists all the way to the starting position $x_q = 1$ m. The forward and backward paths are evidently different.

The hysteresis for $M = 0.1$ shown in Fig. 2.5(b) displays qualitatively the same properties, but the overlap between the forward and backward paths has become much smaller. As the Mach number increases, the two bistable regions become wider and eventually merge into one (see Figs. 2.4(c),(d)). At that point, the hysteresis effect disappears. It is noted that the limit cycle amplitude is rather large (ϵ mildly above 1 at both values of M shown in Fig. 2.5), in agreement with Matveev and Culick (2003b) who stated that *"the oscillating velocity magnitude estimated in the vicinity of the heater tends to be stabilized near the mean flow velocity (slightly exceeding it) in the unstable regimes"*.

Figure 2.6 shows the time histories of the velocity perturbations at the initial condition

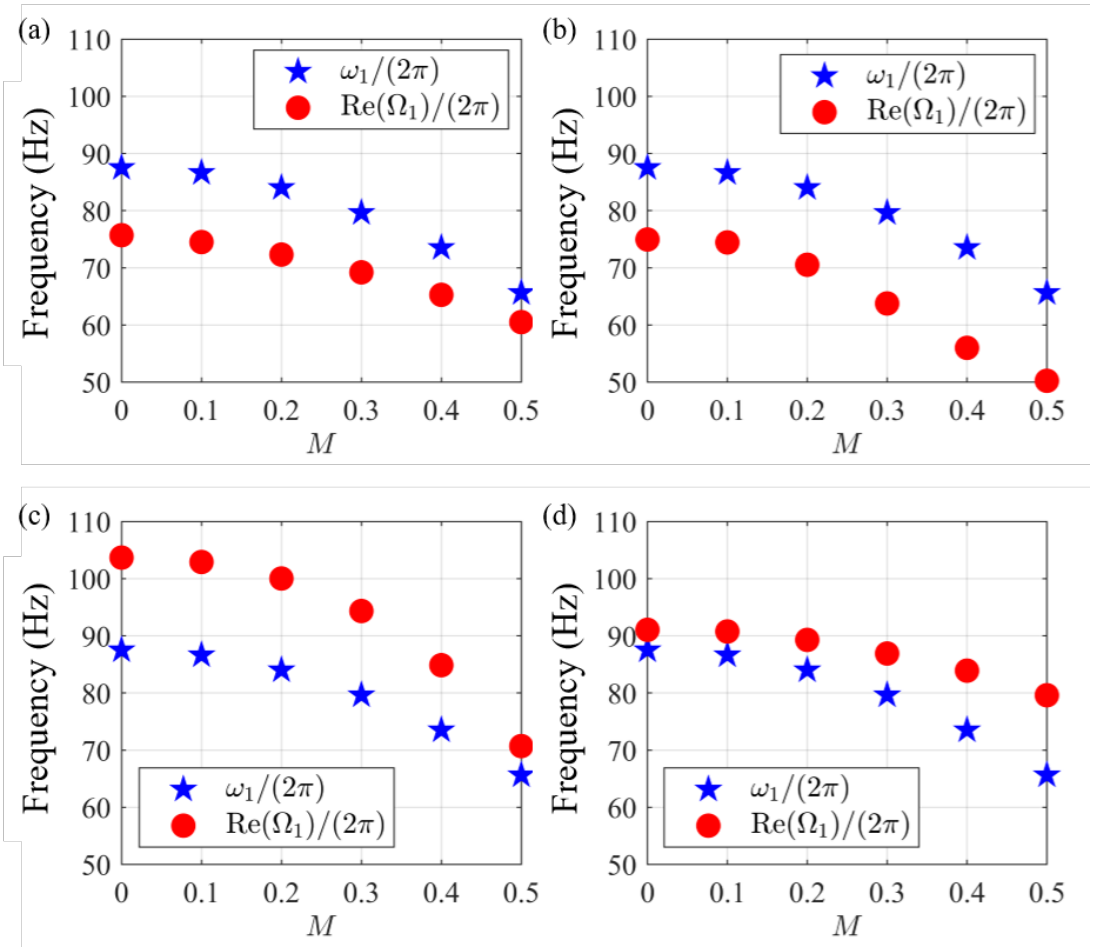

Figure 2.7: Comparison of the first-mode eigenfrequency of the Green's function ($\omega_1/(2\pi)$) and the heat-driven frequency ($\mathrm{Re}(\Omega_1)/(2\pi)$), for varying Mach number. (a, b) The heat source is fixed at $x_q = 0.4$ m; (c, d) the heat source is fixed at $x_q = 1.6$ m; (a, c) small amplitude, $\epsilon = 0.1$; (b, d) large amplitude, $\epsilon = 0.8$.

marked as **A** and **B** in Fig. 2.5(b), respectively. When the mean flow is absent and the heat source is located at $x_q = 1.4$ m, the steady state is always unstable (cf. Fig. 2.5(a)). For the non-zero Mach number of $M = 0.1$, the source position $x_q = 1.4$ m falls in a bistable range, cf. Fig. 2.5(b). Given a large excitation amplitude, for instance, $\epsilon = 0.5$ (point **A**), the system rapidly reaches a stable limit cycle. For low excitation amplitude (point **B**, $\epsilon = 0.1$) the system decays to a steady state quite slowly. These observations, embodied by Fig. 2.6, require time-history calculations.

Figure 2.7 illustrates the comparison between the eigenfrequencies of the Green's function first mode (n = 1, Eq. (2.16)), which do not vary with the amplitude of the acoustic velocity at the flame, and the heat-driven frequencies of mode m = 1, at two values of the amplitude of the acoustic velocity at the position of the source. When the flame is located in the upstream half of the tube ($x_q = 0.4$ m), for both high and low amplitudes, the heat-driven frequencies remain slightly below the eigenfrequencies of the Green's function; the situation is reversed

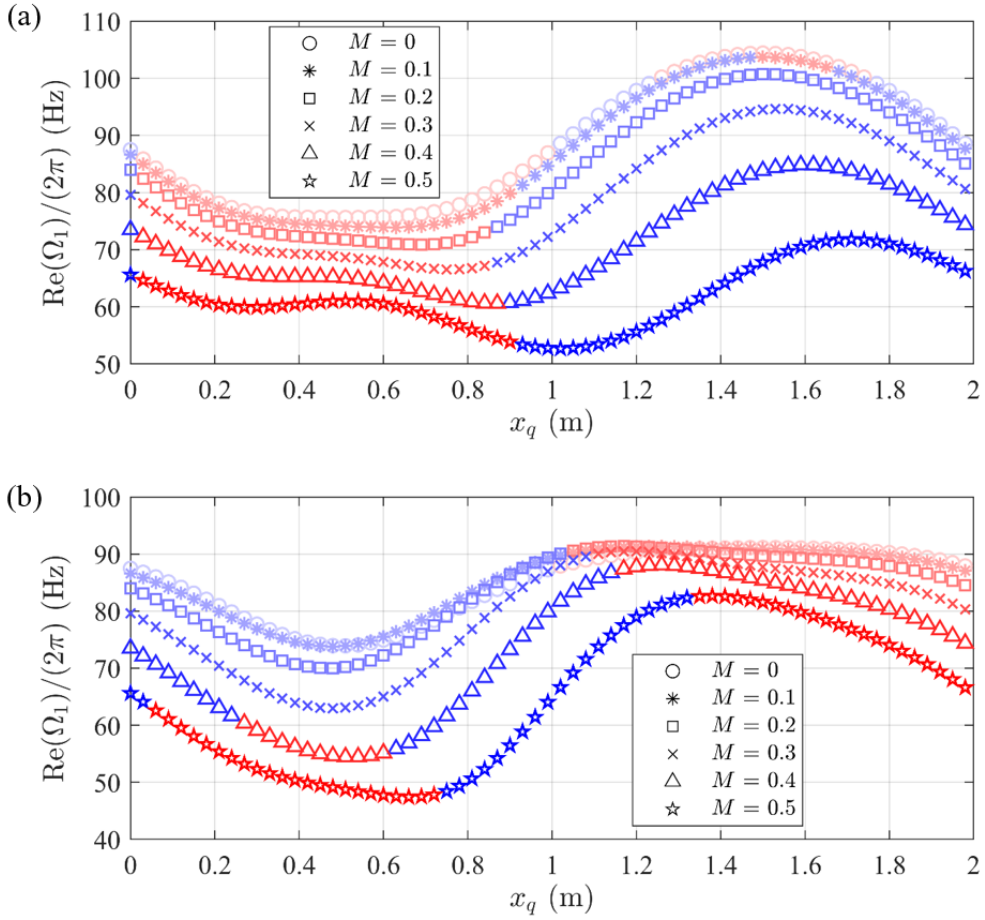

Figure 2.8: Modal frequency variation, $\mathrm{Re}(\Omega_1)/(2\pi)$, as function of the heat source position, x_q, for various Mach number M. $K = 3 \times 10^5$ J kg^{-1}. Blue symbols represent the stable state of mode 1; red symbols represent the unstable state. (a) Small amplitude, $\epsilon = 0.1$; (b) large amplitude, $\epsilon = 0.8$.

when the flame is in the downstream half of the tube ($x_q = 1.6$ m). In all cases, the differences are not major and increasing the Mach number leads to a reduction of the frequencies. As pointed out in several previous studies (Bigongiari and Heckl, 2016; Orchini et al., 2015; Noiray, 2007; Dowling, 1999), the frequency shifts are related to thermoacoustic feedback, which is amplitude-dependent through the heat release law, Eq. (2.3).

Figure 2.8 shows the variation of the heat-driven frequency of the first mode as a function of the position of the heat source for different Mach numbers. Fig. 2.8(a) and (b) illustrate the scenarios, respectively, at low ($\epsilon = 0.1$) and high excitation amplitude ($\epsilon = 0.8$). We observe a consistent trend across all heat source positions: increasing the mean flow velocity reduces the heat-driven frequency. Until $M = 0.1$, differences in frequencies are hardly noticeable. As the Mach number increases, the frequency can decrease quite significantly compared to the $M = 0$ case, especially when the heat source is located in the downstream half of the tube. Conversely,

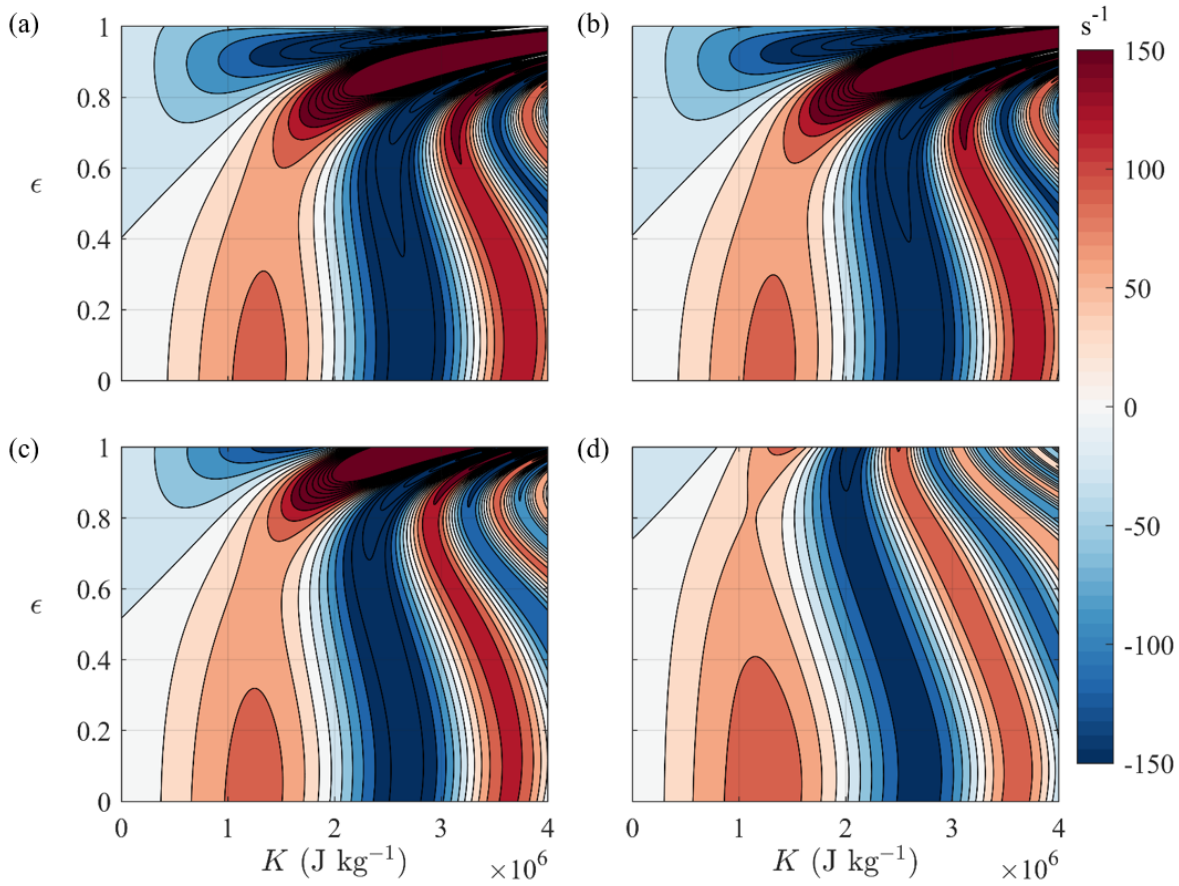

Figure 2.9: Stability maps of a horizontal Rijke tube; the coloured shading denotes the growth rate given on the colour bar on the right; $x_q = 0.1$ m, $L = 2$ m. (a) Mean flow is absent; (b) M = 0.1; (c) M = 0.3; (d) M = 0.5.

for the high amplitude case, the larger discrepancy in frequency appears when the heat source is located in the upstream half of the tube.

2.3.2. Dependence on the coupling between velocity and heat release rate

As explained in section 2.2.1., the parameter K, the heater power, is a measure of the coupling between the heat release rate and the acoustic field. It is worthwhile to focus on this parameter and inspect the stability behaviour if K is varied.

The stability maps based on control parameter K for different mean flow velocities are shown in Fig. 2.9. Eqs. (2.37) and (2.56) reveal that the variation of heater power K does not change the solution of the AGF but affects only the complex modal frequencies Ω_m. The stability maps quantify the effect of the coupling strength on the system's stability. The results

displayed in Figs. 2.9 and 2.10 are in line with the hysteresis zone and the fold point observed in the experiments by Gopalakrishnan and Sujith (2014).

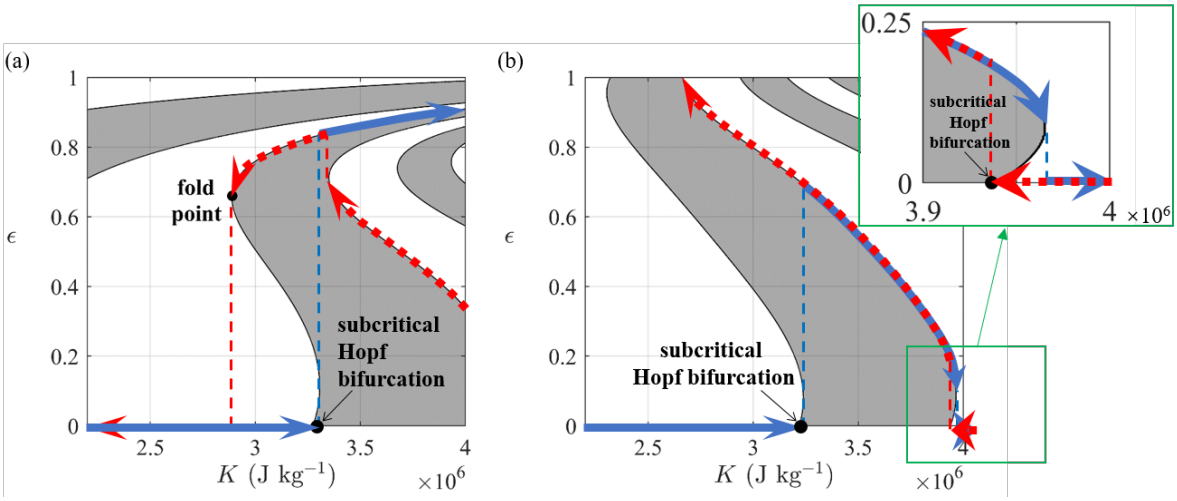

Figure 2.10: Hysteresis effect and bistable regions in a horizontal Rijke tube for variable heater power $2.2 \times 10^6 < K < 4 \times 10^6$ J kg^{-1}, $x_q = 0.1$ m. The white part indicates the stable region and the grey part indicates the unstable region. The blue solid arrows denote the forward (bifurcation) path when the system is switched on with a small perturbation when $K = 2.2 \times 10^6$ J kg^{-1} and the heater power gradually increases to 4×10^6 J kg^{-1}. The red dashed arrows denote the backward (bifurcation) path when the system is switched on with a small perturbation when $K = 4 \times 10^6$ J kg^{-1} and the heater power gradually decreases to 2.2×10^6 J kg^{-1}. (a) Mean flow is absent; (b) M = 0.5.

The comparison of the stability maps for $M = 0, 0.1, 0.3$, and 0.5 suggests that the mean flow effect is only significant when M is sufficiently large. At a low Mach number of M = 0.1, the alteration of the stability map is negligible compared to the $M = 0$ case. A subcritical Hopf bifurcation and a fold point are found (marked in Fig. 2.10), leading to sudden jumps in the forward and backward bifurcation paths. This agrees qualitatively with several experimental observations (Matveev and Culick, 2003a; Gopalakrishnan and Sujith, 2014; Etikyala and Sujith, 2017; Mariappan et al., 2011). As the Mach number increases, the limit cycle amplitude grows when K is low and the growth rate increases. At the same time, the band-shaped unstable region when $K > 3 \times 10^6$ J kg^{-1} becomes narrower and straighter. Fig. 2.10 focuses on the range $2.2 \times 10^6 < K < 4 \times 10^6$ J kg^{-1} for two different Mach numbers: by increasing the mean flow, another bistable region (cf. inset in the figure for $M = 0.5$) is generated when K exceeds 3.94×10^6 J kg^{-1}.

Figure 2.11 shows the variation of the first-mode heat-driven frequency with K for varying Mach numbers. Part (a) illustrates the behaviour when $\epsilon = 0.1$, whereas in part (b) the amplitude is larger ($\epsilon = 0.8$). The mean-flow effect is less prominent when the oscillation amplitude is low. For both low-amplitude and high-amplitude cases, when K is lower than 1.5×10^6 J kg^{-1}, the frequency decreases as the Mach number increases. The reverse effect is found for the high-amplitude case when $K > 1.5 \times 10^6$ J kg^{-1} and the mean-flow impact is more evident.

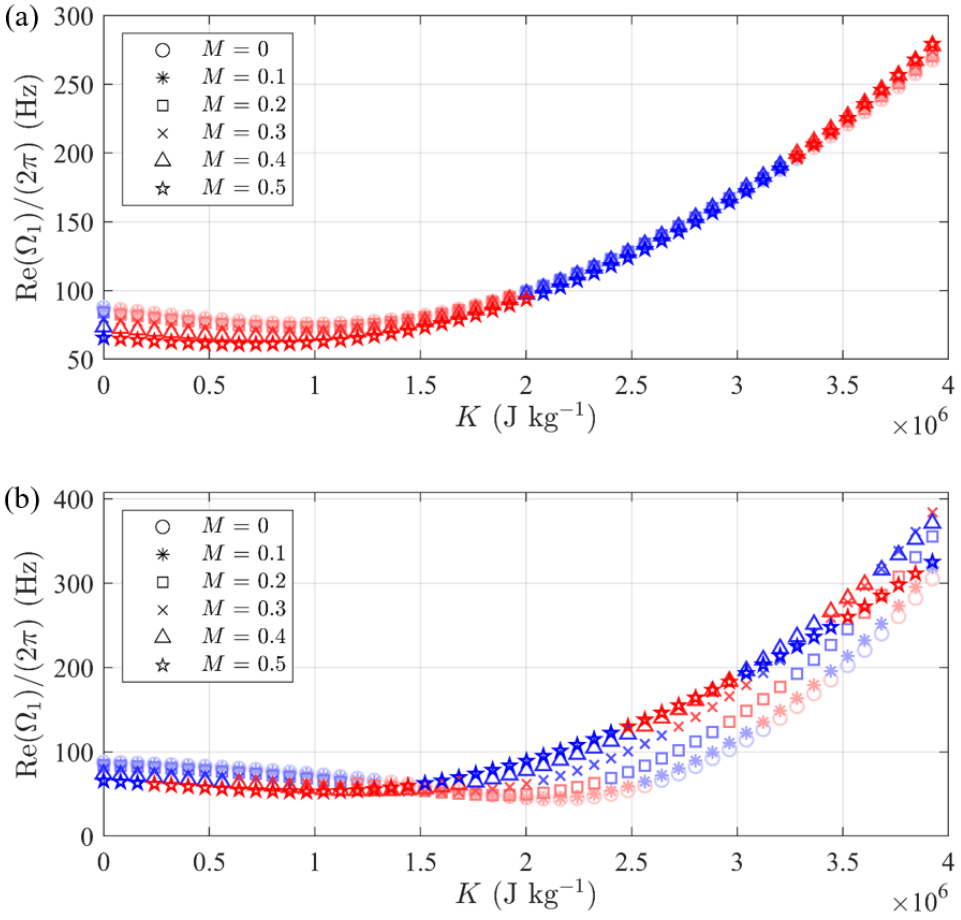

Figure 2.11: Modal frequency variation, $\mathrm{Re}(\Omega_1)/(2\pi)$, as function of the heater power, K, for various Mach numbers M. $x_q = 0.1$ m. Blue symbols represent the stable state of mode 1; red symbols represent the unstable state. (a) Small amplitude, $\epsilon = 0.1$; (b) large amplitude, $\epsilon = 0.8$.

2.3.3. Dependence on the length of the Rijke tube

From the characteristic equation (2.16), it is known that changing the tube length affects the eigenfrequencies of the resonator (ω_n) and hence alters the modal frequency of the thermoacoustic system (Ω_m). Fig. 2.12 shows the stability maps for variations of the control parameter L between the values of 0.4 m and 2 m.

The heat source is fixed at $x_q = 0.01$ m and $K = 3 \times 10^5$ J kg^{-1}. The comparison of the different stability maps highlights the effect of the Mach number. The alteration of the stability boundaries is significant when the Mach number is relatively high. As the Mach number increases, the unstable region where the tube length is longer is expanded and the growth rate in the band-shaped unstable regions increases. Overall, the unstable regions are moving in the direction of decreasing tube length as the mean flow velocity increases.

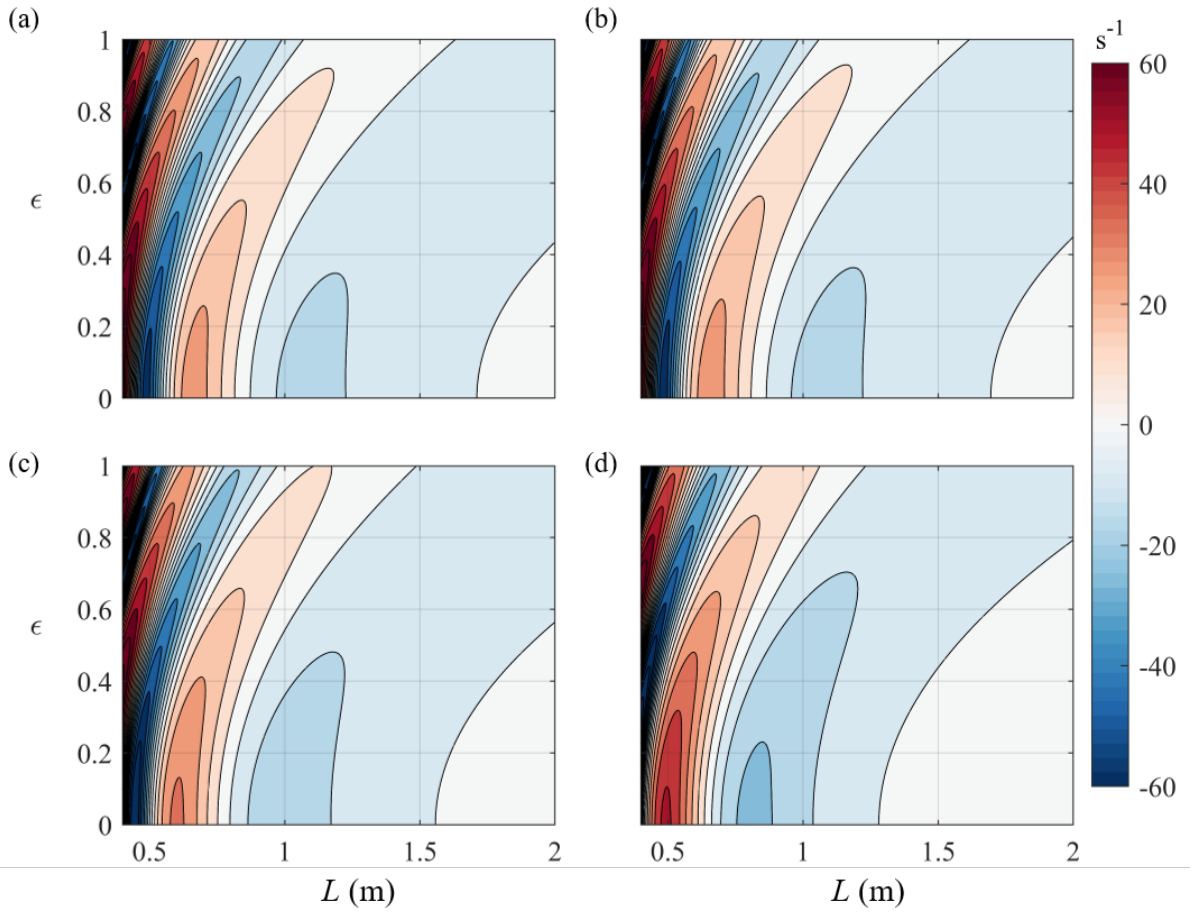

Figure 2.12: Stability maps of a horizontal Rijke tube; the coloured shading denotes the growth rate given on the colour bar on the right. The control parameter is L, the length of the Rijke tube; $x_q = 0.01$ m, $K = 3 \times 10^5$ J kg^{-1}. (a) Mean flow is absent; (b) M = 0.1; (c) M = 0.3; (d) M = 0.5.

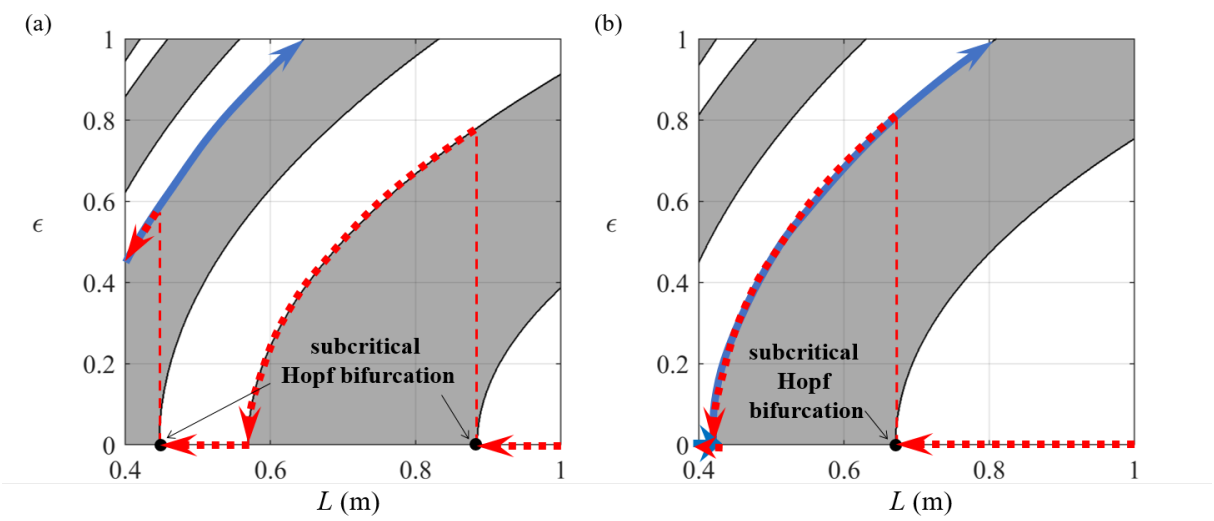

Figure 2.13: Hysteresis effect and bistable regions in a horizontal Rijke tube with changes in the Rijke tube length $0.4 < L < 1$ m, $x_q = 0.01$ m, $K = 3 \times 10^5$ J kg^{-1}. The white part indicates the stable region and the grey part indicates the unstable region. The blue solid arrows denote the forward (bifurcation) path when the system is switched on with a small perturbation when $L = 0.4$ m and the tube length gradually increases to 1 m. The red dashed arrows denote the backward (bifurcation) path when the system is switched on with a small perturbation when $L = 1$ m and tube length gradually decreases to 0.4 m. (a) Mean flow is absent; (b) M = 0.5.

Figure 2.13 focuses on the range 0.4 m $< L <$ 1 m and shows the bifurcation that is observed when L is increased (solid blue curve) or decreased (dashed red curve). Fig. 2.13(a) shows this for $M = 0$. The system is in the limit cycle at the starting point of the forward path ($L = 0.4$ m), and as L increases, the limit cycle is maintained while its amplitude grows. Along the backward path, several transitions occur: at $L = 0.88$ m and $L = 0.45$ m, there are transitions from a linearly stable state to a limit cycle (subcritical Hopf bifurcation); at $L = 0.56$ m, the transition is in the other direction, i.e. from limit cycle to linearly stable (supercritical Hopf bifurcation). The bistable regions are in the ranges $L = 0.45 \sim 0.56$ m and $L = 0.88 \sim 1$ m. For increasing Mach numbers, the bands of instability and hence the Hopf points move to lower L-values; this changes the bistable regions and the transition points as shown in Fig. 2.13(b).

Figure 2.14 depicts the effect of the parameters L, M and ϵ on the oscillation frequency, $\Re(\Omega_1)$, of the thermoacoustic mode 1. As expected, $\Re(\Omega_1)$ decreases with L; it also decreases slightly with M, while the amplitude ϵ has no obvious effect.

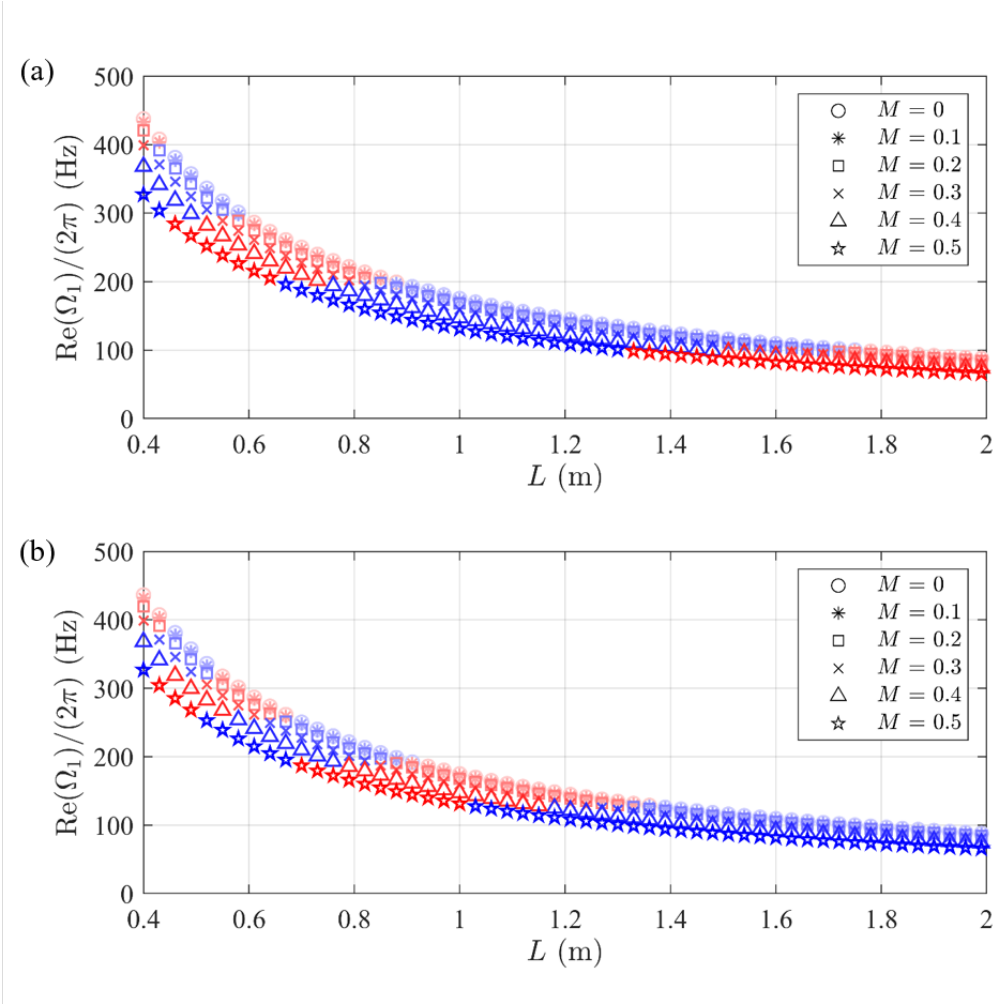

Figure 2.14: Modal frequency variation, $\mathrm{Re}(\Omega_1)/(2\pi)$, as function of the tube length, L, for various Mach number M. $x_q = 0.01$ m, $K = 3 \times 10^5$ J kg^{-1}. Blue symbols represent the stable modes; red symbols represent the unstable modes. (a) Small amplitude, $\epsilon = 0.1$; (b) large amplitude, $\epsilon = 0.8$.

2.4. A MATRIX BURNER CASE

In this section, the aim is to show, on the one hand, the versatility of the adjoint Green's function approach by applying it to a matrix burner test rig developed by Noiray et al. (2008), which has different boundary conditions from the Rijke tube; on the other hand, it is shown that with a properly measured flame describing function, the model prediction has quantitatively good agreement with experiments.

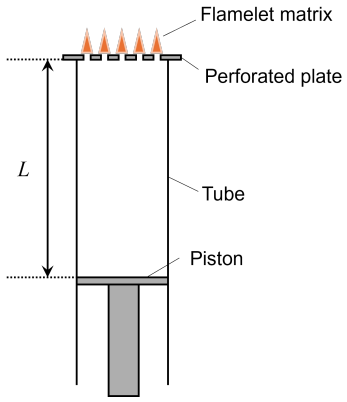

Figure 2.15: Sketch of the matrix burner setup used in Noiray et al. (2008).

The matrix burner system, shown in Fig. 2.15, features a movable piston at the upstream end (where the mixture of fuel and air also comes in), allowing the continuous adjustment of the tube length. The downstream end is fitted with a perforated plate but is otherwise open. A two-dimensional array of flamelets is anchored on the downstream side of the perforations, forming a matrix flame just outside the tube.

Table 2.2: Model parameters to simulate Noiray et al. (2008)'s test rig.

Parameters	Symbol	Value	Unit
Mean temperature	T	296	K
Sound speed	c	345	m s^{-1}
Reflection coefficient (upstream end)	R_0	1	
Reflection coefficient (downstream end)	R_L	-1	
	g_0	1.4	
Fitting parameters	g_1	0.3	
of nonlinear heat release model	τ_0	0.94×10^{-3}	s
	τ_2	2.5×10^{-3}	s
Mach number	M	0.1	
Tube length	L	0.1 ... 0.75	m
Heat source position	x_q	0.01 m to L	
Heater power	K	3×10^5	J kg^{-1}

Noiray (2007) measured the reflection coefficients of both ends of the matrix burner and showed that the piston end could be approximated as a closed boundary ($R_0 = 1$), while the

perforated-plate-flame end had a reflection coefficient around $R_L = -1$. Therefore, this setup is effectively a quarter-wave resonator with a closed end and an open end. The matrix flame and the perforated plate are considered as a single heat source element. Since the present analytical model does not include the mean temperature jump, modelling a flame located outside the tube (at 0.01 m from the downstream end) is expected to yield a good match with the experimental setup. The heat release rate is modelled by Heckl (2015)'s extended time-lag law described by Eqs. (2.3)-(2.4c), with the fitting parameters listed in Table 2.2. Also listed in Table 2.2 are all the other parameter values we use to model Noiray's test rig.

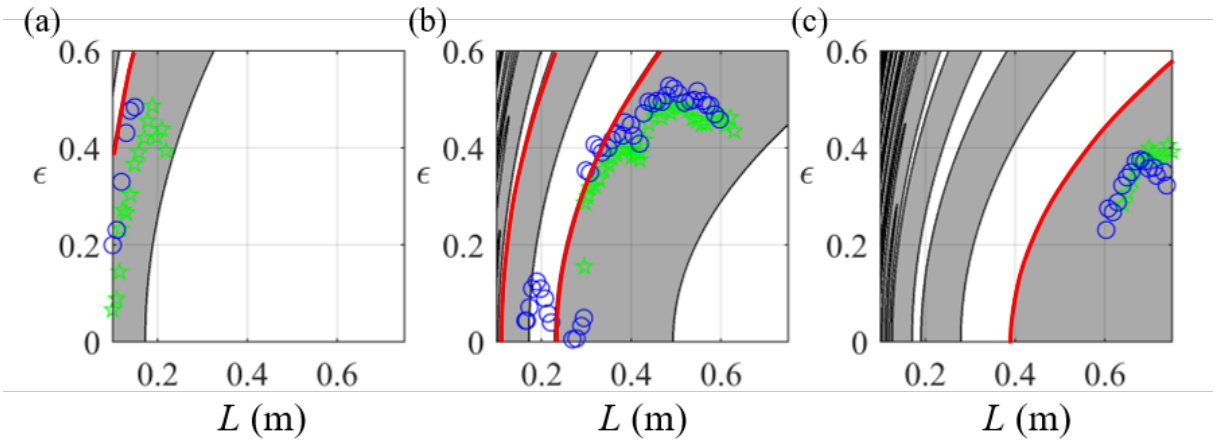

Figure 2.16: Comparison of heat-driven modes of a quarter-wave resonator with tube length L as the control parameter, with experimentally measured results from Noiray et al. (2008). The gray regions denote instability, while the white regions indicate stability. The red solid curves denote the limit-cycle amplitudes. The green stars display the acoustic velocity amplitude measured in experiments when the tube length is progressively increased, whereas the blue circles represent the acoustic velocity amplitude obtained with the tube length progressively decreasing. (a) $m = 1$; (b) $m = 2$; (c) $m = 3$.

Figure 2.16 shows the stability maps calculated with the AGF approach of the first three modes of the matrix burner with the tube length L as the control parameter, together with corresponding data extracted during the limit-cycle phase of the experiments. Our stability maps successfully capture the unstable states except for the small-amplitude limit cycle region of mode 2 in the backward path, around $L = 0.2$ m. The size of the limit cycle region of mode 3 and, generally, the limit cycle amplitudes are over-predicted. This is mostly due to the heat release model incorrectly predicting the high-frequency behaviour of the flame (Heckl, 2015), and also because we have neglected any damping that would be present in an actual combustion chamber.

Figure 2.17 shows the frequency of the oscillatory stable states, i.e. when $\Im(\Omega_m) = 0$, corresponding to the limit cycles indicated by red curves in Fig. 2.16. The agreement between predicted and measured frequencies for all modes is very satisfactory, and this is because the flame is very close to the downstream end of the tube, so the effect of the hot region can be ignored.

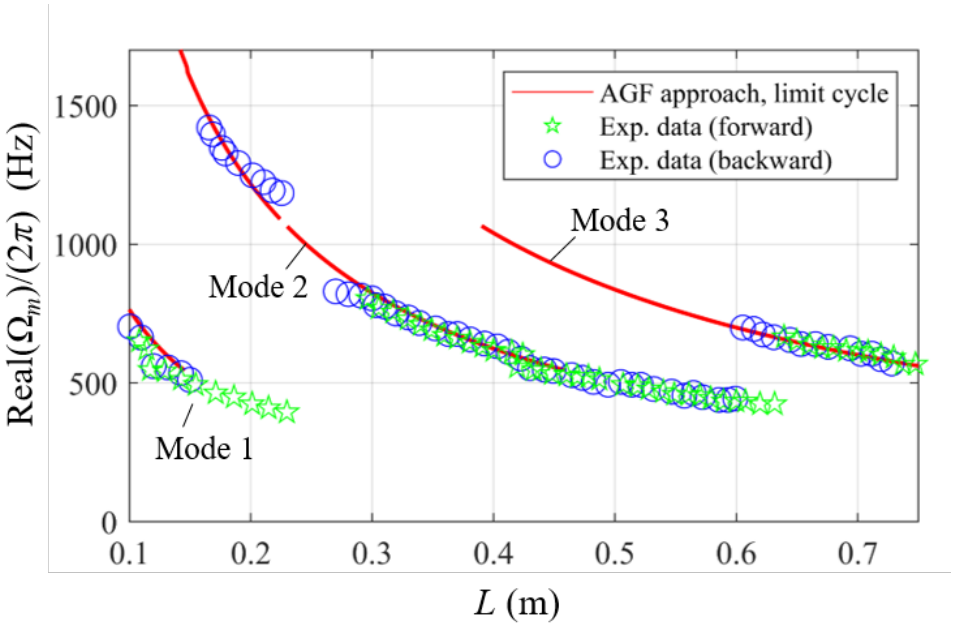

Figure 2.17: Comparison of heat-driven frequencies of modes $m = 1, 2, 3$ at the limit cycle amplitudes, corresponding to the red solid curves in Fig. 2.16; the symbols correspond to experimental measurements by Noiray et al. (2008).

2.5. NON-UNIFORM TEMPERATURE FLOW DUCT

In a more realistic case, besides a steady mean flow in the axial direction of the tube, we include a temperature jump in the vicinity of the compact heat source located at $x = x_q$. The heat source produces a hot region around it and downstream of it. A sketch of this system is illustrated in Fig. 2.18.

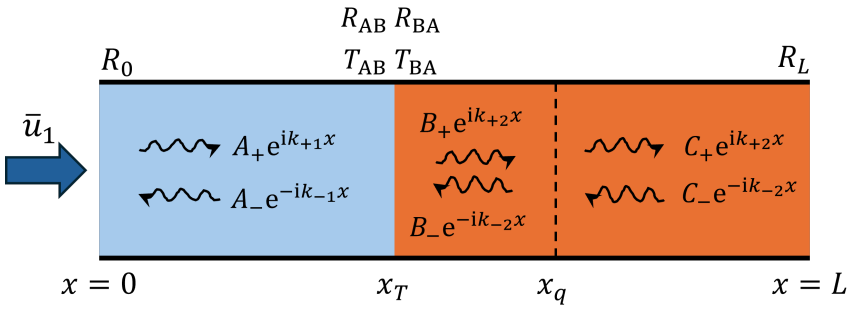

Figure 2.18: Sketch of velocity potential wave propagating in a one-dimensional flow-duct model.

We assume the temperature suddenly changes at a compact virtual plane in $x = x_T$ and the distance $\Delta x = x_q - x_T$ is much smaller than the length of the duct L. The acoustic field in the cold and hot regions are governed by Eq. (2.5), respectively. At the temperature jump interface, the transmission and reflection coefficients of the acoustic waves coming from the upstream

side and the downstream side are denoted as T_{AB}, R_{AB} and T_{BA}, R_{BA}, respectively.

The AGF framework for modelling this thermoacoustic system is very similar to the uniform flow-duct case, which has been shown in the previous sections. In this section, we point out the parts that are different for the non-uniform temperature case.

2.5.1. Reflection and transmission coefficients across a sudden jump in temperature

In the *absence of mean flow*, the derivation of the reflection and transmission coefficients across the abrupt characteristic impedance change, $T_{\mathrm{AB}}^{(p)}$, $R_{\mathrm{AB}}^{(p)}$ and $T_{\mathrm{BA}}^{(p)}$, $R_{\mathrm{BA}}^{(p)}$, is described, for example, by Rienstra and Hirschberg (2004) and Kinsler et al. (2000). The authors thank one of the referees for drawing particular attention to these conditions when the mean flow is present. In this section, we outline the details of our derivation.

Figure 2.19 shows the setup when an abrupt change in temperature occurs in an infinitely long one-dimensional tube. A steady mean flow is present in the tube, from left to right. The

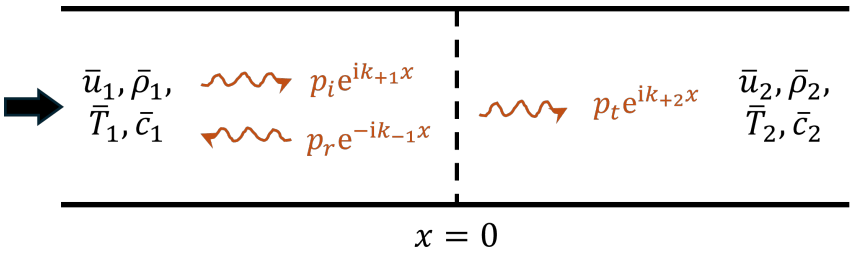

Figure 2.19: Sketch of temperature jump in an infinitely long tube.

incident, reflected, and transmitted pressure wave complex amplitudes are called p_i, p_r, and p_t, respectively. For the convenience of derivation, the position of the temperature jump is set at $x = 0$, and the reflection and transmission coefficients at the jump are defined as

$$R_{\mathrm{AB}}^{(p)} = \frac{p_r}{p_i}, \quad \text{and} \quad T_{\mathrm{AB}}^{(p)} = \frac{p_t}{p_i}, \tag{2.58}$$

respectively.

We start with the linearised mass and momentum conservation equations for the perturbations, which hold at the temperature jump:

$$\rho_1' \bar{u}_1 + u_1' \bar{\rho}_1 = \rho_2' \bar{u}_2 + u_2' \bar{\rho}_2, \tag{2.59a}$$

$$2\bar{\rho}_1 \bar{u}_1 u_1' + \rho_1' \bar{u}_1^2 + p_1' = 2\bar{\rho}_2 \bar{u}_2 u_2' + \rho_2' \bar{u}_2^2 + p_2'. \tag{2.59b}$$

The disturbances can be written as

$$p_1' = p_i e^{ik_{+1}x} + p_r e^{-ik_{-1}x}, \tag{2.60a}$$

$$p_2' = p_t e^{ik_{+2}x}, \tag{2.60b}$$

$$u_1' = \frac{1}{\bar{\rho}_1 c_1} \left(p_i e^{ik_{+1}x} - p_r e^{-ik_{-1}x} \right), \tag{2.60c}$$

$$u_2' = \frac{1}{\bar{\rho}_2 c_2} p_t e^{ik_{+2}x}, \tag{2.60d}$$

and $\rho'_j = p'_j/c_j^2$, with $j = 1, 2$.

Substituting Eqs. (2.60) into Eqs. (2.59) and using Eqs. (2.58), we obtain the following two equations,

$$(M_1 + 1) + R_{\text{AB}}^{(p)}(M_1 - 1) = \frac{c_1}{c_2} T_{\text{AB}}^{(p)}(M_2 + 1), \tag{2.61a}$$

$$(M_1 + 1)^2 + R_{\text{AB}}^{(p)}(M_1 - 1)^2 = T_{\text{AB}}^{(p)}(M_2 + 1)^2. \tag{2.61b}$$

Solving the above for the unknowns $R_{\text{AB}}^{(p)}$ and $T_{\text{AB}}^{(p)}$ yields the reflection and transmission coefficients in terms of pressure:

$$R_{\text{AB}}^{(p)} = \frac{-(M_1 + 1)\left[(M_1 + 1) - \dfrac{c_2}{c_1}(M_2 + 1)\right]}{(M_1 - 1)\left[(M_1 - 1) - \dfrac{c_2}{c_1}(M_2 + 1)\right]}, \tag{2.62a}$$

$$T_{\text{AB}}^{(p)} = \frac{2(1 + M_1)}{(M_2 + 1)\left[(M_2 + 1) - \dfrac{c_1}{c_2}(M_1 - 1)\right]}. \tag{2.62b}$$

Similarly, for the incident wave coming from the downstream direction, we obtain

$$R_{\text{BA}}^{(p)} = \frac{-(M_2 - 1)\left[(M_2 - 1) - \dfrac{c_1}{c_2}(M_1 - 1)\right]}{(M_2 + 1)\left[(M_2 + 1) - \dfrac{c_1}{c_2}(M_1 - 1)\right]}, \tag{2.63a}$$

$$T_{\text{BA}}^{(p)} = \frac{2(1 - M_2)}{(M_1 - 1)\left[(M_1 - 1) - \dfrac{c_2}{c_1}(M_2 + 1)\right]}. \tag{2.63b}$$

In the limiting case of no mean flow ($M_1 = M_2 = 0$), using $c_1/c_2 = (\bar{\rho}_2 c_2)/(\bar{\rho}_1 c_1)$, the above Eqs. (2.62)-(2.63) reduce to the following form

$$\begin{aligned} T_{\text{AB}}^{(p)} &= \frac{2\bar{\rho}_1 c_1}{\bar{\rho}_1 c_1 + \bar{\rho}_2 c_2}, \qquad & T_{\text{BA}}^{(p)} &= \frac{2\bar{\rho}_2 c_2}{\bar{\rho}_1 c_1 + \bar{\rho}_2 c_2}, \\ R_{\text{BA}}^{(p)} &= \frac{\bar{\rho}_1 c_1 - \bar{\rho}_2 c_2}{\bar{\rho}_1 c_1 + \bar{\rho}_2 c_2}, \qquad & R_{\text{BA}}^{(p)} &= \frac{\bar{\rho}_2 c_2 - \bar{\rho}_1 c_1}{\bar{\rho}_1 c_1 + \bar{\rho}_2 c_2}. \end{aligned} \tag{2.64}$$

Comparing Eqs. (2.64) with the results reported by Rienstra and Hirschberg (2004) and Kinsler et al. (2000), we cannot fail to notice that our results are similar, but not identical, to those reported. This is related to the fact that in the study of wave propagation across a contact discontinuity in compressible flows, it is common in the acoustics literature to assume that the disturbance velocity and pressure are continuous across the interface. These assumptions must, however, be relaxed in the presence of variable mean densities, when the disturbance mass flux must be imposed as continuous across the contact discontinuity. In the absence of mean flow, this becomes $\bar{\rho}_1 u'_1 = \bar{\rho}_2 u'_2$ (rather than $u'_1 = u'_2$), and Eqs. (2.64) follow.

Using Eqs. (2.19), we obtain the reflection and transmission coefficients across a sudden temperature jump when a mean flow is present, in terms of the velocity potential disturbances:

$$R_{\mathrm{AB}} = \frac{c_1(M_1+1) - c_2(M_2+1)}{c_1(M_1-1) - c_2(M_2+1)}, \tag{2.65a}$$

$$T_{\mathrm{AB}} = \frac{-2c_2}{c_1(M_1-1) - c_2(M_2+1)}, \tag{2.65b}$$

$$R_{\mathrm{BA}} = \frac{c_1(M_1-1) - c_2(M_2-1)}{c_1(M_1-1) - c_2(M_2+1)}, \tag{2.65c}$$

$$T_{\mathrm{BA}} = \frac{-2c_1}{c_1(M_1-1) - c_2(M_2+1)}. \tag{2.65d}$$

The above coefficients (2.65) are used in the present work.

2.5.2. Natural frequencies of a flow-duct with non-uniform temperature

Similar to the derivation of Eq. (2.16), the natural frequencies of flow-duct with a temperature jump solely depend on the geometry and physical properties of the setup, without considering the additional sources, as shown in Fig. 2.20.

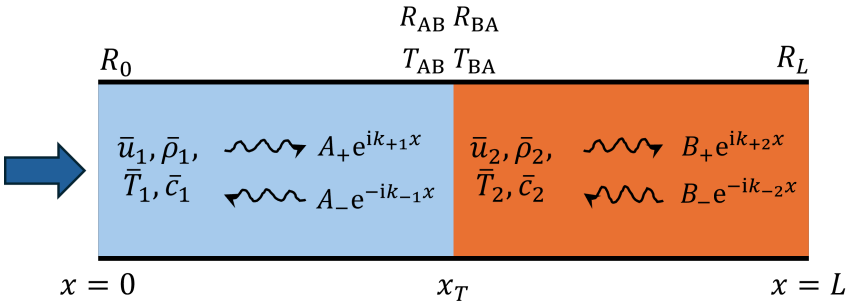

Figure 2.20: Sketch of the flow duct with non-uniform temperature without the presence of the heat source.

The general solution of acoustic velocity potential can then be written as a superposition of forward and backward travelling waves:

$$\hat{\phi}(x,\omega) = \begin{cases} A_+ e^{ik_{+1}x} + A_- e^{-ik_{-1}x} & \text{for} \quad 0 < x < x_T \\ B_+ e^{ik_{+2}x} + B_- e^{-ik_{-2}x} & \text{for} \quad x_T < x < L, \end{cases} \tag{2.66}$$

where A_+, A_-, B_+ and B_- are (generally complex) amplitudes of the velocity potential. The wave numbers are different for hot and cold regions because of the non-uniform temperature. The reflection coefficients R_0 and R_L are used to define the boundary conditions. At $x = 0$ there is

$$R_0 = \left.\frac{A_+ e^{ik_{+1}x}}{A_- e^{-ik_{-1}x}}\right|_{x=0}, \quad \text{giving} \quad A_+ = A_- R_0, \tag{2.67}$$

and likewise at $x = L$,

$$R_L = \left.\frac{B_- \mathrm{e}^{-\mathrm{i}k_{-2}x}}{B_+ \mathrm{e}^{\mathrm{i}k_{+2}x}}\right|_{x=L}, \quad \text{giving} \quad B_- = B_+ R_L \mathrm{e}^{\mathrm{i}(k_{+2}+k_{-2})L}. \tag{2.68}$$

At $x = x_T$, the reflection coefficients, R_{AB} and R_{BA}, and the transmission coefficients, T_{AB} and T_{BA}, give the constraints at the temperature jump,

$$A_- \mathrm{e}^{-\mathrm{i}k_{-1}x_T} = R_{\mathrm{AB}} A_+ \mathrm{e}^{\mathrm{i}k_{+1}x_T} + T_{\mathrm{BA}} B_- \mathrm{e}^{-\mathrm{i}k_{-2}x_T}, \tag{2.69a}$$

$$B_+ \mathrm{e}^{\mathrm{i}k_{+2}x_T} = R_{\mathrm{BA}} B_- \mathrm{e}^{-\mathrm{i}k_{-2}x_T} + T_{\mathrm{AB}} A_+ \mathrm{e}^{\mathrm{i}k_{+1}x_T}. \tag{2.69b}$$

Equations (2.67) - (2.69) give four homogeneous equations for $A_+,\ A_-,\ B_+$ and B_- and leads to the coefficient matrix

$$\mathcal{M}_F = \begin{bmatrix} 1 & -R_0 & 0 & 0 \\ -\mathrm{e}^{\mathrm{i}k_{+1}x_T} R_{\mathrm{AB}} & \mathrm{e}^{-\mathrm{i}k_{-1}x_T} & 0 & -\mathrm{e}^{-\mathrm{i}k_{-2}x_T} T_{\mathrm{BA}} \\ -\mathrm{e}^{\mathrm{i}k_{+1}x_T} T_{\mathrm{AB}} & 0 & \mathrm{e}^{\mathrm{i}k_{+2}x_T} & -\mathrm{e}^{-\mathrm{i}k_{-2}x_T} R_{\mathrm{BA}} \\ 0 & 0 & -\mathrm{e}^{\mathrm{i}(k_{+2}+k_{-2})L} R_L & 1 \end{bmatrix} \tag{2.70}$$

and its determinant gives the characteristic equation

$$\begin{aligned} F(\omega) = \det(\mathcal{M}_F) = &- R_L R_{\mathrm{BA}} \mathrm{e}^{\mathrm{i}(L-x_T)k_{-2} - \mathrm{i}k_{-1}x_T + \mathrm{i}k_{+2}L} + \\ &+ R_0 R_L \left(R_{\mathrm{AB}} R_{\mathrm{BA}} - T_{\mathrm{AB}} T_{\mathrm{BA}}\right) \mathrm{e}^{\mathrm{i}(L-x_T)k_{-2} + \mathrm{i}k_{+1}x_T + \mathrm{i}k_{+2}L} - \\ &- R_0 R_{\mathrm{AB}} \mathrm{e}^{\mathrm{i}x_T(k_{+1}+k_{+2})} + \mathrm{e}^{-\mathrm{i}x_T(k_{-1}-k_{+2})} = 0. \end{aligned} \tag{2.71}$$

The eigenfrequencies ω_n are the solutions of the characteristic equation for mode $n = 1, 2, 3, ...$

2.5.3. AGF of a non-uniform temperature flow duct

The solution for the direct Green's function of the non-uniform temperature flow-duct is

$$g(x, x', t - t') = H(t - t') \sum_{n=1}^{\infty} \mathrm{Re}\left[\hat{g}_n(x, x', \omega_n) e^{-\mathrm{i}\omega_n(t-t')}\right]. \tag{2.72}$$

with

$$\hat{g}_n(x, x', \omega_n) = -\frac{2\pi\, T_{\mathrm{BA}}}{\bar{u}_2 \omega_n F'(\omega_n)} \begin{cases} \eta(x', \omega_n)\, \alpha(x, \omega_n) & \text{for } 0 < x < x_T, \\ \eta(x', \omega_n)\, \beta(x, \omega_n) & \text{for } x_T < x < x', \\ \beta(x', \omega_n)\, \eta(x, \omega_n) & \text{for } x' < x < L. \end{cases} \tag{2.73}$$

The details of derivation can be found in the Appendix A.5. With the reciprocity property, Eq. (2.48), the AGF $G(x', x, t-t')$ can be obtained. The modal amplitude of the AGF represents the receptivity of the system to external forcings throughout the tube.

2.5.4. Validation of linear stability prediction with a wave-based model

In this section, we validate the AGF framework against a wave-based network modelling approach by comparing the linear stability prediction of a non-uniform horizontal Rijke tube system. Hence we drop the nonlinear amplitude dependence of the heat release law for now; instead, we use a linear unsteady $n-\tau$ heat release law,

$$Q'(t) = Kn_1u_1'(t-\tau_q). \tag{2.74}$$

The parameters of the system are listed in Table 2.3.

Table 2.3: Model parameters of the non-uniform horizontal Rijke tube

Parameters	Symbol	Value	Unit
Inlet flow Mach number	M_1	0.02	
Cold region mean temperature	$\bar{T}_{m1}$	304	K
Hot region mean temperature	$\bar{T}_{m2}$	484	K
Cold region sound speed	c_1	349.52	m s^{-1}
Hot region sound speed	c_2	441.02	m s^{-1}
Reflection coefficient (upstream end)	R_0	$-(1+M_1)/(1-M_1)$	
Reflection coefficient (downstream end)	R_L	$-(1-M_2)/(1+M_2)$	
Tube length	L	2	m
Heat source position	x_q	$0 \ldots L$	m
Heater power	K	3×10^5	J kg^{-1}
	n_0	0	
Parameters of	n_1	1.2	
linear heat release model	τ_q	2×10^{-3} and 8×10^{-3}	s

The wave-based network modelling approach used here is adopted from Dowling and Stow (2003) p.756-757, example 4. The tube is divided into two sections: upstream and downstream of the compact flame sheet. The mean flow involved in the system admits entropy and vorticity waves on the downstream side. In the one-dimensional case, the vorticity wave is neglected. The complex eigenfrequency of disturbances is denoted as Ω. Therefore, the general solutions of the acoustic disturbances can be formulated as,

$$p_j'(x,t) = (A_{+j}\mathrm{e}^{-\mathrm{i}\Omega\frac{x}{c_j(1+M_j)}} + A_{-j}\mathrm{e}^{\mathrm{i}\Omega\frac{x}{c_j(1-M_j)}})\mathrm{e}^{\mathrm{i}\Omega t}, \tag{2.75a}$$

$$u_j'(x,t) = \frac{1}{\bar{\rho}_j c_j}(A_{+j}\mathrm{e}^{-\mathrm{i}\Omega\frac{x}{c_j(1+M_j)}} - A_{-j}\mathrm{e}^{\mathrm{i}\Omega\frac{x}{c_j(1-M_j)}})\mathrm{e}^{\mathrm{i}\Omega t}, \tag{2.75b}$$

$$\rho_j'(x,t) = \frac{p_j'(x,t)}{c_j^2} - \frac{S_j\bar{\rho}_j}{c_p}\mathrm{e}^{\mathrm{i}\Omega(t-\frac{x}{\bar{u}_j})}, \tag{2.75c}$$

$$T_j'(x,t) = \frac{p_j'(x,t)}{\bar{\rho}_j c_p} + \frac{S_j c_j^2}{(\gamma-1)}\mathrm{e}^{\mathrm{i}\Omega(t-\frac{x}{\bar{u}_j})}. \tag{2.75d}$$

c_p is the specific heat capacity. The subscripts $j=1,2$ indicate the upstream and downstream sections, respectively. A_{+j}, A_{-j}, and S_j are respective amplitudes of right-travelling, left-travelling, and entropy waves. The upstream of the heat source, the flow is considered isentropic, i.e. $S_1=0$. Both ends of the tube are considered open, i.e.

$$p_1' = 0, \quad \text{at } x=0; \quad \text{and} \quad p_2' = 0, \quad \text{at } x=L. \tag{2.76}$$

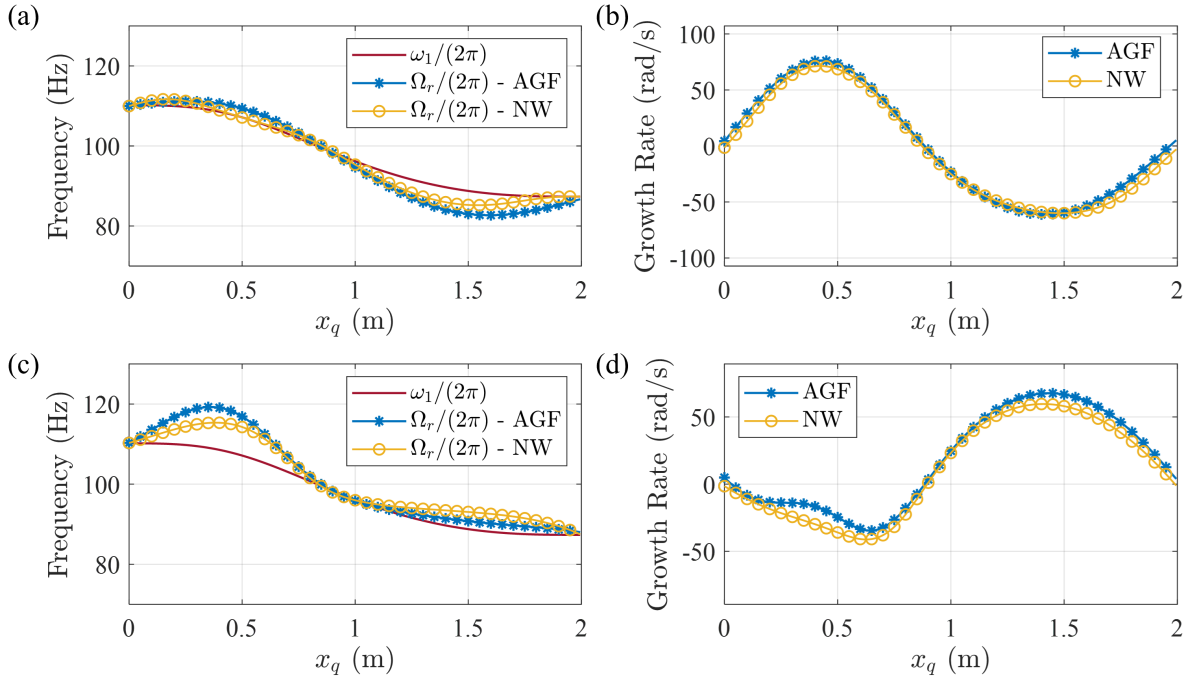

Figure 2.21: A comparison of complex eigenfrequencies obtained with adjoint Green's function approach (AGF) and network modeling approach (NW) with the dependence on the heat source position, x_q. $n_1 = 1.2$, $M_1 = 0.02$. The subfigures in the upper row (a-b) show the results of the case when $\tau_q = 0.002$ s. The bottom row, (c-d), shows the result of the case when $\tau_q = 0.008$ s. Subfigures (a) and (c) also show the dependence of the fundamental natural frequency (ω_1) on x_q.

The sound field in the two sections is constrained and coupled with a series of jump conditions across the compact heat source,

$$\bar{\rho}_1\hat{u}_1 + \hat{\rho}_1\bar{u}_1 = \bar{\rho}_2\hat{u}_2 + \hat{\rho}_2\bar{u}_2, \tag{2.77a}$$

$$\hat{\rho}_1\bar{u}_1^2 + 2\bar{\rho}_1\bar{u}_1\hat{u}_1 + \hat{p}_1 = \hat{p}_2 + \hat{\rho}_2\bar{u}_2^2 + 2\bar{\rho}_2\bar{u}_2\hat{u}_2, \tag{2.77b}$$

$$\bar{\rho}_1\bar{u}_1\hat{H}_1 + \bar{\rho}_1\bar{H}_1\hat{u}_1 + \bar{u}_1\bar{H}_1\hat{\rho}_1 + \bar{\rho}_1\hat{Q} = \bar{\rho}_2\bar{u}_2\hat{H}_2 + \bar{\rho}_2\hat{u}_2\bar{H}_2 + \hat{\rho}_2\bar{u}_2\bar{H}_2 \tag{2.77c}$$

with $\bar{H}_j = c_p\bar{T}_j + \bar{u}_j^2/2$ and $\hat{H}_j = c_p\hat{T}_j + \bar{u}_j\hat{u}_j$ the steady and unsteady enthalpy, respectively. Eqs. (2.77) are Eqs. (10a-10c) in Dowling and Stow (2003) linearized around the mean flow with the flow variables decomposed as $p(x,t) = \bar{p} + p'(x,t)$, $u(x,t) = \bar{u} + u'(x,t)$, $\rho(x,t) = \bar{\rho} + \rho'(x,t)$, $T(x,t) = \bar{T} + T'(x,t)$, $Q(t) = \bar{Q} + Q'(t)$, and taking $p'(x,t) = \hat{p}(x)\,\mathrm{e}^{\mathrm{i}\Omega t}$ and similarly for u', ρ', T', and Q'.

Eqs. (2.74)-(2.77) can be formulated into matrix form $\mathcal{M}(\omega)\mathbf{v} = \mathbf{0}$ with the unknown vector $\mathbf{v}$ consisting of wave amplitudes A_{+j}, A_{-j}, S_2, and $\hat{Q}$. Solving the characteristic equation $\det[\mathcal{M}(\Omega)] = 0$ gives the eigenfrequencies (Ω) of the given thermoacoustic system. The real part, Ω_r, represents the angular frequency of perturbations, and the negative imaginary part, $-\Omega_i$, represents the growth rate of perturbations.

Figure 2.21 shows that the complex eigenvalues computed with the AGF approach agree very well with the results calculated using the wave-based network modelling approach. We

have tested two time delays. The first time delay, $\tau_q = 0.002$ s, lies in the range of $0 < \tau_q < \mathcal{T}_1/2$, where $\mathcal{T}_1 = 2\pi/\omega_1$ is the oscillation period of the fundamental eigenmode. For a Rijke tube whose time delay lies in this range, the system is unstable when the heat source is located in the upstream half of the tube, and it is stable when the heat source lies in the downstream half of the tube (Raun et al., 1993), as shown in Fig. 2.21(b). When $\tau_q = 0.008$ s lies in the range of $\mathcal{T}_1/2 < \tau_q < \mathcal{T}_1$, the regions of stability and instability are interchanged, as shown in Fig. 2.21(d). Fig. 2.21(a) and (c) show the comparison between the eigenfrequencies of the Green's function first mode ($n = 1$, Eq. (2.71)), which do not vary with the heat release law of the flame, and the heat-driven frequencies of mode $m = 1$, at two values of time delays. It is observed that the difference between the two frequencies is not major, and the frequency shift is caused by the thermoacoustic feedback through the heat release law (Noiray, 2007; Orchini et al., 2015; Dowling, 1999).

The good agreement between the heat-driven eigenfrequencies calculated by the network modelling and the AGF approaches indicates that, although the entropy wave is not treated explicitly in the derivation of the AGF approach, its contribution appears via the inclusion of the heat source.

2.5.5. The open-end acoustic boundary conditions in a non-uniform flow duct

The *acoustic pressure* p' is related to the velocity potential by the linearised momentum equation in the form

$$p' = -\bar{\rho}\left(\frac{\partial \phi}{\partial t} + \bar{u}\frac{\partial \phi}{\partial x}\right) \tag{2.78}$$

In this section, the acoustic boundary conditions of the open ends in the presence of a steady mean flow are discussed.

Upstream open-end boundary condition

For a thin-walled open-end tube, a free jet in the tube forms because of flow separation at the edges. Due to the shape of the edges and wall thickness, the width of the formed jets varies, described by a *vena contracta* factor α. This factor indicates the ratio of the free jet cross-section to the pipe cross-section. It has been shown that, for the unflanged, sharp-edged open pipe termination, the losses at inlet and outlet are comparable (Levine and Schwinger, 1948). However, in this study, we assume that at the inlet of the pipe, the open edges are such that there is no inflow separation. The pressure of the mixing flow at the inlet is equal to the ambient pressure, giving the following open-inlet boundary condition:

$$R_0^{(p)} = -1, \quad \text{i.e.,} \quad R_0 = -\frac{1 + M_1}{1 - M_1}. \tag{2.79}$$

Downstream open-end boundary condition

In the one-dimensional Rijke tube configurations considered in this study, the pipe length is much larger than its diameter D, and the analysis focuses on the low-frequency regime corresponding to the fundamental acoustic modes. This gives the Helmholtz number $He = kD \ll 1$.

The system's acoustic behaviour is dominated by plane wave propagation. Given that the Mach number is not negligible and the flow has a significant impact on the acoustic behaviour, the Strouhal number is $St = He/M \ll 1$. In this limit, the flow condition at the open outlet of the tube can be assumed as quasi-steady.

In the steady subsonic free jet formed at the open outlet of the tube, the pressure in the jet is equal to the surrounding pressure (Shapiro, 1953). At low frequencies, the acoustic fluctuations of the surrounding pressure can be neglected. In the first approximation, the pressure in the jet is also equal to the pressure at the outlet termination. Consequently, the quasi-steady assumption implies that the acoustic pressure perturbation at the open outlet vanishes, leading to the downstream boundary condition:

$$R_L^{(p)} = -1, \quad \text{i.e.,} \quad R_L = -\frac{1 - M_2}{1 + M_2}. \tag{2.80}$$

It should be emphasised that this condition accounts for the absorption of acoustic energy, which arises from vortex shedding at the free jet shear layer.

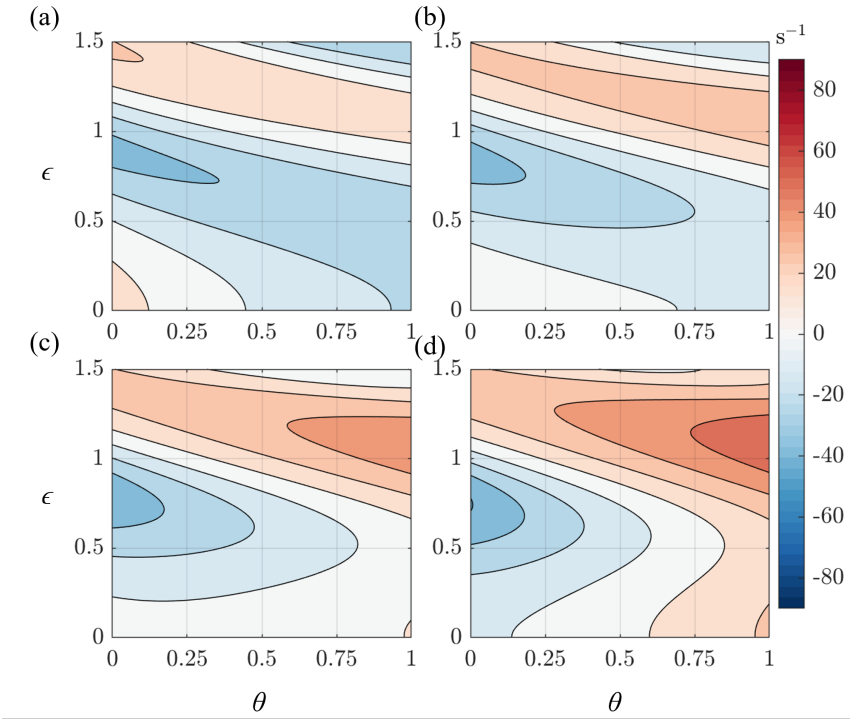

Figure 2.22: Stability maps with the control parameter being θ, the relative temperature difference. $x_q = 0.1$ m, the cold flow temperature is fixed as $\bar{T}_{m1} = 304$ K. (a) $M_1 = 0$; (b) $M_1 = 0.04$; (c) $M_1 = 0.08$; (d) $M_1 = 0.12$.

2.5.6. Effect of non-uniform temperature field

We consider a temperature jump across the compact flame that separates the geometry into cold and hot regions. The non-uniformity of the temperature field is described by the relative temperature difference, defined as,

$$\theta = \frac{T_{m2} - T_{m1}}{T_{m1}}. \tag{2.81}$$

The relative temperature difference θ is examined as a control parameter to assess the impact of burnt gas temperature on the system's stability.

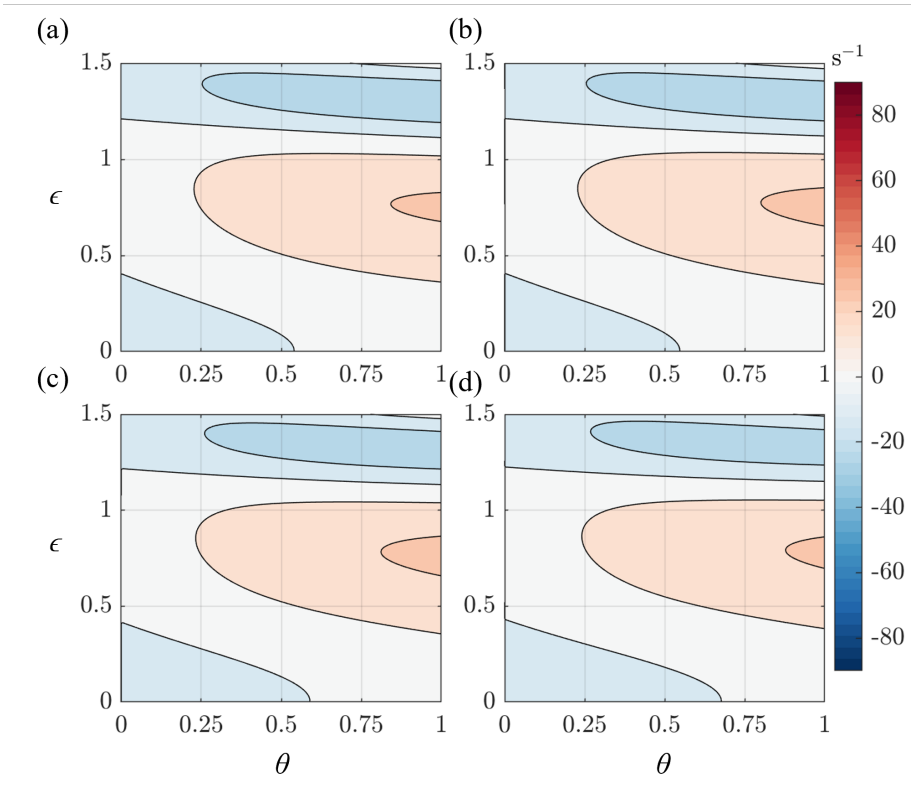

Figure 2.23: Same as Fig. 2.22 for $x_q = 1.0$ m.

We now examine the relative temperature difference θ as a control parameter to assess the impact of burnt gas temperature on the system's stability. Figs. 2.22 and 2.23 show the stability maps when the heat source position is chosen as $x_q = 0.1$ m and $x_q = 1.0$ m, respectively. For each case, stability maps are provided for varying mean flow velocities: $M_1 = 0, 0.04, 0.08, 0.12$. Fig. 2.22 shows that, when the heat source is located in the upstream half of the flow duct, an increase of mean flow velocity significantly changes the stability behaviour of the system. As the mean flow velocity increases, the stable region (blue shades) shrinks, and the growth rates in the unstable region become higher. However, when the heat source is in the mid-to-downstream half of the tube, as shown in Fig. 2.23, the effect of mean

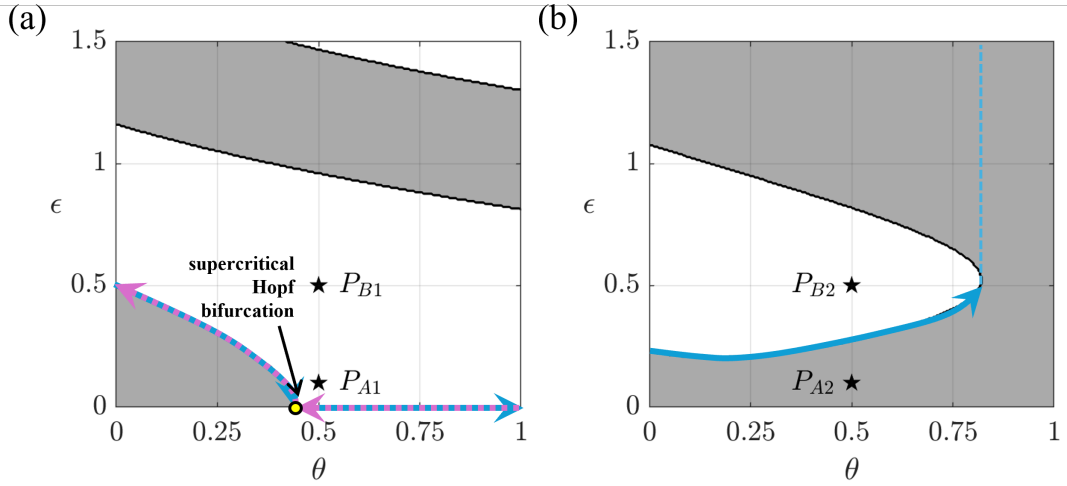

Figure 2.24: Hysteresis, bistable regions, and bifurcation paths in Fig. 2.22 (a) and (c), when changing relative temperature difference $0 < \theta < 1$. The white part indicates the stable region, and the grey part indicates the unstable region. The blue solid arrows denote the forward (bifurcation) path when the system is switched on with a small perturbation when $\theta = 0$ and the hot region temperature gradually increases to $\theta = 1$. The pink dashed arrows denote the backward (bifurcation) path when the system is switched on with a small perturbation when $\theta = 1$ and the hot region gradually cools down to $\theta = 0$. (a) Mean flow is absent, $M_1 = 0$; (b) $M_1 = 0.08$.

flow is less significant. It is observed that the stable region expands slightly as the mean flow velocity increases.

Figure 2.24 illustrates the same results as Fig. 2.22(a) and (c) for $M_1 = 0$ and $M_1 = 0.08$, emphasising the presence of bistable regions and the occurrence of bifurcation. The stable regions are depicted in white, while unstable regions are shaded in grey. The heat source position is fixed at $x_q = 0.1$ m. The light blue arrows show the stability behaviour path when the temperature on the downstream side of the heat source gradually increases from $T_{m2} = T_{m1}$ to $T_{m2} = 2T_{m1}$ while the pink dashed arrows indicate the gradual decrease from $T_{m2} = 2T_{m1}$ to $T_{m2} = T_{m1}$. When the mean flow is absent, Fig. 2.24(a) shows that the system undergoes a supercritical bifurcation as it is initialised with an infinitesimal amplitude and then heated or cooled down. The stability behaviour follows the same path, as indicated by the blue and pink arrows. Another unstable region of stripe shape is found, for normalised amplitude $\epsilon > 0.8$. As the mean flow velocity increases, the area of the stable region becomes smaller and eventually the two unstable regions merge, as shown in Fig. 2.24(b).

To illustrate the dynamics under different mean flow velocities, two initial conditions are selected: $(\theta, \epsilon) = (0.5, 0.1)$ and $(\theta, \epsilon) = (0.5, 0.5)$. These points are marked as P_{A1} and P_{B1} for $M_1 = 0$ and correspondingly P_{A2} and P_{B2} for $M_1 = 0.08$. Their time histories are shown in Fig. 2.25. It is clear that both points P_{A1} and P_{B1} were in the stable region, and the system asymptotically decays to a linearly stable state. Now, given a small mean flow, for the initial condition at point P_{A2}, the system amplitude grows until reaching a limit cycle state; while for point P_{B2}, the amplitude decays to the oscillating limit cycle state.

Figure 2.26 shows the variation of the heat-driven frequency of the first mode as a function

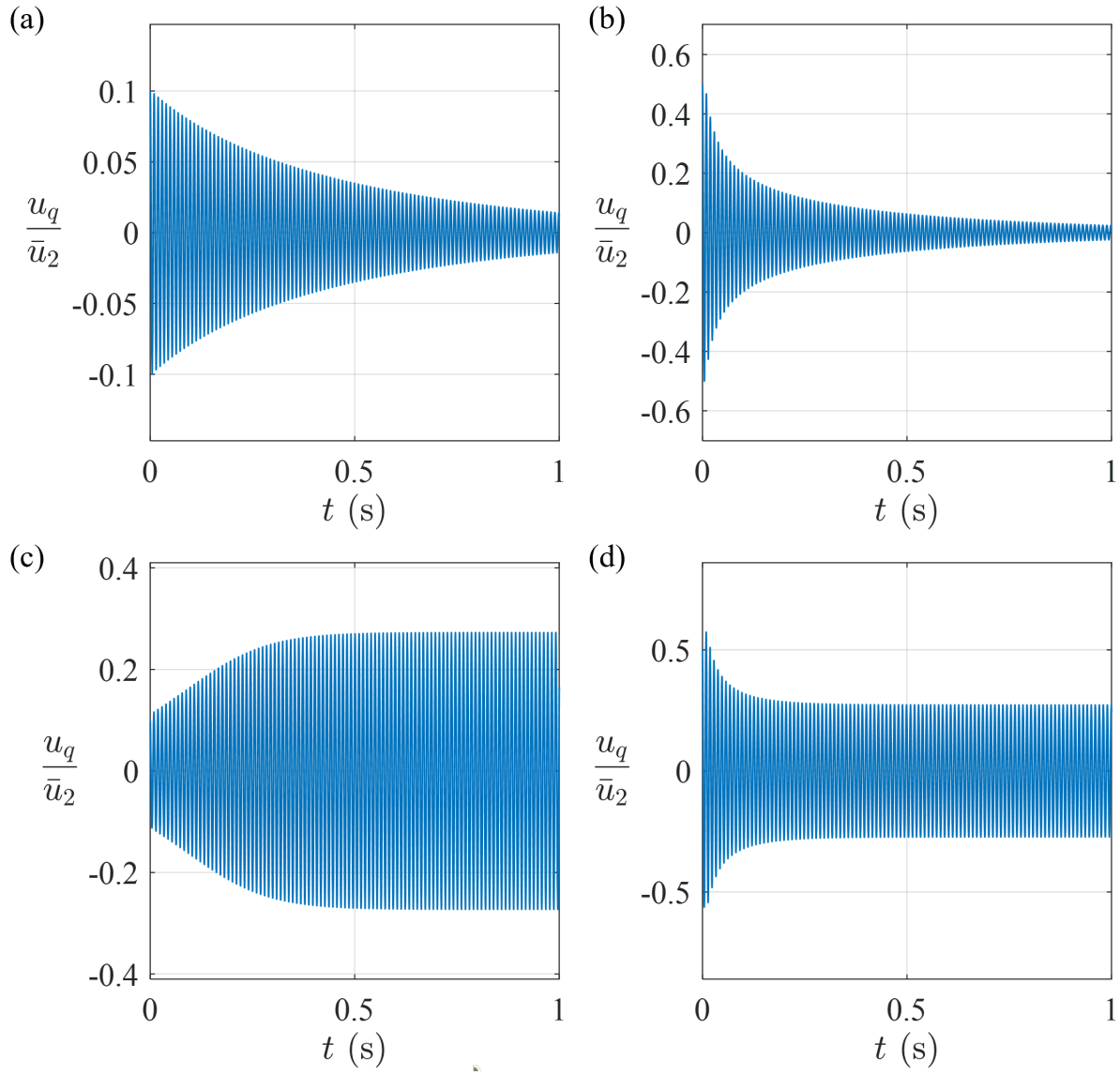

Figure 2.25: Time histories of normalized acoustic velocity under different initial conditions (the relative temperature difference θ, and the excitation amplitude ϵ), marked in Fig. 2.24. The heat source is fixed at $x_q = 0.1$ m; $\theta = 0.5$. (a) P_{A1}: $\epsilon = 0.1$, $M_1 = 0$; (b) P_{B1}: $\epsilon = 0.5$, $M_1 = 0$; (c) P_{A2}: $\epsilon = 0.1$, $M_1 = 0.08$; (d) P_{B2}: $\epsilon = 0.5$, $M_1 = 0.08$.

of the heat source position for different hot region temperatures when the mean flow velocity is fixed at $M_1 = 0.04$. Part (a) illustrates the results when $\epsilon = 0.1$, whereas in part (b), the amplitude is larger ($\epsilon = 0.8$). It is observed that for both low-amplitude and high-amplitude excitations, when the heat source is located in the upstream half of the tube, the increase of θ leads to an increase in heat-driven oscillation frequencies. However, for low $\epsilon = 0.1$, the reverse effect is found when x_q is in the downstream half of the tube: increasing θ leads to lower heat-driven oscillation frequencies.

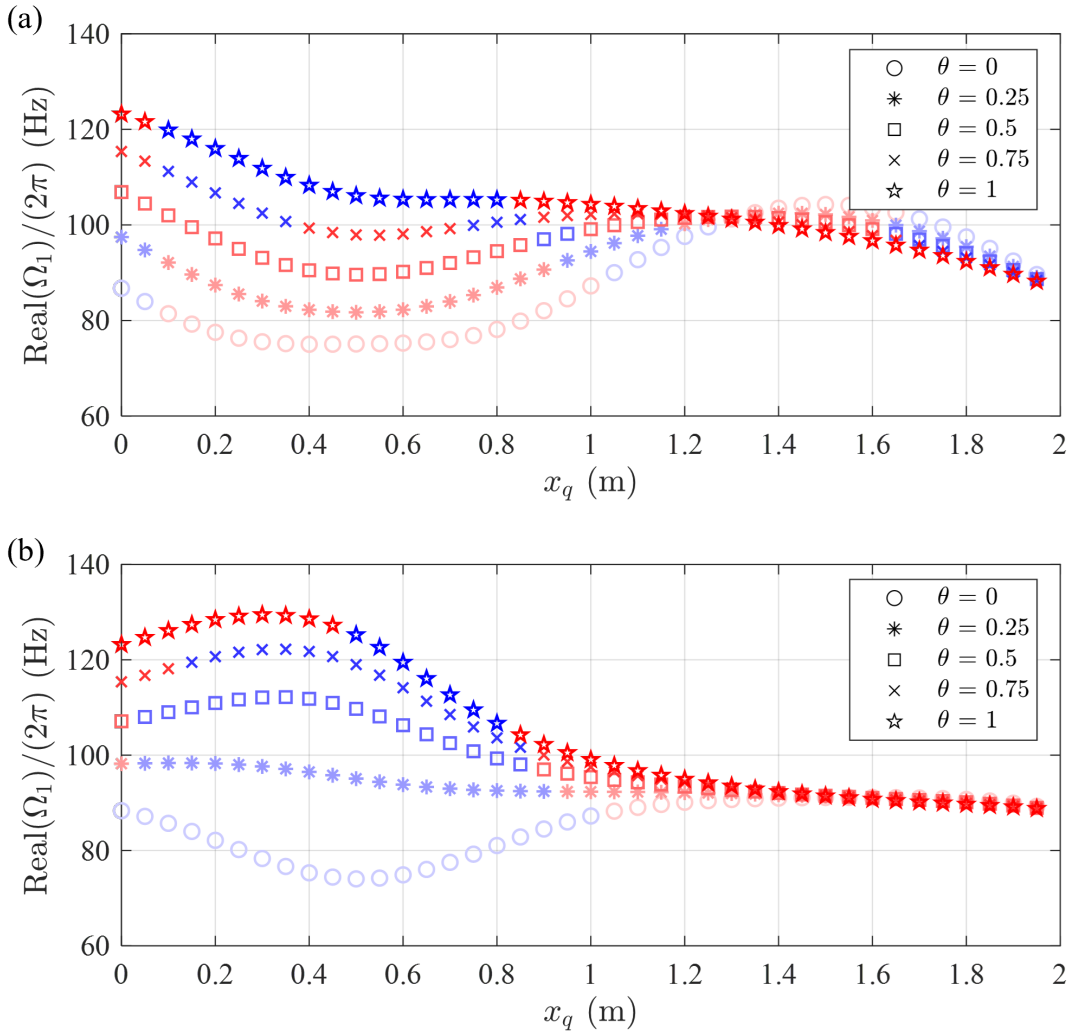

Figure 2.26: Heat-driven frequency variation of fundamental mode ($m = 1$), $\mathrm{Re}(\Omega_1)/(2\pi)$, as a function of the heat source position, x_q, for various relative temperature differences, θ. $M_1 = 0.04$. Blue symbols represent the stable state; red symbols represent the unstable state. (a) Small amplitude, $\epsilon = 0.1$; (b) large amplitude, $\epsilon = 0.8$.

2.5.7. The effect of Mach number

In this section we explore the nonlinear behaviour that emerges in thermoacoustic systems due to changes in the heat source position and in the amplitude of the acoustic excitation velocity.

The stability maps based on the control parameter x_q for different mean flow velocities through the tube are shown in Fig. 2.27. Figure 2.28 shows the results of Fig. 2.27 (a–b) highlighting the bifurcation path and the bistable regions. The relative temperature difference is fixed at $\theta = 0.6$. For the case $M_1 = 0$, shown in Fig. 2.27(a), the system is linearly unstable for 0.23 m $\leq x_q \leq$ 0.88 m and 0.95 m $\leq x_q \leq$ 1.53 m. When the mean flow increases, the top and

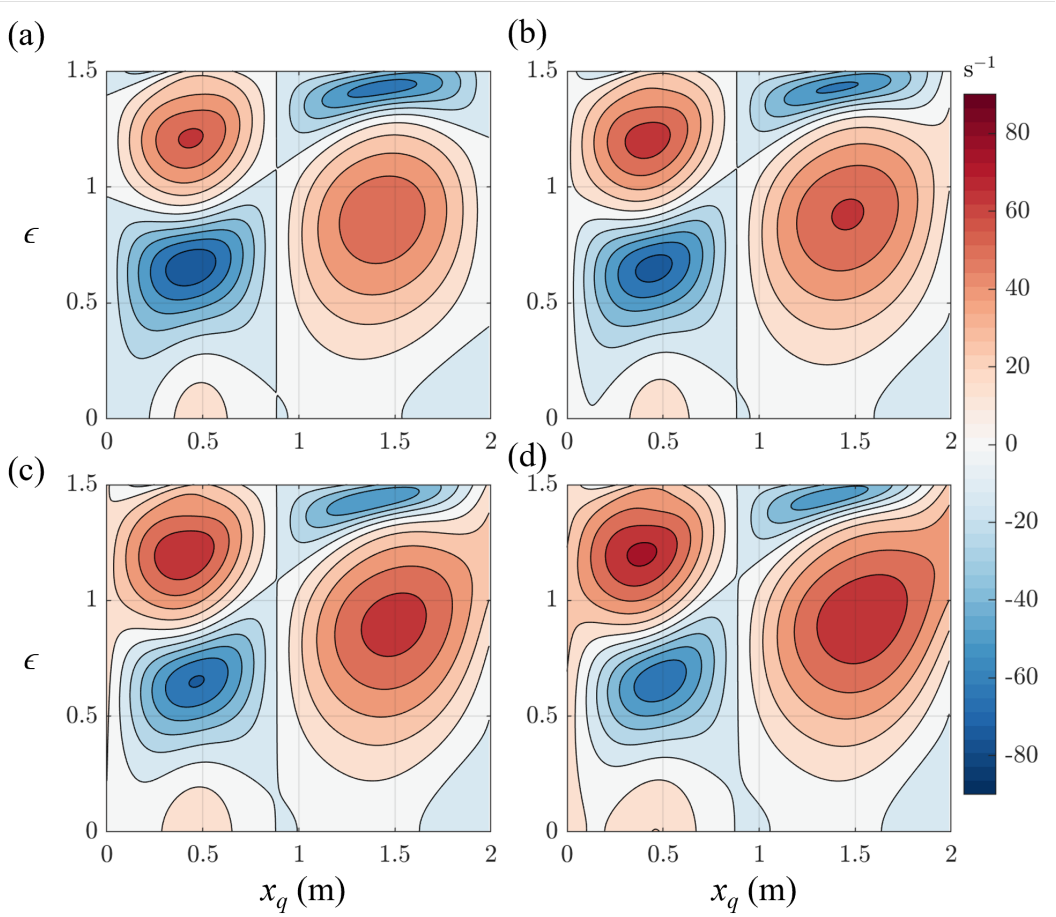

Figure 2.27: Stability maps with the control parameter being x_q, the position of the heat source. $\theta = 0.6$. (a) absent mean flow; (b) $M_1 = 0.04$; (c) $M_1 = 0.08$; (d) $M_1 = 0.12$.

bottom unstable regions when $x_q < 0.89$ m are merged together. The linearly stable region of the no-mean-flow case (0 m $< x_q <$ 0.23 m) disappears when the mean flow is present. In the meantime, the linearly stable region when x_q is around the middle of the tube expands. From the growth rate values, it is observed that, generally, increasing the mean flow velocity increases the growth rate.

As shown in Fig. 2.28(a), when the system is switched on when $x_q = 0$ m with a small excitation amplitude, the system is linearly stable. As the heat source moves toward the downstream end, the system first experiences a supercritical bifurcation at $x_q = 0.22$ m: the oscillations gradually increase in amplitude as x_q is varied, marked by the light-blue solid arrows. When the system is switched on at $x_q = 2$ m with a small excitation amplitude and moving towards the upstream end, the system remains linearly stable until the subcritical bifurcation point at $x_q = 1.53$ m and suddenly jumps to a high-amplitude limit-cycle state and then follows the path marked by the pink dashed arrow.

When a low-Mach-number mean flow is introduced into the system, as shown in Fig. 2.27(b), $M_1 = 0.04$, a new supercritical bifurcation point of $x_q = 0.89$ m and a subcritical bifurcation point $x_q = 0.95$ m appear, as shown in Fig. 2.28(b). Two bistable regions in the range 0.90 m

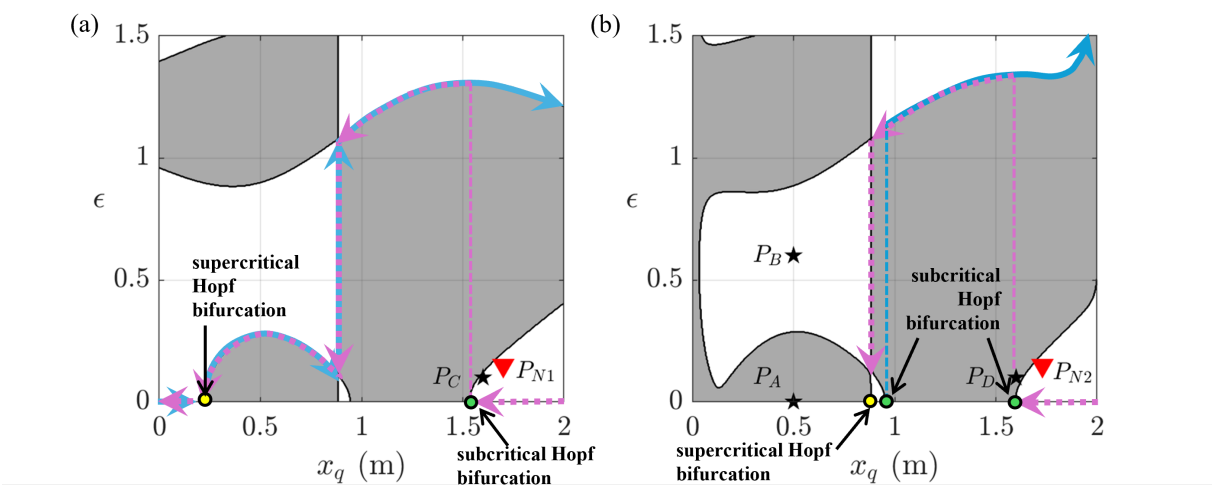

Figure 2.28: Hysteresis, bistable regions and bifurcation paths in Fig. 2.27 (a) and (b), when changing the heat source position, 0 m $< x_q <$ 2 m. (a) Mean flow is absent, $M_1 = 0$; (b) $M_1 = 0.04$.

$< x_q <$0.95 m and 1.59 m $< x_q <$2 m emerge. As the Mach number keeps increasing, as shown in Fig. 2.27(c-d), it is observed that the bistable regions close to the downstream end become narrower while the bistable region of x_q around the middle of the tube becomes wider. The size of the hysteresis zone slightly decreases as the mean flow velocity increases. These observations are in broad agreement with experimental findings by Gopalakrishnan and Sujith (2014), indicating that an increase in the mass flow rate eventually leads to a reduction of the hysteresis zone when $x_q > 0.89$ m and an expansion of the unstable zone when $x_q < 0.89$ m.

Figure 2.29 shows the time histories of the normalized acoustic velocity at the heat source for different initial conditions, marked in Fig. 2.28 as P_A, P_B, P_C, P_D. The first type of behaviour appears when the system is given a small perturbation, and the initial condition is located in an unstable region. The amplitude of u_q grows until saturation and remains in an oscillatory state with a relatively high amplitude. Fig. 2.29 (a) shows an example for point P_A, (x_q, ϵ) = (0.5 m, 10^{-6}). The second type of behaviour occurs when the system is excited at a high amplitude, and the initial state is located in a stable region. The amplitude will decay until it reaches the closest limit cycle state, as shown in Fig. 2.29(b) for point P_B, (x_q, ϵ) = (0.5 m, 0.6) or until the amplitude gradually dies out, as shown in Fig. 2.29(c) for point P_C, (x_q, ϵ) = (1.6 m, 0.1). The third type of behaviour is when the system is excited at a high amplitude, and the initial state is located in an unstable region. The amplitude will keep growing until it reaches the saturation state, the limit cycle. An example is shown in Fig. 2.29(d) for point P_D, (x_q, ϵ) = (1.6 m, 0.1), $M_1 = 0$. The comparison of subfigures (c) and (d) confirms the observation that a mean flow can reduce the bistable region for x_q close to the downstream end.

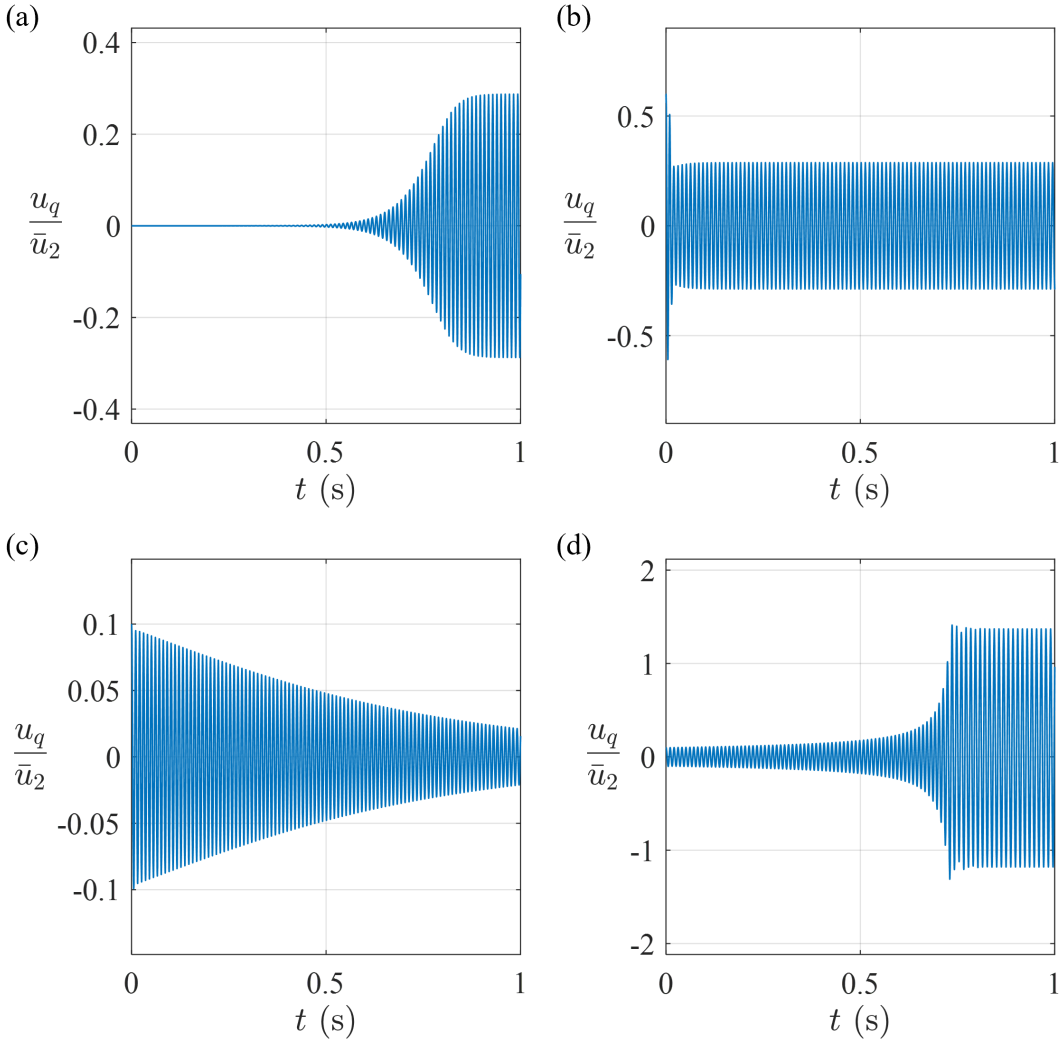

Figure 2.29: Time histories of normalized acoustic velocity under different initial conditions (the heat source position x_q, and the excitation amplitude ϵ), marked in Fig. 2.28. (a) P_A: $x_q = 0.5$ m, $\epsilon = 10^{-6}$, $M_1 = 0.04$, an unstable state with small excitation; (b) P_B: $x_q = 0.5$ m, $\epsilon = 0.6$, $M_1 = 0.04$, amplitude decaying to an oscillatory stable state; (c) P_C: $x_q = 1.6$ m, $\epsilon = 0.1$, $M_1 = 0$, gradually decaying to a stable stationary state; (d) P_D: $x_q = 1.6$ m, $\epsilon = 0.1$, $M_1 = 0.04$, relatively large excitation amplitude growing to a limit cycle state.

2.6. NOISE-INDUCED DYNAMICS

In previous sections, we have examined the nonlinear dynamics in deterministic systems. In this section, we use the AGF framework to investigate the effect of additive noise on the stability of a Rijke tube with nonuniform temperature. Although white noise is frequently used as a forcing condition in the literature, it has been demonstrated that the existing noise in the combustion chamber has a low-pass characteristic typical of colored noise, specifically pink noise (Rajaram and Lieuwen, 2009). Therefore, we will examine two types of noise, white and pink noise.

2.6.1. The integral governing equation

The system, including an additive noise source, is defined by the PDE,

$$\frac{\partial^2\phi}{\partial t^2} + 2\bar{u}_i\frac{\partial^2\phi}{\partial t\partial x} + (\bar{u}_i^2 - c_i^2)\frac{\partial^2\phi}{\partial x^2} = -(\gamma-1)q + \xi N, \tag{2.82}$$

where $\bar{u}_i$ is the mean flow velocity, and c_i is the speed of sound, with $i = 1, 2$ indicating the cold and hot region, respectively. Besides the volumetric unsteady heat release rate generated by the source, $q(x,t)$, the function $N(x,t)$ is added in Eq. (2.82) representing a random signal that models the additive noise source in the system at the heat source position. The definition of N is determined by the type of noise being considered. ξ is a constant number that represents the noise level.

The integral equation for the velocity fluctuation at the heat source position is

$$\begin{aligned} u_q(t) = &-(\gamma-1)\int_{t'=0}^{t}\left.\frac{\partial G(x_q,x,t',t)}{\partial x}\right|_{x=x_q} q(t')\mathrm{d}t' + \xi\int_{t'=0}^{t}\left.\frac{\partial G(x_q,x,t',t)}{\partial x}\right|_{x=x_q} N(t')\mathrm{d}t' \\ &+ \left[\varphi_0'\frac{\partial G(x',x,t',t)}{\partial x} - \varphi_0\frac{\partial}{\partial x}\left(\frac{\partial G}{\partial t'} + \bar{u}_1\frac{\partial G}{\partial x'}\right)\right]_{\substack{x'=x_q\\ x=x_q\\ t'=0}}, \end{aligned} \tag{2.83}$$

The first term on the right-hand side describes the contribution of the heat source to the acoustic field. The second term quantifies the noise effect, and the last term is related to the initial condition.

2.6.2. The external stochastic noise

Given that combustion chambers are noisy environments, we now consider two types of noise. Although white noise is frequently used as a noise term in the literature, it has been demonstrated that the existing noise in the combustion chamber has a low-pass characteristic typical of colored noise, specifically pink noise (Rajaram and Lieuwen, 2009). Therefore, we will examine both white and pink noise in this study. Both types of noise have Gaussian distributions

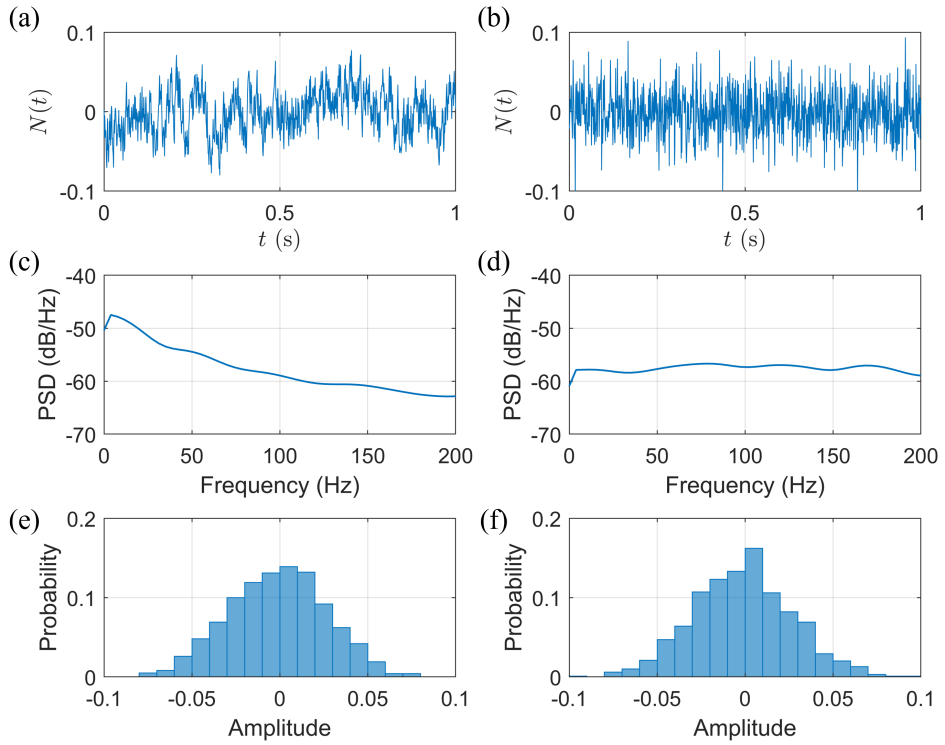

Figure 2.30: Characterization of noise signals. Left column: pink noise; right column: white noise. (a-b) Noise signals; (c-d) averaged power spectral density; (e-f) relative probability of amplitude values.

and are generated within the amplitude range [-0.1, 0.1]. The noise level is determined by the parameter β, a coefficient of the distribution function.

It is important to note that the noise intensity parameter β defined in Arabi and Heckl (2025) is not directly equivalent to the parameter ξ used in the present study. In their work, the governing PDE incorporates a factor of $1/(c_2^2 - \bar{u}_2^2)$, compared to the PDE used in the present work, which propagates through the solutions of the Green's functions. As a result, the sensitivity to stochastic forcing in the current study is lower than that observed in their framework. The relationship between the two noise intensity parameters is given by $\beta = \xi/(c_2^2 - \bar{u}_2^2)$.

Figure 2.30 illustrates the characteristics of white and pink noise signals, $N(t)$. Both types of noise are generated using built-in functions in MATLAB (2024) and have Gaussian distributions within the amplitude range [-0.1, 0.1]. Both noise signals have a time-averaged value of zero. The left column illustrates the features of pink noise, including a sample of noise signals in the time domain, the averaged power spectral density (PSD) that presents the energy distribution across frequencies, and the relative probability of different amplitude values within the noise signal. White noise (right column in Fig. 2.30) is distinguished by its uniform energy distribution across all frequencies, as reflected in its relatively flat PSD. In contrast, pink noise exhibits a spectrum where the power spectral density is inversely proportional to the frequency. This characteristic means that as the frequency increases, the power decreases. In the frequency range of the fundamental mode studied in this work (60–140 Hz), the acoustic energies carried by these two noise types are of comparable values.

2.6.3. Noise effect on the transition time

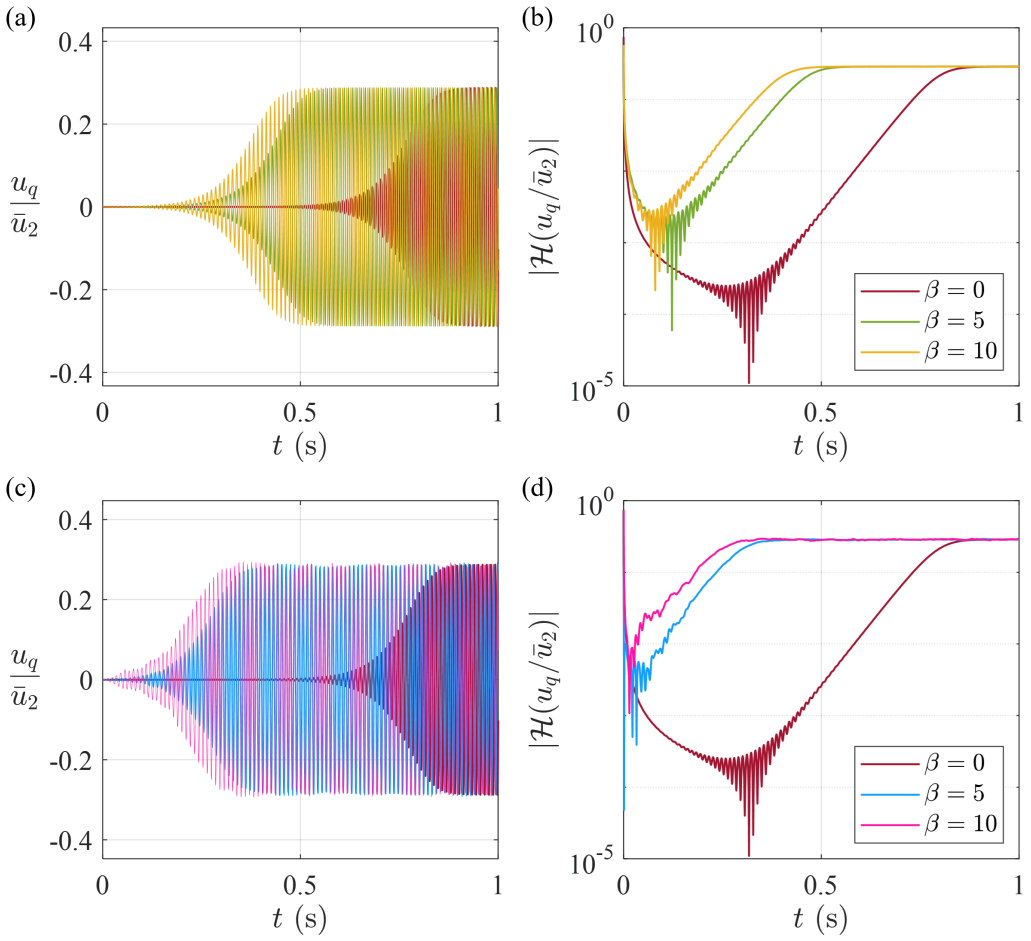

Figure 2.31: Effect of noise on reducing saturation time. Top row, white noise; bottom row: pink noise. Subfigures (a) and (c) are the time histories of normalized acoustic velocity; (b) and (d) are the time histories of envelope amplitude in logarithmic scale. Initial condition is chosen as point P_A marked in Fig. 2.28 (b): $x_q = 0.5$, $\epsilon = 10^{-6}$. $M_1 = 0.04$, $\theta = 0.6$.

The *transition time* or *saturation time* refers to the duration it takes for the acoustic velocity signal to evolve from its initial state to the limit cycle amplitude, marking the saturation of the oscillation. Fig. 2.31 illustrates the impact of noise on the transition time. The initial condition is selected in the unstable region, $(x_q, \epsilon) = (0.5\,\text{m}, 10^{-6})$, and we compare the time histories for cases without noise, $\beta = 0$, and with two different levels of white noise and pink noise $\beta = 5, 10$. When the noise is absent, the transition time to reach the saturation state for the initial condition P_A is $T_{\text{satur}} = 0.91$ s. From Fig. 2.31(a) and (c), it is evident that both white noise and pink noise significantly reduce the transition time for the acoustic velocity to reach the limit cycle compared with the noise-free case. Fig. 2.31(b) and (d) present the envelope amplitude of the corresponding signals on a logarithmic scale, derived from the absolute value of their Hilbert transforms, $|\mathcal{H}(u_q/\bar{u}_2)|$. The time evolution of the envelope amplitudes shows

that the signals reach their saturation states with identical slopes, indicating that the reduction in transition time due to noise is not related to changes in the growth rate. This is in line with the analytical calculation results of Arabi and Heckl (2025).

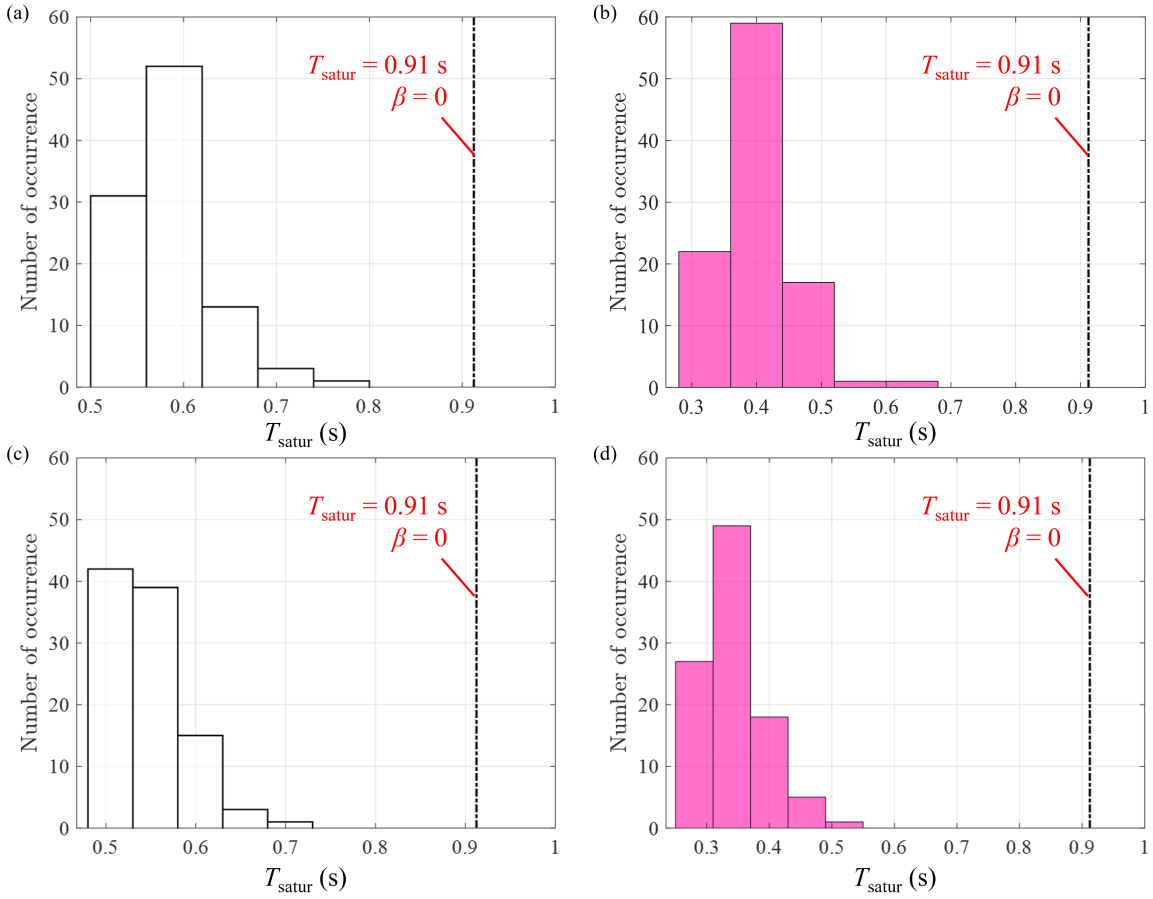

Figure 2.32: Histogram of saturation time T_{satur} obtained in 100 calculations with initial condition at point P_A, in the presence of: (a) white noise, $\beta = 5$; (b) pink noise, $\beta = 5$; (c) white noise, $\beta = 10$; (d) pink noise, $\beta = 10$, respectively.

The change in transition time is due to the change in the initial state caused by the presence of noise. Since the stochastic noise signal has negative values, in theory, it is also possible that the noise could reduce the initial state amplitude, thereby postponing the system from reaching the limit cycle state. However, the probability of this happening is very low. Fig. 2.32 shows the number of occurrences of different saturation times when the system is excited with the initial condition at P_A for 100 repetitions. In our observations, postponement of saturation is never observed. The comparison between Fig. 2.32 (a) and (b) also reveals that pink noise is more effective than white noise in reducing the transition time to reach the limit cycle under the same noise intensity level, despite the fact that the noise signals contain a similar amount of acoustic energy. It is also observed that increasing the noise level, β, is more likely to increase the extent of acceleration.

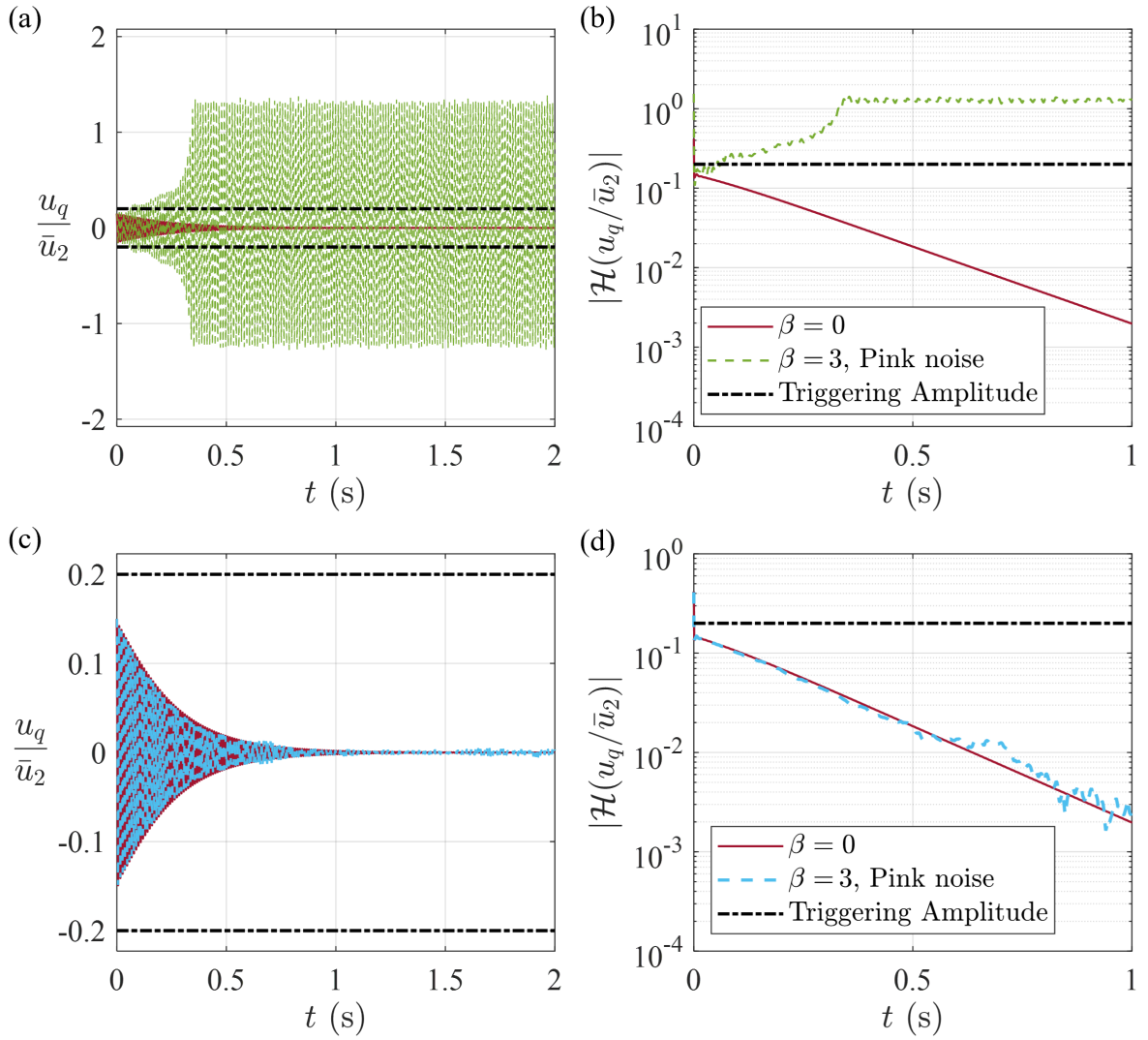

Figure 2.33: Time histories of normalized acoustic velocity and the corresponding envelope amplitude evolution of the system with given initial conditions: (a-b) point P_{N1}, $x_q = 1.7$ m, $\epsilon = 0.15$, absent of mean flow ($M_1 = 0$), marked in Fig.2.28(a); (c-d) point P_{N2}, $x_q = 1.73$ m, $\epsilon = 0.15$, $M_1 = 0.04$, marked in Fig.2.28(b). In both cases, the system is forced by pink noise with $\beta = 3$.

2.6.4. Mean-flow effect on noise-induced triggering

A stable thermoacoustic system can transition into self-sustained oscillations when exposed to a disturbance that exceeds a critical amplitude threshold. This process is known as triggering, and the critical amplitude threshold is referred to as the *triggering amplitude*. If the initial disturbance amplitude is below this threshold, the system asymptotically returns to a stable state. Triggering typically takes place when the system operates within the bistable region on the stability map. Arabi and Heckl (2025) have demonstrated that pink noise can induce instability in a horizontal Rijke tube when the mean flow is absent. In this section, we investigate the effect of mean flow on noise-induced triggering in a thermoacoustic system. For each specified noise

level, β, the system is initiated 100 times from the same initial condition, and the time histories of the normalised acoustic velocity signals are computed. If triggering is not observed in any of the trials, it is considered unlikely to occur under the given conditions.

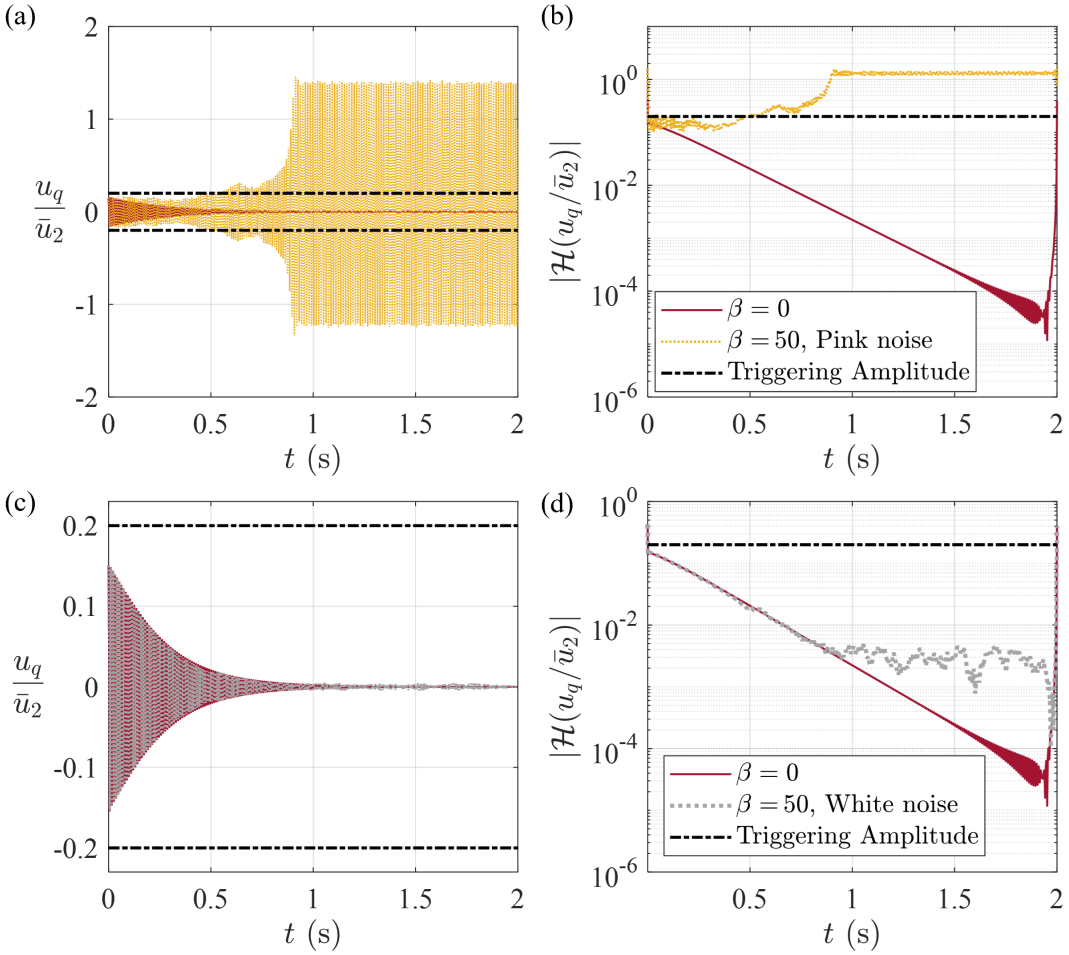

Figure 2.34: Time histories of normalized acoustic velocity and the corresponding envelope amplitude evolution of the system with given initial condition at point P_{N2}, $x_q = 1.73$ m, $\epsilon = 0.15$, $M_1 = 0.04$, $\theta = 0.6$, marked in Fig.2.28(b). The system is forced by different types of noise signals of the same intensity $\beta = 50$. (a-b) Pink noise; (c-d) White noise.

We choose two initial conditions, P_{N1} ($x_q = 1.70$ m, $\epsilon = 0.15$, $M_1 = 0$) and P_{N2} ($x_q = 1.73$ m, $\epsilon = 0.15$, $M_1 = 0.04$), marked as red downward triangles in Fig.2.28. Both points are in the bistable region and close to the stability margin, and they have the same excitation amplitude and the same triggering amplitude, $\epsilon_{\text{trig}} = 0.2$, marked as the black dash-dot line in Fig. 2.33 and the following figures. For the case of P_{N1} where the mean flow is absent, triggering is observed when the system is subjected to pink noise with intensity $\beta = 3$. The acoustic velocity affected by noise initially grows to reach the triggering amplitude and causes the oscillation to be triggered in the unstable region and grow to the limit cycle state, as illustrated in Fig. 2.33(a-b). When $M_1 = 0.04$, the effect of pink noise at the same level on the system is greatly weakened. The initial growth caused by noise becomes negligible.

For the case where a mean flow of $M_1 = 0.04$ is present and the initial condition is set at point P_{N2}, the noise level β is gradually increased from 0 in increments of 5, as shown in Figs. 2.34(a-b). Despite the noise signal having an intensity level ten times greater than that in Figs. 2.33(c-d), the initial transient amplitude approaches the triggering amplitude at a slower rate. This suggests that it is significantly more difficult for noise to induce instabilities in a system with a mean flow compared to one without.

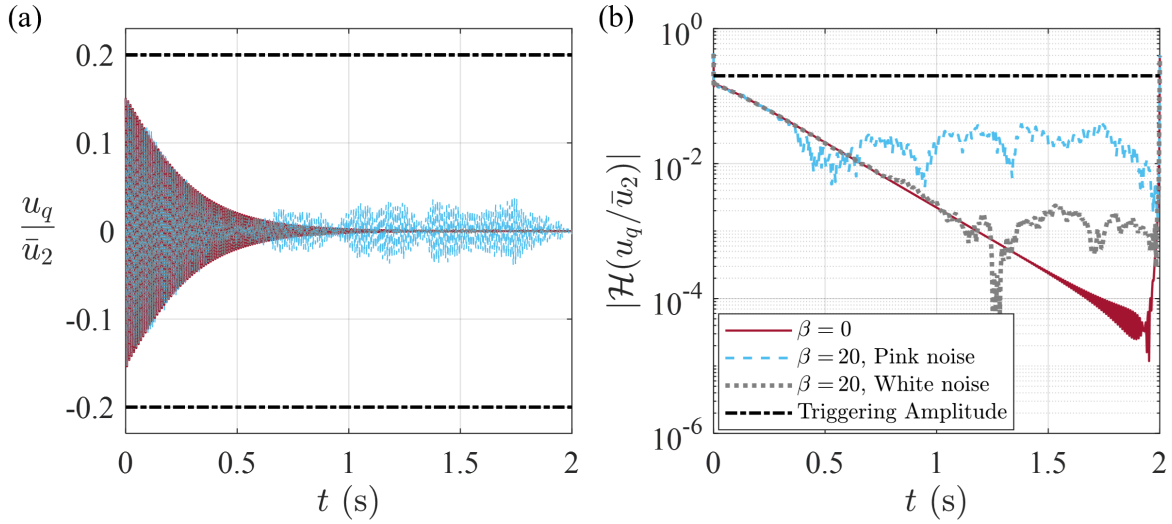

Figure 2.35: Time histories of normalized acoustic velocity, with initial condition of point P_{N2}, $x_q = 1.73$ m, $\epsilon = 0.15$, $M_1 = 0.04$, $\theta = 0.6$, marked in Fig.2.28(b). The system is forced by different types of noise signals of $\beta = 20$. (a) Time histories; (b) Evolution of the envelope amplitudes.

Figure 2.34(c-d) shows the system at initial condition P_{N2} subjected to white noise of $\beta = 50$. The results indicate that the effect of white noise is minimal compared to pink noise. In another example, shown in Fig. 2.35, even when the noise level is insufficient to trigger instabilities, the residual noise in the system subjected to pink noise is noticeably stronger than that in the system influenced by white noise. This difference is attributed to pink noise carrying more energy at lower frequencies. In this study, the focus is on the fundamental mode $(m = 1)$ of the thermoacoustic system, which has modal frequencies ranging from 80 to 120 Hz. This characteristic makes the fundamental mode more responsive to pink noise than to white noise. Furthermore, the heat release model employed in the analysis reflects the flame's behaviour as a low-pass filter (Noiray, 2007; Ducruix et al., 2000; Heckl, 2015), which enhances the impact of pink noise on the system dynamics.

2.7. CONCLUSIONS

This work has introduced an analytical framework utilizing the AGF to investigate self-excited oscillations within a generalized thermoacoustic system. The system incorporates mean flow and accounts for feedback interactions between the acoustic field and a heat source. The governing equation of the system has the form of the acoustic analogy equation, with a convective

term and a heat source described by a generalized time-lag heat release law. A key aspect of the theory is the transformation of the governing partial differential equation of a non-self-adjoint system into an integral equation utilizing the Lagrange-Green's identity. The resulting integral equation provides extensive flexibility to find solutions to the system; without modifications in the AGF and without further derivations, we can easily assess the effect of changes in the initial conditions or various external forcings. Another benefit is that the integral equation yields both time-domain and frequency-domain results for multiple modes. The integral equation is also used to derive an algebraic equation for the thermoacoustic eigenfrequencies. The theory is validated against a widely used wave-based network modelling approach. The extended AGF framework was applied to analyse a horizontal Rijke tube system with non-uniform mean flow, paying special attention to the acoustic conditions at the contact discontinuity and at the open ends of the duct.

The reciprocity relation between direct and adjoint Green's functions is demonstrated. The direct Green's function describes the acoustic field generated by an impulsive point source, while the AGF marches backward in time, revealing the system's receptivity to forcing terms, as well as initial conditions. Exploiting this relationship, we derive an analytical solution for the AGF and demonstrate the application of the AGF framework in different thermoacoustic configurations. The results provide key insights into:

- *Stability and nonlinear dynamics*: The AGF model successfully identifies Hopf bifurcations, hysteresis phenomena, and bistable regions, with robustness in systems of different boundary conditions. A laboratory matrix burner with a closed-end has been modelled, and stability predictions and frequency variation of the first three modes obtained with the AGF approach have shown good agreement with experimental measurements. For a Rijke tube, taking different control parameters, such as heat source position, heater power, and tube length, reveals rich nonlinear dynamics qualitatively agreed with those observed in experiments.

- *Mean flow convection effects:* Mean flow convection plays a crucial role in thermoacoustic systems with non-uniform temperature fields. As the mean flow velocity increases, the growth rate of the system under the same initial condition increases. When the relative mean temperature difference and the heat source location serve as the control parameters, the instability region changes, and the bistable region shifts even when a mean flow of a small velocity is introduced. For a stochastic system, the existence of the mean flow hinders the noise-induced triggering.

- *Impact of temperature jump:* The relative difference in downstream and upstream mean temperatures across the compact flame strongly affects heat-driven oscillation frequencies and the stability behaviour. When the heat source is located in the upstream half of the tube, the influence is more pronounced. An increased temperature difference leads to higher oscillation frequencies. When the heat source is located in the mid-to downstream half of the tube, the opposite effect is observed for oscillation frequencies.

- *Influence of additive noise:* Both white noise and pink noise can change the transient phase by reducing or increasing the time required for acoustic disturbances to reach the limit-cycle amplitude. In general, a reduction is very likely to take place. This occurs

through the alteration of disturbance amplitude rather than through a modification of the transient growth rate. Additionally, noise-induced triggering is observed, with pink noise being more effective than white noise of the same intensity. The presence of even small mean flow velocities in the system significantly reduces noise-induced effects compared to systems without mean flow.

In summary, this study provides a comprehensive AGF framework and presents new insights into the complex interplay of temperature fields, mean flow, and additive noise in a one-dimensional thermoacoustic system prototype. By addressing these critical aspects, the findings reported here contribute to a better understanding of thermoacoustic stability mechanisms, which are crucial for improving instability predictions and developing control strategies.

通于一而万事毕。

——《庄子·天地》

"Grasp the Way, and everything falls into place."

ADJOINT-BASED SENSITIVITY ANALYSIS

The aim of this chapter is to show, for a prototypical thermoacoustic system, the application of all three types of adjoint sensitivity analysis listed in section 1.2.2., for the assessment of uncertainties and the identification of steady and perturbation feedback passive control strategies.

The structure of the present contribution is as follows: in section 3.1., details of the lumped model of the combustor reported in the literature are given. Linear stability analysis yields the eigenspectrum, highlighting some discrepancies with the literature, particularly with respect to the amplification rate of the eigenmodes. In section 3.2., we investigate the reasons for these discrepancies, relating them to base-flow uncertainties by applying the adjoint base-state sensitivity analysis. In sections 3.3. and 3.4., we aim to find optimal control strategies to mitigate thermoacoustic instabilities with a focus on the two most unstable eigenmodes. In section 3.3., the sensitivity to structural modifications in the base flow is evaluated against variations in the flame position within the combustor. In section 3.4., we apply the structural sensitivity analysis to evaluate the eigenvalue drift due to feedback forcings in the disturbance field. Section 3.5. summarizes the main conclusions of this work.

3.1. THE 1-D PREMIXED COMBUSTOR MODEL

3.1.1. General description

The prototypical thermoacoustic system examined in this work is the quasi-one-dimensional combustor reported in Dowling and Stow (2003), displayed in Fig. 3.1. The simplified combustor geometry is based on the assumption of sufficiently low oscillation frequencies in the combustor so that radial modes are cut off, and only plane waves transport acoustic energy.

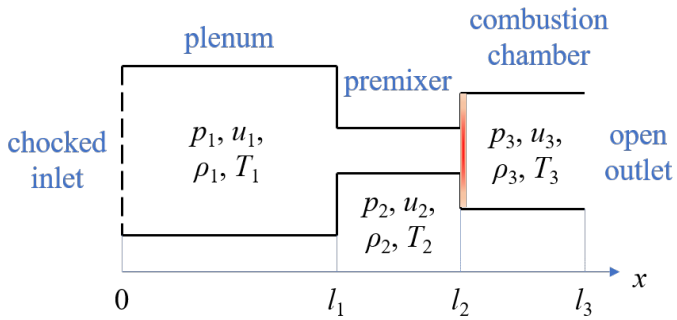

Figure 3.1: Sketch (not-to-scale) of the one-dimensional three-duct combustor geometry, with notations and boundary conditions. The positions of the ducts' intersections are $x = l_1$ and $x = l_2$ (where the compact flame is also located); the outlet of the system is at $x = l_3$.

Table 3.1: Geometrical parameters of the three-duct combustor.

Section	Length		Cross-sectional Area	
Plenum	L_1	1.7 m	a_1	0.0129 m^2
Premixer	L_2	0.0345 m	a_2	0.00142 m^2
Combustion Chamber	L_3	1.0 m	a_3	0.00385 m^2

The system consists of a plenum, a premix duct, and a combustion chamber, modelled as three straight ducts connected by discontinuities where jump conditions must be enforced. The area changes, and the unsteady heat source (modelling the flame) are short enough to be considered acoustically compact. The compact flame is located at the outlet of the premixer. The combustor has a choked inlet to model the flow supplied by a centrifugal blower and an open outlet as the burned gases are discharged into an open space or another large plenum. The dimensions of the system are given in Table 3.1.

3.1.2. The low-order modelling approach

The simple combustion system in Fig. 3.1 is treated with the lumped approach described by Dowling and Stow (2003). The flow is described by a set of equations, including governing equations, boundary conditions, and jump conditions, with the ideal gas assumption. The equations are linearized around the base flow; thus, in each duct, the flow variables are decomposed into a mean steady value plus a perturbation, viz. $p(x,t) = \bar{p} + p'(x,t)$, $u(x,t) = \bar{u} + u'(x,t)$, $\rho(x,t) = \bar{\rho} + \rho'(x,t)$, $T(x,t) = \bar{T} + T'(x,t)$, $Q(x,t) = \bar{Q} + Q'(x,t)$, where Q is the heat release rate generated by the flame. The base flow parameters, denoted as $\bar{\mathbf{q}} = (\bar{\rho}_j, \bar{u}_j, \bar{p}_j, \bar{T}_j, \bar{Q})$, are considered uniform and steady in each duct. The independent perturbation variables are denoted as $\mathbf{q}' = (\rho'_j, u'_j, p'_j)$ with $j = 1, 2, 3$ representing each duct.

In the combustion chamber section, the mean temperature is the same as the flame temperature T_f, and the mean pressure is the ambient pressure. At the area-increasing intersection, $x = l_2$, the Borda-Carnot equation is used; at the sudden contraction in $x = l_1$, the flow is assumed to behave isentropically. The set of equations used to find the base state, $\mathbf{B}(\bar{\mathbf{q}}) = 0$, is given in Appendix B.1.

In each section of the system (denoted by $j = 1, 2, 3$), the perturbations are governed by differential equations representing the conservation of mass, momentum, and energy:

$$\frac{\partial \rho'_j}{\partial t} + \bar{u}_j \frac{\partial \rho'_j}{\partial x} + \bar{\rho}_j \frac{\partial u'_j}{\partial x} = 0, \tag{3.1a}$$

$$\bar{\rho}_j \frac{\partial u'_j}{\partial t} + \bar{\rho}_j \bar{u}_j \frac{\partial u'_j}{\partial x} + \frac{\partial p'_j}{\partial x} = 0, \tag{3.1b}$$

$$\frac{\partial p'_j}{\partial t} + \bar{u}_j \frac{\partial p'_j}{\partial x} + \gamma \bar{p}_j \frac{\partial u'_j}{\partial x} = 0. \tag{3.1c}$$

In the system above no summation is intended over the j index. A wave decomposition is introduced for the perturbation variables; pressure, density, and velocity fluctuations in the frequency domain ($\mathbf{q}'(x,t) = \hat{\mathbf{q}}(x)\mathrm{e}^{\mathrm{i}\omega t}$) are decoupled as forward and backward travelling acoustic waves

plus an entropy wave convected by the mean flow:

$$\hat{p}_j = A_{+j}\mathrm{e}^{\mathrm{i}k_{+j}x} + A_{-j}\mathrm{e}^{\mathrm{i}k_{-j}x}, \tag{3.2a}$$

$$\hat{\rho}_j = \frac{1}{\bar{c}_j^2}A_{+j}\mathrm{e}^{\mathrm{i}k_{+j}x} + \frac{1}{\bar{c}_j^2}A_{-j}\mathrm{e}^{\mathrm{i}k_{-j}x} - \frac{1}{\bar{c}_j^2}A_{ej}\mathrm{e}^{\mathrm{i}k_{0j}x}, \tag{3.2b}$$

$$\hat{u}_j = -\frac{k_{+j}}{\bar{\rho}_j\alpha_{+j}}A_{+j}\mathrm{e}^{\mathrm{i}k_{+j}x} - \frac{k_{-j}}{\bar{\rho}_j\alpha_{-j}}A_{-j}\mathrm{e}^{\mathrm{i}k_{-j}x}, \tag{3.2c}$$

where $k_{\pm j} = -\dfrac{\omega}{\bar{u}_j \pm \bar{c}_j}$, $k_{0j} = -\dfrac{\omega}{\bar{u}_j}$, and $\alpha_{\pm j} = \omega + \bar{u}_j k_{\pm j}$.

At the area-decreasing intersection, the flow can be assumed as isentropic. With mass and energy conservation equations, the jump conditions at $x = l_1$ read,

$$a_1\left(\bar{\rho}_1\hat{u}_1 + \hat{\rho}_1\bar{u}_1\right) = a_2\left(\bar{\rho}_2\hat{u}_2 + \hat{\rho}_2\bar{u}_2\right), \tag{3.3a}$$

$$\gamma\frac{\hat{\rho}_1}{\bar{\rho}_1} - \frac{\hat{p}_1}{\bar{p}_1} = \gamma\frac{\hat{\rho}_2}{\bar{\rho}_2} - \frac{\hat{p}_2}{\bar{p}_2}, \tag{3.3b}$$

$$\hat{H}_1 = C_p\hat{T}_1 + \bar{u}_1\hat{u}_1 = \hat{H}_2 = C_p\hat{T}_2 + \bar{u}_2\hat{u}_2, \tag{3.3c}$$

where $H = C_pT + \frac{1}{2}u^2$ is the stagnation enthalpy per unit mass and C_p the specific heat at constant pressure, assumed constant. The specific heat ratio is denoted by $\gamma = C_p/C_v$.

At $x = l_2$, where the area increases, the mass, energy, and momentum conservation apply:

$$a_2\left(\bar{\rho}_2\hat{u}_2 + \hat{\rho}_2\bar{u}_2\right) = a_3\left(\bar{\rho}_3\hat{u}_3 + \hat{\rho}_3\bar{u}_3\right), \tag{3.4a}$$

$$a_2\hat{\rho}_2\bar{u}_2^2 + 2a_2\bar{\rho}_2\bar{u}_2\hat{u}_2 = a_3\left(\hat{p}_3 - \hat{p}_2\right) + a_3\hat{\rho}_3\bar{u}_3^2 + 2a_3\bar{\rho}_3\bar{u}_3\hat{u}_3, \tag{3.4b}$$

$$a_2\left(\bar{\rho}_2\bar{u}_2\hat{H}_2 + \bar{\rho}_2\hat{u}_2\bar{H}_2 + \hat{\rho}_2\bar{u}_2\bar{H}_2\right) = a_3\left(\bar{\rho}_3\bar{u}_3\hat{H}_3 + \bar{\rho}_3\bar{H}_3\hat{u}_3 + \bar{u}_3\bar{H}_3\hat{\rho}_3 - \hat{Q}\right). \tag{3.4c}$$

Note that the heat released by the compact flame is introduced in the jump condition. This might differ from what Dowling and Stow (2003) did, since it is not clear from their paper whether the area change, from a_2 to a_3, and the energy source term Q were treated in one step (at the $x = l_2$ interface) or in two successive steps. In any event, we have modelled the problem in two ways: one is the fully coupled approach embodied by equations (3.4) above, and the second considers two steps (and two separate sets of equations) with the area change first, and the heat release term immediately downstream. The results of the two models are close to one another, and also close to those by Dowling and Stow (2003), but not identical. We have thus decided to maintain only the fully coupled approach above.

The fluctuating heat release rate generated by an unsteady flame is governed by a time-delayed model correlated with the mass flow rate in the premixer section:

$$\hat{Q} = -\kappa\bar{Q}\frac{\hat{\dot{m}}_2}{\bar{\dot{m}}_2}\mathrm{e}^{-\mathrm{i}\omega\tau}, \tag{3.5}$$

where $\tau = 0.006$ s is the time delay, and the coefficient κ acts as an unsteady flame switcher, with its value ranging from 0 to 1 (Dowling and Stow, 2003).

Choked inlets usually model a compressor exit, where the mass and energy flow rates are nearly constant. An open outlet can be approximated with a zero-pressure oscillation. Hence,

the boundary conditions are:

$$\text{Choked inlet (Stow et al., 2002):} \qquad \frac{\hat{\rho}_1(0)}{\bar{\rho}_1} + \frac{\hat{u}_1(0)}{\bar{u}_1} = 0, \tag{3.6a}$$

$$\hat{p}_1(0) = \bar{c}_1^2 \hat{\rho}_1(0), \tag{3.6b}$$

$$\text{Open outlet:} \qquad \hat{p}_3(l_3) = 0. \tag{3.7}$$

Equations (3.3)-(3.7) form the direct system of perturbation flow in the combustor.

From the equation of state of ideal gases, with R_g the perfect gas constant, the first-order linearization of $\hat{T}$ yields

$$\hat{T} = \frac{\hat{p}/R_g - \bar{T}\hat{\rho}}{\bar{\rho}}, \tag{3.8}$$

so that

$$\hat{H} = \frac{\gamma}{(\gamma-1)\bar{\rho}}\hat{p} - \frac{C_p \bar{T}}{\bar{\rho}}\hat{\rho} + \bar{u}\hat{u}. \tag{3.9}$$

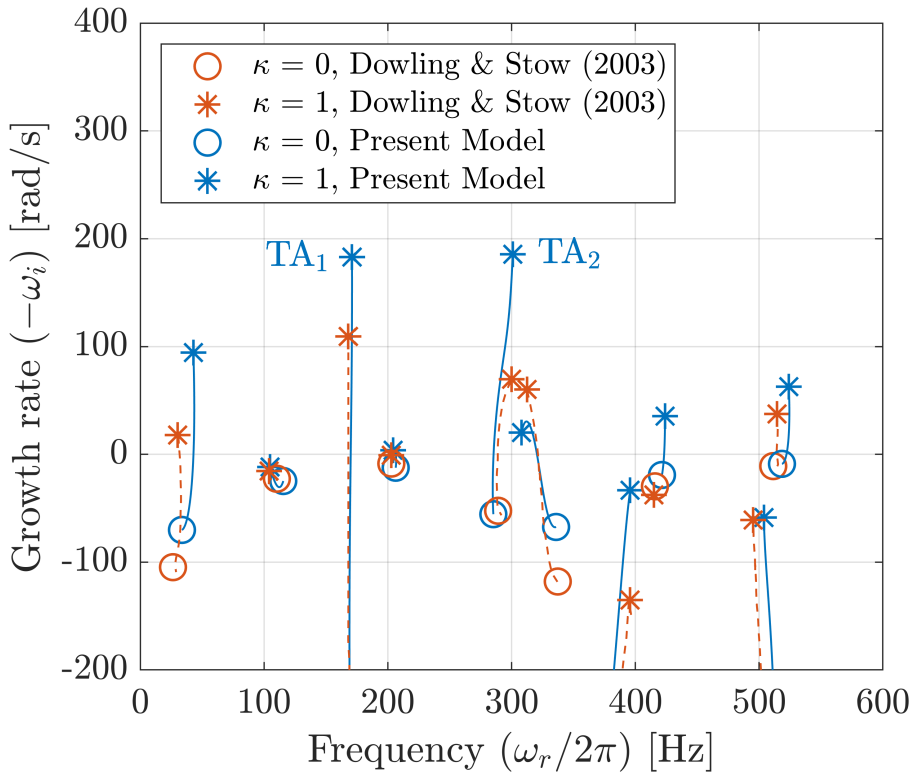

Figure 3.2: Comparison of the eigenvalue trajectories against literature results (Dowling and Stow, 2003), with varying κ, from $\kappa = 0$ (no unsteady heat release at the flame) to $\kappa = 1$. The solid blue lines represent the trajectories of the present model; the dashed red lines represent the trajectories reported in Dowling and Stow (2003). The two most unstable eigenmodes are labelled as TA$_1$ and TA$_2$.

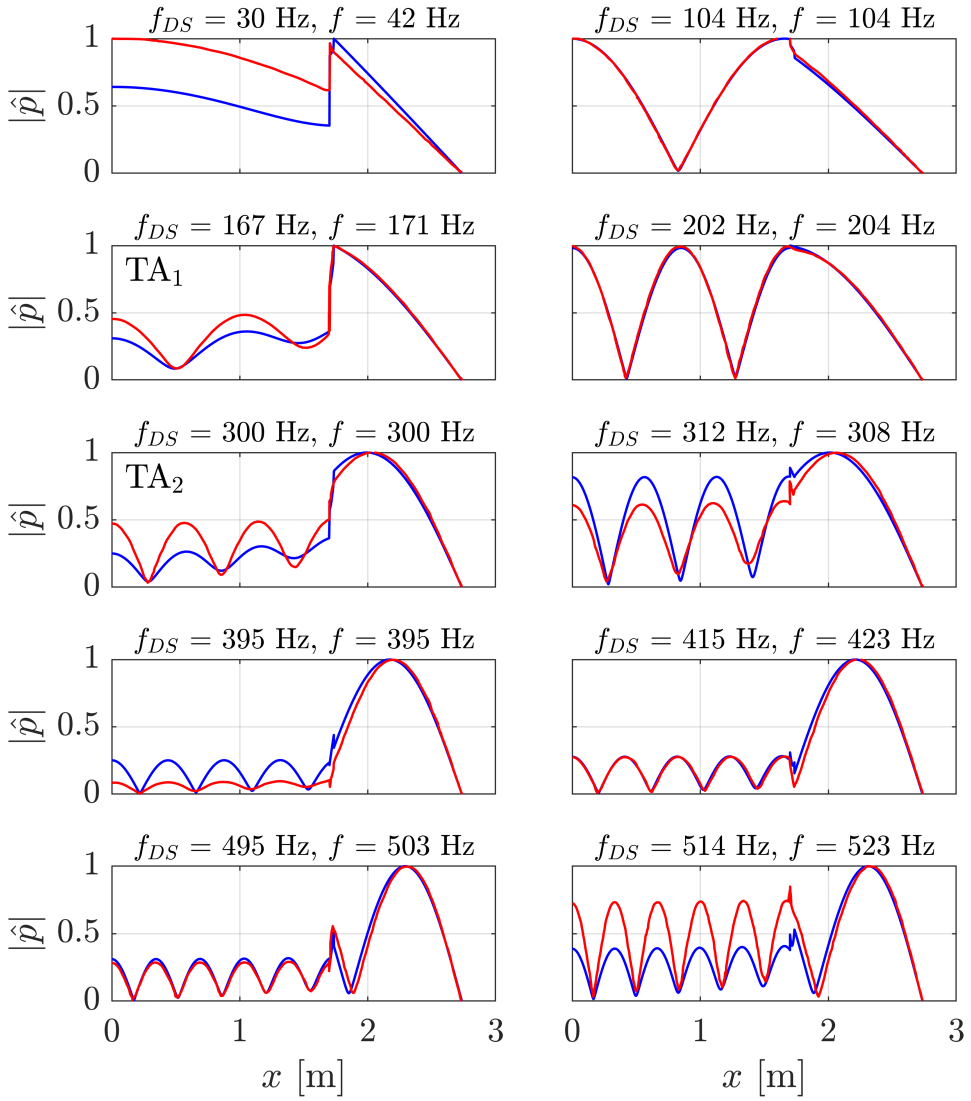

Figure 3.3: Shapes of the pressure fluctuation eigenmodes (normalized with the respective maximum amplitudes), in the case of heat release located at $x = 1.7345$ m. Above each individual frame, the oscillation frequency computed by Dowling and Stow (2003) is indicated as f_{DS}, while the value found here is denoted simply by f. Red curves: mode shapes from the literature; blue curves: mode shapes predicted by the present study. The two most unstable modes are labelled TA_1 and TA_2 within the appropriate frames.

With the base flow solutions and the wave decomposition in equations (3.2), the stability of the perturbation flow system is solved as an eigenvalue problem of the form:

$$\mathcal{A}(\bar{\mathbf{q}}, \omega)\mathbf{x} = 0. \tag{3.10}$$

The elements of the vector $\mathbf{x}$ are the decoupled wave amplitudes A_{+j}, A_{-j}, A_{ej} $(j = 1, 2, 3)$

plus the heat release rate fluctuation $\hat{Q}$; $\mathcal{A}$ is the coefficient matrix, as outlined below:

$$\begin{bmatrix} \text{Heat release model (Eq. 3.5)} \\ \text{Mass conservation equation at } x = l_1 \text{ (Eq. 3.3(a))} \\ \text{Isentropic condition at } x = l_1 \text{ (Eq. 3.3(b))} \\ \text{Energy conservation equation at } x = l_1 \text{ (Eq. 3.3(c))} \\ \text{Mass conservation equation at } x = l_2 \text{ (Eq. 3.4(a))} \\ \text{Linear momentum conservation at } x = l_2 \text{ (Eq. 3.4(b))} \\ \text{Energy conservation equation at } x = l_2 \text{ (Eq. 3.4(c))} \\ \text{Choked inlet condition (Eq. 3.6(a))} \\ \text{Isentropic inlet condition (Eq. 3.6(b))} \\ \text{Open outlet condition (Eq. 3.7)} \end{bmatrix} \begin{bmatrix} A_{+1} \\ A_{-1} \\ A_{e1} \\ A_{+2} \\ A_{-2} \\ A_{e2} \\ A_{+3} \\ A_{-3} \\ A_{e3} \\ \hat{Q} \end{bmatrix} = 0. \tag{3.11}$$

The non-zero elements of the matrix $\mathcal{A}$ are given in Appendix B.2.. The nonlinear eigenvalue problem is solved by the inverse iteration algorithm (Watkins, 2002); an advantage of this approach is that for each eigenmode, the left and right eigenvectors are simultaneously obtained. Any complex ω that gives zero determinant of $\mathcal{A}$ is an eigenvalue of the direct system, and the corresponding vector $\mathbf{x}$ is an eigenvector.

The spectrum is formed by ten eigenmodes, shown in Fig. 3.2. The spectrum shows the trajectories of eigenvalues when the coefficient κ varies. The unsteady flame position is fixed at $l_2 = 1.7345$ m. The comparison of the eigenvalues and the trajectories shows that the frequencies match quite closely those found by Dowling and Stow (2003), whereas the growth rates do not. We also observe that both sets of results yield the same sign of the growth rates for nine modes out of ten, when $\kappa = 1$.

The mode shapes of the perturbation variables can be reconstructed from the eigenvector by the use of Eqs (3.2). The absolute values of the resonant pressure fluctuations, in the presence of unsteady heat release, are compared with the literature results in Fig. 3.3. The eigenvalues and the mode shapes of the modes are found to differ mildly from the results of the literature. This could stem from differences in the values of the base flow variables, values not given in the paper by Dowling and Stow (2003). This points to possible uncertainties in the base flow, affecting the amplitude of the perturbations and the complex eigenvalues.

3.2. UNCERTAINTY IN BASE FLOW

Our first goal is to identify a possible source of discrepancy in the eigenvalues between our results and those in Dowling and Stow (2003). We thus employ the adjoint base-state sensitivity analysis to quantify how eigenvalues are affected by small arbitrary variations in base flow variables $\bar{\mathbf{q}}$. The approach used here is similar to the base state sensitivity study carried out by Aguilar et al. (2017) and Juniper (2018). However, the purposes are different. The authors above have calculated the effect of system parameters, such as heat release model time delays and reflection coefficients, with the goal of optimizing the system. Here, we aim to evaluate the sensitivity of generic modifications to base flow quantities. In a real physical system, generic base flow modifications can stem from uncertainties in experimental measurements or in numerical computations.

3.2.1. Base-state sensitivity analysis

Introducing a small deviation $\delta\bar{\mathbf{q}}$ of base flow into the direct system, Eq. (3.10), causes variations in both eigenfrequency and eigenvector, so that, upon linearization, we have

$$\delta\mathcal{A}\,\mathbf{x} + \mathcal{A}\,\delta\mathbf{x} = 0, \tag{3.12}$$

with

$$\delta\mathcal{A} = \frac{\partial\mathcal{A}(\bar{\mathbf{q}},\omega)}{\partial\bar{q}}\,\delta\bar{q} + \frac{\partial\mathcal{A}(\bar{\mathbf{q}},\omega)}{\partial\omega}\,\delta\omega, \tag{3.13}$$

where $\bar{q}$ denotes a component of the vector $\bar{\mathbf{q}}$, and a sum over all the components is tacitly assumed.

Left-multiplying Eq. (3.12) by the adjoint eigenvector, $\mathbf{y}^\dagger$, solution of

$$\mathcal{A}^*(\bar{\mathbf{q}},\omega)\,\mathbf{y}^\dagger = 0, \tag{3.14}$$

with $*$ denoting conjugate transpose, we have:

$$\mathbf{y}^{\dagger *}\frac{\partial\mathcal{A}(\bar{\mathbf{q}},\omega)}{\partial\bar{q}}\,\mathbf{x}\,\delta\bar{q} + \mathbf{y}^{\dagger *}\frac{\partial\mathcal{A}(\bar{\mathbf{q}},\omega)}{\partial\omega}\,\mathbf{x}\,\delta\omega + \mathbf{y}^{\dagger *}\mathcal{A}(\bar{\mathbf{q}},\omega)\delta\mathbf{x} = 0, \tag{3.15}$$

with the last term on the left-hand-side equal to zero by virtue of Eq. (3.14).

The eigenvalue drift due to a generic base flow modification can thus be written as

$$\delta\omega = \mathcal{S}_{\bar{q}}\,\delta\bar{q}, \tag{3.16}$$

with the sensitivity defined, for each component of the vector $\bar{\mathbf{q}}$, by:

$$\mathcal{S}_{\bar{q}} = -\frac{\mathbf{y}^{\dagger *}\dfrac{\partial\mathcal{A}(\bar{\mathbf{q}},\omega)}{\partial\bar{q}}\,\mathbf{x}}{\mathbf{y}^{\dagger *}\dfrac{\partial\mathcal{A}(\bar{\mathbf{q}},\omega)}{\partial\omega}\,\mathbf{x}}. \tag{3.17}$$

3.2.2. Effects of fractional change of base flow on eigenvalues

We evaluate the variation of any eigenvalue due to a fractional change in the base flow parameters, which can be expressed as

$$\delta\omega = \mathcal{S}_{\bar{q}\%}\,\frac{\delta\bar{q}}{\bar{q}}, \tag{3.18}$$

with the complex, scaled sensitivities defined by

$$\mathcal{S}_{\bar{q}\%} = \mathcal{S}_{\bar{q}}\,\bar{q}. \tag{3.19}$$

These scaled sensitivities represent the response of the given eigenvalue to a percentage change in the respective base flow parameters.

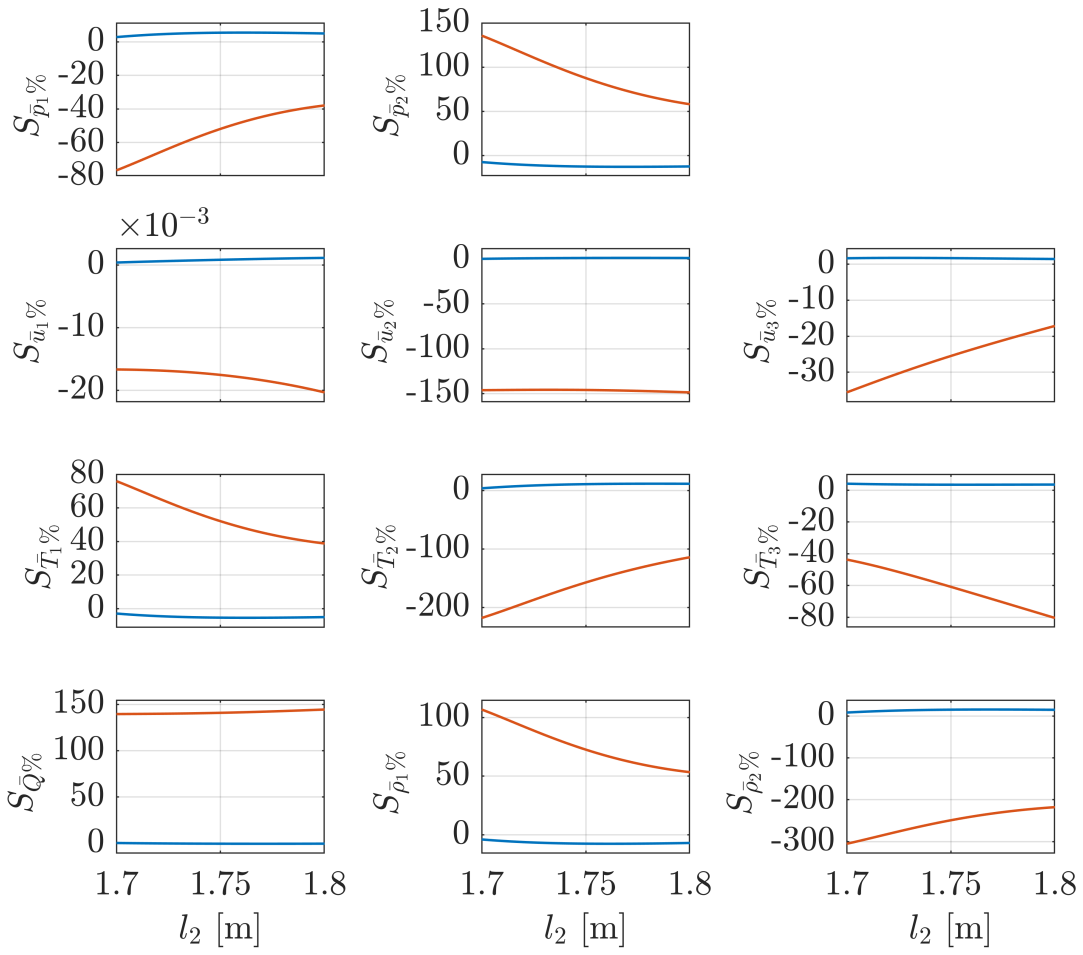

Figure 3.4: Sensitivity to uncertainties in different base flow variables for eigenmode TA_1, as a function of the position l_2 of the compact flame. Blue curves: sensitivity of oscillation frequency ($\omega_r/(2\pi)$ [Hz]). Red curves: sensitivity of growth rate ($-\omega_i$ [rad/s]).

Figures 3.4 and 3.6 illustrate the sensitivities of complex eigenvalues to uncertainties in base flow parameters $\bar{\mathbf{q}}$ for the two most unstable modes, TA_1 and TA_2, with oscillation frequencies of 171 Hz and 300 Hz, respectively. We choose these two eigenmodes because they are the two most unstable modes, and they show large discrepancies in growth rates in the eigenspectrum when compared to the reference results. We also examine how the sensitivities change with varying flame positions (l_2) from 1.7 m to 1.8 m, corresponding to a premixer length, L_2, varying from 0 to 0.1 m.

The sensitivities to modifications of mean pressure and mean density in the combustion chamber ($\bar{\rho}_3$ and $\bar{p}_3$) are zero, as matrix $\mathcal{A}$ does not depend on them. The sensitivity results have been validated against gradients calculated using the finite difference approach, showing excellent agreement. A Taylor test is conducted to perform a debugging check for adjoint codes: if the small deviation in the base flow quantity is ϵ to calculate the sensitivity with the first-order accurate finite difference approach, then the difference of the eigenvalue drift from that obtained with the adjoint approach ($|\delta\omega_{FD} - \delta\omega_{AD}|$) must increase in proportion to ϵ^2 (Juniper, 2018; Juniper and Sujith, 2018). We show in Fig. 3.5 an example of changing base flow parameter $\bar{u}_1$. It plots the eigenvalue drift difference for all eigenmodes against ϵ^2 and shows that it is indeed a straight line through the origin.

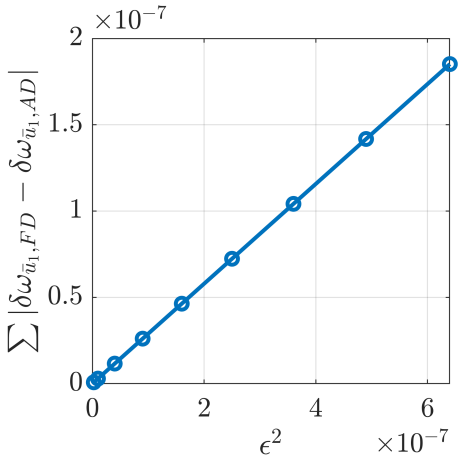

Figure 3.5: The difference between the eigenvalue drift of all eigenmodes, calculated from a first-order finite difference method with step size ϵ (FD) and an adjoint approach (AD), for changing base-state parameter $\bar{u}_1$.

Our findings indicate that for both eigenmodes TA_1 and TA_2, the relative difference in oscillation frequencies resulting from base-flow modifications is generally negligible and significantly less pronounced than the relative difference in growth rates. As shown in Fig. 3.2, the growth rates of modes TA_1 and TA_2 are overestimated by up to approximately 100 rad/s when compared to Dowling and Stow (2003). However, when comparing oscillation frequencies, a good agreement can be made; our uncertainty calculations confirm this observation.

Among the eleven different base flow modifications considered independently, the effect of mean flow velocity variations in the plenum is the least significant. A change of 1% in $\bar{u}_1$ leads to a deviation below 0.0204 rad/s in growth rate and below 0.0011 Hz in oscillation frequencies for mode TA_1 for whatever value of l_2 in the range considered; for mode TA_2, a change of 1%

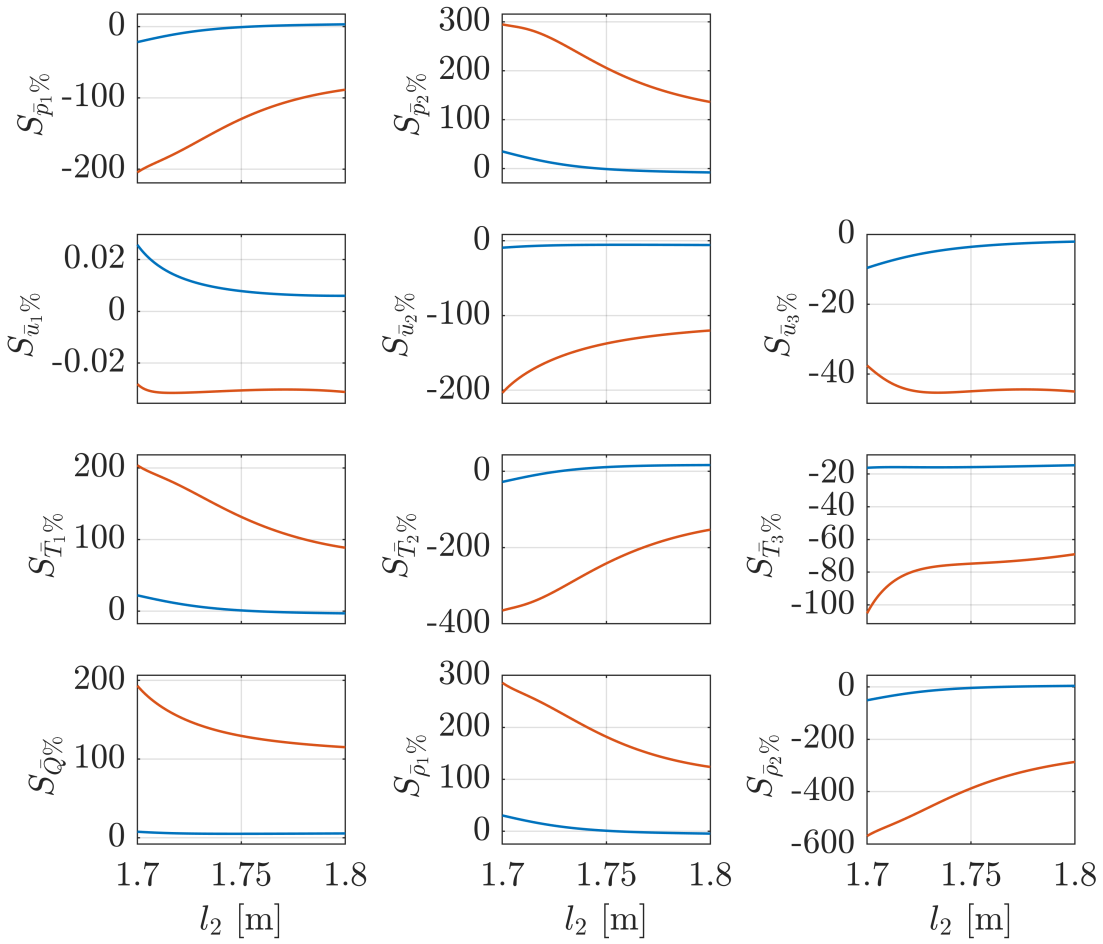

Figure 3.6: Same as Figure 3.4 for eigenmode TA_2.

in $\bar{u}_1$ leads to a maximum deviation in oscillation frequency of 0.0258 Hz, and in growth rate of 0.0281 rad/s. On the other hand, uncertainties in the mean density in the premixer section have the most profound effect on the linear growth rates for both eigenmodes. A 1% underestimation of $\bar{\rho}_2$ yields an increase in growth rate of up to 300 rad/s for mode TA_1 and up to 600 rad/s for mode TA_2. The results reported also show that extending the length of the premixer section, L_2, helps reduce the influence of $\bar{\rho}_1$ and $\bar{\rho}_2$ in altering the eigenvalues.

The differences in complex eigenvalues between the present results and those from the literature stem from the combined effect of all base flow uncertainties. The sensitivities displayed in Figs. 3.4 and 3.6 give an immediate response for each individual effect; it is the base flow variables in the premixer ($\bar{u}_2, \bar{p}_2, \bar{T}_2, \bar{\rho}_2, \bar{Q}$) which hold the most profound influence. This is due to the fact that these parameters directly affect the flame transfer function, which couples the flow in the premixer with the unsteady heat release. The analysis just presented, thus, furnishes indications of where flow control efforts could be directed.

3.3. STRUCTURAL SENSITIVITY TO STEADY FEEDBACK FORCINGS

We now assume general linear feedback forcing acting on the steady base-flow equations and evaluate the corresponding eigenvalue drift, $\delta\omega$. Differently from the previous section, the base flow variation depends on a particular choice of steady feedback process. In the previous section, we have derived the eigenvalue drift due to arbitrary variations of the base flow. Now, we show the expression of the eigenvalue drift caused by a particular feedback forcing in base flow (Pralits et al., 2010).

The base flow system in compact form is

$$\mathbf{B}(\bar{\mathbf{q}}) = 0. \tag{3.20}$$

Let us assume that a small term $\delta\mathbf{H}_B(\bar{\mathbf{q}})$ forces the system, so that the mean flow is perturbed by $\delta\bar{\mathbf{q}}$, i.e. $\mathbf{B}(\bar{\mathbf{q}} + \delta\bar{\mathbf{q}}) = \delta\mathbf{H}_B(\bar{\mathbf{q}} + \delta\bar{\mathbf{q}})$. Linearization yields

$$\frac{\partial \mathbf{B}(\bar{\mathbf{q}})}{\partial \bar{q}}\,\delta\bar{q} = \delta\mathbf{H}_B(\bar{\mathbf{q}}). \tag{3.21}$$

Here, again, summation is tacitly implied on the left-hand-side of the equation over all the elements of the vector $\bar{\mathbf{q}}$. Since the base flow is bounded only by jump conditions and boundary conditions, the feedback source term is introduced at the duct intersections, where jump conditions hold, of the form

$$\delta\mathbf{H}_B(\bar{\mathbf{q}}) = \delta\mathbf{H}_{B0}\,\bar{\mathbf{q}} \tag{3.22}$$

where $\delta\mathbf{H}_{B0}$ is the following coupling coefficient vector,

$$\delta\mathbf{H}_{B0} = [0, 0, 0, \delta\mathcal{H}_{M1}, \delta\mathcal{H}_{M2}, \delta\mathcal{H}_{H1}, \delta\mathcal{H}_{H2}, 0, 0, 0, 0, 0, 0], \tag{3.23}$$

characterizing feedback mass blowing/suction and feedback heating/cooling mechanisms proportional to the upstream mass flow rate ($\bar{\dot{m}}$) and total enthalpy($\bar{\dot{m}}\bar{H}$), respectively.

We now introduce the test variable, $\mathbf{b}^\dagger$, and left-multiply it by Eq. (3.21); by summing Eq. (3.15) it is found:

$$\mathbf{b}^{\dagger *}\frac{\partial \mathbf{B}(\bar{\mathbf{q}})}{\partial \bar{q}}\,\delta\bar{q} + \mathbf{y}^{\dagger *}\frac{\partial \mathcal{A}(\bar{\mathbf{q}},\omega)}{\partial \bar{q}}\,\mathbf{x}\,\delta\bar{q} + \mathbf{y}^{\dagger *}\frac{\partial \mathcal{A}(\bar{\mathbf{q}},\omega)}{\partial \omega}\,\mathbf{x}\,\delta\omega = \mathbf{b}^{\dagger *}\delta\mathbf{H}_{B0}\bar{\mathbf{q}}. \tag{3.24}$$

The adjoint base flow system (given in full form in Appendix B.3.) can be formally written as

$$\mathbf{b}^{\dagger *}\frac{\partial \mathbf{B}(\bar{\mathbf{q}})}{\partial \bar{q}} = -\mathbf{y}^{\dagger *}\frac{\partial \mathcal{A}(\bar{\mathbf{q}},\omega)}{\partial \bar{q}}\mathbf{x}. \tag{3.25}$$

Then, the eigenvalue drift stems naturally from the identity

$$\delta\omega = \mathcal{S}_{\mathbf{H}_{B0}}\,\delta\mathbf{H}_{B0}, \tag{3.26}$$

where the sensitivity of the eigenvalue to a structural forcing at the base flow level is defined by:

$$\mathcal{S}_{\mathbf{H}_{B0}} = \frac{\mathbf{b}^{\dagger *}\,\bar{\mathbf{q}}}{\mathbf{y}^{\dagger *}\dfrac{\partial \mathcal{A}(\bar{\mathbf{q}},\omega)}{\partial \omega}\,\mathbf{x}}. \tag{3.27}$$

The structural sensitivity to the feedback forcing at the base flow level for eigenmodes TA_1 and TA_2 is now examined. Two types of feedback sources are considered at the combustor intersections: steady mass blowing or suction, and steady heating or cooling. The corresponding equations are:

$$\bar{\rho}_1\bar{u}_1a_1 - \bar{\rho}_2\bar{u}_2a_2 = \delta\mathcal{H}_{M1}\,\bar{\dot{m}}, \tag{3.28a}$$
$$\bar{\rho}_2\bar{u}_2a_2 - \bar{\rho}_3\bar{u}_3a_3 = \delta\mathcal{H}_{M2}\,\bar{\dot{m}}, \tag{3.28b}$$
$$\bar{\rho}_1\bar{u}_1a_1\bar{H}_1 - \bar{\rho}_2\bar{u}_2a_2\bar{H}_2 = \delta\mathcal{H}_{H1}\,\bar{\dot{m}}\,\bar{H}_1, \tag{3.28c}$$
$$\bar{\rho}_2\bar{u}_2a_2\bar{H}_2 + a_3\bar{Q} - \bar{\rho}_3\bar{u}_3a_3\bar{H}_3 = \delta\mathcal{H}_{H2}\,\bar{\dot{m}}\,\bar{H}_2. \tag{3.28d}$$

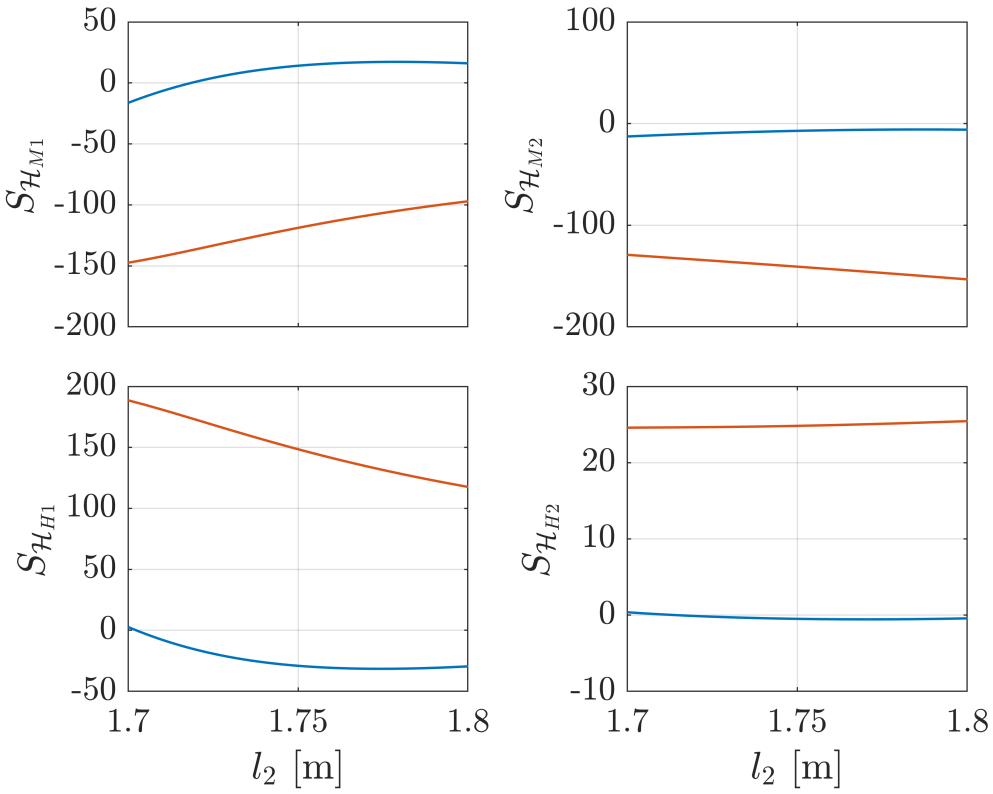

Figure 3.7: Sensitivity of ω to structural feedback in base flow level, for the eigenmode TA_1, $f = 171$ [Hz], with the variation of the compact flame position (l_2). Blue curves: sensitivity of angular eigenfrequencies (ω_r); Red curves: sensitivity of growth rate ($-\omega_i$).

Figures 3.7 and 3.8 show the sensitivities of angular frequency (blue curves) and growth rate (red curves) to steady structural feedback for the two unstable eigenmodes, TA_1 and TA_2, respectively. The sensitivities are evaluated with l_2 ranging from 1.7 m to 1.8 m[1]. The sensitivity results reveal that a small steady mass suction or the introduction of a steady heat release at the

[1]The results have been validated with the gradient calculated by the finite difference approach with percentage differences less than $\mathcal{O}(10^{-3})$. An example of comparison between adjoint and finite difference gradient evaluation will be shown in the next section.

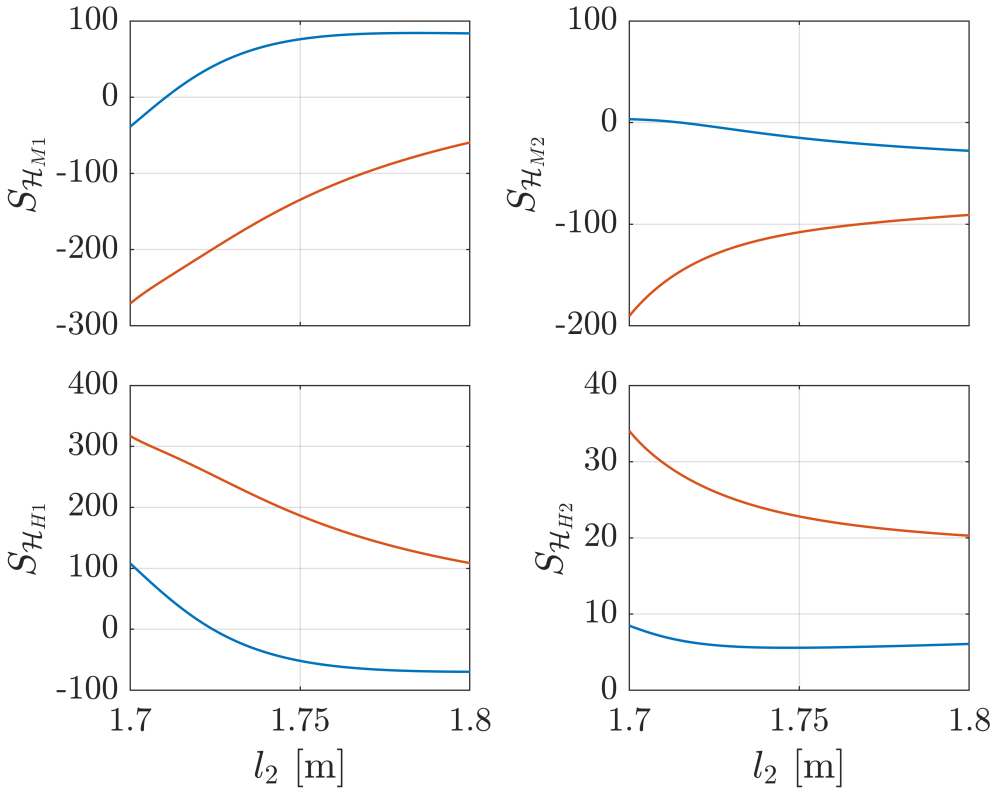

Figure 3.8: Same as Figure 3.7 for mode TA_2, $f = 300$ [Hz].

intersections would reduce the growth rate and therefore stabilize the eigenmodes. The former steady mechanism is achievable with regulated valves and the latter one can be obtained with heating coils placed at the duct intersections (Raghu and Sreenivasan, 1987). For both eigenmodes, sensitivities vary significantly with the length of the premixer, highlighting the fact that a stabilizing or destabilizing geometric configuration for mode TA_1 might produce the opposite effect for TA_2. The results confirm our observations in the previous section: variations of base flow parameters in the premixer, produced at the 1-2 interface and propagating downstream, resulting in the most significant changes in the two eigenvalues examined.

3.4. STRUCTURAL SENSITIVITY TO PERTURBATIONS

We now evaluate the eigenvalue response to a localized feedback source acting on the differential equations (3.1) for the perturbations.

3.4.1. Derivation of structural sensitivity

In some previous literature (e.g. Aguilar et al. (2017)), the structural sensitivity is derived based on a Lagrange multiplier framework. In the present work, the derivation of the structural sensitivity follows Luchini et al. (2008) and Pralits et al. (2010) with a method based on the Lagrange identity, also used by Magri and Juniper (2013). Note that the choice of the derivation method does not lead to different results.

The derivation starts with the direct system in compact form:

$$\mathcal{N}(\omega, \bar{\mathbf{q}})\,\hat{\mathbf{q}} = 0, \tag{3.29a}$$

$$\mathcal{J}(\omega, \bar{\mathbf{q}}, \hat{\mathbf{q}}) = 0, \tag{3.29b}$$

with perturbation variable vector $\hat{\mathbf{q}} = (\hat{\rho}, \hat{u}, \hat{p})$; the equation $\mathcal{J}(\omega, \bar{\mathbf{q}}, \hat{\mathbf{q}}) = 0$ represents the jump conditions, Eqs. (3.3)-(3.4), holding at the ducts' intersections, and $\mathcal{N}(\omega, \bar{\mathbf{q}})$ is the differential operator matrix defined by:

$$\mathcal{N}(\omega, \bar{\mathbf{q}}) = \begin{bmatrix} \mathrm{i}\omega + \bar{u}\dfrac{\mathrm{d}}{\mathrm{d}x} & \bar{\rho}\dfrac{\mathrm{d}}{\mathrm{d}x} & 0 \\ 0 & \mathrm{i}\omega\bar{\rho} + \bar{\rho}\bar{u}\dfrac{\mathrm{d}}{\mathrm{d}x} & \dfrac{\mathrm{d}}{\mathrm{d}x} \\ 0 & \gamma\bar{p}\dfrac{\mathrm{d}}{\mathrm{d}x} & \mathrm{i}\omega + \bar{u}\dfrac{\mathrm{d}}{\mathrm{d}x} \end{bmatrix}. \tag{3.30}$$

Now, we introduce a small structural perturbation localized in space (*via* a Dirac delta function $\delta(x - x_0)$, $x_0 \neq l_1$ and $x_0 \neq l_2$), proportional to a local fluctuating quantity $\hat{\mathbf{q}}$, i.e.

$$\delta\mathbf{H}(\hat{\mathbf{q}}) = \delta\mathbf{H}_0\,\hat{\mathbf{q}}\,\delta(x - x_0), \tag{3.31}$$

where $\delta\mathbf{H}_0$ is the coupling coefficient matrix

$$\delta\mathbf{H}_0 = \begin{bmatrix} \delta\mathcal{M}_\rho & \delta\mathcal{M}_u & \delta\mathcal{M}_p \\ \delta\mathcal{F}_\rho & \delta\mathcal{F}_u & \delta\mathcal{F}_p \\ \delta(\mathcal{Q}_\rho + \bar{c}^2\mathcal{M}_\rho) & \delta(\mathcal{Q}_u + \bar{c}^2\mathcal{M}_u) & \delta(\mathcal{Q}_p + \bar{c}^2\mathcal{M}_p) \end{bmatrix}, \tag{3.32}$$

which encompasses nine different feedback mechanisms, $\mathcal{M}$, $\mathcal{F}$, and $\mathcal{Q}$ denote forcing on the mass, momentum, and energy conservation equation, respectively. For the forcing of the energy conservation equation, the feedback coupling coefficient $\delta(\mathcal{Q}_q + \bar{c}^2\mathcal{M}_q)$ includes an additional term due to the derivation process involving the mass conservation equation. The units of these coupling coefficients are listed in Table 3.2.

Table 3.2: Units of the feedback coupling coefficients.

$\delta\mathcal{M}_p$	$\delta\mathcal{M}_u$	$\delta\mathcal{M}_\rho$	$\delta\mathcal{F}_p$	$\delta\mathcal{F}_u$	$\delta\mathcal{F}_\rho$	$\delta\mathcal{Q}_p$	$\delta\mathcal{Q}_u$	$\delta\mathcal{Q}_\rho$
s m^{-1}	kg m^{-3}	m s^{-}1	1	kg m^{-2} s^{-1}	m^2 s^{-2}	m s^{-}1	Pa	m^2 s^{-2}

Paying attention to not confuse the Dirac delta, $\delta(x - x_0)$, with the δ used to denote small variations, we express the perturbed eigenvalue problem to first order as

$$\delta\mathcal{N}\,\hat{\mathbf{q}} + \mathcal{N}\,\delta\hat{\mathbf{q}} = \delta\mathbf{H}_0\,\hat{\mathbf{q}}\,\delta(x - x_0), \tag{3.33a}$$

$$\delta\mathcal{J} = 0, \tag{3.33b}$$

with the boundary conditions defined as Eqs. (3.6)-(3.7). Fixing the base flow, the above takes the form:

$$\frac{\partial \mathcal{N}(\omega, \bar{\mathbf{q}})}{\partial \omega} \delta\omega \, \hat{\mathbf{q}} + \mathcal{N}(\omega, \bar{\mathbf{q}}) \, \delta\hat{\mathbf{q}} = \delta\mathbf{H}_0 \, \hat{\mathbf{q}} \, \delta(x - x_0), \tag{3.34a}$$

$$\frac{\partial \mathcal{J}(\omega, \bar{\mathbf{q}}, \hat{\mathbf{q}})}{\partial \omega} \delta\omega + \frac{\partial \mathcal{J}(\omega, \bar{\mathbf{q}}, \hat{\mathbf{q}})}{\partial \hat{q}} \delta\hat{q} = 0. \tag{3.34b}$$

We left-multiply by the test variable, $\hat{\mathbf{q}}^\dagger$, and integrate in space, i.e.

$$\begin{aligned} \int \left[\hat{\mathbf{q}}^{\dagger *} \mathcal{N}(\omega, \bar{\mathbf{q}}) \, \delta\hat{\mathbf{q}}\right] \mathrm{d}x + \int \left[\hat{\mathbf{q}}^{\dagger *} \frac{\partial \mathcal{N}(\omega, \bar{\mathbf{q}})}{\partial \omega} \delta\omega \, \hat{\mathbf{q}}\right] \mathrm{d}x + \\ + \hat{\mathbf{f}}^{\dagger *} \left[\frac{\partial \mathcal{J}(\omega, \bar{\mathbf{q}}, \hat{\mathbf{q}})}{\partial \omega} \delta\omega + \frac{\partial \mathcal{J}(\omega, \bar{\mathbf{q}}, \hat{\mathbf{q}})}{\partial \hat{q}} \delta\hat{q}\right] = \int \hat{\mathbf{q}}^{\dagger *} \delta\mathbf{H}_0 \, \hat{\mathbf{q}} \, \delta(x - x_0) \mathrm{d}x. \end{aligned} \tag{3.35}$$

We apply integration by parts, for the first term on the left-hand-side to yield the adjoint equation:

$$\mathcal{N}^*(\omega, \bar{\mathbf{q}}) \, \hat{\mathbf{q}}^\dagger = 0. \tag{3.36}$$

The boundary terms generated from integration by parts plus the term $\hat{\mathbf{f}}^{\dagger *} \dfrac{\partial \mathcal{J}(\omega, \bar{\mathbf{q}}, \hat{\mathbf{q}})}{\partial \hat{q}} \delta\hat{q}$ give the boundary and jump conditions of the adjoint system. The detailed equations of the adjoint disturbance system are listed in Section B.4.. The eigenvalue drift due to a localized structural perturbation can finally be written as

$$\delta\omega = \mathcal{S}_{\mathbf{H}_0} \, \delta\mathbf{H}_0, \tag{3.37}$$

with the sensitivity function defined by:

$$\mathcal{S}_{\mathbf{H}_0} = \frac{\hat{\mathbf{q}}^{\dagger *}(x_0) \, \hat{\mathbf{q}}(x_0)}{\displaystyle\int \left[\hat{\mathbf{q}}^{\dagger *} \frac{\partial \mathcal{N}(\omega, \bar{\mathbf{q}})}{\partial \omega} \, \hat{\mathbf{q}}\right] \mathrm{d}x + \hat{\mathbf{f}}^{\dagger *} \frac{\partial \mathcal{J}(\omega, \bar{\mathbf{q}}, \hat{\mathbf{q}})}{\partial \omega}}. \tag{3.38}$$

3.4.2. Validation with finite difference approach

The sensitivity results are validated with the gradient calculated with a first-order finite difference approach. With the finite difference approach, a set of jump conditions at position x_0 is added to the system:

$$(\bar{u}\hat{\rho} + \bar{\rho}\hat{u})|_{x_{0-}}^{x_{0+}} = \delta\mathcal{M}_q \hat{q}(x_0), \tag{3.39a}$$

$$(\bar{u}\bar{\rho}\hat{u} + \hat{p})|_{x_{0-}}^{x_{0+}} = \delta\mathcal{F}_q \hat{q}(x_0), \tag{3.39b}$$

$$(\bar{u}\hat{p} + \gamma\bar{p}\hat{u})|_{x_{0-}}^{x_{0+}} = (\delta\mathcal{Q}_q + \bar{c}^2\delta\mathcal{M}_q)\hat{q}(x_0). \tag{3.39c}$$

The eigenvalue change due to each feedback disturbance can be evaluated individually at each discrete position x_0.

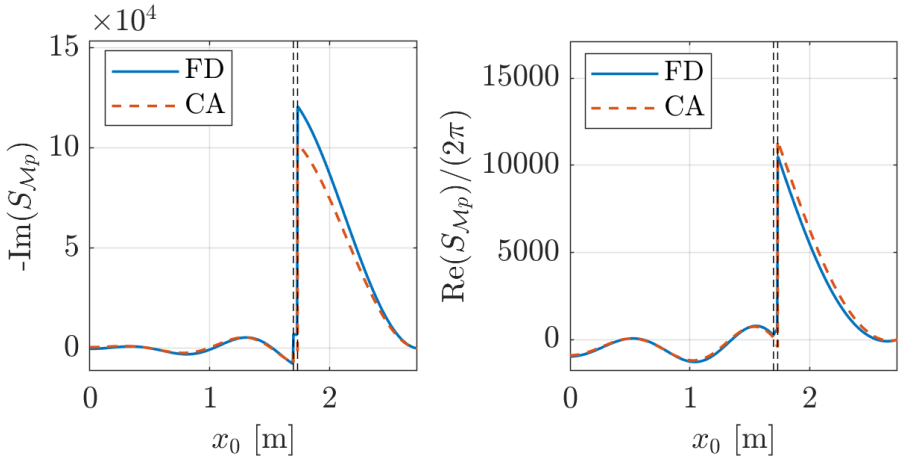

Figure 3.9: Validation with first-order finite difference approach, for mass feedback forcing proportional to pressure oscillations, with $\delta\mathcal{M}_p = 1 \times 10^{-7}$. The structural sensitivity are shown for the least stable eigenmode TA_1 for (a) growth rate and (b) oscillation frequency. The dashed lines represent the positions of the boundaries of each duct. FD: finite difference approach; CA: continuous adjoint approach.

Suppose that the length of the combustor is discretized into n points; a first-order finite-difference approach requires solving nonlinear eigenvalue problems at each discretized point in the combustor and for each feedback mechanism, hence, a total number of $18n$ times. With the adjoint approach, the sensitivity information is obtained by first solving the direct and adjoint nonlinear eigenvalue problem a single time for each eigenmode. The structural sensitivity, as a function of x_0, is then evaluated n times from the direct and adjoint modes. A sample comparison of results is displayed in Figure 3.9, highlighting the good agreement between adjoint sensitivity results and results from the finite-difference approach. A similar agreement is obtained for all other feedback sources. Once the adjoint system is established, the method proposed yields sensitivity information rapidly. On the other hand, deriving adjoint equations requires some effort.

3.4.3. The structural sensitivity of the most unstable eigenmodes

Figures 3.10 and 3.11 show the structural sensitivity defined by Eq. (3.38) for the two most unstable eigenmodes, TA_1 and TA_2. We aim to identify possible feedback mechanisms in the perturbation flow that can stabilize the system. The red curves illustrate the structural sensitivity of the growth rate; the blue curves illustrate the structural sensitivity of the oscillation frequency.

The nine feedback mechanisms can be evaluated comparatively; mass forcing proportional to pressure oscillations appears to have a very significant effect on the eigenvalue, for both modes. Such an effect can be generated by a Helmholtz resonator (Zhao and Li, 2015; Dupere and Dowling, 2005; Juniper, 2018), consisting of a cavity connected to a narrow neck or a small opening. When acoustic waves reach the resonator, the air in the neck oscillates in and out of the cavity, inducing mass flow disturbances. Such disturbances compress the air in the cavity, exciting the resonant frequency of the Helmholtz resonator. When the pressure oscillations

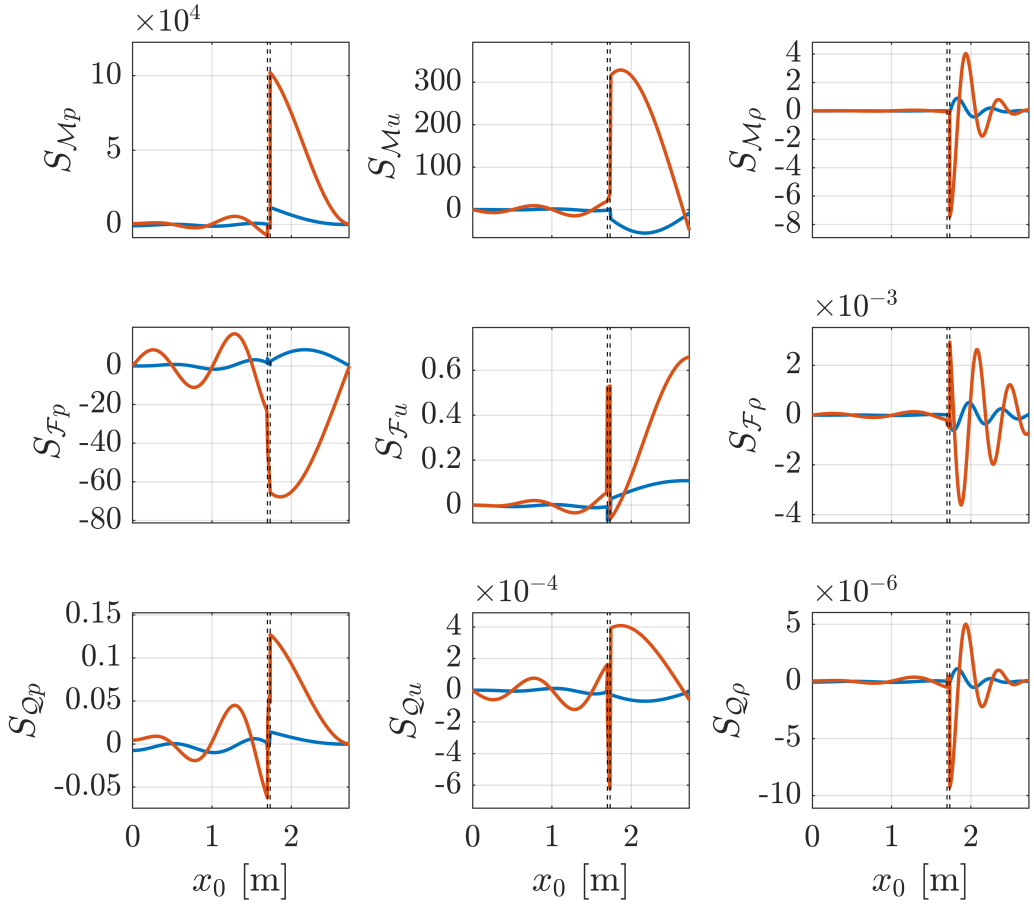

Figure 3.10: The structural sensitivity of eigenvalue to nine different feedback mechanisms placed at position x_0. Eigenmode TA_1, $f = 171$ [Hz]. Blue curves: structural sensitivity of the oscillation frequency ($\omega_r/2\pi$ [Hz]); red curves: structural sensitivity of the growth rate ($-\omega_i$ [rad/s]).

in the combustion system match the resonant frequency of the resonator, the air in the neck oscillates, converting the acoustic energy into kinetic energy and subsequently dissipating it into heat, thereby reducing the amplitude of the pressure oscillations. Focusing on the sensitivity of growth rates, it can be seen that a strong stabilizing effect for the leading unstable mode can be achieved by putting a Helmholtz resonator in the premixer or in the combustion section. In practice, the resonator should be tuned so that the phase between the mass disturbances and the pressure oscillations favors suppression of the instability (Raghu and Sreenivasan, 1987).

Reducing mass flow rate disturbances with a feedback term acting on the local velocity oscillations at the inlet of the premixer or adding a force proportional to the local pressure oscillations at the outlet of the premixer also help stabilize the critical unstable eigenmodes. Active flow control devices are available to achieve these feedback mechanisms, with actuators and sensors specifically designed, such as synthetic jets (McManus et al., 1990) and loudspeaker-microphone devices (Annaswamy and Ghoniem, 1995). The structural sensitivity analysis also reveals that introducing a feedback forcing proportional to the unsteady heat release has a minor effect on the system's stability.

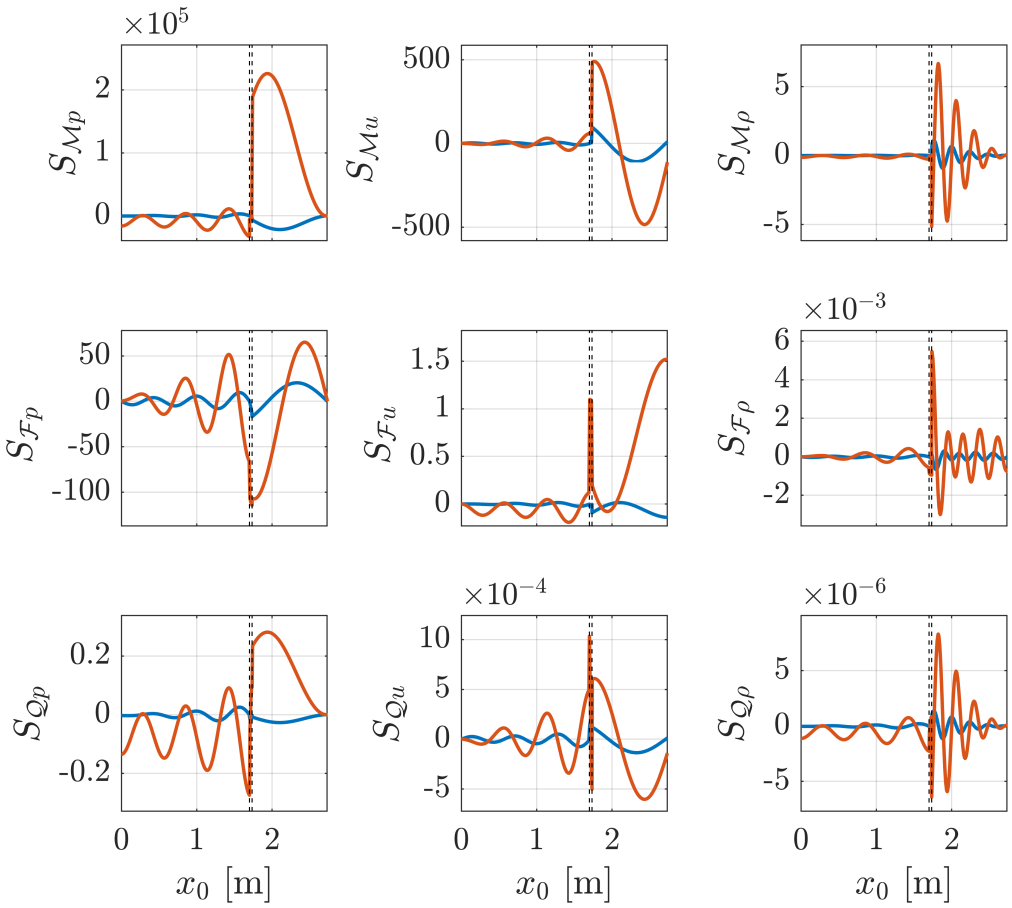

Figure 3.11: Same as Figure 3.10 for eigenmode TA_2.

3.5. CONCLUSIONS

In this study, an adjoint sensitivity analysis was applied to a prototypical thermoacoustic system. We analyzed the eigenvalues of the system and identified the most unstable resonant modes. By focusing on the two least stable modes, we investigated three types of sensitivities using the adjoint method.

First, we compared our eigenvalue spectra with those in the literature and found discrepancies, mainly in the growth rates of the resonant disturbances. Since we believe that these discrepancies might be due to inconsistencies in base flow parameters, we evaluated the effect of generic base-flow modifications on the eigenvalues; our findings indicated that the mean densities of the cold gaseous fuel within the premixing duct had the most significant impact on complex eigenvalues, particularly on altering growth rates. Additionally, we demonstrated that extending the length of the premixer duct significantly reduces the sensitivity of eigenvalues to mean density variations.

Then, we examined the use of steady forcing terms on the base flow equations to stabilize critical eigenmodes. The sensitivity analysis indicated that steady mass reduction or introducing

steady heat release at both ducts' intersections can stabilize the unstable eigenmodes. The stabilizing effect is more significant when the premixer duct is relatively short, i.e., the flame position moves upstream.

Finally, we assessed the sensitivities of the two most unstable eigenmodes to feedback disturbances. We found that mass fluctuation feedback proportional to local pressure perturbations, achievable through a Helmholtz resonator placed in the premixer and/or the combustion chamber, can have a strong effect in stabilizing the instabilities. The structural sensitivity analysis also revealed that active control approaches, such as reduction in mass flow rate fluctuations, proportional to velocity disturbances, and the imposition of an external force, proportional to pressure perturbations, are viable options to modify the system's stability.

In conclusion, even though our model problem is not very high-dimensional, our findings highlight the effectiveness of adjoint-based sensitivity analysis in explaining and quantifying uncertainties in a thermoacoustic system, and in suggesting effective control strategies for mitigating temporally growing modes.

见一叶落，而知岁之将暮。睹一壶之冰，而知天下之寒。

——《淮南子·说山训》

"A single falling leaf whispers the year's end;
A jar of frozen water hums winter's arrival."

UPSCALED MODELS FOR ACOUSTIC PROPAGATION THROUGH RIGID POROUS MATERIAL

Porous materials are inherently heterogeneous across multiple spatial and temporal scales, presenting substantial challenges for both mathematical modelling and computational simulation. The coexistence of disparate length and time scales in such systems complicates the accurate prediction of transport phenomena and often results in significant computational demands. To overcome these difficulties, various upscaling techniques—such as classical homogenization (Mei and Vernescu, 2010), volume averaging (Whitaker, 1999), and the adjoint homogenization method (Bottaro, 2019)—have been developed to derive macroscopic models that effectively encapsulate the key features of microscale physics. A comprehensive review of these methods is provided by Battiato et al. (2019). More recent research has extended traditional upscaling frameworks to account for boundary effects and thin porous layers. For instance, **?** introduced a one-domain averaging method to model a coupled fluid–porous system, capturing both inertial and slip effects within a unified Darcy-like equation featuring a spatially varying apparent permeability tensor. These macroscopic models offer a computationally efficient alternative to direct pore-scale simulations, enabling the study of flow and transport processes at larger, practical scales—such as entire devices or environmental systems. Despite advances in computational power, fully resolved simulations of large-scale porous domains remain infeasible. Therefore, homogenization and related techniques are crucial for bridging the gap between detailed microscale behaviour and system-level modelling, ensuring both accuracy and computational tractability in engineering, environmental, and industrial applications.

Classical homogenized models of wave propagation in porous media are typically formulated for infinitely extended domains, where they effectively describe the bulk acoustic properties of the material. However, these models fall short in accurately capturing the acoustic behavior near the interface between air and heterogeneous porous structures. To address this limitation, Marigo and Maurel (2017) developed a second-order homogenization method tailored for periodically stratified slabs, which incorporates finite-size effects. This method improves the predictive accuracy of wave propagation by accounting for second-order discontinuities, thereby enhancing the representation of sub-wavelength structural features. While effective, their approach is restricted to geometries with stratified slab configurations.

Inspired by the asymptotic matching strategy introduced by Marigo and Maurel (2016), this chapter presents a generalized framework for modelling acoustic propagation in porous materials of finite dimensions. A prototype system composed of parallel rigid micro-cylindrical scatterers is used to represent the porous medium. The resulting effective model depends solely on the material's porosity and the characteristics of the incident plane wave, offering a simplified yet robust description of the acoustic field. First, section 4.1. illustrates the limitations of classical homogenization in capturing interface effects. Then, in Section 4.2., a combined homogenization approach with asymptotic matching is introduced to develop effective jump conditions for acoustic propagation through the interface between an air domain and rigid porous material. In Section 4.3., the homogenization approach is applied to a case where acoustic

waves propagate through a single array of rigid inclusions. The reflection and transmission coefficients calculated with the model are compared with experimental measurements. In the end, the conclusions are given in Section 4.4.

4.1. THE CLASSICAL HOMOGENIZATION MODEL

Figure 4.1 shows the field and sketch of porous material consisting of parallel rigid micro cylindrical acoustic scatterers. Throughout the whole domain, the acoustic field is governed by the linearized Euler equations; taken together with the energy conservation equation and expressed in dimensional form, they are:

$$\bar{\rho}\frac{\partial u_i'}{\partial \tilde{t}} + \frac{\partial p'}{\partial \tilde{x}_i} = 0, \tag{4.1a}$$

$$\frac{1}{\bar{\rho}c_s^2}\frac{\partial p'}{\partial \tilde{t}} + \frac{\partial u_i'}{\partial \tilde{x}_i} = 0, \tag{4.1b}$$

$$\frac{\partial \tilde{E}}{\partial \tilde{t}} + \frac{\partial (p'u_i')}{\partial \tilde{x}_i} = 0. \tag{4.1c}$$

The isentropic condition, $p' = \rho' c_s^2$, has been used to express the constraint of momentum conservation. $\tilde{E}$ is the acoustic energy density defined as,

$$\tilde{E} = \frac{p'^2}{2\bar{\rho}c_s^2} + \frac{\bar{\rho}u_i'^2}{2}. \tag{4.2}$$

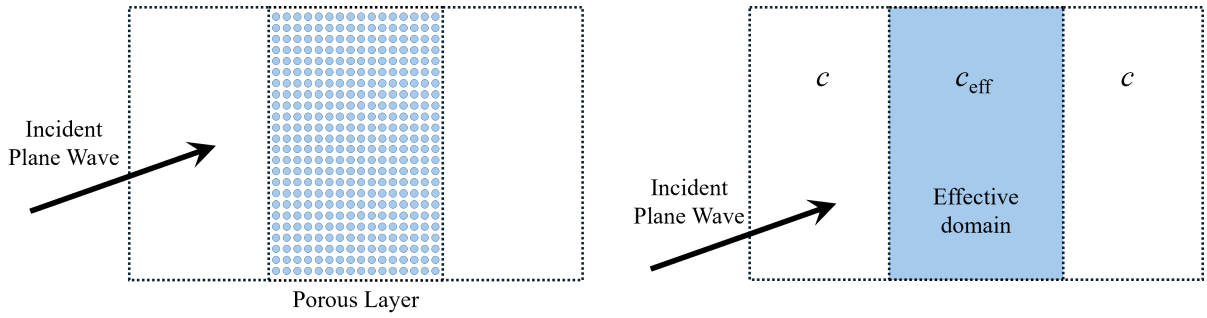

Figure 4.1: Incident acoustic plane wave propagates through a block of porous material.

To reformulate the problem in dimensionless form, the following variables are introduced:

$$\tau = kc_s\tilde{t}, \quad X_i = k\tilde{x}_i, \quad p = \frac{p'}{\Delta p_{ref}}, \quad u_i = \frac{\bar{\rho}c_s u_i'}{\Delta p_{ref}}. \tag{4.3}$$

where $k = 2\pi f/c_s$ is the wavenumber with f the frequency of the acoustic wave (unit Hz), and Δp_{ref} is a chosen reference pressure, usually the ambient pressure. Eqs. (4.1) in dimensionless

form read:

$$\frac{\partial u_i}{\partial \tau} + \frac{\partial p}{\partial X_i} = 0, \tag{4.4a}$$

$$\frac{\partial p}{\partial \tau} + \frac{\partial u_i}{\partial X_i} = 0, \tag{4.4b}$$

$$\frac{1}{2}\frac{\partial (p^2 + u_i^2)}{\partial \tau} + \frac{\partial (p u_i)}{\partial X_i} = 0. \tag{4.4c}$$

At the solid boundary, the Neumann boundary condition applies, i.e.:

$$u_i n_i = 0, \quad \text{at } \mathcal{A}_{\beta\sigma}, \tag{4.5}$$

with n_i the unit normal vector pointing away from the β-phase, as shown in Fig. 4.4(b). We also introduce two averaging operators: the superficial and the intrinsic averaging operators, applied to the generic microscopic variable ψ are, respectively, defined by

$$\text{Superficial averaging:} \quad \langle \psi \rangle = \frac{1}{V} \int_{\mathcal{V}_\beta} \psi \, \mathrm{d}\mathcal{V}, \tag{4.6a}$$

$$\text{Intrinsic averaging:} \quad \langle \psi \rangle^\beta = \frac{1}{V_\beta} \int_{\mathcal{V}_\beta} \psi \, \mathrm{d}\mathcal{V}, \tag{4.6b}$$

where V_β is the volume of the fluid phase and V is the volume of the total volume. The relation $\langle \psi \rangle = \phi \, \langle \psi \rangle^\beta$ holds in the bulk region.

The upscaled model using the homogenization approach in the bulk porous region has been reported in Mei and Vernescu (2010):

$$\frac{\partial^2 p^{(0)}}{\partial \tau^2} - \mathcal{C}_{ik} \frac{\partial^2 p^{(0)}}{\partial X_i \partial X_k} = 0, \tag{4.7}$$

with the coefficient $\mathcal{C}_{ik}$ the refraction tensor dependent on the bulk unit cell solution.

When the geometry of the bulk-region unit cell is isotropic, it is $\mathcal{C}_{ik} = \mathcal{C}\,\delta_{ik}$. This gives the wave equation in the bulk region at order $\mathcal{O}(\epsilon^0)$ in the following form:

$$\frac{\partial^2 p^{(0)}}{\partial \tau^2} - \mathcal{C} \frac{\partial^2 p^{(0)}}{\partial X_i^2} = 0. \tag{4.8}$$

The above equation implies that in the bulk region of the porous material, at order $\mathcal{O}(\epsilon^0)$, the pressure wave propagates as if the wave speed were scaled up by $\sqrt{\mathcal{C}}$ compared to the propagation speed in the free field far away from the porous region. Therefore, in the bulk porous region, an effective sound speed is defined as

$$c_{\text{eff}} = c_s \sqrt{\mathcal{C}}. \tag{4.9}$$

and a refractive index is defined as

$$\mathcal{R}_{ik} = \sqrt{\frac{1}{\mathcal{C}_{ik}}}, \quad \text{for anisotropic material}, \tag{4.10a}$$

$$\mathcal{R} = \sqrt{\frac{1}{\mathcal{C}}}, \quad \text{for isotropic material}. \tag{4.10b}$$

For the parallel cylindrical scatterer in square unit cells, the dependence of $\mathcal{R}$ on porosity can be found in Mei and Vernescu (2010). We apply the upscaled model in the porous material and compare the solution of the pressure field with exact numerical solutions. The porous media region contains lattices of 40×20 cylindrical acoustic scatterers. The fully resolved pressure fields are solved by numerical simulations in COMSOL. The cases are run with the exact geometry of porous media. The upscaled model is implemented within COMSOL. The porous media are characterized by porosity ϕ. The parallel cylinders are arranged in a square configuration with lattice constant l = 5 cm and have identical diameters of $d = \sqrt{4l(1-\phi)/\pi}$. The problems are two-dimensional and are solved in the frequency domain, taking the time evolution $p' = \hat{p}\,\mathrm{e}^{\mathrm{i}\omega t}$.

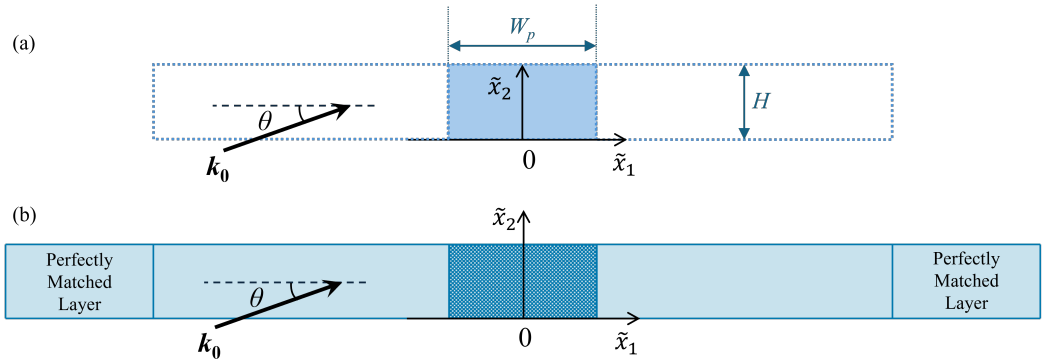

Figure 4.2: Sketch of geometry and computational domain of incident wave propagating through a layer of porous media.

Figure 4.2 shows the computational domain for the upscaled model and for simulations of real geometry. The incident acoustic wave hits the porous media at angle θ, and the corresponding wave vector of the incident wave is

$$\mathbf{k}_0 = (k_x, k_y) = (k_0 \cos\theta, k_0 \sin\theta). \tag{4.11}$$

k_x is the wave number component in $\tilde{x}_1$ direction and k_y in $\tilde{x}_2$ direction. Periodic Floquet boundary conditions, Eq. (4.12), are applied on the top and bottom boundaries to model infinite periodic structures in $\tilde{x}_2$ direction.

$$\hat{p}(\tilde{x}_1, \tilde{x}_2)\,\mathrm{e}^{-\mathrm{i}k_y H} = \hat{p}(\tilde{x}_1, \tilde{x}_2 + H), \tag{4.12}$$

where H is the vertical dimension of the computational domain.

Figures 4.3 show the comparison of the pressure field for several cases of porous material with varying porosities, subject to incident plane waves at different frequencies and incident angles. The highest frequency of incident waves examined is 340 Hz. Its wavelength, $\lambda = 20l$, ensures the separation of length scales. In these figures, it can be observed that the refraction of wave propagation within the porous material is well captured, indicating that the bulk region upscaled model is able to reproduce the general behaviour of wave transmission in the porous medium. However, it is also apparent that on the left side of the porous material and within the material itself, the pressure field is poorly captured, exhibiting significant discrepancies in

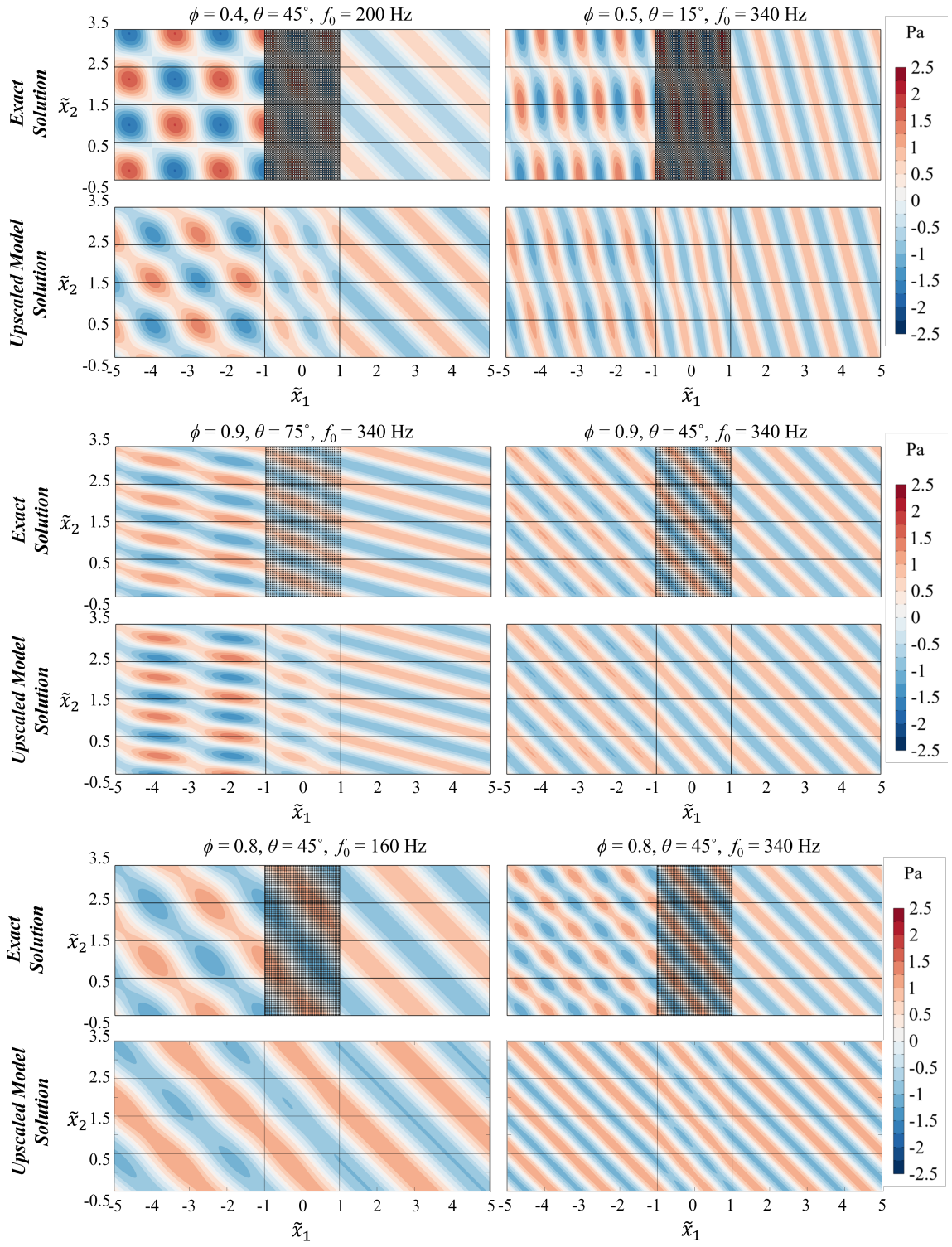

Figure 4.3: Comparison of total pressure field between the exact numerical solution and the upscaled model solution, assuming continuity of the pressure at the fluid-porous dividing surface.

amplitude and phase compared to the exact solutions. This limitation arises because reflective waves are generated at the interface between the free-air domain and the porous material, and these reflected waves are not accurately modelled when relying solely on the bulk region upscaled model. Consequently, to improve the accuracy of the pressure field predictions, particularly near the interface, it is crucial to treat the interface region with greater care. In the next section, an interface jump condition model is introduced and implemented to enhance the accuracy of the pressure field prediction throughout the entire domain.

4.2. EFFECTIVE JUMP CONDITIONS ACROSS INTERFACE BETWEEN FREE FIELD AND POROUS MATERIAL

4.2.1. Development of effective jump conditions

In order to capture the impact of the porous material surface on the pressure field, we aim to develop the jump conditions for the acoustic wave propagating through the interface of the free field and the porous material. The whole domain is considered to be two-dimensional and is divided into three regions: an outer free-field region, an outer bulk-porous region, and an inner interface region.

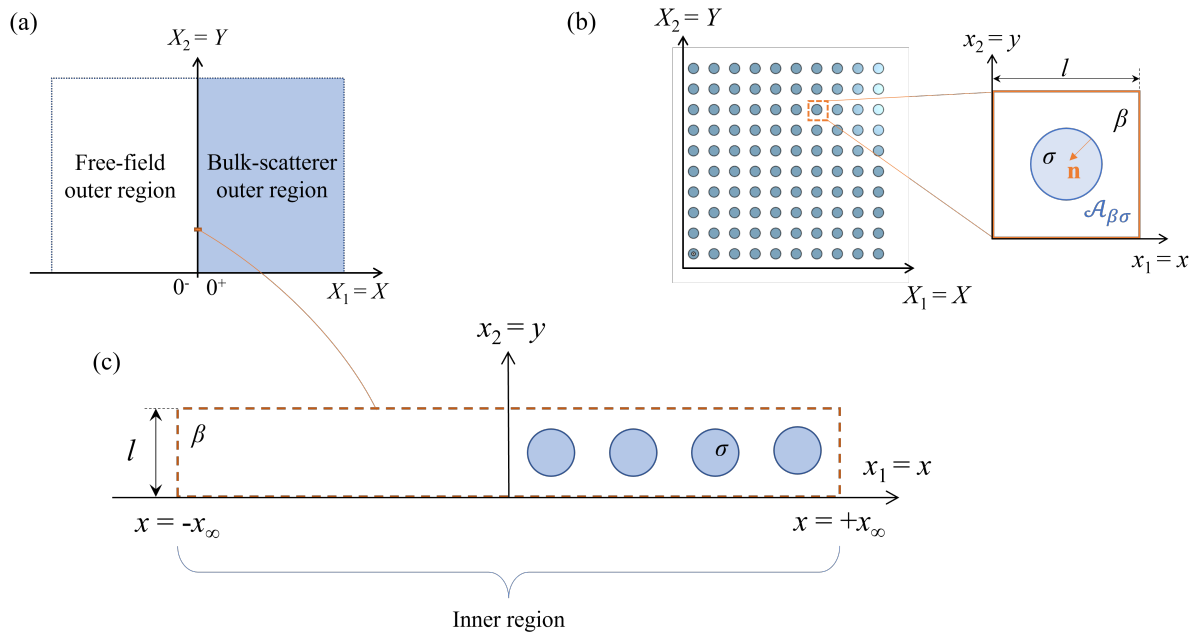

Figure 4.4: (a) Schematics of the acoustic propagation from the free field to a bulk scatterer region; (b) sketch of rigid cylindrical scatterers in the bulk of the porous medium with a corresponding unit cell; (c) unit cell for the interface region. The unit normal vector $\mathbf{n}$ points away from the β-phase.

Figure 4.4 shows the geometry of the unit cells. The unit cell encompasses all the structural

information in a periodic elementary volume. The periodicity of the rigid cylindrical scatterers, l, is chosen to be the microscopic characteristic length. The wavelength of the acoustic wave is the macroscopic characteristic length. It is assumed that separation of scales exists, $\epsilon = kl \ll 1$ with k being the wave number of the acoustic wave, i.e., low-frequency waves are considered. The fluid phase is denoted by β, while the solid phase is σ; the boundary between the fluid and the solid phase is denoted by $\mathcal{A}_{\beta\sigma}$. The bulk-region unit cell has a total volume equal to V, while the fluid volume is V_β; the solid volume of a cylinder is V_σ. The unit cell for the interface region has a fluid volume equal to V_{in}. The geometry is thus characterized by the porosity $\phi = V_\beta/V$. The incident acoustic wave is modeled by applying a background pressure field. The incident acoustic waves have a wave vector $\mathbf{k}_0$. The incident background pressure field is given as:

$$\hat{p}_{inc} = \mathrm{e}^{-\mathrm{i}(\mathbf{k}_0 \cdot \mathbf{X})} = \mathrm{e}^{-\mathrm{i}k_x X_1 - \mathrm{i}k_y X_2}. \tag{4.13}$$

We write the solutions of Eq. (4.4) in a power series expansion in each of the three regions. In the outer free region, the solutions are only functions of macroscopic spatial coordinates, X_i, and thus:

$$P = P^{(0)}(X_i, \tau) + \epsilon P^{(1)}(X_i, \tau) + \mathcal{O}(\epsilon^2), \tag{4.14a}$$

$$U_i = U_i^{(0)}(X_i, \tau) + \epsilon U_i^{(1)}(X_i, \tau) + \mathcal{O}(\epsilon^2). \tag{4.14b}$$

In the outer bulk region, the solutions are periodic along both microscopic coordinates x_1 and x_2, defined as $x_i = \tilde{x}_i/l$, and the slow variation of the solutions is a function of the macroscopic spatial coordinates, X_i. We thus write,

$$p = p^{(0)}(X_i, x_i, \tau) + \epsilon p^{(1)}(X_i, x_i, \tau) + \mathcal{O}(\epsilon^2), \tag{4.15a}$$

$$u_i = u_i^{(0)}(X_i, x_i, \tau) + \epsilon u_i^{(1)}(X_i, x_i, \tau) + \mathcal{O}(\epsilon^2). \tag{4.15b}$$

In the inner interface region, the solutions are periodic only along microscopic direction x_2. Since the interface region is assumed to be infinitesimally thin, the slow variation of the solution in the interface region is only a function of the macroscopic coordinate X_2:

$$\pi = \pi^{(0)}(X_2, x_i, \tau) + \epsilon \pi^{(1)}(X_2, x_i, \tau) + \mathcal{O}(\epsilon^2), \tag{4.16a}$$

$$v_i = v_i^{(0)}(X_2, x_i, \tau) + \epsilon v_i^{(1)}(X_2, x_i, \tau) + \mathcal{O}(\epsilon^2). \tag{4.16b}$$

Because of the above, the chain rule in the three regions yields:

$$\text{Outer free region: } \frac{\partial}{\partial X_i} \to \frac{\partial}{\partial X_i}, \tag{4.17a}$$

$$\text{Interface region: } \frac{\partial}{\partial X_i} \to \frac{1}{\epsilon}\frac{\partial}{\partial x_i} + \frac{\partial}{\partial X_2}\delta_{2i}, \tag{4.17b}$$

$$\text{Outer bulk region: } \frac{\partial}{\partial X_i} \to \frac{1}{\epsilon}\frac{\partial}{\partial x_i} + \frac{\partial}{\partial X_i}. \tag{4.17c}$$

The three regions are related through matching conditions at $X_1 \to 0^{\pm}$, corresponding to $x_1 \to \pm x_\infty$. Taylor expansions at $X_1 = 0^{\pm}$ of the leading order solutions of Eq. (4.14) and

Eq. (4.15) are adopted, with using $X_i = \epsilon x_i$, to obtain:

$$P^{(0)} = P^{(0)}(0^-, X_2, \tau) - \epsilon x_\infty \frac{\partial P^{(0)}}{\partial X_1}(0^-, X_2, \tau) + \mathcal{O}(\epsilon^2), \tag{4.18a}$$

$$U_i^{(0)} = U_i^{(0)}(0^-, X_2, \tau) - \epsilon x_\infty \frac{\partial U_i^{(0)}}{\partial X_1}(0^-, X_2, \tau) + \mathcal{O}(\epsilon^2), \tag{4.18b}$$

$$p^{(0)} = p^{(0)}(0^+, X_2, x_i, \tau) + \epsilon x_\infty \frac{\partial p^{(0)}}{\partial X_1}(0^+, X_2, x_i, \tau) + \mathcal{O}(\epsilon^2), \tag{4.18c}$$

$$u_i^{(0)} = u_i^{(0)}(0^+, X_2, x_i, \tau) + \epsilon x_\infty \frac{\partial u_i^{(0)}}{\partial X_1}(0^+, X_2, x_i, \tau) + \mathcal{O}(\epsilon^2). \tag{4.18d}$$

On the left and right boundaries of the inner region unit cell, the pressure and acoustic velocity are continuous (cf. Fig. 4.1(c)), for the leading order matching conditions to read:

$$P^{(0)}(0^-, X_2, \tau) = \lim_{x_1 \to -x_\infty} \pi^{(0)}(X_2, x_i, \tau), \tag{4.19a}$$

$$U_i^{(0)}(0^-, X_2, \tau) = \lim_{x_1 \to -x_\infty} v_i^{(0)}(X_2, x_i, \tau), \tag{4.19b}$$

$$\lim_{x_1 \to x_\infty} p^{(0)}(0^+, X_2, x_i, \tau) = \lim_{x_1 \to x_\infty} \pi^{(0)}(X_2, x_i, \tau), \tag{4.19c}$$

$$\lim_{x_1 \to x_\infty} u_i^{(0)}(0^+, X_2, x_i, \tau) = \lim_{x_1 \to x_\infty} v_i^{(0)}(X_2, x_i, \tau). \tag{4.19d}$$

Matching at order $\mathcal{O}(\epsilon)$ yields:

$$P^{(1)}(0^-, X_2, \tau) = \lim_{x_1 \to -x_\infty} \left(\pi^{(1)} + x_\infty \frac{\partial P^{(0)}}{\partial X_1}(0^-, X_2, \tau) \right), \tag{4.20a}$$

$$U_i^{(1)}(0^-, X_2, \tau) = \lim_{x_1 \to -x_\infty} \left(v_i^{(1)} + x_\infty \frac{\partial U_i^{(0)}}{\partial X_1}(0^-, X_2, \tau) \right), \tag{4.20b}$$

$$\lim_{x_1 \to x_\infty} p^{(1)}(0^+, X_2, x_i, \tau) = \lim_{x_1 \to x_\infty} \left(\pi^{(1)} - x_\infty \frac{\partial p^{(0)}}{\partial X_1}(0^+, X_2, x_i, \tau) \right), \tag{4.20c}$$

$$\lim_{x_1 \to x_\infty} u_i^{(1)}(0^+, X_2, x_i, \tau) = \lim_{x_1 \to x_\infty} \left(v_i^{(1)} - x_\infty \frac{\partial u_i^{(0)}}{\partial X_1}(0^+, X_2, x_i, \tau) \right). \tag{4.20d}$$

Equations (4.4) in dimensionless form in the outer free region at $\mathcal{O}(\epsilon^N)$, $N = 0, 1$ are:

$$\frac{\partial P^{(N)}}{\partial \tau} + \frac{\partial U_i^{(N)}}{\partial X_i} = 0, \tag{4.21a}$$

$$\frac{\partial U_i^{(N)}}{\partial \tau} + \frac{\partial P^{(N)}}{\partial X_i} = 0. \tag{4.21b}$$

In the inner region and outer bulk region, substituting Eqs. (4.16) and Eqs. (4.17b),(4.17c) into Eqs. (4.4), we obtain problems up to order $\mathcal{O}(1)$.

Order ϵ^{-1}

Inner interface region:

$$\frac{\partial v_i^{(0)}}{\partial x_i} = 0, \tag{4.22a}$$

$$\frac{\partial \pi^{(0)}}{\partial x_i} = 0. \tag{4.22b}$$

Outer bulk region of porous medium:

$$\frac{\partial u_i^{(0)}}{\partial x_i} = 0, \tag{4.23a}$$

$$\frac{\partial p^{(0)}}{\partial x_i} = 0. \tag{4.23b}$$

The last equation above indicates that $p^{(0)}$ depends only on the macroscopic coordinates X_i and time τ. Using the divergence theorem, integration of Eq. (4.22a) over the domain V_β gives

$$\int_0^1 v_1^{(0)} \Big|_{x_1=-x_\infty}^{x_\infty} \mathrm{d}x_2 = \int_0^1 u_1^{(0)}(X_1 = 0^+)\,\mathrm{d}x_2 - U_1^{(0)}(X_1 = 0^-) = 0, \tag{4.24}$$

Eq. (4.22b) shows that $\pi^{(0)}$ only depends on macroscopic spatial coordinates, i.e. $\pi^{(0)}$ *is constant in the inner-region unit cell*. Hence,

$$\pi^{(0)}(x_1 = x_\infty) - \pi^{(0)}(x_1 = -x_\infty) = p^{(0)}(X_1 = 0^+) - P^{(0)}(X_1 = 0^-) = 0, \tag{4.25}$$

i.e.

$$\pi^{(0)} = p^{(0)}(X_1 = 0^+) = P^{(0)}(X_1 = 0^-) \tag{4.26}$$

The macroscale jump conditions at order ϵ^0 are denoted as

$$[\![p]\!]^{(0)} = 0, \tag{4.27a}$$

$$[\![u_1]\!]^{(0)} = 0. \tag{4.27b}$$

At leading order, there is thus no jump in either pressure or x_1-velocity across the interface.

Order ϵ^0

Inner interface region:

$$\frac{\partial \pi^{(0)}}{\partial \tau} + \frac{\partial v_i^{(1)}}{\partial x_i} + \frac{\partial v_i^{(0)}}{\partial X_2}\delta_{i2} = 0, \tag{4.28a}$$

$$\frac{\partial v_i^{(0)}}{\partial \tau} + \frac{\partial \pi^{(1)}}{\partial x_i} + \frac{\partial \pi^{(0)}}{\partial X_2}\delta_{i2} = 0, \tag{4.28b}$$

$$v_i^{(0)} n_i = 0, \qquad \text{at } \mathcal{A}_{\beta\sigma}. \tag{4.28c}$$

Outer bulk region of porous medium:

$$\frac{\partial p^{(0)}}{\partial \tau} + \frac{\partial u_i^{(1)}}{\partial x_i} + \frac{\partial u_i^{(0)}}{\partial X_i} = 0, \tag{4.29a}$$

$$\frac{\partial u_i^{(0)}}{\partial \tau} + \frac{\partial p^{(1)}}{\partial x_i} + \frac{\partial p^{(0)}}{\partial X_i} = 0, \tag{4.29b}$$

$$u_i^{(0)} n_i = 0, \qquad \text{at } \mathcal{A}_{\beta\sigma}. \tag{4.29c}$$

With manipulating the equations (cf. Appendix C.1.), we get the problem for $\pi^{(1)}$ in the inner-region unit cell as follows,

$$\frac{\partial^2 \pi^{(1)}}{\partial x_i^2} = 0, \tag{4.30a}$$

$$\left(\frac{\partial \pi^{(1)}}{\partial x_i} + \frac{\partial P^{(0)}}{\partial X_2}(0^-, X_2, \tau)\delta_{2i} \right) n_i = 0, \qquad \text{at } \mathcal{A}_{\beta\sigma}, \tag{4.30b}$$

$$\lim_{x_1 \to +x_\infty} \frac{\partial \pi^{(1)}}{\partial x_1} = \frac{\partial P^{(0)}}{\partial X_1}(0^-, X_2, \tau), \tag{4.30c}$$

$$\lim_{x_1 \to -x_\infty} \frac{\partial \pi^{(1)}}{\partial x_1} = \frac{\partial P^{(0)}}{\partial X_1}(0^-, X_2, \tau). \tag{4.30d}$$

We can see that the system for $\pi^{(1)}$ is forced by $\dfrac{\partial P^{(0)}}{\partial X_j}(0^-, X_2, \tau)$. Hence, the solution for $\pi^{(1)}$ can be written as

$$\pi^{(1)} = a_j \frac{\partial P^{(0)}}{\partial X_j}(0^-, X_2, \tau); \tag{4.31}$$

substituting the above general solution (4.31) into Eqs. (4.30), the auxiliary problem for the closure variable a_j in an interface-region unit cell is

$$\frac{\partial^2 a_j}{\partial x_i^2} = 0, \tag{4.32a}$$

$$\left(\frac{\partial a_j}{\partial x_i} + \delta_{j2}\delta_{2i} \right) n_i = 0, \quad \text{at } \mathcal{A}_{\beta\sigma}, \tag{4.32b}$$

$$\lim_{x_1 \to \pm x_\infty} \frac{\partial a_j}{\partial x_1} = \delta_{j1}, \tag{4.32c}$$

$$a_j \text{ periodic along } x_2. \tag{4.32d}$$

In the bulk region of the porous medium, the formulation leads to an $\mathcal{O}(\epsilon^0)$ problem for $p^{(1)}$, i.e.

$$\frac{\partial^2 p^{(1)}}{\partial x_i^2} = 0, \tag{4.33a}$$

$$n_i \frac{\partial p^{(1)}}{\partial x_i} = -n_i \frac{\partial p^{(0)}}{\partial X_i}, \qquad \text{at } \mathcal{A}_{\beta\sigma}. \tag{4.33b}$$

Therefore, the solution of $p^{(1)}$ in the bulk region can be expressed as

$$p^{(1)} = -s_j \frac{\partial p^{(0)}}{\partial X_j}. \tag{4.34}$$

The elementary problem for s_j in a bulk-region unit cell (cf. Fig. 4.1(b)) is

$$\frac{\partial^2 s_j}{\partial x_i^2} = 0, \tag{4.35a}$$

$$\frac{\partial s_j}{\partial x_i} n_i = n_j, \quad \text{at } \mathcal{A}_{\beta\sigma}, \tag{4.35b}$$

$$s_j \text{ periodic along } x_1 \text{ and } x_2, \tag{4.35c}$$

$$\langle s_j \rangle^\beta = 0. \tag{4.35d}$$

The last condition is necessary to ensure uniqueness of s_1 and s_2. Solving Eq. (4.35) yields the solution for $p^{(1)}$.

As solutions for $p^{(1)}$ and $\pi^{(1)}$ are known, the following jump conditions at order $\mathcal{O}(\epsilon)$ can be obtained,

$$[\![p]\!]^{(1)} = \mathcal{M}_i \frac{\partial P^{(0)}}{\partial X_i}(0^-, X_2, \tau), \tag{4.36a}$$

$$[\![u_1]\!]^{(1)} = \mathcal{S}_{ij} \frac{\partial U_j^{(0)}}{\partial X_i}(0^-, X_2, \tau), \tag{4.36b}$$

with the coefficients

$$\mathcal{M}_i = \int_0^1 a_i \Big|_{x_1=-x_\infty}^{x_\infty} \mathrm{d}x_2 - x_\infty \delta_{1i} - x_\infty \delta_{1j} \int_0^1 B_{ji}^{-1} \Big|_{X_1=0^+} \mathrm{d}x_2, \tag{4.37a}$$

$$\mathcal{S}_{ij} = \begin{bmatrix} x_\infty(\phi - 1) & 0 \\ -\int_{V_{in}} (A_{21}) \, \mathrm{d}V & \int_{V_{in}} (1 - A_{22}) \, \mathrm{d}V \end{bmatrix}, \tag{4.37b}$$

and

$$A_{ij} = \frac{\partial a_j}{\partial x_i} + \delta_{j2}\delta_{2i}, \tag{4.38a}$$

$$B_{ij} = \begin{bmatrix} 1 - \dfrac{\partial s_1}{\partial x_1} & -\dfrac{\partial s_2}{\partial x_1} \\ 0 & 1 \end{bmatrix}. \tag{4.38b}$$

For details of the derivation please refer to Appendix C.2..

Finally, with $[\![p]\!] = [\![p]\!]^{(0)} + \epsilon [\![p]\!]^{(1)} + \mathcal{O}(\epsilon^2)$, and similarly for $[\![u_1]\!]$, the jump conditions of the acoustic field up to second-order are

$$[\![p]\!] = \epsilon \, \mathcal{M}_i \frac{\partial P^{(0)}}{\partial X_i}(0^-, X_2, \tau), \tag{4.39a}$$

$$[\![u_1]\!] = \epsilon \, \mathcal{S}_{ij} \frac{\partial U_j^{(0)}}{\partial X_i}(0^-, X_2, \tau). \tag{4.39b}$$

4.2.2. Solution of auxiliary problems and coefficients

From Eqs. (4.36)-(4.38), it is obvious that the coefficients in the jump condition depend on the solution of the auxiliary variables and the choice of interface region size x_∞. In this section, we calculate the auxiliary problems for various ϕ and x_∞. Some example fields are shown in this section, and the expressions for model coefficients dependent on the variables are given.

Bulk region vector field s_j and refractive index

The auxiliary problem of s_j, Eqs. (4.35), solved for the porosity range of 0.3-0.9. It gives the solution of $p^{(1)}$ and the coefficient $\mathcal{C}$. An example of s_j field for $\phi = 0.8$ is shown in Fig. 4.5.

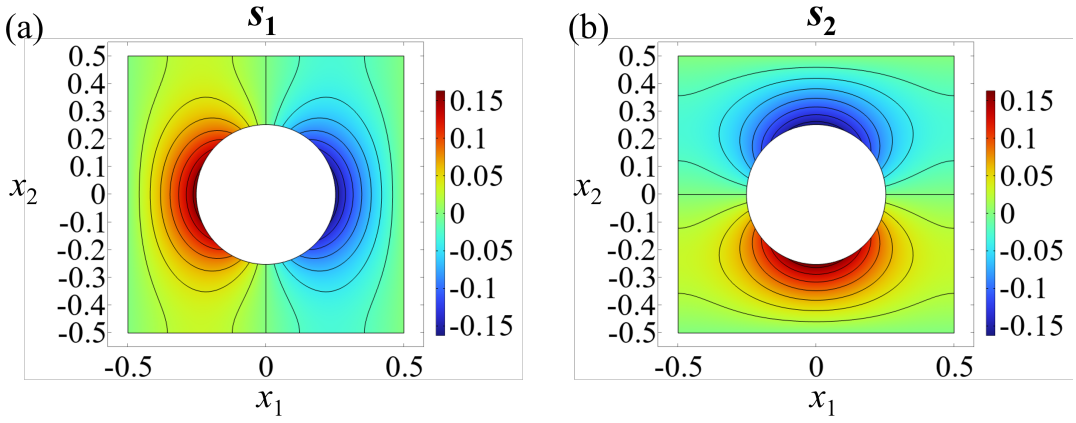

Figure 4.5: Field of s_j for $\phi = 0.8$ in a bulk region unit cell. (a) s_1; (b) s_2

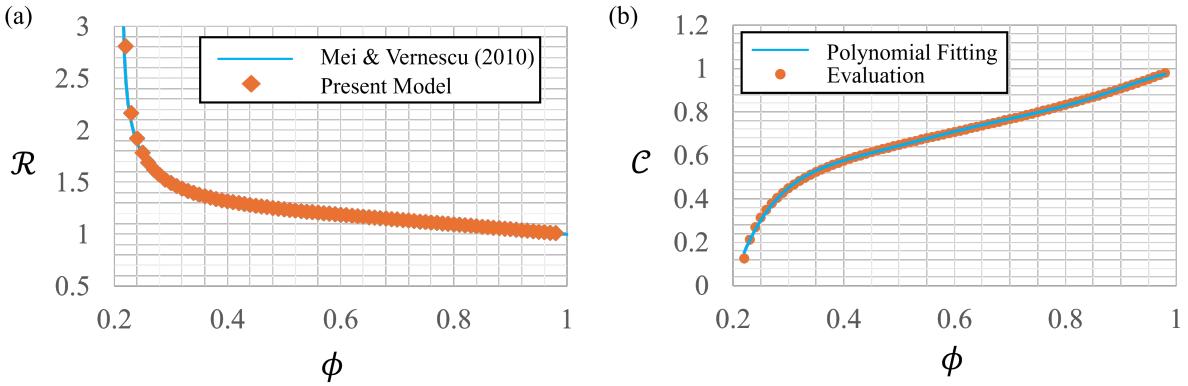

Figure 4.6: (a) Validation of refractive index $\mathcal{R}$ against Mei and Vernescu (2010); and (b) dependence of effective coefficient $\mathcal{C}$ on porosity.

The formulation of coefficient $\mathcal{C}_{ik}$ is (cf. (Mei and Vernescu, 2010) and Appendix C.3.),

$$\mathcal{C}_{ik} = \langle \frac{\partial s_k}{\partial x_j}\frac{\partial s_i}{\partial x_j} - 2\frac{\partial s_i}{\partial x_k} + \delta_{ik} \rangle^\beta. \tag{4.40}$$

Figure 4.6(a) shows validation of the refractive index against the literature result. The dependence of $\mathcal{C}$ on the porosity is shown in Fig. 4.6(b), together with a simple and accurate polynomial fitting:

$$\mathcal{C}(\phi) = -90.712\phi^6 + 360.53\phi^5 - 583.05\phi^4 + 491.59\phi^3 - 228.24\phi^2 + 56.073\,\phi - 5.1889. \quad (4.41)$$

Interface region vector field a_j and effective coefficients

The auxiliary problem of a_j in the interface region, (4.32), are solved for various material porosity ϕ and different unit cell sizes x_∞. An example of the solution of a_j is shown for a unit cell of size $x_\infty = 5$, and the porosity of the material being $\phi = 0.8$.

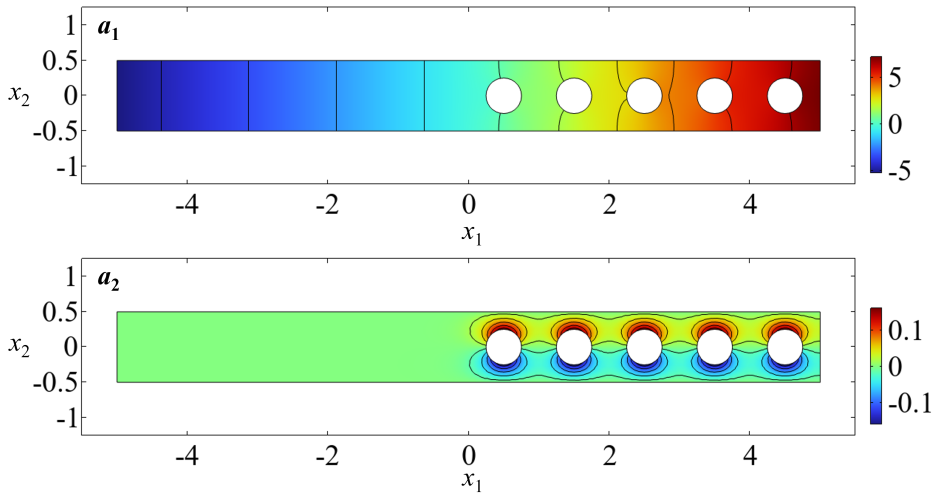

Figure 4.7: Field of a_j for $\phi = 0.8$ and $x_\infty = 5$ in an interface region unit cell.

The coefficients in Eqs. (4.37) are then evaluated for various material porosity ϕ and different unit cell sizes x_∞. The evaluation shows that $\mathcal{M}_2$ is trivial. Fig. 4.8 shows the dependence of $\mathcal{M}_1$ on unit cell size x_∞ for each fixed value of ϕ. It is clear that for a fixed porosity, $\mathcal{M}_1$ is linearly dependent on x_∞. Hence, we assume the coefficient $\mathcal{M}_1$ has the expression of the following form:

$$\mathcal{M}_1 = m_1(\phi)x_\infty + m_2(\phi), \quad (4.42)$$

with m_1 and m_2 functions of ϕ only and the polynomial fitting yields

$$\begin{aligned} m_1(\phi) &= -444.39\,\phi^5 + 1492.9\,\phi^4 - 1991.1\,\phi^3 + 1325.7\,\phi^2 - 449.34\,\phi + 65.472, \\ m_2(\phi) &= 3.3181\,\phi^4 - 10.21\,\phi^3 + 12.263\,\phi^2 - 6.9251\,\phi + 1.5682. \end{aligned} \quad (4.43)$$

The evaluation of $\mathcal{S}_{ij}$ shows that $\mathcal{S}_{21}$ is trivial. $\mathcal{S}_{22}$ changes with unit cell size x_∞, as shown in Fig. 4.9. As previously, $\mathcal{S}_{22}$ can be formulated as

$$\mathcal{S}_{22} = w_1(\phi)x_\infty + w_2(\phi), \quad (4.44)$$

with w_1 and w_2 obtained from polynomial fitting

$$\begin{aligned} w_1(\phi) &= -0.952\,\phi^3 + 1.1425\,\phi^2 - 0.3968\,\phi + 0.2065, \\ w_2(\phi) &= -0.3446\,\phi^4 + 0.9745\,\phi^3 - 1.0496\,\phi^2 + 0.5268\,\phi - 0.1088. \end{aligned} \quad (4.45)$$

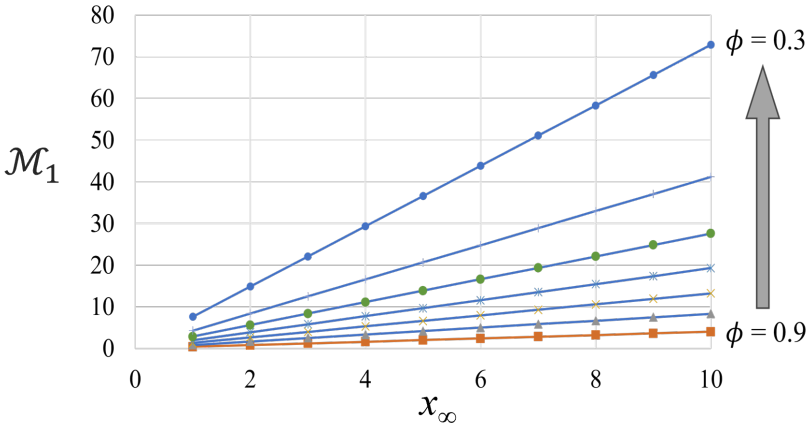

Figure 4.8: Dependence of $\mathcal{M}_1$ on porosity ϕ and interface-region unit cell size x_∞.

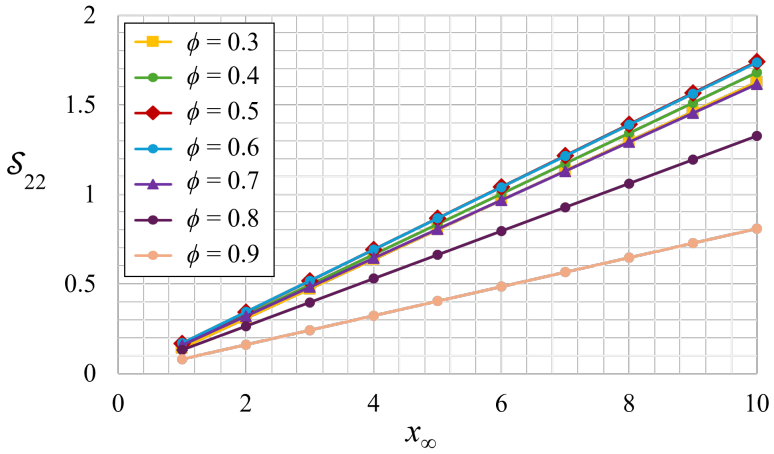

Figure 4.9: Dependence of $\mathcal{S}_{22}$ on porosity ϕ and interface-region unit cell size x_∞.

Evaluation of coefficients shows that the final interface jump conditions when $x_\infty = 0$ are,

$$[\![p]\!] = \epsilon\, m_2(\phi) \frac{\partial P^{(0)}}{\partial X_1}(0^-, X_2, \tau), \tag{4.46a}$$

$$[\![u_1]\!] = \epsilon\, w_2(\phi) \frac{\partial U_2^{(0)}}{\partial X_2}(0^-, X_2, \tau). \tag{4.46b}$$

with the dependence of coefficients $m_2(\phi)$ and $w_2(\phi)$ as shown in Fig. 4.10.

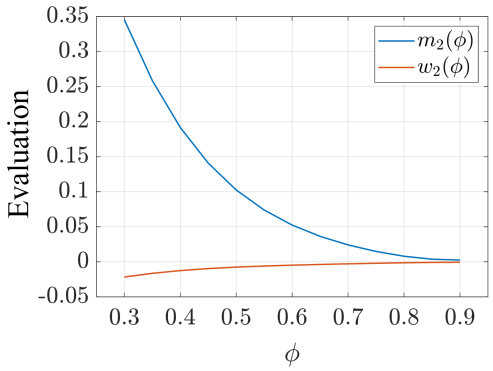

Figure 4.10: Dependence of $m_2(\phi)$ and $w_2(\phi)$ on porosity ϕ, when $x_\infty = 0$.

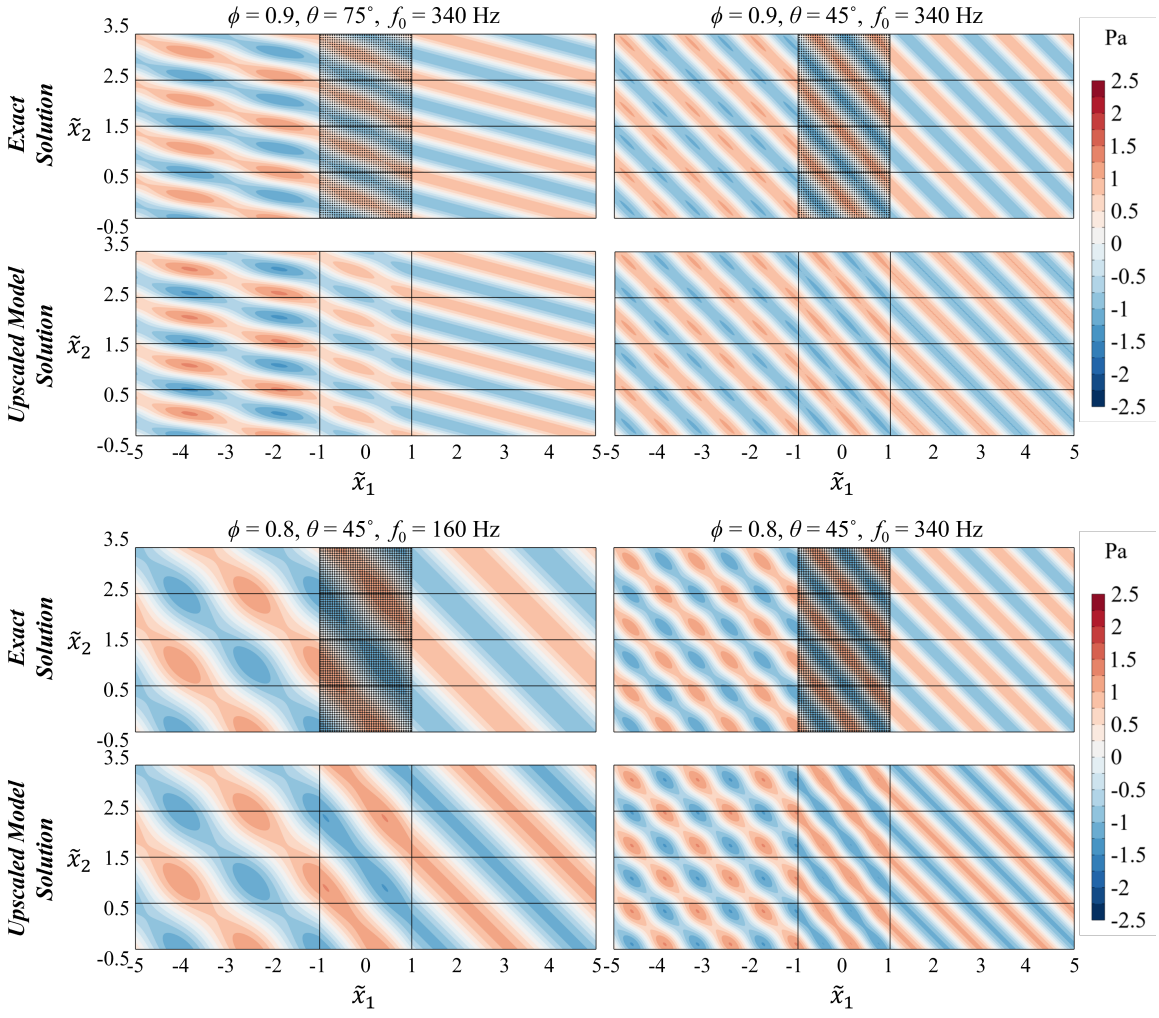

Figure 4.11: Comparison of total pressure field between the exact numerical solution and the upscaled model solution with effective jump conditions incorporated. High porosity cases.

4.2.3. Assessment of the validity of the interface model

To validate the proposed interface model and assess its accuracy across various porosity and incident wave scenarios, we conducted a series of numerical simulations, using the Pressure Acoustics module in COMSOL Multiphysics. The following subsections present detailed comparisons of pressure fields for representative cases. Both the jump conditions (4.46) and the bulk-region upscaled model (4.8) are implemented in numerical simulations.

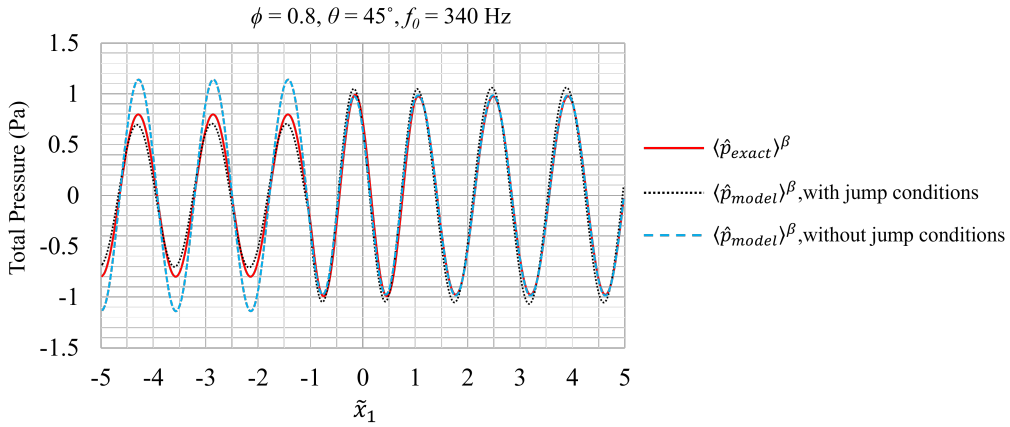

Figure 4.12: Comparison of intrinsic-averaged total pressure along $\tilde{x}_2 = 0$. $\phi = 0.8, \theta = 45^{\circ}$, $f_0 = 340$ Hz.

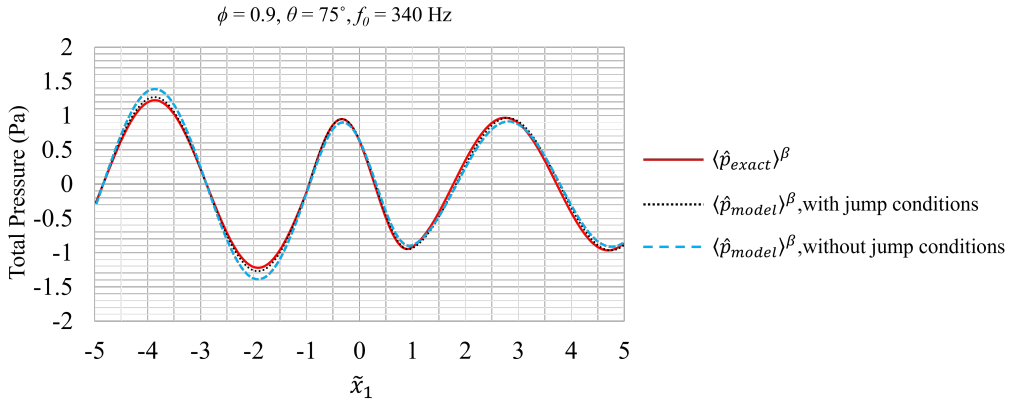

Figure 4.13: Comparison of intrinsic-averaged total pressure along $\tilde{x}_2 = 0$. $\phi = 0.9, \theta = 75^{\circ}$, $f_0 = 340$ Hz.

Figure 4.11 presents the comparison of the total pressure acoustic field for selected cases with porosities $\phi = 0.8$ and $\phi = 0.9$, from Fig. 4.3. The results clearly show that incorporating the jump conditions at the interface enhances the accuracy of the predicted pressure field, especially in the free field on the left-hand side and in the porous material. This shows that

our interface model successfully captures the complex interactions at the interface. Figures 4.12 and 4.13 illustrate the intrinsic-averaged total pressure distribution along $\tilde{x}_2 = 0$ for two representative cases: $\phi = 0.8, \theta = 45°, f_0 = 340$ Hz, and $\phi = 0.9, \theta = 75°, f_0 = 340$ Hz. The comparison highlights that for high-porosity materials, the total pressure predictions are substantially more accurate when the interface jump conditions are incorporated.

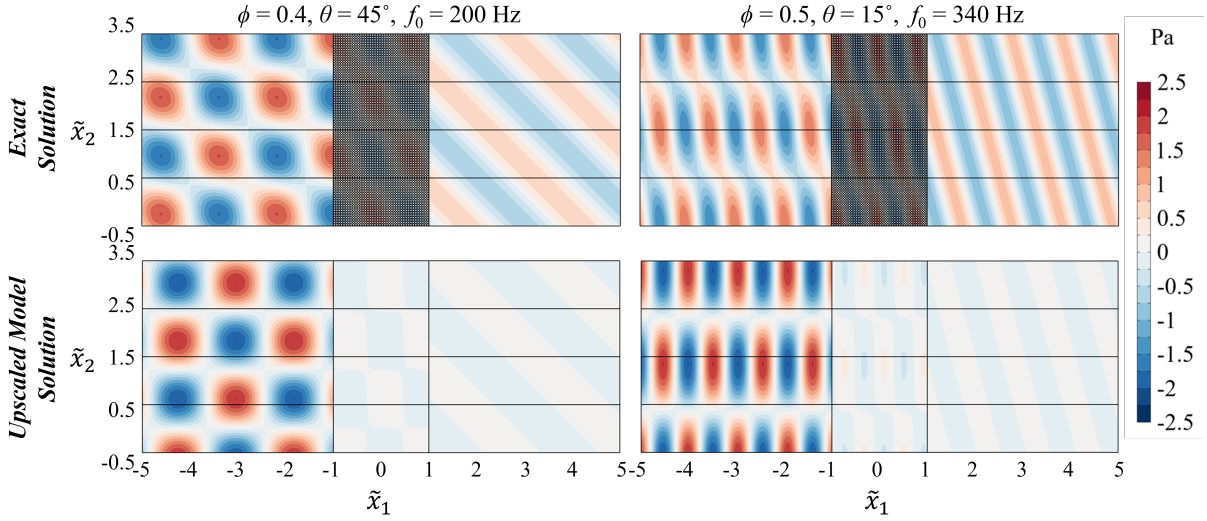

Figure 4.14: Comparison of total pressure field between the exact numerical solution and the upscaled model solution with effective jump conditions incorporated. Low porosity cases.

Figure 4.14 shows the total pressure field of two cases of low porosity: $\phi = 0.4, \theta = 45°, f_0 = 200$ Hz, and $\phi = 0.5, \theta = 15°, f_0 = 340$ Hz. The comparison reveals that the interface model tends to mispredict the phase of the reflected waves in these low-porosity cases, leading to poor agreement with the expected results. Consequently, this results in significantly reduced transmission in the free-field region on the right side. The comparison of scattered pressure along $\tilde{x}_2 = 0$ shown in Fig. 4.15 confirm this.

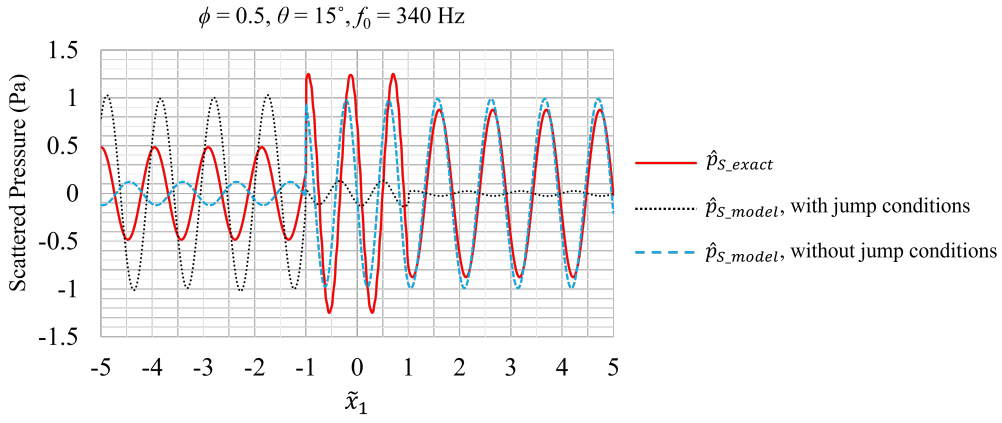

Figure 4.15: Comparison of scattered pressure along $\tilde{x}_2 = 0$. $\phi = 0.5, \theta = 15°, f_0 = 340$ Hz.

In order to assess the effectiveness of the interface jump conditions, we define a global error $\mathcal{E}$ as follows,

$$\mathcal{E} = \frac{1}{L_{tot}} \int_{L_{tot}} \left(\frac{\langle \hat{p}_{exact} \rangle^{\beta} - \langle \hat{p}_{model} \rangle^{\beta}}{Amp(\hat{p}_{inc})} \right)^2 \mathrm{d}\tilde{x}_1, \tag{4.47}$$

where L_{tot} is the horizontal dimension of the computational field, excluding the perfectly matched layers. The intrinsic average of total pressure amplitude is evaluated in each unit cell at the centerline of the computational field. The prediction deviation of the total pressure is normalized by the amplitude of the incident wave, $Amp(\hat{p}_{inc}) = 1$ Pa.

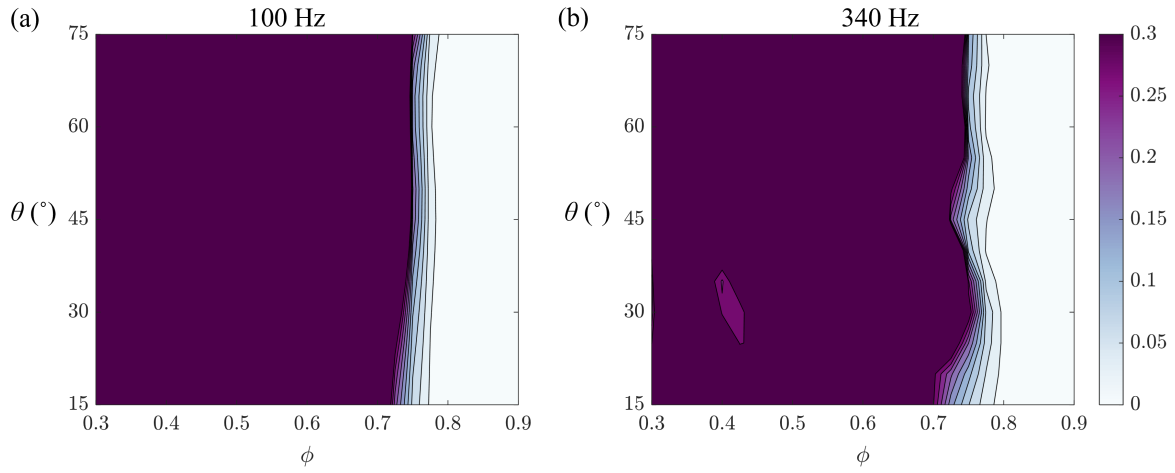

Figure 4.16: Global error $\mathcal{E}$ dependence on the porosity ϕ and incidence angle θ. (a) $f_0 = 100$ Hz; (b) $f_0 = 340$ Hz.

Figure 4.16 illustrates how the global error $\mathcal{E}$ depends on the porosity and incident angle θ for incident waves at frequencies of 100 Hz and 340 Hz. The results demonstrate that the implementation of the interface model yields accurate predictions of the pressure field for porous materials with high porosity ($\phi \geq 0.8$), with the global error $\mathcal{E} < 0.05$. Conversely, for materials with lower porosity, the global error increases notably, suggesting that the interface model's performance is more sensitive to the material's porosity than to the frequency of the incident plane wave. The strong dependence on the size of the solid inclusions and on the distance between neighbouring inclusions in the porous medium lies probably in the fact that homogenization theory can model the behaviour in the inhomogeneous region only provided that the wave scattered by each elementary cylinder vanishes within a distance of order l, the size of the unit cell, from the centre of each cylinder (Hu and Chan, 2005). When the porosity is low, this is hardly the case, and this is correlated to the rapid increase above 1 of the refractive index $\mathcal{R}$, with the solid fraction $\phi_s = 1 - \phi$ (Mei and Vernescu, 2010).

From the above comparisons, we can conclude that the interface jump condition model is particularly well-suited for accurately modelling wave propagation in highly porous materials across a range of incident angles and at relatively low frequencies.

4.3. ACOUSTIC PROPAGATION THROUGH AN ARRAY OF RIGID INCLUSIONS

In this section, an upscaled model for the inviscid propagation of acoustic waves through a regular array of rigid circular cylinders is proposed. The experimental data used in this section is obtained by the PhD student Charitha Vaddamani in the Marcus Wallenberg Laboratory (MWL) for Sound and Vibration at KTH Royal Institute of Technology.

4.3.1. Development of the upscaled model

The computational domain for numerical simulation of the exact-geometry setup and the upscaled model is shown in Fig. 4.17. The direct numerical simulation uses the geometry from the experimental setup (top). Radiation boundary conditions are applied to both ends of the duct that represent anechoic terminations.

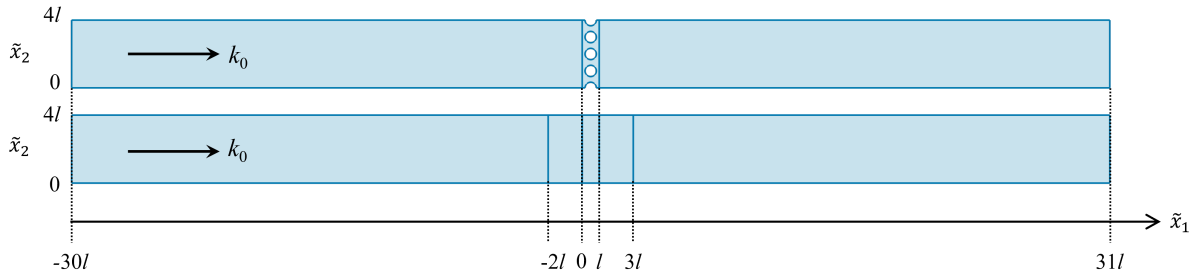

Figure 4.17: Computational domain of exact-geometry direct simulation (top), and of effective domain implemented with the upscaled model.

Figure 4.18 shows the geometries of the investigated domain, the acoustic scatterers, and the unit cell. The lengths l and L are the characteristic microscopic and macroscopic lengths, respectively. The former corresponds to the periodicity of the unit cell (the center-to-center distance of the rigid cylinders), while the latter is, for example, the wavelength of the incident acoustic wave. To ensure the separation of scales, it exists $l \ll L$, i.e. low-frequency waves are considered. As shown in Fig. 4.18, the fluid phase is denoted by β, while the solid phase is σ; the boundary between the fluid and the solid phase is denoted as $\mathcal{A}_{\beta\sigma}$. The unit cell has a total volume equal to V, while the fluid volume is V_β; the cylinder volume is V_σ. The geometry is characterized by the pitch ratio $D_p = d/l$, where d is cylinder diameter. In this problem, the pitch ratio is fixed at $D_p = 2/3$, the same as the experimental setup.

Everywhere in the fluid phase, the acoustic pressure field is governed by the Helmholtz

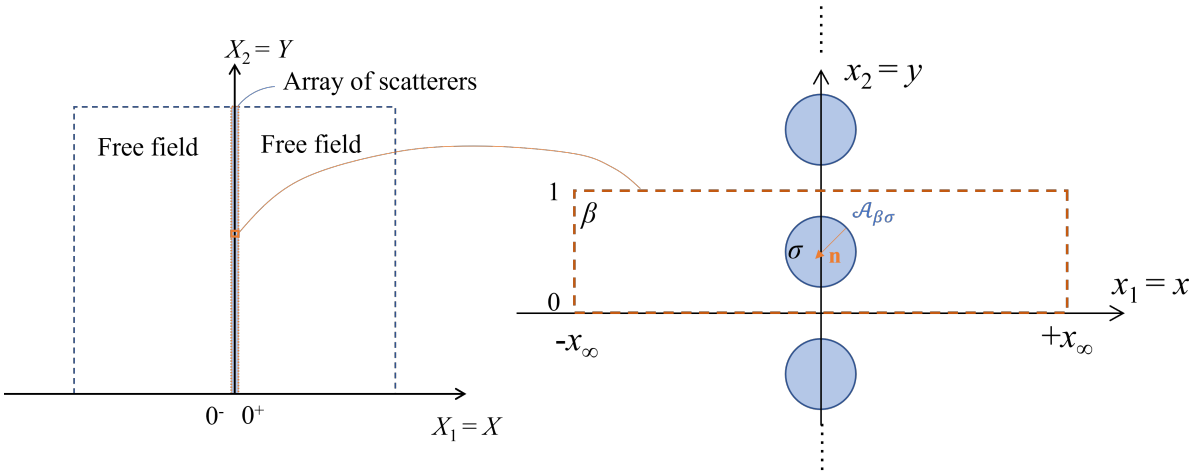

Figure 4.18: The geometries of an array of rigid cylinders acting as a membrane with a close-up of a periodic, rectangular unit cell. The unit normal vector $\mathbf{n}$ points away from the β-phase.

equation along with the acoustically rigid boundary condition at the cylinder surface, as below

$$\tilde{k}^2\tilde{p} + \frac{\partial^2\tilde{p}}{\partial\tilde{x}_i^2} = 0, \quad \text{in } V_\beta, \tag{4.48a}$$

$$\frac{\partial\tilde{p}}{\partial\tilde{x}_i}n_i = 0, \quad \text{at } \mathcal{A}_{\beta\sigma}. \tag{4.48b}$$

where n_i is the vector normal to the surface $\mathcal{A}_{\beta\sigma}$ and pointing outwards the β-phase, and $\tilde{}$ marks the dimensional quantities. $\tilde{k} = \omega/c_s$ is the wave number of the incident acoustic wave. Furthermore, continuous condition is enforced between the outer free field (denoted by superscript O) and the inner-region (denoted by superscript I), as

$$\tilde{p}^I(x = \pm x_\infty) = \tilde{p}^O(X = 0^\pm). \tag{4.49}$$

In this problem, the long-wave assumption is used, i.e. $\tilde{k} \sim \mathcal{O}(1/L)$. To reformulate the problem in dimensionless form the following variables are introduced:

$$p = \frac{\tilde{p}}{\Delta\tilde{p}_{ref}}, \quad k = \tilde{k}L, \quad \epsilon = \frac{l}{L}, \quad X_i = \tilde{k}\frac{\tilde{x}_i}{L}. \tag{4.50}$$

x_i and X_i are dimensionless microscopic and macroscopic spatial variables, respectively. They are assumed to be independent so that the chain rule allows to write

$$\frac{\partial}{\partial\tilde{x}_i} = \frac{1}{l}\frac{\partial}{\partial x_i} + \frac{1}{L}\frac{\partial}{\partial X_i}. \tag{4.51}$$

Equations (4.48) in dimensionless form then become

$$\epsilon^2k^2p + \left(\frac{\partial^2p}{\partial x_i^2} + 2\epsilon\frac{\partial^2p}{\partial x_i\partial X_i} + \epsilon^2\frac{\partial^2p}{\partial X_i^2}\right) = 0, \quad \text{in } V_\beta, \tag{4.52a}$$

$$\left(\frac{\partial p}{\partial x_i} + \epsilon\frac{\partial p}{\partial X_i}\right)n_i = 0, \quad \text{at } \mathcal{A}_{\beta\sigma}; \tag{4.52b}$$

applying the power series expansions

$$p = p_0 + \epsilon p_1 + \epsilon^2 p_2 + \mathcal{O}(\epsilon^3) \tag{4.53}$$

to Eq. (4.52) and then collecting like-order terms, yields the problems which follow at different orders.

Order ϵ^0

$$\frac{\partial^2 p_0}{\partial x_i^2} = 0, \quad \text{in } V_\beta, \tag{4.54a}$$

$$\frac{\partial p_0}{\partial x_i} n_i = 0, \quad \text{at } \mathcal{A}_{\beta\sigma}, \tag{4.54b}$$

$$p_0 = p^O, \quad \text{at } x = \pm x_\infty. \tag{4.54c}$$

From Eq. (4.54), it is simple to see that the leading order pressure, p_0, depends only on the spatial macroscale, i.e.

$$p_0 = p_0(X_i) \tag{4.55}$$

Order ϵ^1

$$\frac{\partial^2 p_1}{\partial x_i^2} = 0, \quad \text{in } V_\beta, \tag{4.56a}$$

$$\frac{\partial p_1}{\partial x_i} n_i = -\frac{\partial p_0}{\partial X_i} n_i, \quad \text{at } \mathcal{A}_{\beta\sigma}, \tag{4.56b}$$

$$p_1 = 0, \quad \text{at } x = \pm x_\infty. \tag{4.56c}$$

The solution for p_1 can be expressed separating variables as

$$p_1 = -s_j \frac{\partial p_0}{\partial X_j}; \tag{4.57}$$

the closure variable s_j depends only on the microscale spatial variables and stems from the solution of the following auxiliary problem in the unit cell:

$$\frac{\partial^2 s_j}{\partial x_i^2} = 0, \quad \text{in } V_\beta, \tag{4.58a}$$

$$\frac{\partial s_j}{\partial x_i} n_i = n_j, \quad \text{at } \mathcal{A}_{\beta\sigma}, \tag{4.58b}$$

$$s_j \text{ periodic along } y \tag{4.58c}$$

$$s_j = 0, \quad \text{at } x = \pm x_\infty. \tag{4.58d}$$

Order ϵ^2

$$k^2 p_0 + \frac{\partial^2 p_2}{\partial x_i^2} + 2\frac{\partial^2 p_1}{\partial x_i \partial X_i} + \frac{\partial^2 p_0}{\partial X_i^2} = 0, \quad \text{in } V_\beta, \tag{4.59a}$$

$$\frac{\partial p_2}{\partial x_i} n_i = -\frac{\partial p_1}{\partial X_i} n_i, \quad \text{at } \mathcal{A}_{\beta\sigma}, \tag{4.59b}$$

$$p_1 = 0, \quad \text{at } x = \pm x_\infty. \tag{4.59c}$$

Taking the superficial average, (4.6a), of Eq (4.59a), we obtain the equation of leading order pressure:

$$\xi_{ij}\frac{\partial^2 p_0}{\partial X_i \partial X_j} + \frac{k^2}{\phi} p_0 = 0, \tag{4.60}$$

with

$$\xi_{ij} = \langle -2\frac{\partial s_i}{\partial x_j} + \frac{\partial s_j}{\partial x_k}\frac{\partial s_i}{\partial x_k} + \delta_{ij}\rangle. \tag{4.61}$$

Note that although the form of the tensor ξ_{ij} is similar to Eq. (4.40), the effective tensor for a homogeneous porous material, in the current problem, the tensor is evaluated in a different unit cell.

4.3.2. Solution of the auxiliary problems and effective coefficients

The auxiliary problem, Eqs. (4.58), is solved in a unit cell for various choices of unit cell sizes (x_∞). An example of the solution field is shown in Fig. 4.19. The effective coefficient, tensor ξ_{ij} is evaluated using Eqs. (4.61). The evaluation reveals that ξ_{ij} is a diagonal tensor. The variations of ξ_{11}, ξ_{22} respect to x_∞ is shown in Fig. 4.20.

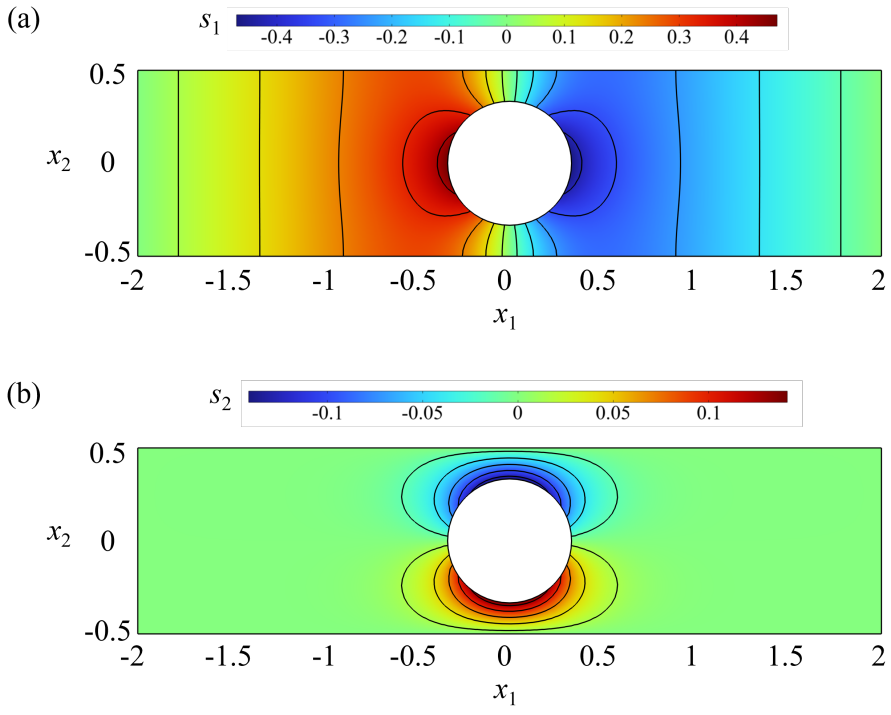

Figure 4.19: Example solution of auxiliary problem for s_j. $x_\infty = 2$.

As observed, the values of ξ_{11}, ξ_{22} asymptotically reach towards 1 as the chosen size of the unit cell becomes larger. It describes that choosing an infinitely large unit cell is not suitable as

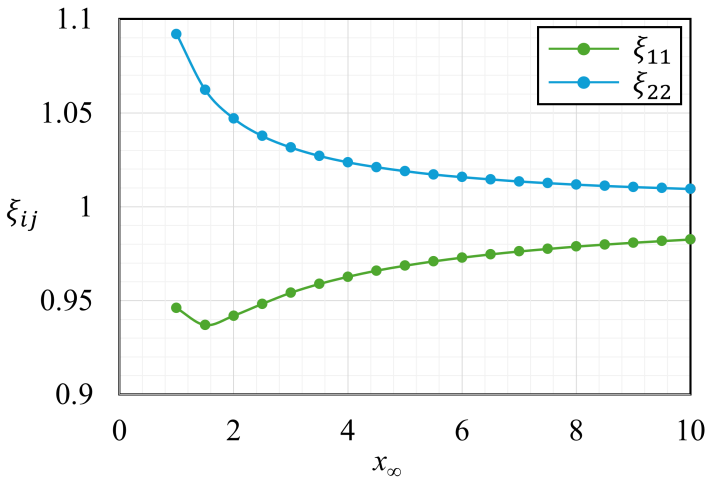

Figure 4.20: Dependence of ξ_{ij} on the unit cell size x_∞.

it gives the field as if the rigid inclusions are invisible. The choice of x_∞ should be large enough to contain the information of the evanescent pressure field in the vicinity of the rigid inclusions and not so large that the microscopic physics is diluted.

4.3.3. Reflection and transmission coefficients

The PDE coefficient module in COMSOL Multiphysics is used to solve the Helmholtz equation for the direct simulation case and a modified Helmholtz equation for the case implemented with the upscaled model. The simulation implemented with the upscaled model uses an effective domain from $-2l \leq \tilde{x}_1 \leq 3l$, as shown in Fig. 4.17. The incident plane wave comes from the left end and hits the rigid inclusion region in the normal direction. We evaluated the cases where incident wave frequency ranges in 100 Hz $\leq f_0 \leq$ 2000 Hz.

We considered the rigid inclusions as a slab of thickness l and evaluated the reflection and transmission coefficient using a transfer matrix method. The transfer matrix method relates the acoustic pressure $\tilde{p}$ and the normal acoustic velocity $\tilde{u}$ between the left- ($\tilde{x}_1 = 0$) and right-hand-side ($\tilde{x}_1 = l$) surfaces of the slab, using a transfer matrix as below,

$$\begin{pmatrix} \tilde{p}(0) \\ \tilde{u}(0) \end{pmatrix} = \begin{pmatrix} \mathbf{T}_{11} & \mathbf{T}_{12} \\ \mathbf{T}_{21} & \mathbf{T}_{22} \end{pmatrix} \begin{pmatrix} \tilde{p}(l) \\ \tilde{u}(l) \end{pmatrix}, \tag{4.62}$$

where the vectors are called the state vectors.

Using the two-port theory, the acoustic pressure and velocity at $\tilde{x}_1 = 0$ and $\tilde{x}_1 = l$ are evaluated twice, for the incident wave coming from left end and from the right end, and the transfer matrix can be calculated by

$$\begin{pmatrix} \mathbf{T}_{11} & \mathbf{T}_{12} \\ \mathbf{T}_{21} & \mathbf{T}_{22} \end{pmatrix} = \begin{pmatrix} \tilde{p}(0)_1 & \tilde{p}(0)_2 \\ \tilde{u}(0)_1 & \tilde{u}(0)_2 \end{pmatrix} \begin{pmatrix} \tilde{p}(l)_1 & \tilde{p}(l)_2 \\ \tilde{u}(l)_1 & \tilde{u}(l)_2 \end{pmatrix}^{-1}, \tag{4.63}$$

where the subscripts "1" and "2" represent the two measurements, respectively. Fig. 4.21 shows the absolute values of the transfer matrix obtained by simulations. As observed, in the upscaled model, the transfer matrix satisfies,

$$\mathbf{T}_{11} = \mathbf{T}_{22} = 1, \tag{4.64}$$

which coincides with the fact that the geometry of the rigid inclusions is isotropic. For isotropic materials, the transfer matrix has properties of reciprocity and symmetry (Song and Bolton, 2000). However, the full-geometry assessment shows different results, which implies the acoustic scattering is not symmetrical from both sides.

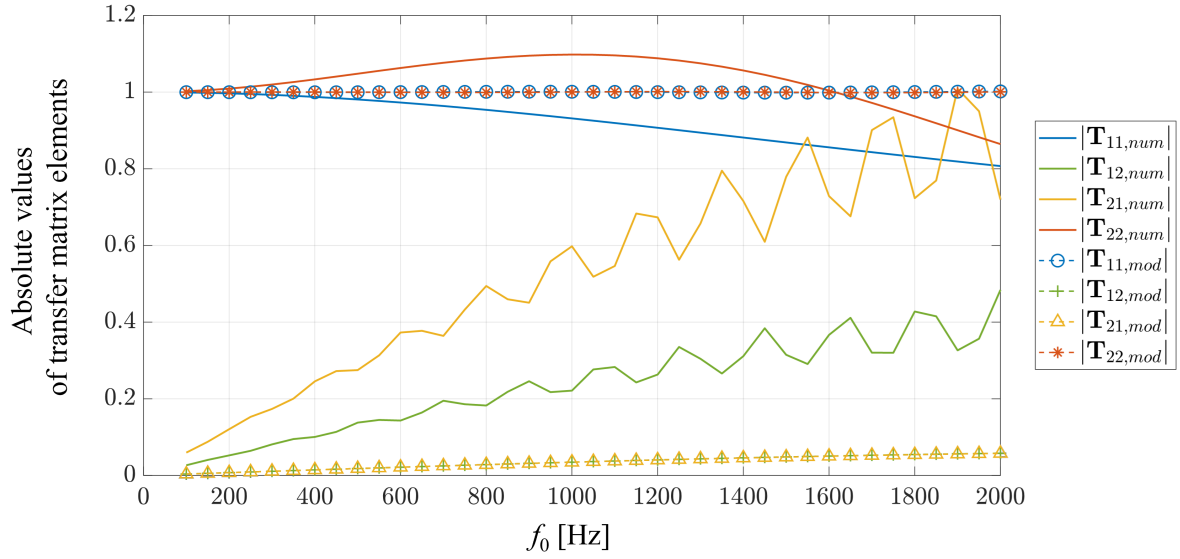

Figure 4.21: Absolute values of transfer matrix elements, comparisons of direct numerical simulation (num), and upscaled model solution (mod).

The incident wave applied has an amplitude of 1. On the left-hand side, there is,

$$\tilde{p}(0) = 1 + R, \tag{4.65}$$

where R is the reflection coefficient. The transmission coefficients can be calculated based on the transfer matrix (Song and Bolton, 2000), by

$$T = \frac{2\mathrm{e}^{\mathrm{i}k_0 l}}{T_{11} + (T_{12}/Z_0) + Z_0 T_{21} + T_{22}}, \tag{4.66}$$

where Z_0 is the characteristic impedance of air given by

$$Z_0 = \frac{1 - R}{\tilde{u}(0)}. \tag{4.67}$$

The absolute values of R and T at various frequencies are shown in Fig. 4.22. The comparison between the experimental measurements and the direct numerical simulation results shows

the effects of dissipation in the system, such as viscosity and boundary losses. The comparison also shows that the agreement of the upscaled model with the experiment is good in the lower frequency range, and the agreement is poorer as the frequency increases. This is because the lengthscale separation condition ϵ increases up to around 0.2 as the incident wavelength decreases.

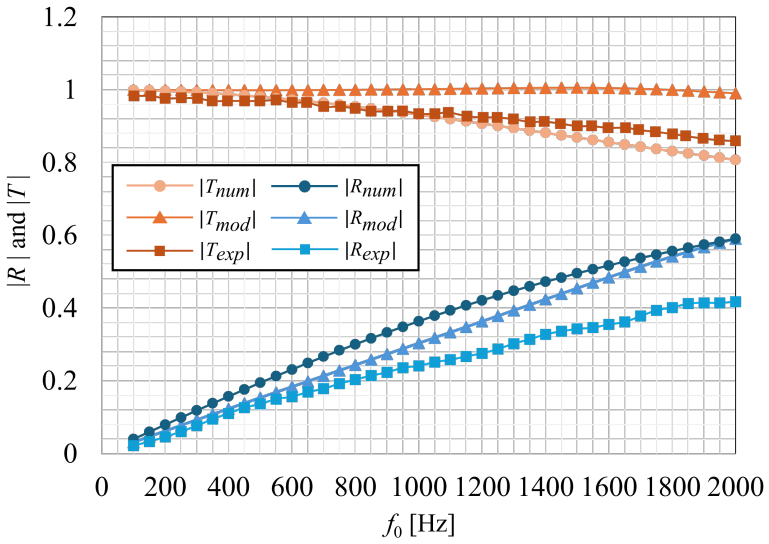

Figure 4.22: Comparisons of reflection and transmission coefficients among experimental measurements (exp), direct numerical simulation (num), and upscaled model solution (mod).

4.4. CONCLUSIONS

This chapter investigated the acoustic propagation properties of noise passive control devices, such as porous materials and perforated plates, using the homogenization approach.

In the first part of the chapter, we developed an effective jump condition at the interface between a free air region and a porous material using an asymptotic homogenization approach. Our results demonstrated that classical homogenization, which assumes an infinitely extended porous medium, fails to accurately model interface behaviour. By incorporating interface-specific jump conditions, the new model significantly improved the prediction of acoustic pressure fields for high-porosity materials, capturing the crucial reflection effect at the interface region. However, for materials with lower porosity, the current model struggles to accurately capture reflected wave behaviour, resulting in reduced accuracy and transmission. This limitation is closely related to the structural configuration of the porous medium. In low-porosity regimes, the assumptions of homogenization theory become less valid—specifically, the scattered wave field from each inclusion does not decay sufficiently within the characteristic cell size. These findings highlight the importance of considering porosity effects when applying the interface model and motivate further refinement for low-porosity scenarios.

In the second part, we extended the homogenization framework to a single array of rigid cylindrical inclusions by introducing an effective slab domain of finite thickness. The resulting upscaled model was used to calculate reflection and transmission coefficients, which were then validated against experimental data. The model exhibited strong agreement with measurements at low frequencies, affirming its validity within the long-wavelength regime. However, as frequency increased and the wavelength approached the microstructural scale, deviations emerged due to the breakdown of scale separation—a key assumption of homogenization approach.

万物并作，吾以观复。夫物芸芸，各复归其根。

——《道德经》

"I observe all things flourish and thrive, then yet each returns to its origin."

SUMMARY AND OUTLOOKS

This dissertation addresses the problem of thermoacoustic instabilities from three perspectives, mainly with adjoint methods: (1) modelling and prediction of nonlinear dynamics in thermoacoustic systems; (2) identification of mean-flow uncertainties and potential feedback control approaches with adjoint-based sensitivity analysis, and (3) effective acoustic models of passive control devices involving hierarchy length scales. The summary of findings and the outlooks of each project are listed in this chapter.

5.1. PREDICTION OF THERMOACOUSTIC INSTABILITIES WITH AGF APPROACH

A comprehensive theoretical framework based on the adjoint Green's function (AGF) is developed to predict thermoacoustic instabilities in non-self-adjoint systems, specifically with mean flow. The main findings are listed below:

- The reciprocity property of a non-self-adjoint direct Green's function and its AGF are derived based on the Lagrange-Green's identity, which is later used to find the solution of AGF analytically. The solution of the AGF represents the receptivity of the unforced system to external forcings.

- In the cases studied, the nonlinearity of the system lies in the amplitude-dependent heat release model. The AGF model predicts rich nonlinear dynamics of the examined systems, such as bifurcations, saturation, and hysteresis.

- The inclusion of mean flow modifies both the heat release model and the AGF, exhibiting a stabilizing effect in thermoacoustic systems. In addition, it significantly reduces noise-induced effects compared to systems without mean flow.

- For a flow-duct system, the boundary condition of zero-net acoustic power through the open outlet is more accurate compared to the zero-pressure-disturbance condition.

- The mean temperature change across the compact flame strongly affects heat-driven oscillation frequencies. An increased temperature difference leads to higher oscillation frequencies. Hysteresis behaviour is observed when the hot region temperature rises and then decreases.

- The presence of external noise, both pink noise and white noise, can possibly reduce the transient time needed to reach the limit cycle by changing the disturbance amplitude. Increasing the noise level increases the possibility of the extent of reduction to transient time.

- Pink noise is more effective in triggering instability from an initial stable state near a system stability margin, as compared to white noise.

The AGF framework can be potentially extended to systems with more complex geometries. For such cases, a numerical scheme utilizing backward marching in time can be employed to solve the AGF; thereby, calculations for direct Green's function can be bypassed.

Additionally, the framework can be applied to systems incorporating multiple external sources or feedback control devices. Devices such as quarter-wave resonators and Helmholtz resonators can be modelled as an additional acoustic resonator system. The local oscillation in the thermoacoustic system, where the control device is applied, acts as an external forcing of the feedback device system. The acoustic field within the feedback devices can be modelled by the AGF approach. In return, the acoustic oscillation from the feedback control device acts on the thermoacoustic system. The AGF approach can enable a comprehensive treatment of the entire system as a network of coupled oscillators. This perspective provides a more integrated approach to analysing and controlling thermoacoustic instabilities in practical applications.

5.2. ADJOINT-BASED SENSITIVITY ANALYSIS FRAMEWORK

Three types of adjoint sensitivities are calculated for a gas turbine combustor prototype, focusing on the two most unstable modes. The work provides a framework for explaining errors and uncertainty quantification in a thermoacoustic system and for suggesting effective control strategies for stabilizing unstable modes.

- Base-state sensitivity highlights how uncertainties in base flow parameters, like premixer cold gas conditions, significantly impact the growth rates of the eigenmodes.
- Structural sensitivity to steady feedback forcings uncovers steady control strategies such as local mass suction and heating as effective stabilizing mechanisms.
- Structural perturbation sensitivity identifies potential stabilizing feedback control devices with small energy amplitude, and pinpoints their optimal placement.

Optimization with feedback devices can be applied based on the structural sensitivity results with an iterative scheme.

5.3. UPSCALED MODELS OF ACOUSTIC PROPAGATION THROUGH POROUS MATERIAL

We investigated the acoustic propagation properties of noise control devices using the homogenization approach, focusing on porous materials and thin rigid inclusions.

- An effective jump condition for acoustics at the interface between free air and porous materials successfully captures reflection effects, which are not accounted for in classical

homogenization methods, significantly improving the prediction accuracy of the pressure field, particularly for high porosity materials.

- An upscaled model was developed for acoustic propagation through a rigid cylinder array, treated as a slab with a chosen thickness. The reflection and transmission coefficients of the thin rigid inclusions were validated against experimental data, showing good agreement at lower frequencies.

Future extensions of these models could incorporate thermal and viscous dissipation effects, as well as the fluid flow in the system.

APPENDIX FOR CHAPTER 2

A.1. THE DIRECT GREEN'S FUNCTION FOR A UNIFORM-TEMPERATURE FLOW DUCT

We consider the same flow-duct as in Fig. A.1, but replace the unsteady heat source with a hypothetical point source, which is situated at position x' and emits an impulsive acoustic signal at time t'.

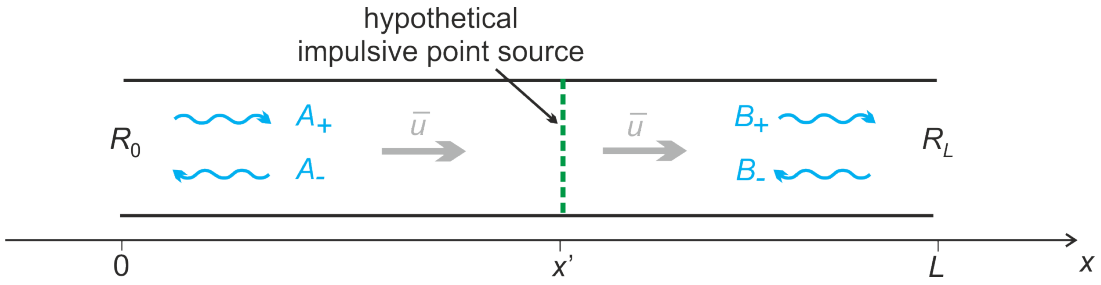

Figure A.1: Configuration considered for the calculation of the direct Green's function.

The direct Green's function is the impulse response, i.e. the acoustic field generated by the hypothetical point source and measured by an observer at position x and time t. Its governing equations are (2.21)-(2.23), together with the boundary conditions given in terms of the reflection coefficients R_0 and R_L. These equations are solved in two steps. Section A.1.1. shows the first step, which leads to an expression of the direct Green's function in the frequency domain. This is transformed into the time domain in the second step, which is detailed in Section A.1.2..

A.1.1. Frequency-domain analysis

Recall the governing equation (2.25) for the direct Green's function $\hat{g}(x, x', \omega)$ in the frequency-domain is

$$\omega^2 \hat{g}(x, x', \omega) + 2\bar{u}(\mathrm{i}\omega)\frac{\partial \hat{g}}{\partial x} + (c^2 - \bar{u}^2)\frac{\partial^2 \hat{g}}{\partial x^2} = -\delta(x - x'). \tag{A.1}$$

A suitable trial solution is provided by Eq. (2.26), which gives $\hat{g}(x, x', \omega)$ by two expressions: one for the region $0 < x < x'$ (upstream side of the source), and one for $x' < x < L$ (downstream side). We can convert Eq. (2.26) into a single expression by using the Heaviside functions $H(x' - x)$ and $H(x - x')$,

$$\begin{aligned}\hat{g}(x, x', \omega) =& H(x' - x)A_-(x', \omega)[R_0 \mathrm{e}^{\mathrm{i}k_+ x} + \mathrm{e}^{-\mathrm{i}k_- x}] + \\ & H(x - x')B_+(x', \omega)[\mathrm{e}^{\mathrm{i}k_+(x-L)} + R_L \mathrm{e}^{-\mathrm{i}k_-(x-L)}].\end{aligned} \tag{A.2}$$

The differentiation, using

$$\frac{\partial H(x-x')}{\partial x} = \delta(x-x'), \quad \text{and} \quad \frac{\partial H(x'-x)}{\partial x} = -\delta(x-x'), \tag{A.3}$$

yields

$$\begin{aligned}\frac{\partial \hat{g}}{\partial x} =& -\delta(x-x')A_-[R_0\mathrm{e}^{\mathrm{i}k_+x} + \mathrm{e}^{-\mathrm{i}k_-x}] \\ &+ H(x'-x)A_-[\mathrm{i}k_+R_0\mathrm{e}^{\mathrm{i}k_+x} - \mathrm{i}k_-\mathrm{e}^{-\mathrm{i}k_-x}] \\ &+ \delta(x-x')B_+[\mathrm{e}^{\mathrm{i}k_+(x-L)} + R_L\mathrm{e}^{-\mathrm{i}k_-(x-L)}] \\ &+ H(x-x')B_+[\mathrm{i}k_+\mathrm{e}^{\mathrm{i}k_+(x-L)} - R_L\mathrm{i}k_-\mathrm{e}^{-\mathrm{i}k_-(x-L)}]\end{aligned} \tag{A.4}$$

and

$$\begin{aligned}\frac{\partial^2 \hat{g}}{\partial x^2} =& -\delta'(x-x')A_-[R_0\mathrm{e}^{\mathrm{i}k_+x} + \mathrm{e}^{-\mathrm{i}k_-x}] \\ &- 2\delta(x-x')A_-[\mathrm{i}k_+R_0\mathrm{e}^{\mathrm{i}k_+x} - \mathrm{i}k_-\mathrm{e}^{\mathrm{i}k_-x}] \\ &- H(x'-x)A_-[k_+^2R_0\mathrm{e}^{\mathrm{i}k_+x} + k_-^2\mathrm{e}^{-\mathrm{i}k_-x}] \\ &+ \delta'(x-x')B_+[\mathrm{e}^{\mathrm{i}k_+(x-L)} + R_L\mathrm{e}^{-\mathrm{i}k_-(x-L)}] \\ &+ 2\delta(x-x')B_+[\mathrm{i}k_+\mathrm{e}^{\mathrm{i}k_+(x-L)} - \mathrm{i}k_-R_L\mathrm{e}^{-\mathrm{i}k_-(x-L)}] \\ &- H(x-x')B_+[k_+^2\mathrm{e}^{\mathrm{i}k_+(x-L)} + k_-^2R_L\mathrm{i}k_-\mathrm{e}^{-\mathrm{i}k_-(x-L)}].\end{aligned} \tag{A.5}$$

The expressions (A.2), (A.4) and (A.5) are substituted into Eq. (A.1). The resulting equation contains several terms, which multiply the Heaviside functions $H(x'-x)$ and $H(x-x')$. These terms cancel because k_+ and k_- satisfy

$$(c^2-\bar{u}^2)k_\pm^2 \pm 2\bar{u}\omega k_\pm - \omega^2 = 0, \tag{A.6}$$

which is a consequence of the fact that k_+ and k_- occur in the solution of Eq. (2.8). This leaves Eq. (A.1) now as,

$$\begin{aligned}&\delta(x-x')\Bigg[-2\mathrm{i}\omega\bar{u}A_-\left(R_0\mathrm{e}^{\mathrm{i}k_+x} + \mathrm{e}^{-\mathrm{i}k_-x}\right) + 2\mathrm{i}\omega\bar{u}B_+\left[\mathrm{e}^{\mathrm{i}k_+(x-L)} + R_L\mathrm{e}^{-\mathrm{i}k_-(x-L)}\right] \\ &-2(c^2-\bar{u}^2)A_-\left(\mathrm{i}k_+R_0\mathrm{e}^{\mathrm{i}k_+x} - \mathrm{i}k_-\mathrm{e}^{-\mathrm{i}k_-x}\right) \\ &+2(c^2-\bar{u}^2)B_+\left[\mathrm{i}k_+\mathrm{e}^{\mathrm{i}k_+(x-L)} - \mathrm{i}k_-R_L\mathrm{e}^{-\mathrm{i}k_-(x-L)}\right]\Bigg] \\ &+\delta'(x-x')\Bigg[-A_-(c^2-\bar{u}^2)\left(R_0\mathrm{e}^{\mathrm{i}k_+x} + \mathrm{e}^{-\mathrm{i}k_-x}\right) \\ &+B_+(c^2-\bar{u}^2)\left[\mathrm{e}^{\mathrm{i}k_+(x-L)} + R_L\mathrm{e}^{-\mathrm{i}k_-(x-L)}\right]\Bigg] = -\delta(x-x').\end{aligned} \tag{A.7}$$

It is convenient to integrate this equation now, knowing that for any smooth function $h(x)$, the following identities hold,

$$\int_{-\infty}^{+\infty}\delta(x-x')h(x)dx = h(x'), \tag{A.8}$$

and

$$\int_{-\infty}^{+\infty} \delta'(x-x')h(x)dx = -\int_{-\infty}^{+\infty} \delta(x-x')h'(x)dx = -h'(x'). \tag{A.9}$$

Then

$$\begin{aligned}
&-2\mathrm{i}\omega\bar{u}A_-[R_0\mathrm{e}^{-\mathrm{i}k_-x'} + \mathrm{e}^{-\mathrm{i}k_-x'}] + 2\mathrm{i}\omega\bar{u}B_+[\mathrm{e}^{\mathrm{i}k_+(x'-L)} + R_L\mathrm{e}^{-\mathrm{i}k_-(x'-L)}] \\
&-A_-(c^2-\bar{u}^2)[\mathrm{i}k_+R_0\mathrm{e}^{\mathrm{i}k_+x'} - \mathrm{i}k_-\mathrm{e}^{-\mathrm{i}k_-x'}] \\
&+B_+(c^2-\bar{u}^2)[\mathrm{i}k_+\mathrm{e}^{\mathrm{i}k_+(x'-L)} - \mathrm{i}k_-R_L\mathrm{e}^{-\mathrm{i}k_-(x'-L)}] = -1.
\end{aligned} \tag{A.10}$$

This equation can be further simplified by collecting terms with factors A_- and B_+, and subsequently collecting like exponential terms in the coefficients of A_- and B_+. The result is

$$\begin{aligned}
&A_-\Bigg[-\mathrm{e}^{\mathrm{i}k_+x'}R_0\underbrace{[2\mathrm{i}\omega\bar{u} + (c^2-\bar{u}^2)\mathrm{i}k_+]}_{T_+} + \mathrm{e}^{-\mathrm{i}k_-x'}\underbrace{[-2\mathrm{i}\omega\bar{u} + (c^2-\bar{u}^2)\mathrm{i}k_-]}_{T_-}\Bigg] + \\
&B_+\Bigg[\mathrm{e}^{\mathrm{i}k_+(x'-L)}\underbrace{[2\mathrm{i}\omega\bar{u} + (c^2-\bar{u}^2)\mathrm{i}k_+]}_{T_+} - \mathrm{e}^{-\mathrm{i}k_-(x'-L)}R_L\underbrace{[-2\mathrm{i}\omega\bar{u} + (c^2-\bar{u}^2)\mathrm{i}k_-]}_{T_-}\Bigg] \\
&= -1.
\end{aligned} \tag{A.11}$$

The terms labelled T_+ and T_- in Eq. (A.11) can be simplified with the definitions of k_+ and k_- given in Eq. (2.9),

$$T_+ = \mathrm{i}\omega(c+\bar{u}), \quad T_- = \mathrm{i}\omega(c-\bar{u}). \tag{A.12}$$

Equation (A.11) then reduces to

$$\begin{aligned}
&A_-\mathrm{i}\omega[-R_0\mathrm{e}^{\mathrm{i}k_+x'}(c+\bar{u}) + \mathrm{e}^{-\mathrm{i}k_-x'}(c-\bar{u})] \\
&+B_+(\mathrm{i}\omega)[\mathrm{e}^{\mathrm{i}k_+(x'-L)}(c+\bar{u}) - R_L\mathrm{e}^{-\mathrm{i}k_-(x'-L)}(c-\bar{u})] = -1.
\end{aligned} \tag{A.13}$$

This is a linear equation for the amplitude coefficients A_- and B_+. A second equation is needed to close the problem and retrieve the two amplitude coefficients. Since the source represented by $\delta(x-x')$ in Eq. (A.1) describes a one-dimensional monopole, and the pressure (and hence the velocity potential) across such a monopole is continuous, we can impose

$$\lim_{x\to x'^-} \hat{g}(x,x',\omega) = \lim_{x\to x'^+} \hat{g}(x,x',\omega). \tag{A.14}$$

This leads to

$$A_-[-R_0\mathrm{e}^{\mathrm{i}k_+x'} - \mathrm{e}^{-\mathrm{i}k_-x'}] + B_+[\mathrm{e}^{\mathrm{i}k_+(x'-L)} + R_L\mathrm{e}^{-\mathrm{i}k_-(x'-L)}] = 0. \tag{A.15}$$

Equations (A.12) and (A.15) form a 2×2 set of linear equations for A_- and B_+; the main determinant is

$$det = \begin{vmatrix} (\mathrm{i}\omega)[-R_0\mathrm{e}^{\mathrm{i}k_+x'}(c+\bar{u}) + \mathrm{e}^{-\mathrm{i}k_-x'}(c-\bar{u})] & (\mathrm{i}\omega)[\mathrm{e}^{\mathrm{i}k_+(x'-L)}(c+\bar{u}) - R_L\mathrm{e}^{-\mathrm{i}k_-(x'-L)}(c-\bar{u})] \\ -R_0\mathrm{e}^{\mathrm{i}k_+x'} - \mathrm{e}^{\mathrm{i}k_-x'} & \mathrm{e}^{\mathrm{i}k_+(x'-L)} + R_L\mathrm{e}^{-\mathrm{i}k_-(x'-L)} \end{vmatrix} \tag{A.16}$$

This can be simplified to give

$$det = -2(\mathrm{i}\omega)c\,\mathrm{e}^{-\mathrm{i}k_- x'}\mathrm{e}^{\mathrm{i}k_+ x'}\mathrm{e}^{-\mathrm{i}k_+ L}[R_0 R_L \mathrm{e}^{\mathrm{i}(k_+ + k_-)L} - 1]. \tag{A.17}$$

The term in square brackets above is identical to the characteristic function $F(\omega)$ in Eq. (2.16) and this gives

$$det = -2(\mathrm{i}\omega)c\,\mathrm{e}^{\mathrm{i}(k_+ - k_-)x'}\mathrm{e}^{-\mathrm{i}k_+ L}F(\omega). \tag{A.18}$$

The fact that at the eigenfrequencies ω_n of the direct Green's function, $F(\omega_n) = 0$ will be useful in A.1.2..

The equations for A_- and B_+ can now be solved with Cramer's rule,

$$A_- = \frac{det_A}{det}, \quad B_+ = \frac{det_B}{det}, \tag{A.19}$$

where

$$\begin{aligned} det_A &= \begin{vmatrix} -1 & (\mathrm{i}\omega)[\mathrm{e}^{\mathrm{i}k_+(x'-L)}(c+\bar{u}) - R_L\mathrm{e}^{-\mathrm{i}k_-(x'-L)}(c-\bar{u})] \\ 0 & \mathrm{e}^{\mathrm{i}k_+(x'-L)} + R_L\mathrm{e}^{-\mathrm{i}k_-(x'-L)} \end{vmatrix} \\ &= -\mathrm{e}^{\mathrm{i}k_+(x'-L)} - R_L\mathrm{e}^{-\mathrm{i}k_-(x'-L)} \end{aligned} \tag{A.20}$$

$$\begin{aligned} det_B &= \begin{vmatrix} (\mathrm{i}\omega)[-R_0\mathrm{e}^{\mathrm{i}k_+ x'}(c+\bar{u}) + \mathrm{e}^{-\mathrm{i}k_- x'}(c-\bar{u})] & -1 \\ -R_0\mathrm{e}^{\mathrm{i}k_+ x'} - \mathrm{e}^{-\mathrm{i}k'_-} & 0 \end{vmatrix} \\ &= -R_0\mathrm{e}^{\mathrm{i}k_+ x'} - \mathrm{e}^{-\mathrm{i}k_- x'}. \end{aligned} \tag{A.21}$$

This gives

$$A_-(x',\omega) = \frac{1}{2c\mathrm{i}\omega F(\omega)}\mathrm{e}^{-\mathrm{i}(k_+ - k_-)x'}\mathrm{e}^{\mathrm{i}k_+ L}[\mathrm{e}^{\mathrm{i}k_+(x'-L)} + R_L\mathrm{e}^{-\mathrm{i}k_-(x'-L)}], \tag{A.22}$$

$$B_+ = \frac{1}{2c\mathrm{i}\omega F(\omega)}\mathrm{e}^{-\mathrm{i}(k_+ - k_-)x'}\mathrm{e}^{\mathrm{i}k_+ L}[R_0\mathrm{e}^{\mathrm{i}k_+ x'} + \mathrm{e}^{-\mathrm{i}k_- x'}]. \tag{A.23}$$

The amplitude coefficients in Eq. (2.35) are now fully determined. They can be written in a compact form with the abbreviations (in line with Eqs. (2.28) and (2.29))

$$a(x',\omega) = R_0\mathrm{e}^{\mathrm{i}k_+ x'} + \mathrm{e}^{-\mathrm{i}k_- x'}, \tag{A.24a}$$

$$b(x',\omega) = \mathrm{e}^{\mathrm{i}k_+(x'-L)} + R_L\mathrm{e}^{-\mathrm{i}k_-(x'-L)}. \tag{A.24b}$$

Subsequent substitution into Eq. (2.26) yields Eq. (2.27) in the main text. The frequency-domain direct Green's function (2.27) is not reciprocal to itself, i.e. $\hat{g}(x,x',\omega) \neq \hat{g}(x',x,\omega)$, unless $k_+ - k_- = 0$, which is valid only for the case with zero mean flow ($\bar{u} = 0$). The lack of reciprocity may be surprising, but it is plausible for our flow duct: if the source is upstream of the receiver, the emitted sound wave travels with the flow; however if the source and receiver are swapped over, the wave has to travel against the flow.

In its most general sense, the reciprocity principle states that the response of a linear system to a time-harmonic disturbance applied at some point by an external source is invariant with respect to the exchange of source and receiver positions. The principle holds in many problems in continuum mechanics, electricity, magnetism, and optics, and it has seen contributions from

several towering figures in physics and engineering (Masoud and Stone, 2019). However, there are cases, where this principle is broken. One example of a non-reciprocal phenomenon is that of a linear acoustic wave travelling through a moving medium. This is because the term $\bar{u}$ in the governing equation is *time-odd*, i.e. time reversal switches its direction. As discussed by Rasmussen et al. (2021), "reciprocity is restored if the time-odd quantities are reversed along with the source and receiver positions."

A.1.2. Time domain analysis

The time-domain direct Green's function $g(x, x', t - t')$ is calculated from

$$g(x, x', t - t') = \frac{1}{2\pi} \int_{-\infty}^{\infty} \hat{g}(x, x', \omega) \mathrm{e}^{-\mathrm{i}\omega(t-t')} \mathrm{d}\omega. \tag{A.25}$$

It must satisfy causality, i.e. the response must not start before the impulse that triggered it. Hence we have

$$g(x, x', t - t') = 0 \quad \text{for} \quad t - t' < 0. \tag{A.26}$$

For $t - t' > 0$, i.e. after the impulse, we expect the response to be a superposition of modes with frequencies ω_n. We now proceed to calculate this response by evaluating the integral in Eq. (A.25) with the residue theorem.

Equation (2.27) shows that $\hat{g}(x, x', \omega)$ has singularities at $\omega = 0$ and at the Green's function frequencies $\omega = \omega_n$, therefore the integrand in Eq. (A.25) has singularities at the same frequencies. Their position in the complex plane is shown in Figure A.2. For the integration path, we

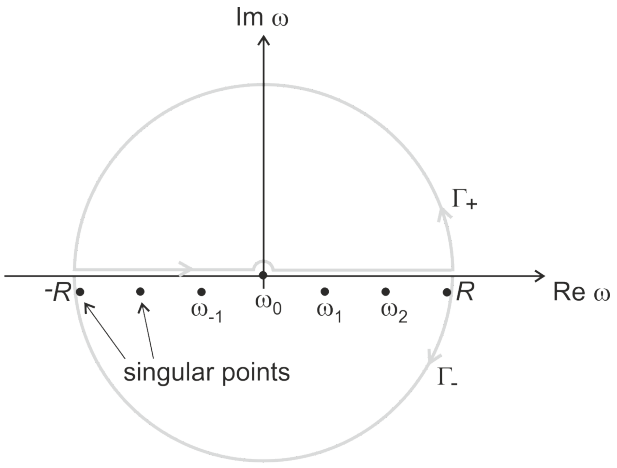

Figure A.2: Singular points in in the complex ω-plane.

choose the closed curve composed of the real axis and the semi-circular arc Γ_- in the lower half-plane; this curve encloses all singular points. Application of the residue theorem gives (the

path is traversed in the negative direction, hence the minus sign in $-2\pi\mathrm{i}$)

$$\begin{aligned}&\int_{-\infty}^{\infty}\hat{g}(x,x',\omega)\mathrm{e}^{-\mathrm{i}\omega(t-t')}\mathrm{d}\omega = \\ &-2\pi\mathrm{i}\sum_{n=-\infty}^{\infty}Res_{\omega_n}[\hat{g}(x,x',\omega)\mathrm{e}^{-\mathrm{i}\omega(t-t')}] \\ &\underbrace{-\lim_{R\to\infty}\int_{\Gamma_-}\hat{g}(x,x',\omega)\mathrm{e}^{-\mathrm{i}\omega(t-t')}\mathrm{d}\omega}_{=0}.\end{aligned} \tag{A.27}$$

The sum in this equation includes the term $n = 0$, which represents the singularity at $\omega_0 = 0$. The integral along Γ_- is zero for $t - t' > 0$ because the exponential function tends to zero as the radius of the semicircle tends to infinity,

$$\mathrm{e}^{-\mathrm{i}\omega(t-t')} = \underbrace{\mathrm{e}^{-\mathrm{i}(\omega_r+\mathrm{i}\omega_i)(t-t')}}_{\text{bounded}}\mathrm{e}^{\omega_i(t-t')} \to 0 \quad \text{as} \quad \omega_i \to -\infty. \tag{A.28}$$

It now remains to calculate the residues of $\hat{g}(x,x',\omega)\mathrm{e}^{-\mathrm{i}\omega(t-t')}$. We introduce the abbreviation

$$\psi(x,\omega) = -\frac{1}{c}\mathrm{e}^{-\mathrm{i}(k_+-k_-)x}\mathrm{e}^{-ik_+L} = -\frac{1}{c}\mathrm{e}^{\mathrm{i}\omega x\frac{2\bar{u}}{c^2-\bar{u}^2}}\mathrm{e}^{-\mathrm{i}\frac{\omega}{c+\bar{u}}L}, \tag{A.29}$$

and use Eq. (2.27) to write the residue term as

$$\hat{g}(x,x',\omega)\mathrm{e}^{-\mathrm{i}\omega(t-t')} = \frac{\mathrm{i}}{2\omega F(\omega)}\begin{cases}\psi(x',\omega)b(x',\omega)a(x,\omega)\mathrm{e}^{-\mathrm{i}\omega(t-t')} & \text{for} \quad x<x' \\ \psi(x',\omega)a(x',\omega)b(x,\omega)\mathrm{e}^{-\mathrm{i}\omega(t-t')} & \text{for} \quad x>x'.\end{cases} \tag{A.30}$$

The general formula for the calculation of the residue of a quotient can be applied,

$$Res_{\omega_n} = \left[\frac{P(\omega)}{Q(\omega)}\right] = \frac{P(\omega_n)}{Q'(\omega_n)}. \tag{A.31}$$

with

$$P(\omega) = \mathrm{i}\begin{cases}\psi(x',\omega)b(x',\omega)a(x,\omega)\mathrm{e}^{-\mathrm{i}\omega(t-t')} & \text{for} \quad x<x' \\ \psi(x',\omega)a(x',\omega)b(x,\omega)\mathrm{e}^{-\mathrm{i}\omega(t-t')} & \text{for} \quad x>x'\end{cases} \tag{A.32}$$

$$Q(\omega) = 2\omega F(\omega), \tag{A.33}$$

$$Q'(\omega_n) = \frac{\mathrm{d}Q}{\mathrm{d}\omega} = [2F(\omega) + 2\omega F'(\omega)]_{\omega_n} = 2\omega_n F'(\omega_n). \tag{A.34}$$

This gives the residue in (A.27)

$$\begin{aligned}&Res_{\omega_n}[\hat{g}(x,x',\omega)\mathrm{e}^{-\mathrm{i}\omega(t-t')}] = \\ &\qquad\frac{\mathrm{i}\psi(x',\omega_n)\mathrm{e}^{-\mathrm{i}\omega_n(t-t')}}{2\omega_n F'(\omega_n)}\begin{cases}b(x',\omega_n)a(x,\omega_n) & \text{for} \quad x<x' \\ a(x',\omega_n)b(x,\omega_n) & \text{for} \quad x>x'\end{cases}\end{aligned} \tag{A.35}$$

This result is not valid for $\omega_0 = 0$ because ω_0 is not a frequency that satisfies $F(\omega) = 0$; its residue therefore has to be calculated separately. This can be done by expanding the expression $\hat{g}(x, x', \omega)\mathrm{e}^{-\mathrm{i}\omega(t-t')}$ into a Laurent series about $\omega = 0$; the coefficient of ω^{-1} will then give the required residue.

It is important to take into account that the reflection coefficients R_0 and R_L will, in general, also depend on ω. We assume that near $\omega = 0$, they can be approximated by

$$R_0 = -1 + \alpha_0\omega, \qquad \text{and} \qquad R_L = -1 + \alpha_L\omega, \tag{A.36}$$

where α_0 and α_L are complex constants that describe the end correction of an open tube end. The four expressions $F(\omega),\ a(x,\omega),\ b(x,\omega)$ and $\psi(x,\omega)$ can then be expanded into Taylor series about $\omega = 0$ and subsequently inserted into (A.30). The resulting Laurent series has no terms with negative powers of ω. We can, therefore, conclude that the coefficient of ω^{-1} is zero, and hence, the residue at $\omega_0 = 0$ is also zero.

The remaining terms in (A.27) are then

$$\int_{-\infty}^{\infty} \hat{g}(x, x', \omega)\mathrm{e}^{-\mathrm{i}\omega(t-t')}\mathrm{d}\omega = 2\pi \sum_{\substack{n=-\infty \\ n\neq 0}}^{\infty} \frac{g_n(x, x', \omega_n)}{2\omega_n F'(\omega_n)}\mathrm{e}^{-\mathrm{i}\omega_n(t-t')}, \tag{A.37}$$

with

$$g_n(x, x', \omega_n) = \begin{cases} \psi(x', \omega_n)b(x', \omega_n)a(x, \omega_n) & \text{for} \quad x < x' \\ \psi(x', \omega_n)a(x', \omega_n)b(x, \omega_n) & \text{for} \quad x > x' \end{cases} \tag{A.38}$$

The sum in (A.37) includes terms with positive and negative mode numbers. The latter can be converted into terms with positive mode numbers by using

$$\sum_{n=-1}^{-\infty} \frac{g_n(x, x', \omega_n)}{2\omega_n F'(\omega_n)}\mathrm{e}^{-\mathrm{i}\omega_n(t-t')} = \sum_{n=1}^{\infty} \frac{g_n(x, x', \omega_{-n})}{2\omega_{-n} F'(\omega_{-n})}\mathrm{e}^{-\mathrm{i}\omega_{-n}(t-t')}, \tag{A.39}$$

and using the fact that

$$\omega_{-n} = -\omega_n^*, \tag{A.40}$$

which can be shown from $F(\omega_n) = 0$ (Heckl, 2023); the symbol $*$ denotes the complex conjugate. This manipulation of equations gives

$$\sum_{n=-1}^{-\infty} \frac{g_n(x, x', \omega_n)}{2\omega_n F'(\omega_n)}\mathrm{e}^{-\mathrm{i}\omega_n(t-t')} = \left[\sum_{n=1}^{\infty} \frac{g_n(x, x', \omega_n)}{2\omega_n F'(\omega_n)}\mathrm{e}^{-\mathrm{i}\omega_n(t-t')}\right]^*. \tag{A.41}$$

The final result for the direct Green's function in the time domain becomes

$$g(x, x', t-t') = \sum_{n=1}^{\infty} \Re\left[\frac{g_n(x, x', \omega_n)}{\omega_n F'(\omega_n)}\mathrm{e}^{-\mathrm{i}\omega_n(t-t')}\right]. \tag{A.42}$$

This result is valid for observer times after the impulse ($t > t'$). It can be combined with the result for $g(x, x', t-t')$ before the impulse ($t < t'$), which is given in Eq. (A.26), by using the Heaviside function $H(t-t')$. This leads to Eq. (2.30) in the main text.

A.2. DERIVATION OF ADJOINT GREEN'S FUNCTION

This section demonstrates the detailed mathematical steps that give some crucial equations in the adjoint Green's function framework in the main text.

A.2.1. Derivation of Equation (2.34)

Recall that the governing equation of the direct system, Eq. (2.5),

$$\frac{\partial^2\phi}{\partial t^2} + 2\bar{u}\frac{\partial^2\phi}{\partial t\partial x} - (c^2 - \bar{u}^2)\frac{\partial^2\phi}{\partial x^2} = -(\gamma - 1)q(t)\delta(x - x_q), \tag{A.43}$$

and the initial conditions (2.6) and (2.7)

$$\phi(x,t)|_{t=0} = \varphi_0\delta(x - x_q), \tag{A.44}$$

$$\left[\frac{\partial\phi}{\partial t} + \bar{u}\frac{\partial\phi}{\partial x}\right]_{t=0} = \varphi_0'\delta(x - x_q). \tag{A.45}$$

The following mathematical operations are performed:

- write the PDE (A.43) in terms of the new variables $x',\ t'$ (instead of x, t)
- apply the inner product of Eq. (A.43) and an arbitrary test function (or an "adjoint variable") $G(x', x, t', t)$
- integrate the result $\int_{t'=0}^{T_t}\int_{x'=0}^{L}...G(x', x, t', t)...\mathrm{d}t'\mathrm{d}x'$ (with T_t yet to be defined)
- shift the derivatives from ϕ to G by repeated use of integration by parts.

After the first three operations, the following result is obtained.

$$\begin{aligned}
&\underbrace{\int_{t'=0}^{T_t}\int_{x'=0}^{L}\frac{\partial^2\phi}{\partial t'^2}G\mathrm{d}t'\mathrm{d}x'}_{\mathcal{I}_1} + \\
&2\bar{u}\underbrace{\int_{t'=0}^{T_t}\int_{x'=0}^{L}\frac{\partial^2\phi}{\partial t'\partial x'}G\mathrm{d}t'\mathrm{d}x'}_{\mathcal{I}_2} - \\
&(c^2 - \bar{u}^2)\underbrace{\int_{t'=0}^{T_t}\int_{x'=0}^{L}\frac{\partial^2 g}{\partial x'^2}G\mathrm{d}x'\mathrm{d}t'}_{\mathcal{I}_3} = \\
&-(\gamma - 1)\int_{t'=0}^{T_t} q(t)G(x_q, x, t', t)\mathrm{d}t'.
\end{aligned} \tag{A.46}$$

The three integrals $\mathcal{I}_1,\ \mathcal{I}_2,\ \mathcal{I}_3$, can be rewritten with integration by parts. For $\mathcal{I}_1$ we get

$$\mathcal{I}_1 = \int_{x'}^{L} \left[\frac{\partial\phi}{\partial t'}G - \frac{\partial G}{\partial t'}\right]_{t'=0}^{T_t} \mathrm{d}x' + \int_{x'}^{L}\int_{t'=0}^{T_t} \phi\frac{\partial^2 G}{\partial t'^2}\mathrm{d}t'\mathrm{d}x'. \tag{A.47}$$

The integral $\mathcal{I}_2$ can be manipulated in two different ways: integrate first with respect to t and then x, or vice versa. The first way gives

$$\begin{aligned}\mathcal{I}_2 &= \int_{x'}^{L}\int_{t'=0}^{T_t} \frac{\partial^2\phi}{\partial t'\partial x'}G(x',x,t',t)\mathrm{d}t'\mathrm{d}x' = \\ &\int_{x'=0}^{L}\left[\frac{\partial\phi}{\partial x'}G\right]_{t'=0}^{T_t}\mathrm{d}x' - \int_{t'=0}^{T_t}\left[\phi\frac{\partial G}{\partial t'}\right]_{x'=0}^{L}\mathrm{d}t' + \\ &\int_{t'=0}^{T_t}\int_{x'=0}^{L}\phi\frac{\partial^2 G}{\partial t'\partial x'}\mathrm{d}x'\mathrm{d}t'.\end{aligned} \tag{A.48}$$

The second way gives

$$\begin{aligned}\mathcal{I}_2 &= \int_{t'}^{T_t}\int_{x'=0}^{L} \frac{\partial^2\phi}{\partial t'\partial x'}G(x',x,t',t)\mathrm{d}t'\mathrm{d}x' = \\ &\int_{t'=0}^{T_t}\left[\frac{\partial\phi}{\partial t'}G\right]_{x'=0}^{L}\mathrm{d}t' - \int_{x'=0}^{L}\left[\phi\frac{\partial G}{\partial x'}\right]_{t'=0}^{T_t}\mathrm{d}x' + \\ &\int_{x'=0}^{L}\int_{t'=0}^{T_t}\phi\frac{\partial^2 G}{\partial x'\partial t'}\mathrm{d}t'\mathrm{d}x'.\end{aligned} \tag{A.49}$$

For $\mathcal{I}_3$ we get

$$\mathcal{I}_3 = \int_{t'=0}^{T_t}\left[\frac{\partial\phi}{\partial x'} - \frac{\partial G}{\partial x'}\phi\right]_{x'=0}^{L}\mathrm{d}t' + \int_{t'=0}^{T_t}\int_{x'=0}^{L}\phi\frac{\partial^2 G}{\partial x'^2}\mathrm{d}x'\mathrm{d}t'. \tag{A.50}$$

The left-hand side of (A.46) then becomes after some rearrangements

$$\begin{aligned}&\mathcal{I}_1 + \bar{u}\mathcal{I}_2 + \bar{u}\mathcal{I}_2 - (c^2-\bar{u}^2)\mathcal{I}_3 = \\ &\int_{t'=0}^{T_t}\int_{x'=0}^{L}\left[\frac{\partial^2 G}{\partial t'^2} + 2\bar{u}\frac{\partial^2 G}{\partial t'\partial x'} - (c^2-\bar{u}^2)\frac{\partial^2 G}{\partial x'^2}\right]\phi(x',t')\mathrm{d}x'\mathrm{d}t' + \\ &\int_{x'=0}^{L}\left[G(\frac{\partial\phi}{\partial t'} + \bar{u}\frac{\partial\phi}{\partial x'}) - \phi(\frac{\partial G}{\partial t'} + \bar{u}\frac{\partial G}{\partial x'})\right]_{t'=0}^{T_t}\mathrm{d}x' + \\ &\int_{t'=0}^{T_t}\left[\bar{u}(G\frac{\partial\phi}{\partial t'} - \phi\frac{\partial G}{\partial t'}) - (c^2-\bar{u}^2)(G\frac{\partial\phi}{\partial x'} - \phi\frac{\partial G}{\partial x'})\right]_{x'=0}^{L}\mathrm{d}t'.\end{aligned} \tag{A.51}$$

In order to obtain Eq. (2.34) in the main text, one needs to express the left-hand side of (A.46) with the result in (A.51) and then arrange the terms in a suitable order.

A.2.2. Derivation of Equations (2.45) and (2.46)

Our starting point is the PDE (2.21) for $\hat{g}$,

$$\omega^2\hat{g}(x,x',\omega) + 2\bar{u}\mathrm{i}\omega\frac{\partial\hat{g}}{\partial x} + (c^2-\bar{u}^2)\frac{\partial^2\hat{g}}{\partial x^2} = -\delta(x-x'). \tag{A.52}$$

We perform the following mathematical operations:

- multiply by the test function $\hat{G}(x,x^*,\omega)$
- integrate $\int_{x=0}^{L}...\hat{G}(x,x^*,\omega)...\mathrm{d}x$
- shift the derivatives from $\hat{g}$ to $\hat{G}$ by repeated use of integration by parts.

The first two operations lead to

$$\begin{aligned}\omega^2\int_{x=0}^{L}\hat{g}\hat{G}dx + 2\bar{u}\mathrm{i}\omega\underbrace{\int_{x=0}^{L}\frac{\partial\hat{g}}{\partial x}\hat{G}\mathrm{d}x}_{=\mathcal{I}_1} + (c^2-\bar{u}^2)\underbrace{\int_{x=0}^{L}\frac{\partial^2\hat{g}}{\partial x^2}\hat{G}dx}_{=\mathcal{I}_2} = \\ \underbrace{-\int_{x=0}^{L}\delta(x-x')\hat{G}(x,x^*,\omega)\mathrm{d}x.}_{=-\hat{G}(x,x^*,\omega)}\end{aligned} \tag{A.53}$$

The two integrals $\mathcal{I}_1$ and $\mathcal{I}_2$ can be rewritten with integration by parts; this gives

$$\mathcal{I}_1 = \left[\hat{g}\hat{G}\right]_{x=0}^{L} - \int_{x=0}^{L}\hat{g}\frac{\partial\hat{G}}{\partial x}\mathrm{d}x, \tag{A.54}$$

$$\mathcal{I}_2 = \left[\hat{G}\frac{\partial\hat{g}}{\partial x} - \hat{g}\frac{\partial\hat{G}}{\partial x}\right]_{x=0}^{L} + \int_{x=0}^{L}\hat{g}\frac{\partial^2\hat{G}}{\partial x^2}\mathrm{d}x. \tag{A.55}$$

We substitute these results into (A.53) and then obtain

$$\int_{x=0}^{L}\hat{g}\left[\omega^2\hat{G} - 2\bar{u}\mathrm{i}\omega\frac{\partial\hat{G}}{\partial x} + (c^2-\bar{u}^2)\frac{\partial^2\hat{G}}{\partial x^2}\right]dx + BT3 = -\hat{G}(x',x^*,\omega), \tag{A.56}$$

with

$$BT3 = 2\bar{u}\mathrm{i}\omega\left[\hat{g}\hat{G}\right]_{x=0}^{L} + (c^2-\bar{u}^2)\left[\hat{G}\frac{\partial\hat{g}}{\partial x}\right]_{x=0}^{L} \tag{A.57}$$

We define $\hat{G}(x,x^*,\omega)$ by the PDE

$$\omega^2\hat{G}(x,x^*,\omega) - 2\bar{u}\mathrm{i}\omega\frac{\partial\hat{G}}{\partial x} + (c^2-\bar{u}^2)\frac{\partial^2\hat{G}}{\partial x^2} = -\delta(x-x^*). \tag{A.58}$$

We further define $\hat{G}(x, x^*, \omega)$ by boundary conditions, which will make the unwelcome boundary term $BT3$ zero. Comparison of (A.58) and (A.52) shows that $\hat{G}$ and $\hat{g}$ satisfy very similar PDEs; they only differ by the sign of the mean flow speed $\bar{u}$.

$\hat{g}$ is known by the expressions (2.26) on either side of the point x',

$$\hat{g}(x, x', \omega) = \begin{cases} A_-(x', \omega)[R_0 \mathrm{e}^{\frac{\mathrm{i}\omega}{c+\bar{u}}x} + \mathrm{e}^{-\frac{\mathrm{i}\omega}{c-\bar{u}}x}] & \text{near} \quad x = 0 \\ B_+(x', \omega)[\mathrm{e}^{\frac{\mathrm{i}\omega}{c+\bar{u}}(x-L)} + R_L \mathrm{e}^{-\frac{\mathrm{i}\omega}{c-\bar{u}}(x-L)}] & \text{near} \quad x = L \end{cases} \tag{A.59}$$

We construct from (A.59) a solution for $\hat{G}$ with the following rationale:

- change the sign of $\bar{u}$
- assume the same reflection coefficients, R_0 and R_L, as for $\hat{g}$
- allow for different amplitudes ($\tilde{A_-}$ instead of A_-, and $\tilde{B}_+$ instead of B_+)

The result is

$$\hat{G}(x, x', \omega) = \begin{cases} \tilde{A}_-(x', \omega) \left[R_0 \mathrm{e}^{\frac{\mathrm{i}\omega}{c-\bar{u}}x} + \mathrm{e}^{-\frac{\mathrm{i}\omega}{c+\bar{u}}x}\right] & \text{near} \quad x = 0 \\ \tilde{B}_+(x', \omega) \left[\mathrm{e}^{\frac{\mathrm{i}\omega}{c-\bar{u}}(x-L)} + R_L \mathrm{e}^{-\frac{\mathrm{i}\omega}{c+\bar{u}}(x-L)}\right] & \text{near} \quad x = L \end{cases} \tag{A.60}$$

which is identical to Eq. (2.46) in the main text.

It remains to show that the boundary term BT3, (A.57), is indeed zero with this definition. The derivatives of Eqs. (A.59) and (A.60) are

$$\frac{\partial \hat{g}}{\partial x}(x, x', \omega) = \begin{cases} A_-(x', \omega)\mathrm{i}\omega \left[\dfrac{1}{c+\bar{u}} R_0 \mathrm{e}^{\frac{\mathrm{i}\omega}{c+\bar{u}}x} - \dfrac{1}{c-\bar{u}} \mathrm{e}^{-\frac{\mathrm{i}\omega}{c-\bar{u}}x}\right] & \text{near} \quad x = 0 \\ B_+(x', \omega)\mathrm{i}\omega \left[\dfrac{1}{c+\bar{u}} \mathrm{e}^{\frac{\mathrm{i}\omega}{c+\bar{u}}(x-L)} - \dfrac{1}{c-\bar{u}} R_L \mathrm{e}^{-\frac{\mathrm{i}\omega}{c-\bar{u}}(x-L)}\right] & \text{near} \quad x = L \end{cases} \tag{A.61}$$

and

$$\frac{\partial \hat{G}}{\partial x}(x, x', \omega) = \begin{cases} \tilde{A}_-(x', \omega)\mathrm{i}\omega \left[\dfrac{1}{c-\bar{u}} R_0 \mathrm{e}^{\frac{\mathrm{i}\omega}{c-\bar{u}}x} - \dfrac{1}{c+\bar{u}} \mathrm{e}^{-\frac{\mathrm{i}\omega}{c+\bar{u}}x}\right] & \text{near} \quad x = 0 \\ \tilde{B}_+(x', \omega)\mathrm{i}\omega \left[\dfrac{1}{c-\bar{u}} \mathrm{e}^{\frac{\mathrm{i}\omega}{c-\bar{u}}(x-L)} - \dfrac{1}{c+\bar{u}} R_L \mathrm{e}^{-\frac{\mathrm{i}\omega}{c+\bar{u}}(x-L)}\right] & \text{near} \quad x = L \end{cases} \tag{A.62}$$

We can now evaluate Eqs. (A.57)–(A.62) at the duct ends: $x = 0$ and $x = L$. At $x = 0$, we get

$$\hat{g}(0, x', \omega) = A_-(x', \omega)(R_0 + 1), \tag{A.63a}$$

$$\hat{G}(0, x', \omega) = \tilde{A}_-(x', \omega)(R_0 + 1), \tag{A.63b}$$

$$\left.\frac{\partial \hat{g}}{\partial x}\right|_{x=0} = A_-(x', \omega)\mathrm{i}\omega \left[\frac{1}{c+\bar{u}} R_0 - \frac{1}{c-\bar{u}}\right], \tag{A.63c}$$

$$\left.\frac{\partial \hat{G}}{\partial x}\right|_{x=0} = \tilde{A}_-(x', \omega)\mathrm{i}\omega \left[\frac{1}{c-\bar{u}} R_0 - \frac{1}{c+\bar{u}}\right]. \tag{A.63d}$$

Then we get for the boundary at $x = 0$ of the term $BT3$ in (A.57)

$$
\begin{aligned}
&[BT3]_{x=0} = 2\bar{u}\mathrm{i}\omega[\hat{g}\hat{G}]_{x=0} + (c^2 - \bar{u}^2)\left[\hat{G}\frac{\partial \hat{g}}{\partial x} - \hat{g}\frac{\partial \hat{G}}{\partial x}\right]_{x=0} = \\
&2\bar{u}\mathrm{i}\omega A_-(x',\omega)\tilde{A}_-(x',\omega)(R_0+1)^2 + \\
&(c^2-\bar{u}^2)A_-(x',\omega)\tilde{A}_-(x',\omega)\mathrm{i}\omega\left[\left(\frac{1}{c+\bar{u}}R_0 - \frac{1}{c-\bar{u}}\right)(R_0+1) - \right. \\
&\left.(R_0+1)\left(\frac{1}{c-\bar{u}}R_0 - \frac{1}{c+\bar{u}}\right)\right] = \\
&A_-(x',\omega)\tilde{A}_-(x',\omega)\mathrm{i}\omega(R_0+1)\Bigg\{(2\bar{u}(R_0+1) + \\
&(c^2-\bar{u}^2)\underbrace{\left[(\frac{1}{c+\bar{u}}R_0 - \frac{1}{c-\bar{u}}) - (\frac{1}{c-\bar{u}}R_0 - \frac{1}{c+\bar{u}})\right]}_{= (R_0+1)\frac{-2\bar{u}}{c^2-\bar{u}^2}}\Bigg\}.
\end{aligned}
\tag{A.64}
$$

The same calculation can be done at $x = L$, and the result is also zero. We can conclude that $BT3 = 0$, and Eq. (A.56) reduces to Eq. (2.45) in the main text.

A.2.3. Derivation of the reciprocity theorem (2.48)

The starting point is the PDE (2.21) for $g(x, x', t - t')$,

$$
\frac{\partial^2 g}{\partial t^2} + 2\bar{u}\frac{\partial^2 g}{\partial t \partial x} - (c^2 - \bar{u}^2)\frac{\partial^2 g}{\partial x^2} = \delta(x - x')\delta(t - t'), \tag{A.65}
$$

and the causality conditions (2.22) and (2.23)

$$
g(x, x', t - t') = 0 \quad \text{for} \quad t < t'. \tag{A.66}
$$

We perform the following mathematical operations on Eq. (A.65)

- multiply by $G(x, x^*, t, t^*)$
- integrate the result with respect to x and t, i.e. $\int_{t=-\infty}^{\infty}\int_{x=0}^{L} ...G(x, x^*, t, t^*)...\mathrm{d}t\mathrm{d}x$
- shift the derivatives from g to G by repeated use of integration by parts.

The first two operations lead to

$$\begin{aligned}
&\underbrace{\int_{t=-\infty}^{\infty}\int_{x=0}^{L}\frac{\partial^2 g}{\partial t^2}G\mathrm{d}t\mathrm{d}x}_{\mathcal{I}_1}+2\bar{u}\underbrace{\int_{t=-\infty}^{\infty}\int_{x=0}^{L}\frac{\partial^2 g}{\partial t\partial x}G\mathrm{d}t\mathrm{d}x}_{\mathcal{I}_2}-\\
&(c^2-\bar{u}^2)\underbrace{\int_{t=-\infty}^{\infty}\int_{x=0}^{L}\frac{\partial^2 g}{\partial x^2}G\mathrm{d}x\mathrm{d}t}_{\mathcal{I}_3}=\\
&\underbrace{\int_{t=-\infty}^{\infty}\int_{x=0}^{L}\delta(x-x')\delta(t-t')G(x,x^*,t,t^*)\mathrm{d}x\mathrm{d}t.}_{=G(x',x^*,t',t^*)}
\end{aligned}\tag{A.67}$$

The three integrals $\mathcal{I}_1,\ \mathcal{I}_2,\ \mathcal{I}_3$, can be rewritten with integration by parts. The result for $\mathcal{I}_1$ is

$$\mathcal{I}_1=\int_{x=0}^{L}\left[\frac{\partial g}{\partial t}G-\frac{\partial G}{\partial t}g\right]_{t=-\infty}^{\infty}dx+\int_{x=0}^{L}\int_{t=-\infty}^{\infty}g\frac{\partial^2 G}{\partial t^2}G\mathrm{d}t\mathrm{d}x \tag{A.68}$$

$\mathcal{I}_2$ can be manipulated in two different ways: integrate first with respect to t and then x, or vice versa. The first way gives

$$\mathcal{I}_2=\int_{x=0}^{L}\left[\frac{\partial g}{\partial x}G\right]_{t=-\infty}^{\infty}\mathrm{d}x-\int_{t=-\infty}^{\infty}\left[g\frac{\partial G}{\partial t}\right]_{x=0}^{L}\mathrm{d}t+\int_{t=-\infty}^{\infty}\int_{x=0}^{L}g\frac{\partial^2 G}{\partial t\partial x}\mathrm{d}x\mathrm{d}t. \tag{A.69}$$

The second way gives

$$\tilde{\mathcal{I}}_2=\int_{t=-\infty}^{\infty}\left[\frac{\partial g}{\partial t}G\right]_{x=0}^{L}\mathrm{d}t-\int_{x=0}^{L}\left[g\frac{\partial G}{\partial x}\right]_{t=-\infty}^{\infty}\mathrm{d}x+\int_{x=0}^{L}\int_{t=-\infty}^{\infty}g\frac{\partial^2 G}{\partial t\partial x}\mathrm{d}t\mathrm{d}x. \tag{A.70}$$

The result for $\mathcal{I}_3$ is

$$\mathcal{I}_3=\int_{t=-\infty}^{\infty}\left[\frac{\partial g}{\partial x}G-g\frac{\partial G}{\partial x}\right]_{x=0}^{L}\mathrm{d}t+\int_{t=-\infty}^{\infty}\int_{x=0}^{L}g\frac{\partial^2 G}{\partial x^2}\mathrm{d}x\mathrm{d}t. \tag{A.71}$$

The left-hand side of Eq. (A.67) then becomes

$$\begin{aligned}
&\mathcal{I}_1 + \bar{u}\mathcal{I}_2 + \bar{u}\tilde{\mathcal{I}}_2 - (c^2 - \bar{u}^2)\mathcal{I}_3 = \\
&\int_{x=0}^{L}\int_{t=-\infty}^{\infty} g(x,x',t-t') \underbrace{\left[\frac{\partial^2 G}{\partial t^2} + 2\bar{u}\frac{\partial^2 G}{\partial t \partial x} - (c^2-\bar{u}^2)\frac{\partial^2 G}{\partial x^2}\right]}_{=\delta(t-t^*)\delta(x-x^*)} \mathrm{d}t\,\mathrm{d}x + \\
&\int_{x=0}^{L}\left(\left[\frac{\partial g}{\partial t}G - \frac{\partial G}{\partial t}g\right]_{t=-\infty}^{\infty} + \bar{u}\left[\frac{\partial g}{\partial x}G\right]_{t=-\infty}^{\infty} - \bar{u}\left[g\frac{\partial G}{\partial x}\right]_{t=-\infty}^{\infty}\right)\mathrm{d}x + \\
&\int_{t=-\infty}^{\infty}\left(-\bar{u}\left[g\frac{\partial G}{\partial t}\right]_{x=0}^{L} + \bar{u}\left[\frac{\partial g}{\partial t}G\right]_{x=0}^{L} - (c^2-\bar{u}^2)\left[\frac{\partial g}{\partial x}G - g\frac{\partial G}{\partial x}\right]_{x=0}^{L}\right)\mathrm{d}t = \\
&g(x^*,x',t^*,t') + BT4 + BT5.
\end{aligned} \tag{A.72}$$

with

$$BT4 = \int_{x=0}^{L}\left[G\left(\frac{\partial g}{\partial t} + \bar{u}\frac{\partial g}{\partial x}\right) - g\left(\frac{\partial G}{\partial t} + \bar{u}\frac{\partial G}{\partial x}\right)\right]_{t=-\infty}^{\infty}\mathrm{d}x \tag{A.73}$$

and

$$BT5 = \int_{t=-\infty}^{\infty}\left[\bar{u}\left(\frac{\partial g}{\partial t}G - g\frac{\partial G}{\partial t}\right) - (c^2-\bar{u}^2)\left(\frac{\partial g}{\partial x}G - g\frac{\partial G}{\partial x}\right)\right]_{x=0}^{L}\mathrm{d}t. \tag{A.74}$$

According to Eq. (A.67), this has to be equal to $G(x',x^*,t',t^*)$. We will get a meaningful result if we can show that the boundary terms $BT4$ and $BT5$ are zero. In order to determine $BT4$, we use the causality condition and terminal condition. From the causality condition (A.66), we can conclude that

$$g(x,x',t-t') = 0 \quad \text{for} \quad t \to -\infty, \tag{A.75}$$

because t' is finite. From the terminal condition, which we extended in (2.42), we can conclude that

$$G(x,x^*,t,t^*) = 0 \quad \text{for} \quad t \to \infty, \tag{A.76}$$

because T_t is finite. As a consequence of Eqs. (A.75) and (A.76),

$$BT4 = 0. \tag{A.77}$$

The term $BT5$ in Eq. (A.74) is analogous to the term $BT2$ in Eq. (2.36), with g in place of ϕ. In the frequency domain, g and ϕ have the same wave numbers (k_+ for forward travelling waves; k_- for backward travelling waves) and the same boundary conditions at the tube ends $x = 0, L$. Hence the method applied in Section A.3. can also be applied in this case, leading to

$$BT5 = 0. \tag{A.78}$$

A.3. CALCULATION OF THE BOUNDARY TERM $BT2$

The boundary term in Eq. (2.34) is given by

$$BT2 = \int_{t'=0}^{T_t} \left[\bar{u}(G\frac{\partial \phi}{\partial t'} - \phi\frac{\partial G}{\partial t'}) - (c^2 - \bar{u}^2)(G\frac{\partial \phi}{\partial x'} - \phi\frac{\partial G}{\partial x'}) \right]_{x'=0}^{L} \mathrm{d}t'. \tag{A.79}$$

For times t' outside the integration range, ϕ and G are not defined, so we can choose

$$\phi(x', t') = 0 \quad \text{for} \quad t' < 0, \tag{A.80}$$

$$G(x', x, t', t) = 0 \quad \text{for} \quad t' > T_t. \tag{A.81}$$

This allows us to extend the integration limits from $\int_{t'=0}^{T_t}$ to $\int_{t'=-\infty}^{\infty}$ and to make use of Fourier transforms, with

$$\phi(x', t') = \frac{1}{2\pi} \int_{\omega=-\infty}^{\infty} \hat{\phi}(x', \omega) \mathrm{e}^{-\mathrm{i}\omega t'} \mathrm{d}\omega, \tag{A.82}$$

$$G(x', x, t', t) = \frac{1}{2\pi} \int_{\omega=-\infty}^{\infty} \hat{G}(x', x, \tilde{\omega}) \mathrm{e}^{-\mathrm{i}\tilde{\omega}(t-t')} \mathrm{d}\tilde{\omega}. \tag{A.83}$$

Each of the product terms in Eq. (A.79), $G\frac{\partial \phi}{\partial t'},\ \phi\frac{\partial G}{\partial t'},\ G\frac{\partial \phi}{\partial x'},\ \phi\frac{\partial G}{\partial x'}$ is a double integral of the form $\int_{\omega=-\infty}^{\infty}\int_{\tilde{\omega}=-\infty}^{\infty} ...\mathrm{d}\tilde{\omega}\mathrm{d}\omega$. Each integrand of these double integrals has the same time-dependence, $\mathrm{e}^{-\mathrm{i}\omega t'}\mathrm{e}^{-\mathrm{i}\tilde{\omega}(t-t')} = \mathrm{e}^{-\mathrm{i}\tilde{\omega}t}\mathrm{e}^{-\mathrm{i}(\omega-\tilde{\omega})t'}$, which can be integrated with respect to t'.

$$\int_{t'=-\infty}^{\infty} \mathrm{e}^{-\mathrm{i}\tilde{\omega}t}\mathrm{e}^{-\mathrm{i}(\omega-\tilde{\omega})t'} \mathrm{d}t' = \mathrm{e}^{-\mathrm{i}\tilde{\omega}t} \int_{t'=-\infty}^{\infty} \mathrm{e}^{-\mathrm{i}(\omega-\tilde{\omega})t'} \mathrm{d}t' = \mathrm{e}^{-\mathrm{i}\tilde{\omega}t} 2\pi\delta(\omega - \tilde{\omega}). \tag{A.84}$$

As a consequence of the term $\delta(\omega - \tilde{\omega})$, the double integral over ω and $\tilde{\omega}$ reduces to a single integral over ω. This allows us to consider a single frequency component of ϕ and G when calculating the product terms, as follows

$$\phi_\omega(x', t') = \tilde{\phi}(x', \omega)\mathrm{e}^{-\mathrm{i}\omega t'}, \tag{A.85}$$

$$G_\omega(x', x, t', t) = \hat{G}(x', x, \tilde{\omega})\mathrm{e}^{-\mathrm{i}\tilde{\omega}(t-t')}. \tag{A.86}$$

We first consider the boundary at $x' = 0$. Near there, recall Eq. (2.13), we have

$$\phi_\omega(x', t') = A_-(R_0\mathrm{e}^{\mathrm{i}k_+x'} + \mathrm{e}^{-\mathrm{i}k_-x'})\mathrm{e}^{-\mathrm{i}\omega t'}, \tag{A.87a}$$

$$\frac{\partial \phi_\omega}{\partial t'} = (-\mathrm{i}\omega)A_-(R_0\mathrm{e}^{\mathrm{i}k_+x'} + \mathrm{e}^{-\mathrm{i}k_-x'})\mathrm{e}^{-\mathrm{i}\omega t'}, \tag{A.87b}$$

$$\frac{\partial \phi_\omega}{\partial x'} = A_-(\mathrm{i}k_+R_0\mathrm{e}^{\mathrm{i}k_+x'} - \mathrm{i}k_-\mathrm{e}^{-\mathrm{i}k_-x'})\mathrm{e}^{-\mathrm{i}\omega t'}, \tag{A.87c}$$

With Eq. (2.46) near $x' = 0$, we have

$$G_\omega(x', x, t', t) = \tilde{A}_-(x, \omega)(R_0 \mathrm{e}^{\mathrm{i}k_- x'} + \mathrm{e}^{-\mathrm{i}k_+ x'})\mathrm{e}^{-\mathrm{i}\omega(t-t')}, \tag{A.88a}$$

$$\frac{\partial G_\omega}{\partial t'} = (\mathrm{i}\omega)\tilde{A}_-(x, \omega)(R_0 \mathrm{e}^{ik_- x'} + \mathrm{e}^{-\mathrm{i}k_+ x'})\mathrm{e}^{-\mathrm{i}\omega(t-t')}, \tag{A.88b}$$

$$\frac{\partial G_\omega}{\partial x'} = \tilde{A}_-(x, \omega)(\mathrm{i}k_- R_0 \mathrm{e}^{\mathrm{i}k_- x'} - \mathrm{i}k_+ \mathrm{e}^{-\mathrm{i}k_+ x'})\mathrm{e}^{-\mathrm{i}\omega(t-t')}. \tag{A.88c}$$

Simplification of the above terms at $x' = 0$ gives

$$\phi_\omega(x', t')|_{x'=0} = A_-(R_0 + 1)\mathrm{e}^{-\mathrm{i}\omega t'}, \tag{A.89a}$$

$$\left.\frac{\partial \phi_\omega}{\partial t'}\right|_{x'=0} = -\mathrm{i}\omega A_-(R_0 + 1)\mathrm{e}^{-\mathrm{i}\omega t'}, \tag{A.89b}$$

$$\left.\frac{\partial \phi_\omega}{\partial x'}\right|_{x'=0} = A_-(\mathrm{i}k_+ R_0 - ik_-)\mathrm{e}^{-\mathrm{i}\omega t'}. \tag{A.89c}$$

and

$$\left.G_\omega(x', x, t', t)\right|_{x'=0} = \tilde{A}_-(x, \omega)(R_0 + 1)\mathrm{e}^{-\mathrm{i}\omega(t-t')}, \tag{A.90a}$$

$$\left.\frac{\partial G_\omega}{\partial t'}\right|_{x'=0} = (\mathrm{i}\omega)\tilde{A}_-(x, \omega)(R_0 + 1)\mathrm{e}^{-\mathrm{i}\omega(t-t')}, \tag{A.90b}$$

$$\left.\frac{\partial G_\omega}{\partial x'}\right|_{x'=0} = \tilde{A}_-(x, \omega)(\mathrm{i}k_- R_0 - \mathrm{i}k_-)\mathrm{e}^{-\mathrm{i}\omega(t-t')}. \tag{A.90c}$$

The integrand in Eq. (A.79) at $x' = 0$ then becomes

$$\begin{aligned}
&\left[\bar{u}(G_\omega)\frac{\partial \phi_\omega}{\partial t'} - \phi_\omega \frac{\partial G_\omega}{\partial t'}) - (c^2 - \bar{u}^2)(G_\omega \frac{\partial \phi_\omega}{\partial x'} - \phi_\omega \frac{\partial G_\omega}{\partial x'})\right]_{x'=0} = \\
&\bar{u}[\tilde{A}_-(R_0+1)(-\mathrm{i}\omega)A_-(R_0+1) - A_-(R_0+1)(\mathrm{i}\omega)\tilde{A}_-(R_0+1)]\mathrm{e}^{-\mathrm{i}\omega t'}\mathrm{e}^{-\mathrm{i}\omega(t-t')} - \\
&(c^2 - \bar{u}^2)[\tilde{A}_-(R_0+1)A_-(\mathrm{i}k_+ R_0 - \mathrm{i}k_-) - A_-(R_0+1)\tilde{A}_-(\mathrm{i}k_- R_0 - \mathrm{i}k_+)]\mathrm{e}^{-\mathrm{i}\omega t'}\mathrm{e}^{-\mathrm{i}\omega(t-t')} = \\
&\tilde{A}_- A_-(R_0+1)\mathrm{e}^{-\mathrm{i}\omega t}[\bar{u}(-2\mathrm{i}\omega)(R_0+1) - (c^2 - \bar{u}^2)\underbrace{(\mathrm{i}k_+ R_0 - \mathrm{i}k_- - \mathrm{i}k_- R_0 + \mathrm{i}k_+)}_{=(R_0+1)(\mathrm{i}k_+ - \mathrm{i}k_-)}] = \\
&\tilde{A}_- A_-(R_0+1)^2\mathrm{e}^{-\mathrm{i}\omega t}[-2\mathrm{i}\omega\bar{u} - (c^2 - \bar{u}^2)\underbrace{(\mathrm{i}k_+ - \mathrm{i}k_-)}_{\mathrm{i}\omega\frac{-2\bar{u}}{c^2-\bar{u}^2}}] = 0.
\end{aligned} \tag{A.91}$$

The same calculation can be done for the boundary at $x' = L$, and the result is also zero. To summarize, we have shown that

$$BT2 = 0, \tag{A.92}$$

which confirms Eq. (2.42) in the main text.

A.4. FOURIER TRANSFORM PAIR OF AGF

We have defined G and $\hat{G}$ in such a way that they satisfy the PDEs

$$\frac{\partial^2 G}{\partial t'^2} + 2\bar{u}\frac{\partial^2 G}{\partial t'\partial x'} - (c^2 - \bar{u}^2)\frac{\partial^2 G}{\partial x'^2} = \delta(x' - x)\delta(t' - t) \tag{A.93}$$

(see Eq. (2.37) in the main text), and

$$\omega^2\hat{G}(x', x, \omega) - 2\bar{u}\mathrm{i}\omega\frac{\partial\hat{G}}{\partial x'} + (c^2 - \bar{u}^2)\frac{\partial^2\hat{G}}{\partial x'^2} = -\delta(x' - x). \tag{A.94}$$

(see Eq. (2.45) in the main text). In order to test whether they form a Fourier transform pair, we propose the following "trial relationship" between these two functions

$$G(x', x, t', t) = \frac{1}{2\pi}\int_{\omega=-\infty}^{\infty}\hat{G}(x', x, \omega)\mathrm{e}^{-\mathrm{i}\omega(t-t')}\mathrm{d}\omega. \tag{A.95}$$

Then

$$\frac{\partial G}{\partial t'} = \frac{1}{2\pi}\int_{\omega=-\infty}^{\infty}\mathrm{i}\omega\hat{G}(x', x, \omega)\mathrm{e}^{-\mathrm{i}\omega(t-t')}\mathrm{d}\omega, \tag{A.96a}$$

$$\frac{\partial^2 G}{\partial t'^2} = \frac{1}{2\pi}\int_{\omega=-\infty}^{\infty}(-\omega^2)\hat{G}(x', x, \omega)\mathrm{e}^{-\mathrm{i}\omega(t-t')}\mathrm{d}\omega, \tag{A.96b}$$

$$\frac{\partial^2 G}{\partial t'\partial x'} = \frac{1}{2\pi}\int_{\omega=-\infty}^{\infty}(-\mathrm{i}\omega)\frac{\partial\hat{G}}{\partial x'}\mathrm{e}^{-\mathrm{i}\omega(t-t')}\mathrm{d}\omega, \tag{A.96c}$$

$$\frac{\partial^2 G}{\partial x'^2} = \frac{1}{2\pi}\int_{\omega=-\infty}^{\infty}\frac{\partial^2\hat{G}}{\partial x'^2}\mathrm{e}^{-\mathrm{i}\omega(t-t')}\mathrm{d}\omega. \tag{A.96d}$$

We multiply the PDE (A.94) by $\frac{1}{2\pi}\mathrm{e}^{-\mathrm{i}\omega(t-t')}$ and then integrate $\frac{1}{2\pi}\int_{\omega=-\infty}^{\infty}...\mathrm{e}^{-\mathrm{i}\omega(t-t')}\mathrm{d}\omega$. This leads to

$$\begin{aligned}
&\underbrace{\frac{1}{2\pi}\int_{\omega=-\infty}^{\infty}\omega^2\hat{G}(x', x, \omega)\mathrm{e}^{-\mathrm{i}\omega(t-t')}\mathrm{d}\omega}_{=-\frac{\partial^2 G}{\partial t'^2}} - 2\bar{u}\underbrace{\frac{1}{2\pi}\int_{\omega=-\infty}^{\infty}\mathrm{i}\omega\frac{\partial\hat{G}}{\partial x'}\mathrm{e}^{-\mathrm{i}\omega(t-t')}\mathrm{d}\omega}_{=\frac{\partial^2 G}{\partial t'\partial x'}} + \\
&(c^2 - \bar{u}^2)\underbrace{\frac{1}{2\pi}\int_{\omega=-\infty}^{\infty}\frac{\partial^2\hat{G}}{\partial x'^2}\mathrm{e}^{-\mathrm{i}\omega(t-t')}\mathrm{d}\omega}_{=\frac{\partial^2 G}{\partial x'^2}} = -\delta(x' - x)\underbrace{\frac{1}{2\pi}\int_{\omega=-\infty}^{\infty}\mathrm{e}^{-\mathrm{i}\omega(t-t')}\mathrm{d}\omega}_{\delta(t'-t)}.
\end{aligned} \tag{A.97}$$

We can thus rewrite the above equation as

$$\frac{\partial^2 G}{\partial t'^2} + 2\bar{u}\frac{\partial^2 G}{\partial t'\partial x'} - (c^2 - \bar{u}^2)\frac{\partial^2 G}{\partial x'^2} = \delta(x - x')\delta(t - t'); \tag{A.98}$$

this agrees with (A.93), and therefore our test relationship in (A.95) has been validated. We can conclude that $G(x', x, t', t)$ and $\hat{G}(x', x, \omega)$ are indeed a Fourier transform pair.

A.5. CALCULATION OF AGF FOR A FLOW DUCT WITH NON-UNIFORM TEMPERATURE

In this part, we show the calculation of direct Green's function and AGF for a duct flow with a temperature jump in the vicinity of the heat source. The details follow Section A.1., and the different steps are shown here. Recall the general solution of the direct Green's function in the frequency domain,

$$\hat{g}(x,x',\omega)=\begin{cases}A_{+}\mathrm{e}^{\mathrm{i}k_{+1}x}+A_{-}\mathrm{e}^{-\mathrm{i}k_{-1}x} & \text{for} \quad 0<x<x_T,\\ B_{+}\mathrm{e}^{\mathrm{i}k_{+2}x}+B_{-}\mathrm{e}^{-\mathrm{i}k_{-2}x} & \text{for} \quad x_T<x<x',\\ C_{+}\mathrm{e}^{\mathrm{i}k_{+2}x}+C_{-}\mathrm{e}^{-\mathrm{i}k_{-2}x} & \text{for} \quad x'<x<L.\end{cases} \tag{A.99}$$

Applying the interface condition and the boundary condition, there are,

$$A_{+}=A_{-}R_0, \qquad \text{at } x=0, \tag{A.100a}$$
$$C_{-}=C_{+}R_L\mathrm{e}^{\mathrm{i}(k_{+2}+k_{-2})L}, \qquad \text{at } x=L, \tag{A.100b}$$
$$A_{-}\mathrm{e}^{-\mathrm{i}k_{-1}x_T}=R_{\mathrm{AB}}A_{+}\mathrm{e}^{\mathrm{i}k_{+1}x_T}+T_{\mathrm{BA}}B_{-}\mathrm{e}^{-\mathrm{i}k_{-2}x_T}, \qquad \text{at } x=x_T, \tag{A.100c}$$
$$B_{+}\mathrm{e}^{\mathrm{i}k_{+2}x_T}=R_{\mathrm{BA}}B_{-}\mathrm{e}^{-\mathrm{i}k_{-2}x_T}+T_{\mathrm{AB}}A_{+}\mathrm{e}^{\mathrm{i}k_{+1}x_T}, \qquad \text{at } x=x_T. \tag{A.100d}$$

The above conditions help reduce the unknowns, and Eq. (A.99) now becomes

$$\hat{g}(x,x',\omega)=\begin{cases}A_{-}(x',\omega)\,\alpha(x,\omega) & \text{for} \quad 0<x<x_T,\\ A_{-}(x',\omega)\,\beta(x,\omega) & \text{for} \quad x_T<x<x',\\ C_{+}(x',\omega)\,\eta(x,\omega) & \text{for} \quad x'<x<L,\end{cases} \tag{A.101}$$

with

$$\alpha(x,\omega)=R_0\mathrm{e}^{\mathrm{i}k_{+1}x}+\mathrm{e}^{-\mathrm{i}k_{-1}x}, \tag{A.102a}$$
$$\beta(x,\omega)=S_2\,\mathrm{e}^{\mathrm{i}k_{+2}x}+S_1\mathrm{e}^{-\mathrm{i}k_{-2}x}, \tag{A.102b}$$
$$\eta(x,\omega)=\mathrm{e}^{\mathrm{i}k_{+2}x}+S_3\,\mathrm{e}^{-\mathrm{i}k_{-2}x}, \tag{A.102c}$$

and

$$S_1=\frac{1}{T_{\mathrm{BA}}}\left(\mathrm{e}^{-\mathrm{i}k_{-1}x_T}-R_{\mathrm{AB}}R_0\mathrm{e}^{\mathrm{i}k_{+1}x_T}\right)\mathrm{e}^{\mathrm{i}k_{-2}x_T}, \tag{A.103a}$$
$$S_2=\left(R_{\mathrm{BA}}S_1\mathrm{e}^{-\mathrm{i}k_{-2}x_T}+T_{\mathrm{AB}}R_0\mathrm{e}^{\mathrm{i}k_{+1}x_T}\right)\mathrm{e}^{-\mathrm{i}k_{+2}x_T}, \tag{A.103b}$$
$$S_3=R_L\mathrm{e}^{\mathrm{i}(k_{+2}+k_{-2})L}. \tag{A.103c}$$

We can convert Eq. (A.101) in the hot region ($x>x_T$) into a single expression by using the Heaviside functions $H(x'-x)$ and $H(x-x')$,

$$\hat{g}(x,x',\omega)=H(x'-x)A_{-}(x',\omega)\beta(x,\omega)+H(x-x')C_{+}(x',\omega)\eta(x,\omega). \tag{A.104}$$

Substituting Eq. (A.104) in the governing equation (2.21), and after simplification, we have two linear equations for the unknowns $A_-(x',\omega)$ and $C_+(x',\omega)$:

$$-A_-(x',\omega)\beta(x',\omega) + C_+(x',\omega)\eta(x',\omega) = 0, \tag{A.105a}$$

$$(c_2^2 - \bar{u}_2^2)\left[C_+(x',\omega)\left.\frac{\mathrm{d}\eta}{\mathrm{d}x}\right|_{x=x'} - A_-(x',\omega)\left.\frac{\mathrm{d}\beta}{\mathrm{d}x}\right|_{x=x'}\right] = -1. \tag{A.105b}$$

Using Cramer's rule, the solution of $A_-(x',\omega)$ and $C_+(x',\omega)$ can be calculated as

$$A_-(x',\omega) = \frac{det_A}{det}, \qquad C_+(x',\omega) = \frac{det_C}{det} \tag{A.106}$$

where the determinants are (with the assumption $x' \to x_T$)

$$det = \begin{vmatrix} -\beta(x',\omega) & \eta(x',\omega) \\ -(c_2^2 - \bar{u}_2^2)\left.\frac{\mathrm{d}\beta}{\mathrm{d}x}\right|_{x=x'} & (c_2^2 - \bar{u}_2^2)\left.\frac{\mathrm{d}\eta}{\mathrm{d}x}\right|_{x=x'} \end{vmatrix} = \frac{2\mathrm{i}\omega\bar{u}_2 F(\omega)}{T_{\mathrm{BA}}}, \tag{A.107}$$

$$det_A = \begin{vmatrix} 0 & \eta(x',\omega) \\ -1 & (c_2^2 - \bar{u}_2^2)\left.\frac{\mathrm{d}\eta}{\mathrm{d}x}\right|_{x=x'} \end{vmatrix} = \eta(x',\omega), \tag{A.108}$$

$$det_C = \begin{vmatrix} -\beta(x',\omega) & 0 \\ -(c_2^2 - \bar{u}_2^2)\left.\frac{\mathrm{d}\beta}{\mathrm{d}x}\right|_{x=x'} & -1 \end{vmatrix} = \beta(x',\omega). \tag{A.109}$$

The expression of $\hat{g}(x,x',\omega)$ now is

$$\hat{g}(x,x',\omega) = \frac{T_{\mathrm{BA}}}{2\mathrm{i}\omega\bar{u}_2 F(\omega)} \begin{cases} \eta(x',\omega)\,\alpha(x,\omega) & \text{for } 0 < x < x_T, \\ \eta(x',\omega)\,\beta(x,\omega) & \text{for } x_T < x < x', \\ \beta(x',\omega)\,\eta(x,\omega) & \text{for } x' < x < L. \end{cases} \tag{A.110}$$

The time-domain direct Green's function $g(x,x',t-t')$ is calculated by applying the residue theorem, and the final expression of the direct Green's function in the time domain is

$$g(x,x',t-t') = H(t-t')\sum_{n=1}^{\infty} \Re\left[\hat{g}_n(x,x',\omega_n)e^{-i\omega_n(t-t')}\right], \tag{A.111}$$

with

$$\hat{g}_n(x,x',\omega_n) = -\frac{2\pi\, T_{\mathrm{BA}}}{\bar{u}_2\omega_n F'(\omega_n)} \begin{cases} \eta(x',\omega_n)\,\alpha(x,\omega_n) & \text{for } 0 < x < x_T, \\ \eta(x',\omega_n)\,\beta(x,\omega_n) & \text{for } x_T < x < x', \\ \beta(x',\omega_n)\,\eta(x,\omega_n) & \text{for } x' < x < L. \end{cases} \tag{A.112}$$

The AGF can be obtained by replacing the $\bar{u}_1, \bar{u}_2$ in the solution of the direct Green's function with $-\bar{u}_1, -\bar{u}_2$.

APPENDIX FOR CHAPTER 3

B.1. THE BASE FLOW SYSTEM

The equations governing the base flow, $\mathbf{B}(\bar{\mathbf{q}}) = 0$, are listed below:

1. Ideal gas assumption in each duct:

$$\bar{p}_i = \bar{\rho}_i R_g \bar{T}_i, \tag{B.1}$$

   where R_g is the perfect gas constant.

2. Mass conservation equations at the duct intersections, at $x = l_1$ and $x = l_2$:

$$\bar{\dot{m}} = \bar{\rho}_1 \bar{u}_1 a_1 = \bar{\rho}_2 \bar{u}_2 a_2 = \bar{\rho}_3 \bar{u}_3 a_3. \tag{B.2}$$

3. Energy conservation equations at the duct intersections, at $x = l_1$ and $x = l_2$:

$$\bar{\rho}_1 \bar{u}_1 a_1 \bar{H}_1 = \bar{\rho}_2 \bar{u}_2 a_2 \bar{H}_2, \tag{B.3a}$$

$$\bar{\rho}_2 \bar{u}_2 a_2 \bar{H}_2 + a_3 \bar{Q} = \bar{\rho}_3 \bar{u}_3 a_3 \bar{H}_3, \tag{B.3b}$$

   where $\bar{H} = C_p \bar{T} + \frac{1}{2}\bar{u}^2$, with C_p the specific heat capacity. The mean heat released by the flame ($\bar{Q}$) appears in the energy conservation equation at the premixer-chamber intersection.

4. Isentropic condition at $x = l_1$ where the cross-sectional area decreases suddenly:

$$\bar{p}_1 / \bar{p}_2 = (\bar{\rho}_1 / \bar{\rho}_2)^{\gamma}, \tag{B.4}$$

   with $\gamma = C_p / C_v$ the specific heat ratio.

5. Conservation of linear momentum across the sudden expansion at $x = l_2$ (also known as Borda-Carnot equation):

$$\bar{\rho}_3 \bar{u}_3^2 a_3 - \bar{\rho}_2 \bar{u}_2^2 a_2 = a_3 (\bar{p}_2 - \bar{p}_3). \tag{B.5}$$

6. The boundary conditions provide the following parameters of the problem:

$$\bar{T}_1 = 300 \text{ K}, \quad \bar{p}_3 = 101000 \text{ Pa}, \quad \bar{T}_3 = T_f = 2000 \text{ K}. \tag{B.6}$$

The mass flow rate across the system is

$$\bar{\dot{m}} = 0.05 \text{ kg/s}; \tag{B.7}$$

solving the equations above, the base flow variables attain the values listed in Table B.1.

Table B.1: Values of the base flow variables in the three-duct combustor.

Velocity [m/s]	Pressure [Pa]	Temperature [K]	Density [kg/m^3]	Heat release rate [J/(m^{-2})]
$\bar{u}_1 = 3.27$	$\bar{p}_1 = 1.0209 \times 10^5$	$\bar{T}_1 = 300$	$\bar{\rho}_1 = 1.1857$	
$\bar{u}_2 = 29.80$	$\bar{p}_2 = 1.0157 \times 10^5$	$\bar{T}_2 = 299.5655$	$\bar{\rho}_2 = 1.1814$	$\bar{Q} = 2.2334 \times 10^7$
$\bar{u}_3 = 73.81$	$\bar{p}_3 = 1.0100 \times 10^5$	$\bar{T}_3 = 2000$	$\bar{\rho}_3 = 10.1760$	

.

B.2. NON-ZERO ELEMENTS OF MATRIX $\mathcal{A}$

The non-zero elements in the matrix $\mathcal{A}$ are listed below:

$$\mathcal{A}(1,4) = \frac{\left(-k_{+2}\,\bar{c}_2^2 + \bar{u}_2\alpha_{+2}\right)\kappa\bar{Q}\mathrm{e}^{\mathrm{i}k_{+2}l_2 - \mathrm{i}\omega\tau}}{\alpha_{+2}\bar{\rho}_2\bar{u}_2\,\bar{c}_2^2}, \tag{B.8}$$

$$\mathcal{A}(1,5) = \frac{\left(-k_{-2}\,\bar{c}_2^2 + \bar{u}_2\alpha_{-2}\right)\kappa\bar{Q}\mathrm{e}^{\mathrm{i}k_{-2}l_2 - \mathrm{i}\omega\tau}}{\alpha_{-2}\bar{\rho}_2\bar{u}_2\,\bar{c}_2^2}, \tag{B.9}$$

$$\mathcal{A}(1,6) = -\frac{\mathrm{e}^{\mathrm{i}k_{02}l_2 - \mathrm{i}\omega\tau}\bar{Q}\kappa}{\bar{\rho}_2\,\bar{c}_2^2}, \tag{B.10}$$

$$\mathcal{A}(1,10) = 1, \tag{B.11}$$

$$\mathcal{A}(2,1) = \frac{\left(-k_{+1}\,\bar{c}_1^2 + \bar{u}_1\alpha_{+1}\right)a_1\mathrm{e}^{\mathrm{i}k_{+1}l_1}}{\alpha_{+1}\,\bar{c}_1^2}, \tag{B.12}$$

$$\mathcal{A}(2,2) = \frac{\left(-k_{-1}\,\bar{c}_1^2 + \bar{u}_1\alpha_{-1}\right)a_1\mathrm{e}^{\mathrm{i}k_{-1}l_1}}{\alpha_{-1}\,\bar{c}_1^2}, \tag{B.13}$$

$$\mathcal{A}(2,3) = -\frac{\mathrm{e}^{\mathrm{i}k_{01}l_1}\bar{u}_1a_1}{\bar{c}_1^2}, \tag{B.14}$$

$$\mathcal{A}(2,4) = \frac{a_2\left(k_{+2}\,\bar{c}_2^2 - \bar{u}_2\alpha_{+2}\right)\mathrm{e}^{\mathrm{i}k_{+2}l_1}}{\alpha_{+2}\,\bar{c}_2^2}, \tag{B.15}$$

$$\mathcal{A}(2,5) = \frac{a_2\left(k_{-2}\,\bar{c}_2^2 - \bar{u}_2\alpha_{-2}\right)\mathrm{e}^{\mathrm{i}k_{-2}l_1}}{\alpha_{-2}\,\bar{c}_2^2}, \tag{B.16}$$

$$\mathcal{A}(2,6) = \frac{\mathrm{e}^{\mathrm{i}k_{02}l_1}\bar{u}_2a_2}{\bar{c}_2^2}, \tag{B.17}$$

$$\mathcal{A}(3,1) = \frac{\left(-\bar{c}_1^2\bar{\rho}_1 + \gamma\bar{p}_1\right)\mathrm{e}^{\mathrm{i}k_{+1}l_1}}{\bar{c}_1^2\bar{\rho}_1\bar{p}_1}, \tag{B.18}$$

$$\mathcal{A}(3,2) = \frac{\left(-\bar{c}_1^2\bar{\rho}_1 + \gamma\bar{p}_1\right)\mathrm{e}^{\mathrm{i}k_{-1}l_1}}{\bar{c}_1^2\bar{\rho}_1\bar{p}_1}, \tag{B.19}$$

$$\mathcal{A}(3,3) = -\frac{\gamma\mathrm{e}^{\mathrm{i}k_{01}l_1}}{\bar{c}_1^2\bar{\rho}_1}, \tag{B.20}$$

$$\mathcal{A}(3,4) = -\frac{(-\bar{\rho}_2\,\bar{c}_2^2 + \gamma\bar{p}_2)\,\mathrm{e}^{\mathrm{i}k_{+2}l_1}}{\bar{c}_2^2\bar{\rho}_2\bar{p}_2}, \tag{B.21}$$

$$\mathcal{A}(3,5) = -\frac{(-\bar{\rho}_2\,\bar{c}_2^2 + \gamma\bar{p}_2)\,\mathrm{e}^{\mathrm{i}k_{-2}l_1}}{\bar{c}_2^2\bar{\rho}_2\bar{p}_2}, \tag{B.22}$$

$$\mathcal{A}(3,6) = \frac{\gamma\mathrm{e}^{\mathrm{i}k_{02}l_1}}{\bar{c}_2^2\bar{\rho}_2}, \tag{B.23}$$

$$\mathcal{A}(4,1) = -\frac{\left[C_p\left(R_g\bar{T}_1 - \bar{c}_1^2\right)\alpha_{+1} + k_{+1}R_g\bar{u}_1\,\bar{c}_1^2\right]\mathrm{e}^{\mathrm{i}k_{+1}l_1}}{\bar{\rho}_1 R_g\,\bar{c}_1^2\alpha_{+1}}, \tag{B.24}$$

$$\mathcal{A}(4,2) = -\frac{\left[C_p\left(R_g\bar{T}_1 - \bar{c}_1^2\right)\alpha_{-1} + k_{-1}R_g\bar{u}_1\,\bar{c}_1^2\right]\mathrm{e}^{\mathrm{i}k_{-1}l_1}}{\bar{\rho}_1 R_g\,\bar{c}_1^2\alpha_{-1}}, \tag{B.25}$$

$$\mathcal{A}(4,3) = \frac{C_p\mathrm{e}^{\mathrm{i}k_{01}l_1}\bar{T}_1}{\bar{\rho}_1\,\bar{c}_1^2}, \tag{B.26}$$

$$\mathcal{A}(4,4) = \frac{\left[C_p\left(R_g\bar{T}_2 - \bar{c}_2^2\right)\alpha_{+2} + k_{+2}R_g\bar{u}_2\,\bar{c}_2^2\right]\mathrm{e}^{\mathrm{i}k_{+2}l_1}}{R_g\bar{\rho}_2\,\bar{c}_2^2\alpha_{+2}}, \tag{B.27}$$

$$\mathcal{A}(4,5) = \frac{\left[C_p\left(R_g\bar{T}_2 - \bar{c}_2^2\right)\alpha_{-2} + k_{-2}R_g\bar{u}_2\,\bar{c}_2^2\right]\mathrm{e}^{\mathrm{i}k_{-2}l_1}}{R_g\bar{\rho}_2\,\bar{c}_2^2\alpha_{-2}}, \tag{B.28}$$

$$\mathcal{A}(4,6) = -\frac{C_p\mathrm{e}^{\mathrm{i}k_{02}l_1}\bar{T}_2}{\bar{\rho}_2\,\bar{c}_2^2}, \tag{B.29}$$

$$\mathcal{A}(5,4) = \frac{(-k_{+2}\,\bar{c}_2^2 + \bar{u}_2\alpha_{+2})\,a_2\mathrm{e}^{\mathrm{i}k_{+2}l_2}}{\alpha_{+2}\,\bar{c}_2^2}, \tag{B.30}$$

$$\mathcal{A}(5,5) = \frac{(-k_{-2}\,\bar{c}_2^2 + \bar{u}_2\alpha_{-2})\,a_2\mathrm{e}^{\mathrm{i}k_{-2}l_2}}{\alpha_{-2}\,\bar{c}_2^2}, \tag{B.31}$$

$$\mathcal{A}(5,6) = -\frac{\mathrm{e}^{\mathrm{i}k_{02}l_2}\bar{u}_2a_2}{\bar{c}_2^2}, \tag{B.32}$$

$$\mathcal{A}(5,7) = \frac{a_3\,(k_{+3}\,\bar{c}_3^2 - \bar{u}_3\alpha_{+3})\,\mathrm{e}^{\mathrm{i}k_{+3}l_2}}{\alpha_{+3}\,\bar{c}_3^2}, \tag{B.33}$$

$$\mathcal{A}(5,8) = \frac{a_3\,(k_{-3}\,\bar{c}_3^2 - \bar{u}_3\alpha_{-3})\,\mathrm{e}^{\mathrm{i}k_{-3}l_2}}{\alpha_{-3}\,\bar{c}_3^2}, \tag{B.34}$$

$$\mathcal{A}(5,9) = \frac{\mathrm{e}^{\mathrm{i}k_{03}l_2}\bar{u}_3a_3}{\bar{c}_3^2}, \tag{B.35}$$

$$\mathcal{A}(6,4) = \frac{[(\bar{u}_2^2a_2 + a_3\,\bar{c}_2^2)\,\alpha_{+2} - 2k_{+2}\bar{u}_2a_2\,\bar{c}_2^2]\,\mathrm{e}^{\mathrm{i}k_{+2}l_2}}{\bar{c}_2^2\alpha_{+2}}, \tag{B.36}$$

$$\mathcal{A}(6,5) = \frac{[(\bar{u}_2^2a_2 + a_3\,\bar{c}_2^2)\,\alpha_{-2} - 2k_{-2}\bar{u}_2a_2\,\bar{c}_2^2]\,\mathrm{e}^{\mathrm{i}k_{-2}l_2}}{\bar{c}_2^2\alpha_{-2}}, \tag{B.37}$$

$$\mathcal{A}(6,6) = -\frac{\mathrm{e}^{\mathrm{i}k_{02}l_2}\bar{u}_2^2 a_2}{\bar{c}_2^2}, \tag{B.38}$$

$$\mathcal{A}(6,7) = -\frac{\mathrm{e}^{\mathrm{i}k_{+3}l_2}\left[\left(\bar{u}_3^2+\bar{c}_3^2\right)\alpha_{+3}+2k_{+3}\bar{u}_3\,\bar{c}_3^2\right]a_3}{\bar{c}_3^2\alpha_{+3}}, \tag{B.39}$$

$$\mathcal{A}(6,8) = -\frac{\mathrm{e}^{\mathrm{i}k_{-3}l_2}\left[\left(\bar{u}_3^2+\bar{c}_3^2\right)\alpha_{-3}+2k_{-3}\bar{u}_3\,\bar{c}_3^2\right]a_3}{\bar{c}_3^2\alpha_{-3}}, \tag{B.40}$$

$$\mathcal{A}(6,9) = \frac{\mathrm{e}^{\mathrm{i}k_{03}l_2}\bar{u}_3^2 a_3}{\bar{c}_3^2}, \tag{B.41}$$

$$\mathcal{A}(7,4) = -\frac{a_2\left\{\left[\bar{u}_2\left(C_p\bar{T}_2-\bar{H}_2\right)\alpha_{+2}+\bar{c}_2^2k_{+2}\left(\bar{u}_2^2+\bar{H}_2\right)\right]R_g-C_p\bar{u}_2\,\bar{c}_2^2\alpha_{+2}\right\}\mathrm{e}^{\mathrm{i}k_{+2}l_2}}{R_g\,\bar{c}_2^2\alpha_{+2}}, \tag{B.42}$$

$$\mathcal{A}(7,5) = -\frac{a_2\left\{\left[\bar{u}_2\left(C_p\bar{T}_2-\bar{H}_2\right)\alpha_{-2}+\bar{c}_2^2k_{-2}\left(\bar{u}_2^2+\bar{H}_2\right)\right]R_g-C_p\bar{u}_2\,\bar{c}_2^2\alpha_{-2}\right\}\mathrm{e}^{\mathrm{i}k_{-2}l_2}}{R_g\,\bar{c}_2^2\alpha_{-2}}, \tag{B.43}$$

$$\mathcal{A}(7,6) = \frac{a_2\bar{u}_2\left(C_p\bar{T}_2-\bar{H}_2\right)\mathrm{e}^{\mathrm{i}k_{02}l_2}}{\bar{c}_2^2}, \tag{B.44}$$

$$\mathcal{A}(7,7) = \frac{a_3\left\{\left[\bar{u}_3\left(C_p\bar{T}_3-\bar{H}_3\right)\alpha_{+3}+\bar{c}_3^2k_{+3}\left(\bar{u}_3^2+\bar{H}_3\right)\right]R_g-C_p\bar{u}_3\,\bar{c}_3^2\alpha_{+3}\right\}\mathrm{e}^{\mathrm{i}k_{+3}l_2}}{R_g\,\bar{c}_3^2\alpha_{+3}}, \tag{B.45}$$

$$\mathcal{A}(7,8) = \frac{a_3\left\{\left[\bar{u}_3\left(C_p\bar{T}_3-\bar{H}_3\right)\alpha_{-3}+\bar{c}_3^2k_{-3}\left(\bar{u}_3^2+\bar{H}_3\right)\right]R_g-C_p\bar{u}_3\,\bar{c}_3^2\alpha_{-3}\right\}\mathrm{e}^{\mathrm{i}k_{-3}l_2}}{R_g\,\bar{c}_3^2\alpha_{-3}}, \tag{B.46}$$

$$\mathcal{A}(7,9) = -\frac{a_3\bar{u}_3\left(C_p\bar{T}_3-\bar{H}_3\right)\mathrm{e}^{\mathrm{i}k_{03}l_2}}{\bar{c}_3^2}, \tag{B.47}$$

$$\mathcal{A}(7,10) = a_3, \tag{B.48}$$

$$\mathcal{A}(8,1) = \frac{-k_{+1}\,\bar{c}_1^2+\bar{u}_1\alpha_{+1}}{\bar{c}_1^2\bar{\rho}_1\alpha_{+1}\bar{u}_1}, \tag{B.49}$$

$$\mathcal{A}(8,2) = \frac{-k_{-1}\,\bar{c}_1^2+\bar{u}_1\alpha_{-1}}{\bar{c}_1^2\bar{\rho}_1\alpha_{-1}\bar{u}_1}, \tag{B.50}$$

$$\mathcal{A}(8,3) = -\frac{1}{\bar{c}_1^2\bar{\rho}_1}, \tag{B.51}$$

$$\mathcal{A}(9,3) = 1, \tag{B.52}$$

$$\mathcal{A}(10,7) = \mathrm{e}^{\mathrm{i}k_{+3}l_3}, \tag{B.53}$$

$$\mathcal{A}(10,8) = \mathrm{e}^{\mathrm{i}k_{-3}l_3}. \tag{B.54}$$

B.3. THE ADJOINT BASE FLOW SYSTEM

The adjoint base flow equations (3.25) in the expanded form are:

$$b_7^{\dagger *} a_3 = -\mathbf{y}^{\dagger *} \frac{\partial \mathcal{A}}{\partial \bar{Q}} \mathbf{x}, \tag{B.55}$$

$$\bar{\rho}_1 a_1 \left[ ] b_6^{\dagger *} (\bar{H}_1 + \bar{u}_1^2) + b_{10}^{\dagger *} + b_4^{\dagger *} \right] = -\mathbf{y}^{\dagger *} \frac{\partial \mathcal{A}}{\partial \bar{u}_1} \mathbf{x}, \tag{B.56}$$

$$a_2 \bar{\rho}_2 \left[\left(b_6^{\dagger *} - b_7^{\dagger *} \right) (\bar{H}_2 + \bar{u}_2^2) + 2\bar{u}_2 b_9^{\dagger *} + b_4^{\dagger *} - b_5^{\dagger *} \right] = -\mathbf{y}^{\dagger *} \frac{\partial \mathcal{A}}{\partial \bar{u}_2} \mathbf{x}, \tag{B.57}$$

$$-a_3 \bar{\rho}_3 \left[(\bar{H}_3 + \bar{u}_3^2) b_7^{\dagger *} - 2\bar{u}_3 b_9^{\dagger *} + b_5^{\dagger *} \right] = -\mathbf{y}^{\dagger *} \frac{\partial \mathcal{A}}{\partial \bar{u}_3} \mathbf{x}, \tag{B.58}$$

$$b_1^{\dagger *} + \frac{b_8^{\dagger *}}{\bar{p}_2} = -\mathbf{y}^{\dagger *} \frac{\partial \mathcal{A}}{\partial \bar{p}_1} \mathbf{x}, \tag{B.59}$$

$$\frac{1}{\bar{p}_2^2} \left(b_9^{\dagger *} a_3 - b_8^{\dagger *} \bar{p}_1 \right) + b_2^{\dagger *} = -\mathbf{y}^{\dagger *} \frac{\partial \mathcal{A}}{\partial \bar{p}_2} \mathbf{x}, \tag{B.60}$$

$$-b_9^{\dagger *} a_3 + b_{12}^{\dagger *} + b_3^{\dagger *} = -\mathbf{y}^{\dagger *} \frac{\partial \mathcal{A}}{\partial \bar{p}_3} \mathbf{x} = 0, \tag{B.61}$$

$$-\frac{\gamma}{\bar{\rho}_1} \left(\frac{\bar{\rho}_1}{\bar{\rho}_2} \right)^{\gamma} b_8^{\dagger *} + \left[a_1 \bar{u}_1 \left(\bar{H}_1 b_6^{\dagger *} + b_{10}^{\dagger *} + b_4^{\dagger *} \right) - R_g \bar{T}_1 b_1^{\dagger *} \right] = -\mathbf{y}^{\dagger *} \frac{\partial \mathcal{A}}{\partial \bar{\rho}_1} \mathbf{x}, \tag{B.62}$$

$$-a_2 \bar{u}_2 \left[\left(b_6^{\dagger *} - b_7^{\dagger *} \right) \bar{H}_2 + b_9^{\dagger *} \bar{u}_2 + \left(b_4^{\dagger *} - b_5^{\dagger *} \right) \right] - b_2^{\dagger *} R_g \bar{T}_2 + 2\gamma \left(\frac{\bar{\rho}_1}{\bar{\rho}_2} \right)^{\gamma} b_8^{\dagger *} = -\mathbf{y}^{\dagger *} \frac{\partial \mathcal{A}}{\partial \bar{\rho}_2} \mathbf{x}, \tag{B.63}$$

$$-a_3 \bar{u}_3 \left(b_7^{\dagger *} \bar{H}_3 - b_9^{\dagger *} \bar{u}_3 + b_5^{\dagger *} \right) - b_3^{\dagger *} R_g \bar{T}_3 = -\mathbf{y}^{\dagger *} \frac{\partial \mathcal{A}}{\partial \bar{\rho}_3} \mathbf{x} = 0, \tag{B.64}$$

$$b_6^{\dagger *} C_p \bar{\rho}_1 \bar{u}_1 a_1 - b_1^{\dagger *} R_g \bar{\rho}_1 + b_{11}^{\dagger *} = -\mathbf{y}^{\dagger *} \frac{\partial \mathcal{A}}{\partial \bar{T}_1} \mathbf{x}, \tag{B.65}$$

$$C_p \bar{u}_2 \bar{\rho}_2 a_2 \left(b_6^{\dagger *} - b_7^{\dagger *} \right) + b_2^{\dagger *} R_g \bar{\rho}_2 = -\mathbf{y}^{\dagger *} \frac{\partial \mathcal{A}}{\partial \bar{T}_2} \mathbf{x}, \tag{B.66}$$

$$b_7^{\dagger *} C_p \bar{\rho}_3 \bar{u}_3 a_3 - b_3^{\dagger *} R_g \bar{\rho}_3 + b_{13}^{\dagger *} = -\mathbf{y}^{\dagger *} \frac{\partial \mathcal{A}}{\partial \bar{T}_3} \mathbf{x}. \tag{B.67}$$

B.4. THE ADJOINT DISTURBANCE FLOW SYSTEM

The differential equations of the adjoint disturbance flow system, Eq. (3.36) in full form are:

$$\mathrm{i}\omega^*\hat{\rho}^\dagger + \bar{u}\frac{\mathrm{d}\hat{\rho}^\dagger}{\mathrm{d}x} = 0, \tag{B.68a}$$

$$\mathrm{i}\omega^*\bar{\rho}\hat{u}^\dagger + \bar{\rho}\bar{u}_j\frac{\mathrm{d}\hat{u}^\dagger}{\mathrm{d}x} + \bar{\rho}\frac{\mathrm{d}\hat{\rho}^\dagger}{\mathrm{d}x} + \gamma\bar{p}\frac{\mathrm{d}\hat{p}^\dagger}{\mathrm{d}x} = 0, \tag{B.68b}$$

$$\mathrm{i}\omega^*\hat{p}^\dagger + \bar{u}\frac{\mathrm{d}\hat{p}^\dagger}{\mathrm{d}x} + \frac{\mathrm{d}\hat{u}^\dagger}{\mathrm{d}x} = 0, \tag{B.68c}$$

where $j = 1, 2, 3$ indicates each section of the duct.

The boundary conditions of the adjoint system yielded from the boundary terms at $x = 0$ and $x = l_3$ generated from integration by parts, are:

$$\hat{u}_1^\dagger(0) = 0, \qquad \hat{\rho}_3^\dagger(l_3) = 0, \qquad \bar{u}_3\hat{u}_3^\dagger(l_3) + \bar{c}_3^2\hat{p}_3^\dagger(l_3) = 0. \tag{B.69}$$

The formulations of adjoint variables $\hat{\mathbf{f}}^\dagger$ are:

$$\hat{f}_1^\dagger = \frac{1}{a_2}[\hat{\rho}_2^\dagger(l_1) + \bar{c}_2^2\hat{p}_2^\dagger(l_1)], \tag{B.70a}$$

$$\hat{f}_2^\dagger = \frac{1}{\gamma-1}\bar{p}_2\hat{u}_2^\dagger(l_1) - \bar{u}_2\bar{p}_2\hat{p}_2^\dagger(l_1), \tag{B.70b}$$

$$\hat{f}_3^\dagger = \bar{\rho}_2\hat{u}_2^\dagger(l_1), \tag{B.70c}$$

$$\hat{f}_4^\dagger = \frac{1}{a_3}[\hat{\rho}_3^\dagger(l_2) - \bar{u}_3\hat{u}_3^\dagger(l_2) + \frac{\gamma-1}{2}\bar{u}_3^2\hat{p}_3^\dagger(l_2)], \tag{B.70d}$$

$$\hat{f}_5^\dagger = \frac{1}{a_3}[\hat{u}_3^\dagger(l_2) + (1-\gamma)\bar{u}_3\hat{p}_3^\dagger(l_2)], \tag{B.70e}$$

$$\hat{f}_6^\dagger = \frac{1}{a_3}(\gamma-1)\hat{p}_3^\dagger(l_2). \tag{B.70f}$$

The adjoint jump conditions are:

$$\bar{u}_1\bar{\rho}_1[a_1\hat{\rho}_2^\dagger(l_1) - a_2\hat{\rho}_1^\dagger(l_1)] = \gamma(a_2\bar{u}_2\bar{p}_2 - a_1\bar{u}_1\bar{p}_1)\hat{p}_2^\dagger(l_1), \tag{B.71a}$$

$$a_1\bar{\rho}_1\left[\frac{1}{a_2}\hat{\rho}_2^\dagger(l_1) - \frac{1}{a_1}\hat{\rho}_1^\dagger(l_1)\right] + \bar{u}_1\left[\bar{\rho}_2\hat{u}_2^\dagger(l_1) - \bar{\rho}_1\hat{u}_1^\dagger(l_1)\right] + a_1\bar{\rho}_1\left[\frac{1}{a_2}\bar{c}_2^2\hat{p}_2^\dagger(l_1) - \frac{1}{a_1}\bar{c}_1^2\hat{p}_1^\dagger(l_1)\right] = 0, \tag{B.71b}$$

$$\bar{p}_1\hat{u}_1^\dagger(l_1) + (\bar{p}_2 - \bar{c}_1^2\bar{\rho}_2)\frac{1}{\gamma-1}\hat{u}_2^\dagger(l_1) + \bar{u}_1\bar{p}_1\hat{p}_1^\dagger(l_1) - \bar{u}_2\bar{p}_2\hat{p}_2^\dagger(l_1) = 0, \tag{B.71c}$$

$$a_2\left[\frac{1}{a_3}\hat{\rho}_3^\dagger(l_2) - \frac{1}{a_2}\hat{\rho}_2^\dagger(l_2)\right] = \frac{a_2}{a_3}(\bar{u}_3 - \bar{u}_2)\hat{u}_3^\dagger(l_2) + \left[\frac{a_2}{2a_3}(\bar{u}_3 - \bar{u}_2)^2 - \frac{\kappa\bar{Q}}{\bar{u}_2\bar{\rho}_2}\mathrm{e}^{\mathrm{i}\omega^*\tau}\right](1-\gamma)\hat{p}_3^\dagger(l_2), \tag{B.71d}$$

$$a_3\hat{\rho}_2^\dagger(l_2) - a_2\hat{\rho}_3^\dagger(l_2) + a_3\bar{u}_2\hat{u}_2^\dagger(l_2) + a_2\bar{u}_3\hat{u}_3^\dagger(l_2) - 2a_2\bar{u}_2\hat{u}_3^\dagger(l_2) + a_3\bar{c}_2^2\hat{p}_2^\dagger(l_2) - a_2\bar{c}_2^2\hat{p}_3^\dagger(l_2)$$
$$= (\gamma-1)\hat{p}_3^\dagger(l_2)\left[a_2(\frac{1}{2}\bar{u}_3^2 - 2\bar{u}_2\bar{u}_3 + \frac{3}{2}\bar{u}_2^2) - a_3\frac{\kappa\bar{Q}}{\bar{\rho}_2\bar{u}_2}\mathrm{e}^{\mathrm{i}\omega^*\tau}\right], \tag{B.71e}$$

$$\hat{u}_3^\dagger(l_2) - \hat{u}_2^\dagger(l_2) + \left[\frac{a_2}{a_3}\gamma\bar{u}_2 + (1-\gamma)\bar{u}_3\right]\hat{p}_3^\dagger(l_2) - \bar{u}_2\hat{p}_2^\dagger(l_2) = 0. \tag{B.71f}$$

With the differential equations (B.68), the adjoint variables $\hat{\mathbf{q}}^\dagger = (\hat{p}^\dagger, \hat{\rho}^\dagger, \hat{u}^\dagger)$ can be decoupled as follows,

$$\hat{p}_j^\dagger = A_{+j}^\dagger \mathrm{e}^{\mathrm{i}k_{+j}^\dagger x} + A_{-j}^\dagger \mathrm{e}^{\mathrm{i}k_{-j}^\dagger x} + A_{ej}^\dagger \mathrm{e}^{\mathrm{i}k_{0j}^\dagger x}, \tag{B.72a}$$

$$\hat{\rho}_j^\dagger = -\bar{c}_j^2 A_{ej}^\dagger \mathrm{e}^{\mathrm{i}k_{0j}^\dagger x}, \tag{B.72b}$$

$$\hat{u}_j^\dagger = -\frac{k_{+j}^\dagger \bar{c}_j^2}{\alpha_{+j}^\dagger} A_{+j}^\dagger \mathrm{e}^{\mathrm{i}k_{+j}^\dagger x} - \frac{k_{-}^\dagger \bar{c}_j^2}{\alpha_{-j}^\dagger} A_{-j}^\dagger \mathrm{e}^{\mathrm{i}k_{-j}^\dagger x}, \tag{B.72c}$$

together with the relations:

$$k_{\pm j}^\dagger = -\frac{\omega^*}{\bar{u}_j \pm \bar{c}_j}, \quad k_{0j}^\dagger = -\frac{\omega^*}{\bar{u}_j}, \quad \alpha_{\pm j}^\dagger = \omega^* + \bar{u}_j k_{\pm j}^\dagger. \tag{B.73}$$

Using the decoupling relation (B.72), the boundary conditions (B.69) and the jump conditions (B.71) of the adjoint disturbance system can be organized in matrix form and can be solved with the inverse iteration method. The eigenvector consists of the adjoint decoupled wave amplitudes ($A_{+\,j}^\dagger$, $A_{-\,j}^\dagger$, $A_{e\,j}^\dagger$, $j = 1, 2, 3$ indicating each duct section). The mode shapes of the adjoint perturbation variables can be reconstructed accordingly; they are shown in Figs. B.1 and B.2.

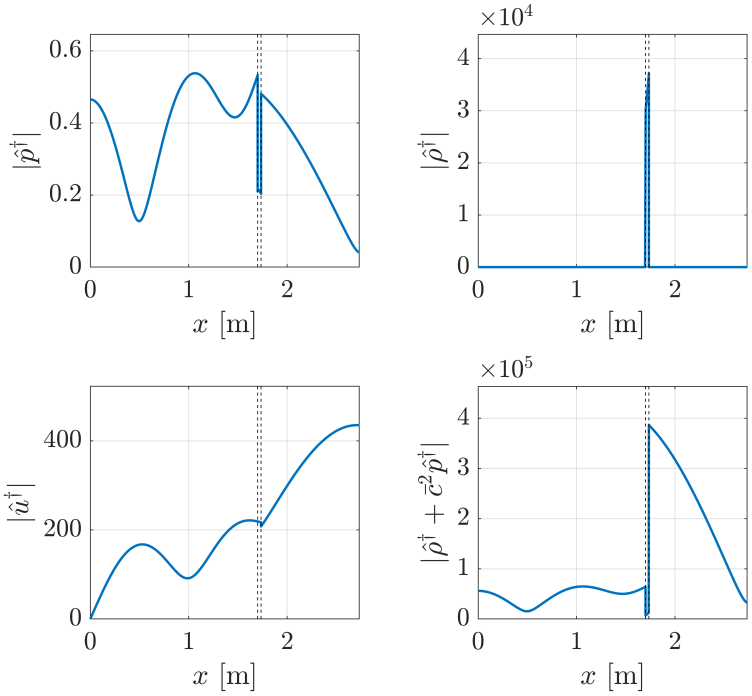

Figure B.1: Absolute values of the mode shapes of the adjoint variables $\hat{p}^\dagger$, $\hat{u}^\dagger$, and $\hat{\rho}^\dagger$ for eigenmode TA_1. The frame on the bottom right represents the receptivity of the system to disturbances in the mass flow rate.

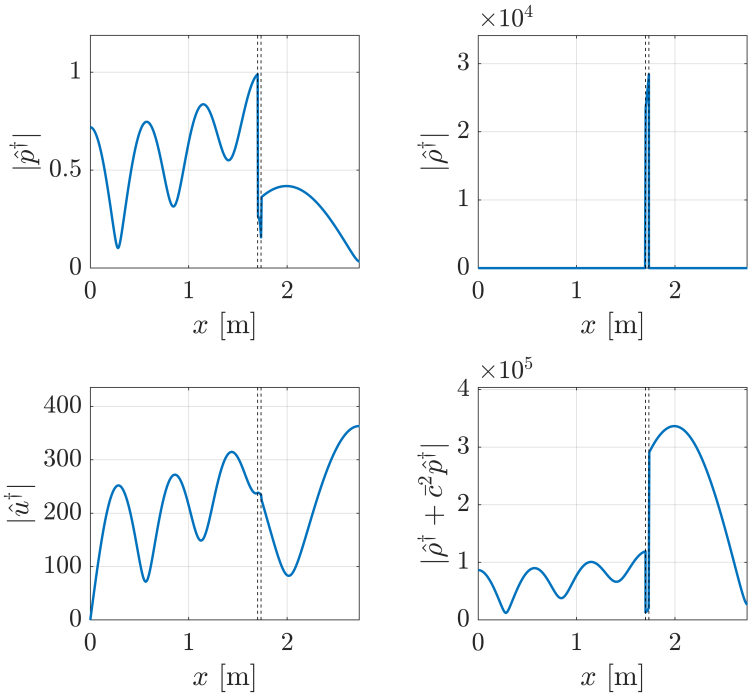

Figure B.2: Same as Figure B.1 for eigenmode TA_2.

APPENDIX FOR CHAPTER 4

C.1. DERIVATION OF THE PROBLEM FOR $\pi^{(1)}$

Subtracting the time derivative of Eq. (4.22a) from the spatial derivative of Eq. (4.28b), we obtain

$$\frac{\partial^2 \pi^{(1)}}{\partial x_i^2} = 0. \tag{C.1}$$

Furthermore, since $\pi^{(0)}$ is only dependent on the X_2 coordinate, it is

$$\frac{\partial \pi^{(0)}}{\partial X_2} = \frac{\partial p^{(0)}}{\partial X_2}(0^+, X_2, \tau) = \frac{\partial P^{(0)}}{\partial X_2}(0^-, X_2, \tau). \tag{C.2}$$

Using Eq. (4.28b), the time derivative of Eq. (4.28c) gives

$$\left(\frac{\partial \pi^{(1)}}{\partial x_i} + \frac{\partial \pi^{(0)}}{\partial X_2}\delta_{2i}\right) n_i = \left(\frac{\partial \pi^{(1)}}{\partial x_i} + \frac{\partial P^{(0)}}{\partial X_2}(0^-, X_2, \tau)\delta_{2i}\right) n_i = 0, \qquad \text{at } \mathcal{A}_{\beta\sigma}. \tag{C.3}$$

From the time derivative of Eq. (4.24) and using Eqs. (4.21b) and (4.29b), it is known that

$$\frac{\partial p^{(0)}}{\partial X_1}(0^+, X_2, \tau) + \frac{\partial p^{(1)}}{\partial x_1}(0^+, X_2, x_i, \tau) = \frac{\partial P^{(0)}}{\partial X_1}(0^-, X_2, \tau). \tag{C.4}$$

Using Eqs. (4.21b), (4.28b), and (4.29b), and with account of Eq. (C.4), the time derivatives of Eq. (4.19b) and Eq. (4.19d) lead to

$$\lim_{x_1 \to +x_\infty} \frac{\partial \pi^{(1)}}{\partial x_1} = \frac{\partial p^{(0)}}{\partial X_1}(0^+, X_2, \tau) + \frac{\partial p^{(1)}}{\partial x_1}(0^+, X_2, x_i, \tau) = \frac{\partial P^{(0)}}{\partial X_1}(0^-, X_2, \tau), \tag{C.5a}$$

$$\lim_{x_1 \to -x_\infty} \frac{\partial \pi^{(1)}}{\partial x_1} = \frac{\partial P^{(0)}}{\partial X_1}(0^-, X_2, \tau). \tag{C.5b}$$

C.2. DERIVATION OF JUMP CONDITIONS (4.36)

Recalling Eq. (C.4), we have

$$\frac{\partial P^{(0)}}{\partial X_1}(0^-, X_2, \tau) = \left(\delta_{1j} - \frac{\partial s_j}{\partial x_1}\right) \frac{\partial p^{(0)}}{\partial X_j}(0^+, X_2, \tau). \tag{C.6}$$

and using Eq. (C.2), we can write the pressure gradient in the free-field region as

$$\frac{\partial P^{(0)}}{\partial X_i}(0^-, X_2, \tau) = B_{ij} \frac{\partial p^{(0)}}{\partial X_j}(0^+, X_2, \tau) \tag{C.7}$$

with

$$B_{ij} = \begin{bmatrix} 1 - \dfrac{\partial s_1}{\partial x_1} & -\dfrac{\partial s_2}{\partial x_1} \\ 0 & 1 \end{bmatrix}. \tag{C.8}$$

Inserting (4.31) into Eq. (4.28b) and using (C.2), we have:

$$\frac{\partial v_i^{(0)}}{\partial \tau} = -\left(\frac{\partial a_j}{\partial x_i} + \delta_{2j}\delta_{i2}\right)\frac{\partial P^{(0)}}{\partial X_j}(0^-, X_2, \tau) = \left(\frac{\partial a_j}{\partial x_i} + \delta_{j2}\delta_{2i}\right)\frac{\partial U_j^{(0)}}{\partial \tau}(0^-, X_2, \tau). \tag{C.9}$$

Time integration gives

$$v_i^{(0)} = A_{ij}U_j^{(0)}(0^-, X_2, \tau) + \chi_i(X_2), \tag{C.10}$$

with $A_{ij} = \dfrac{\partial a_j}{\partial x_i} + \delta_{j2}\delta_{2i}$ and $\chi_i(X_2)$ a constant vector arising from integration. Substituting into Eq. (4.28a), using (4.21a) and (4.26), we have

$$\begin{aligned}\frac{\partial v_i^{(1)}}{\partial x_i} &= (\delta_{jk} - A_{2j}\delta_{k2})\frac{\partial U_j^{(0)}}{\partial X_k}(0^-, X_2, \tau) - \frac{\partial \chi_i}{\partial X_2}\delta_{i2} \\ &= \frac{\partial U_1^{(0)}}{\partial X_1}(0^-, X_2, \tau) - A_{21}\frac{\partial U_1^{(0)}}{\partial X_2}(0^-, X_2, \tau) + (1 - A_{22})\frac{\partial U_2^{(0)}}{\partial X_2}(0^-, X_2, \tau) - \frac{\partial \chi_2}{\partial X_2}.\end{aligned} \tag{C.11}$$

In order to determine the unknown vector $\chi_i(X_2)$, we use the energy conservation equation (4.4c) in the interface inner region at order $\mathcal{O}(\epsilon^{-1})$

$$\frac{\partial \pi^{(0)}}{\partial x_i}v_i^{(0)} + \pi^{(0)}\frac{\partial v_i^{(0)}}{\partial x_i} = 0, \tag{C.12}$$

and at order $\mathcal{O}(\epsilon^0)$,

$$\begin{aligned}\frac{1}{2}\frac{\partial}{\partial \tau}(\pi^{(0)2} + v_i^{(0)2}) + v_i^{(1)}\frac{\partial \pi^{(0)}}{\partial x_i} + v_i^{(0)}\left[\frac{\partial \pi^{(0)}}{\partial X_2}\delta_{2i} + \frac{\partial \pi^{(1)}}{\partial x_i}\right] + \\ + \pi^{(1)}\frac{\partial v_i^{(0)}}{\partial x_i} + \pi^{(0)}\left[\frac{\partial v_i^{(0)}}{\partial X_2}\delta_{2i} + \frac{\partial v_i^{(1)}}{\partial x_i}\right] = 0.\end{aligned} \tag{C.13}$$

From Eq. (C.12) and using Eqs. (4.26) and (C.10), we have

$$\frac{\partial A_{ij}}{\partial x_i} = \frac{\partial^2 a_j}{\partial x_i^2} = 0, \tag{C.14}$$

for any non-zero leading-order pressure field. This is always true as a_j satisfies the auxiliary problem (4.32).

From Eq. (C.13) and using Eqs. (4.26) and (C.10), the following equation holds at $X_1 = 0^-$:

$$\frac{1}{2}\frac{\partial}{\partial \tau}\left[P^{(0)2} + A_{ij}^2 U_j^{(0)2}\right] + \left(A_{ki}A_{ij}\right)U_j^{(0)}\frac{\partial P^{(0)}}{\partial X_k} + P^{(0)}\frac{\partial U_j^{(0)}}{\partial X_k}\delta_{jk} = -\chi_i A_{ij}\left(\frac{\partial U_j^{(0)}}{\partial \tau} + \frac{\partial P^{(0)}}{\partial X_j}\right). \tag{C.15}$$

With Eqs. (4.21), we have

$$\frac{1}{2}\frac{\partial}{\partial\tau}\left[P^{(0)2}+A_{ij}^2U_j^{(0)2}\right]-\left(A_{ki}A_{ij}\right)U_j^{(0)}\frac{\partial U_k^{(0)}}{\partial\tau}-P^{(0)}\frac{\partial P^{(0)}}{\partial\tau}=0, \tag{C.16}$$

which is always satisfied for whatever χ_i. We can thus set $\chi_i(X_2)=0$.

Integrating equation (C.11) in the inner region unit cell, and using Green's theorem, we get the order ϵ jump condition:

$$\begin{aligned}\llbracket u_1\rrbracket^{(1)} &= \int_0^1 v_1^{(1)}\Big|_{x_1=-x_\infty}^{x_\infty}\mathrm{d}x_2 - x_\infty\frac{\partial U_1^{(0)}}{\partial X_1}(0^-,X_2,\tau)-x_\infty\int_0^1\frac{\partial u_1^{(0)}}{\partial X_1}(0^+,X_2,x_i,\tau)\,\mathrm{d}x_2\\ &= (V_{in}-x_\infty)\frac{\partial U_1^{(0)}}{\partial X_1}(0^-,X_2,\tau)-x_\infty\int_0^1\frac{\partial u_1^{(0)}}{\partial X_1}(0^+,X_2,x_i,\tau)\,\mathrm{d}x_2-\\ &\quad-\int_{V_{in}}(A_{21})\mathrm{d}V\frac{\partial U_1^{(0)}}{\partial X_2}(0^-,X_2,\tau)+\int_{V_{in}}(1-A_{22})\mathrm{d}V\frac{\partial U_2^{(0)}}{\partial X_2}(0^-,X_2,\tau).\end{aligned} \tag{C.17}$$

Now we try to find an expression for the second term on RHS of the above equation, to relate it to free field variables. Taking the spatial derivative of Eq.(4.29b) in the X_1-direction we have

$$\frac{\partial^2u_1^{(0)}}{\partial\tau\partial X_1}=-\frac{\partial^2p^{(1)}}{\partial X_1\partial x_1}-\frac{\partial^2p^{(0)}}{\partial X_1^2}. \tag{C.18}$$

Using Eqs. (4.34) and (4.21), the above equation is simplified to be

$$\frac{\partial^2u_1^{(0)}}{\partial\tau\partial X_1}=-\frac{\partial}{\partial X_1}\left(B_{11}\frac{\partial p^{(0)}}{\partial X_1}+B_{12}\frac{\partial p^{(0)}}{\partial X_2}\right)=-\frac{\partial^2P^{(0)}}{\partial X_1^2}=\frac{\partial^2U_1^{(0)}}{\partial\tau\partial X_1}. \tag{C.19}$$

Hence,

$$\frac{\partial u_1^{(0)}}{\partial X_1}=\frac{\partial U_1^{(0)}}{\partial X_1}, \tag{C.20}$$

and consequently, the jump condition for the acoustic velocity becomes

$$\begin{aligned}\llbracket u_1\rrbracket^{(1)} &= (V_{in}-2x_\infty)\frac{\partial U_1^{(0)}}{\partial X_1}(0^-,X_2,\tau)-\int_{V_{in}}(A_{21})\mathrm{d}V\frac{\partial U_1^{(0)}}{\partial X_2}(0^-,X_2,\tau)+\\ &\quad+\int_{V_{in}}(1-A_{22})\mathrm{d}V\frac{\partial U_2^{(0)}}{\partial X_2}(0^-,X_2,\tau),\end{aligned} \tag{C.21}$$

noticing that $V_{in}=2x_\infty-x_\infty\pi d^2/4$, and $V_{in}-2x_\infty=x_\infty(\phi-1)$.

Using matching conditions (4.20a) and (4.20c), we also have

$$\begin{aligned}
[\![p]\!]^{(1)} &= \left(\int_0^1 a_j \Big|_{x_1=-x_\infty}^{x_\infty} \mathrm{d}x_2 - x_\infty \delta_{1j} \right) \frac{\partial P^{(0)}}{\partial X_j}(0^-, X_2, \tau) - x_\infty \delta_{1j} \int_0^1 \frac{\partial p^{(0)}}{\partial X_j}(0^+, X_2, x_i, \tau)\, \mathrm{d}x_2 \\
&= \left(\int_0^1 a_j \Big|_{x_1=-x_\infty}^{x_\infty} \mathrm{d}x_2 - x_\infty \delta_{1j} \right) \frac{\partial P^{(0)}}{\partial X_j}(0^-, X_2, \tau) - x_\infty \delta_{1j} \int_0^1 B_{ji}^{-1} \Big|_{X_1=0^+} \mathrm{d}x_2 \frac{\partial P^{(0)}}{\partial X_i}(0^-, X_2, \tau), \\
&= \left(\int_0^1 a_i \Big|_{x_1=-x_\infty}^{x_\infty} \mathrm{d}x_2 - x_\infty \delta_{1i} - x_\infty \delta_{1j} \int_0^1 B_{ji}^{-1} \Big|_{X_1=0^+} \mathrm{d}x_2 \right) \frac{\partial P^{(0)}}{\partial X_i}(0^-, X_2, \tau).
\end{aligned} \tag{C.22}$$

The jump conditions can be written in a more compact format as

$$[\![p]\!] = \mathcal{M}_i \frac{\partial P^{(0)}}{\partial X_i}(0^-, X_2, \tau), \tag{C.23a}$$

$$[\![u_1]\!] = \mathcal{S}_{ij} \frac{\partial U_j^{(0)}}{\partial X_i}(0^-, X_2, \tau), \tag{C.23b}$$

with

$$\mathcal{M}_i = \int_0^1 a_i \Big|_{x_1=-x_\infty}^{x_\infty} \mathrm{d}x_2 - x_\infty \delta_{1i} - x_\infty \delta_{1j} \int_0^1 B_{ji}^{-1} \Big|_{X_1=0^+} \mathrm{d}x_2, \tag{C.24a}$$

$$\mathcal{S}_{ij} = \begin{bmatrix} x_\infty(\phi - 1) & 0 \\ -\int_{V_{in}} (A_{21})\, \mathrm{d}V & \int_{V_{in}} (1 - A_{22})\, \mathrm{d}V. \end{bmatrix} \tag{C.24b}$$

C.3. WAVE EQUATION IN THE BULK REGION OF POROUS MATERIAL

Solving the whole domain also requires solving the field in the outer bulk region at order $\mathcal{O}(\epsilon^0)$. Recall that the solution of $p^{(1)}$ has been obtained as Eq. (4.34). Using the governing equations in the bulk region at order $\mathcal{O}(\epsilon^0)$, Eqs. (4.29), and $\mathcal{O}(\epsilon^1)$:

$$\frac{\partial p^{(1)}}{\partial \tau} + \frac{\partial u_i^{(2)}}{\partial x_i} + \frac{\partial u_i^{(1)}}{\partial X_i} = 0, \tag{C.25a}$$

$$\frac{\partial u_i^{(1)}}{\partial \tau} + \frac{\partial p^{(2)}}{\partial x_i} + \frac{\partial p^{(1)}}{\partial X_i} = 0, \tag{C.25b}$$

$$u_i^{(1)} n_i = 0, \qquad \text{at } \mathcal{A}_{\beta\sigma}. \tag{C.25c}$$

Taking the microscopic spatial derivative of Eq. (C.25b), it is

$$\frac{\partial^2 u_i^{(1)}}{\partial x_i \partial \tau} = -\frac{\partial^2 p^{(2)}}{\partial x_i^2} - \frac{\partial^2 p^{(1)}}{\partial x_i \partial X_i}. \tag{C.26}$$

Substituting the above equation in the time derivative of Eq. (4.29a), we obtain

$$\frac{\partial^2 p^{(0)}}{\partial \tau^2} - \frac{\partial^2 p^{(2)}}{\partial x_i^2} - \frac{\partial^2 p^{(1)}}{\partial x_i \partial X_i} + \frac{\partial^2 u_i^{(0)}}{\partial \tau \partial X_i} = 0. \tag{C.27}$$

In addition, the macroscopic divergence of Eq. (4.29b) from the above equation yields,

$$\frac{\partial^2 u_i^{(0)}}{\partial \tau \partial X_i} = -\frac{\partial^2 p^{(1)}}{\partial X_i \partial x_i} - \frac{\partial^2 p^{(0)}}{\partial X_i^2}. \tag{C.28}$$

In the end, we obtain a single equation for the acoustic pressure in the outer bulk porous region, and the boundary condition at the solid scatterer surface (obtained from the inner product of n_i and Eq. (C.25b)):

$$\frac{\partial^2 p^{(0)}}{\partial \tau^2} - \frac{\partial^2 p^{(2)}}{\partial x_i^2} - 2\frac{\partial^2 p^{(1)}}{\partial x_i \partial X_i} - \frac{\partial^2 p^{(0)}}{\partial X_i^2} = 0, \tag{C.29a}$$

$$\frac{\partial p^{(2)}}{\partial x_i} n_i = -\frac{\partial p^{(1)}}{\partial X_i} n_i, \quad \text{at } \mathcal{A}_{\beta\sigma}. \tag{C.29b}$$

With Eq. (C.29b), applying the Green's theorem in a unit cell of the bulk region, it holds that

$$\int_{V_\beta} \frac{\partial^2 p^{(2)}}{\partial x_i^2} \,\mathrm{d}V = \int_{\mathcal{A}_{\beta\sigma}} \frac{\partial p^{(2)}}{\partial x_i} \, n_i \,\mathrm{d}S = \frac{\partial^2 p^{(0)}}{\partial X_i \partial X_k} \int_{\mathcal{A}_{\beta\sigma}} (s_k \, n_i) \,\mathrm{d}S. \tag{C.30}$$

In addition, using the auxiliary governing equations (4.35), it is

$$\begin{aligned} 0 = \int_{V_\beta} \left(s_k \frac{\partial^2 s_i}{\partial x_j^2} \right) \mathrm{d}V &= -\int_{V_\beta} \frac{\partial s_k}{\partial x_j} \frac{\partial s_i}{\partial x_j} \,\mathrm{d}V + \int_{\mathcal{A}_{\beta\sigma}} s_k \frac{\partial s_i}{\partial x_j} \, n_j \,\mathrm{d}S \\ &= -\int_{V_\beta} \frac{\partial s_k}{\partial x_j} \frac{\partial s_i}{\partial x_j} \mathrm{d}V + \int_{\mathcal{A}_{\beta\sigma}} s_k n_i \mathrm{d}S \end{aligned} \tag{C.31}$$

so that

$$\int_{\mathcal{A}_{\beta\sigma}} (s_k \, n_i) \,\mathrm{d}S = \int_{V_\beta} \left(\frac{\partial s_k}{\partial x_j} \frac{\partial s_i}{\partial x_j} \right) \mathrm{d}V. \tag{C.32}$$

Substituting Eq. (4.34) into Eq. (C.29a) and taking the intrinsic average, finally we have

$$\frac{\partial^2 p^{(0)}}{\partial \tau^2} - \mathcal{C}_{ik} \frac{\partial^2 p^{(0)}}{\partial X_i \partial X_k} = 0, \tag{C.33}$$

with the coefficient $\mathcal{C}_{ik}$ defined by

$$\mathcal{C}_{ik} = \langle \frac{\partial s_k}{\partial x_j} \frac{\partial s_i}{\partial x_j} - 2\frac{\partial s_i}{\partial x_k} + \delta_{ik} \rangle^\beta. \tag{C.34}$$

Since the geometry of the bulk-region unit cell is isotropic, it is $\mathcal{C}_{ik} = \mathcal{C} \, \delta_{ik}$. This gives the wave equation in the bulk region at order $\mathcal{O}(\epsilon^0)$ in the following form:

$$\frac{\partial^2 p^{(0)}}{\partial \tau^2} - \mathcal{C} \frac{\partial^2 p^{(0)}}{\partial X_i^2} = 0. \tag{C.35}$$

In the free region from Eqs. (4.21), we are able to obtain a similar dimensionless wave equation for the acoustic pressure at order $\mathcal{O}(\epsilon^0)$ as

$$\frac{\partial^2 P^{(0)}}{\partial \tau^2} - \frac{\partial^2 P^{(0)}}{\partial X_i^2} = 0. \tag{C.36}$$

Comparing the two wave equations (C.35) and (C.36), we see that in the bulk region of the porous material, at order $\mathcal{O}(\epsilon^0)$, the pressure wave propagates as if the wave speed were scaled up by $\sqrt{\mathcal{C}}$ compared to the propagation speed in the free field. Therefore, in the bulk porous region, an effective sound speed is defined as

$$c_{\text{eff}} = c_s \sqrt{\mathcal{C}}. \tag{C.37}$$

The upscaled model (C.33) is equivalent to the macroscopic model obtained by Mei and Vernescu (2010) in the frequency domain.

REFERENCES

Æsøy, E., Aguilar, J. G., Wiseman, S., Bothien, M. R., Worth, N. A., and Dawson, J. R. (2020). Scaling and prediction of transfer functions in lean premixed H_2/CH_4-flames. *Combust. Flame*, 215:269–282. https://doi.org/10.1016/j.combustflame.2020.01.045.

Aguilar, J. G. and Juniper, M. P. (2018). Shape optimization in low-order thermoacoustic networks. In *Proceedings of GPPS Forum 18 Global Power and Propulsion Society*.

Aguilar, J. G. and Juniper, M. P. (2020). Thermoacoustic stabilization of a longitudinal combustor using adjoint methods. *Phys. Rev. Fluids*, 5:083902. https://doi.org/10.1103/PhysRevFluids.5.083902.

Aguilar, J. G., Magri, L., and Juniper, M. P. (2017). Adjoint-based sensitivity analysis of low-order thermoacoustic networks using a wave-based approach. *J. Comput. Phys.*, 341:163–181. https://doi.org/10.1016/j.jcp.2017.04.013.

Allard, J. F. and Atalla, N. (2009). *Propagation of Sound in Porous Media: Modelling Sound Absorbing Materials*. John Wiley & Sons Ltd, 2nd edition.

Annaswamy, A. M. and Ghoniem, A. F. (1995). Active control in combustion systems. *IEEE Contr. Syst. Mag.*, 15(6):49–63. https://doi.org/10.1109/37.476386.

Arabi, S. and Heckl, M. (2025). Green's function analysis of nonlinear thermoacoustic effects under the influence of noise in a combustion chamber. *J. Sound Vib.*, 594:118621. https://doi.org/10.1016/j.jsv.2024.118621.

Balasubramanian, K. and Sujith, R. I. (2008a). Non-normality and nonlinearity in combustion–acoustic interaction in diffusion flames. *J. Fluid Mech.*, 594:29–57. https://doi.org/10.1017/S0022112007008737.

Balasubramanian, K. and Sujith, R. I. (2008b). Thermoacoustic instability in a Rijke tube: Non-normality and nonlinearity. *Phys. Fluids*, 20(4):044103. https://doi.org/10.1063/1.2895634.

Battiato, I., Ferrero V, P. T., O'Malley, D., Miller, C. T., Takhar, P. S., Valdés-Parada, F. J., and Wood, B. D. (2019). Theory and applications of macroscale models in porous media. *Transp. Porous. Med.*, 130:5–76. https://doi.org/10.1007/s11242-019-01282-2.

Bellucci, V., Flohr, P., and Paschereit, C. O. (2004). Numerical and experimental study of acoustic damping generated by perforated screens. *AIAA J.*, 42(8):1543–1549. https://doi.org/10.2514/1.9841.

Bellucci, V., Schuermans, B., Nowak, D., Flohr, P., and Paschereit, C. O. (2005). Thermoacoustic modeling of a gas turbine combustor equipped with acoustic dampers. *ASME. J. Turbomach.*, 127(2):372–379. https://doi.org/10.1115/1.1791284.

Bigongiari, A. and Heckl, M. (2018). Analysis of the interaction of thermoacoustic modes with a Green's function approach. *Int. J. Spray Combust.*, 10(4):326–336. https://doi.org/10.1177/1756827718809570.

Bigongiari, A. and Heckl, M. A. (2016). A Green's function approach to the rapid prediction of thermoacoustic instabilities in combustors. *J. Fluid Mech.*, 798:970–996. https://doi.org/10.1017/jfm.2016.332.

Birbaud, A.-L., Ducruix, S., Durox, D., and Candel, S. (2008). The nonlinear response of inverted "V" flames to equivalence ratio nonuniformities. *Combust. Flame*, 154(3):356–367. https://doi.org/10.1016/j.combustflame.2008.05.017.

Bonciolini, G., Boujo, E., and Noiray, N. (2017). Output-only parameter identification of a colored-noise-driven Van-der-Pol oscillator: Thermoacoustic instabilities as an example. *Phys. Rev. E*, 95(6):062217. https://doi.org/10.1103/PhysRevE.95.062217.

Bottaro, A. (2019). Flow over natural or engineered surfaces: an adjoint homogenization perspective. *J. Fluid Mech.*, 877:P1. https://doi.org/10.1017/jfm.2019.607.

Bottaro, A., Corbett, P., and Luchini, P. (2003). The effect of base flow variation on flow stability. *J. Fluid Mech.*, 476:293–302. https://doi.org/10.1017/S002211200200318X.

Bourgouin, J.-F., Durox, D., Moeck, J. P., Schuller, T., and Candel, S. (2015). Characterization and modeling of a spinning thermoacoustic instability in an annular combustor equipped with multiple matrix injectors. *J. Eng. Gas Turb. Power*, 137(2). https://doi.org/10.1115/1.4028257.

Boutin, C. (2013). Acoustics of porous media with inner resonators. *J. Acoust. Soc. Am.*, 134(6):4717–4729. https://doi.org/10.1121/1.4824965.

Brandt, L., Sipp, D., Pralits, J. O., and Marquet, O. (2011). Effect of base-flow variation in noise amplifiers: the flat-plate boundary layer. *J. Fluid Mech.*, 687:503–528. https://doi.org/10.1017/jfm.2011.382.

Chu, B.-T. (1956). Stability of systems containing a heat source: the Rayleigh criterion. In *National Advisory Committee for Aeronautics, RESEARCH MEMORANDUM*.

Crocco, L. (1951). Aspects of Combustion Stability in Liquid Propellant Rocket Motors Part I: Fundamentals. Low Frequency Instability With Monopropellants. *J. Am. Rocket Soc.*, 21(6):163–178. https://doi.org/10.2514/8.4393.

Crocco, L. (1952). Aspects of Combustion Stability in Liquid Propellant Rocket Motors Part II: Low Frequency Instability with Bipropellants. High Frequency Instability. *J. Am. Rocket Soc.*, 22(1):7–16. https://doi.org/10.2514/8.4410.

Crocco, L. and Cheng, S. I. (1956). *Theory of Combustion Instability in Liquid Propellant Rocket Motors*. Butterworths Scientific Publications, 88 Kingsway, London.

Culick, F. E. C. (1987). Short Communication - A Note on Rayleigh's Criterion. *Combust. Sci. Technol.*, 56(4-6):159–166. https://doi.org/10.1080/00102208708947087.

Culick, F. E. C. (1988). Combustion instabilities in liquid-fuelled propulsion systems – An overview. *AGARD Conference Proceedings*, 450:1–73.

De Domenico, F., Rolland, E. O., Rodrigues, J., Magri, L., and Hochgreb, S. (2021). Compositional and entropy indirect noise generated in subsonic non-isentropic nozzles. *J. Fluid Mech.*, 910:A5. https://doi.org/10.1017/jfm.2020.916.

de Lagrange, J. L. (1763). Solution de différens problêmes de calcul intégral. *Miscellanea Taurinensia*, 3:471–668.

Dowling, A. P. (1995). The calculation of thermoacoustic oscillations. *J. Sound Vib.*, 180(4):557–581. https://doi.org/10.1006/jsvi.1995.0100.

Dowling, A. P. (1999). A kinematic model of a ducted flame. *J. Fluid Mech.*, 394:51–72. https://doi.org/10.1017/S0022112099005686.

Dowling, A. P. and Morgans, A. S. (2005). Feedback control of combustion oscillations. *Annu. Rev. Fluid Mech.*, 37:151–182. https://doi.org/10.1146/annurev.fluid.36.050802.122038.

Dowling, A. P. and Stow, S. R. (2003). Acoustic analysis of gas turbine combustors. *J. Propul. Power*, 19(5):751–764. https://doi.org/10.2514/2.6192.

Ducruix, S., Durox, D., and Candel, S. (2000). Theoretical and experimental determinations of the transfer function of a laminar premixed flame. *P. Combust. Inst.*, 28(1):765–773. https://doi.org/10.1016/S0082-0784(00)80279-9.

Dupere, I. D. J. and Dowling, A. P. (2005). The use of Helmholtz resonators in a practical combustor. *J. Eng. Gas Turb. Power*, 127(2):268–275. https://doi.org/10.1115/1.1806838.

Durox, D., Schuller, T., Noiray, N., and Candel, S. (2009). Experimental analysis of nonlinear flame transfer functions for different flame geometries. *P. Comb. Inst.*, 32 I(1):1391–1398. https://doi.org/10.1016/j.proci.2008.06.204.

Eckstein, J. and Sattelmayer, T. (2006). Low-order modeling of low-frequency combustion instabilities in aeroengines. *J. Propul. Power*, 22(2):425–432. https://doi.org/10.1016/10.2514/1.15757 .

Etikyala, S. and Sujith, R. I. (2017). Change of criticality in a prototypical thermoacoustic system. *Chaos*, 27(2). https://doi.org/10.1063/1.4975822.

Evesque, S. and Polifke, W. (2002). Low-order acoustic modelling for annular combustors: validation and inclusion of modal coupling. *Turbo Expo: Power for Land, Sea, and Air*, Volume 1: Turbo Expo 2002:321–331. https://doi.org/10.1115/GT2002-30064.

Falco, S. and Juniper, M. P. (2021). Shape optimization of thermoacoustic systems using a two-dimensional adjoint Helmholtz solver. *J. Eng. Gas Turb. Power*, 143(7):071025. https://doi.org/10.1115/1.4049305.

Ghirardo, G., Di Giovine, C., Moeck, J. P., and Bothien, M. R. (2019). Thermoacoustics of can-annular combustors. *J. Eng. Gas Turb. Power*, 141(1):011007. https://doi.org/10.1115/1.4040743.

Giannetti, F. and Luchini, P. (2007). Structural sensitivity of the first instability of the cylinder wake. *J. Fluid Mech.*, 581:167–197. https://doi.org/10.1017/S0022112007005654.

Gopalakrishnan, E. A. and Sujith, R. I. (2014). Influence of system parameters on the hysteresis characteristics of a horizontal Rijke tube. *Int. J. Spray Comb.*, 6(3):293–316. https://doi.org/10.1260/1756-8277.6.3.293.

Gopalakrishnan, E. A. and Sujith, R. I. (2015). Effect of external noise on the hysteresis characteristics of a thermoacoustic system. *J. Fluid Mech.*, 776:334–353. https://doi.org/10.1017/jfm.2015.330.

Gopinathan, S. M., Iurashev, D., Bigongiari, A., and Heckl, M. (2018). Nonlinear analytical flame models with amplitude-dependent time-lag distributions. *Int. J. Spray Combust.*, 10(4):264–276. https://doi.org/10.1177/1756827717728056.

Green, G. (1828). *An essay on the application of mathematical analysis to the theories of electricity and magnetism*. Printed for the author by T. Wheelhouse, Nottingham, U.K.

Greenberg, M. D. (1978). *Foundations of Applied Mathematics*. Prentice-Hall, Inc., Englewood Cliffs, N.J.

Gullaud, E. and Nicoud, F. (2012). Effect of perforated plates on the acoustics of annular combustors. *AIAA J.*, 50(12):2629–2642. https://doi.org/10.2514/1.J050716.

Heckl, M. (1988). Active control of the noise from a Rijke tube. *J. Sound Vib.*, 124(1):117–133. https://doi.org/10.1016/S0022-460X(88)81408-1.

Heckl, M. (1990). Non-linear acoustic effects in the Rijke tube. *Acustica*, 72(1):63–71.

Heckl, M. A. (2013). Analytical model of nonlinear thermo-acoustic effects in a matrix burner. *J. Sound Vib.*, 332:4021–4036. https://doi.org/10.1016/j.jsv.2012.11.010.

Heckl, M. A. (2015). A new perspective on the flame describing function of a matrix flame. *Int. J. Spray Comb.*, 7(2):91–112. https://doi.org/10.1260/1756-8277.7.2.91.

Heckl, M. A. (2023). An adjoint Green's function approach to model instabilities in a duct with mean flow. Technical report, Keele University, UK. https://doi.org/10.21252/bvre-5s91.

Heckl, M. A., Gopinathan, S. M., and Surendran, A. (2022). A unified framework for acoustic instabilities based on the tailored Green's function. *J. Sound Vib.*, 541:117279. https://doi.org/10.1016/j.jsv.2022.117279.

Heckl, M. A. and Howe, M. S. (2007). Stability analysis of the Rijke tube with a Green's function approach. *J. Sound Vib.*, 305:672–688. https://doi.org/10.1016/j.jsv.2007.04.027.

Hegde, U. G., Reuter, D., and Zinn, B. T. (1988). Sound generation by ducted flames. *AIAA J.*, 26(5):532–537. https://doi.org/10.2514/3.9930.

Hill, D. C. (1995). Adjoint systems and their role in the receptivity problem for boundary layers. *J. Fluid Mech.*, 292:183–204. https://doi.org/10.1017/S0022112095001480.

Hu, X. and Chan, C. T. (2005). Refraction of water waves by periodic cylinder arrays. *Phys. Rev. Lett.*, 95(15):154501. https://doi.org/10.1103/PhysRevLett.95.154501.

Jegadeesan, V. and Sujith, R. (2013). Experimental investigation of noise induced triggering in thermoacoustic systems. *P. Comb. Inst.*, 34(2):3175–3183. https://doi.org/10.1016/j.proci.2012.05.003.

Joseph George, K. and Sujith, R. (2011). On chu's disturbance energy. *J. Sound Vib.*, 330(22):5280–5291. https://doi.org/10.1016/j.jsv.2011.06.016.

Juniper, M. P. (2018). Sensitivity analysis of thermoacoustic instability with adjoint Helmholtz solvers. *Phys. Rev. Fluids*, 3(11):110509. https://doi.org/10.1103/PhysRevFluids.3.110509.

Juniper, M. P. and Sujith, R. I. (2018). Sensitivity and nonlinearity of thermoacoustic oscillations. *Annu. Rev. Fluid Mech.*, 50:661–689. https://doi.org/10.1146/annurev-fluid-122316-045125.

Kabiraj, L., Steinert, R., Saurabh, A., and Paschereit, C. O. (2015). Coherence resonance in a thermoacoustic system. *Phys. Rev. E*, 92:042909. https://doi.org/10.1103/PhysRevE.92.042909.

Kabiraj, L., Vishnoi, N., and Saurabh, A. (2020). *A Review on Noise-Induced Dynamics of Thermoacoustic Systems*, pages 265–281. Springer Singapore, Singapore. https://doi.org/10.1007/978-981-15-0536-2_12.

Kashinath, K., Hemchandra, S., and Juniper, M. P. (2013). Nonlinear thermoacoustics of ducted premixed flames: The influence of perturbation convection speed. *Combust. Flame*, 160(12):2856–2865. https://doi.org/10.1016/j.combustflame.2013.06.019.

Kinsler, L. E., Frey, A. R., Coppens, A. B., and Sanders, J. V. (2000). *Fundamentals of Acoustics*. John Wiley & Sons, 4th edition.

Levine, H. and Schwinger, J. (1948). On the radiation of sound from an unflanged circular pipe. *Physical review*, 73(4):383.

Lieuwen, T. and Zinn, B. T. (1998). The role of equivalence ratio oscillations in driving combustion instabilities in low NOx gas turbines. *Symposium (International) on Combustion*, 27(2):1809–1816. https://doi.org/10.1016/S0082-0784(98)80022-2.

Lieuwen, T. C. (1999). *Investigation of combustion instability mechanisms in premixed gas turbines*. PhD thesis, Georgia Institute of Technology.

Lieuwen, T. C. and Yang, V. (2005). *Combustion Instabilities in Gas Turbine Engines: Operational Experience, Fundamental Mechanisms, and Modeling*. American Institute of Aeronautics and Astronautics, Inc.

Lighthill, M. J. (1952). On sound generated aerodynamically I. General theory. *Proceedings of the Royal Society of London. Series A. Mathematical and Physical Sciences*, 211(1107):564–587. https://doi.org/10.1098/rspa.1952.0060.

Luchini, P. and Bottaro, A. (1998). Görtler vortices: a backward-in-time approach to the receptivity problem. *J. Fluid Mech.*, 363:1–23. https://doi.org/10.1017/S0022112098008970.

Luchini, P. and Bottaro, A. (2014). Adjoint equations in stability analysis. *Annu. Rev. Fluid Mech.*, 46:493–517. https://doi.org/10.1146/annurev-fluid-010313-141253.

Luchini, P., Giannetti, F., and Pralits, J. (2008). Structural sensitivity of linear and nonlinear global modes. In *5th AIAA Theoretical Fluid Mechanics Conference*, pages 1–19. https://doi.org/10.2514/6.2008-4227.

Magri, L. (2019). Adjoint methods as design tools in thermoacoustics. *Appl. Mech. Rev.*, 71(2):080201. https://doi.org/10.1115/1.4042821.

Magri, L. and Juniper, M. P. (2013). Sensitivity analysis of a time-delayed thermoacoustic system via an adjoint-based approach. *J. Fluid Mech.*, 719:183–202. https://doi.org/10.1017/jfm.2012.639.

Magri, L., Juniper, M. P., and Moeck, J. P. (2020). Sensitivity of the Rayleigh criterion in thermoacoustics. *J. Fluid Mech.*, 882:R1. https://doi.org/10.1017/jfm.2019.860.

Marble, F. E. and Candel, S. M. (1977). Acoustic disturbance from gas non-uniformities convected through a nozzle. *J. Sound Vib.*, 55(2):225–243. https://doi.org/10.1016/0022-460X(77)90596-X.

Mariappan, S., Sujith, R., and Schmid, P. (2011). Non-normality of thermoacoustic interactions: an experimental investigation. In *47th AIAA/ASME/SAE/ASEE Joint Propulsion Conference & Exhibit*, page 5555. https://doi.org/10.2514/6.2011-5555.

Marigo, J.-J. and Maurel, A. (2016). Homogenization models for thin rigid structured surfaces and films. *J. Acoust. Soc. Am.*, 140(1):260–273. https://doi.org/10.1121/1.4954756.

Marigo, J.-J. and Maurel, A. (2017). Second order homogenization of subwavelength stratified media including finite size effect. *SIAM J. Appl. Math.*, 77(2):721–743. https://doi.org/10.1137/16M1070542.

Marquet, O., Sipp, D., and Jacquin, L. (2008). Sensitivity analysis and passive control of cylinder flow. *J. Fluid Mech.*, 615:221–252. https://doi.org/10.1017/S0022112008003662.

Masoud, H. and Stone, H. (2019). The reciprocal theorem in fluid dynamics and transport phenomena. *J. Fluid Mech.*, 879:P1. https://doi.org/10.1017/jfm.2019.553.

MATLAB (2024). The Mathworks Inc., Version: 24.1.0.2689473 (R2024a).

Matveev, K. and Culick, F. E. C. (2003a). A study of the transition to instability in a Rijke tube with axial temperature gradient. *J. Sound Vib.*, 264(3):689–706. https://doi.org/10.1016/S0022-460X(02)01217-8.

Matveev, K. I. (2003a). Energy consideration of the nonlinear effects in a Rijke tube. *J. Fluid Struct.*, 18(6):783–794. https://doi.org/10.1016/j.jfluidstructs.2003.07.016.

Matveev, K. I. (2003b). *Thermoacoustic instabilities in the Rijke tube: experiments and modeling*. PhD thesis, California Institute of Technology.

Matveev, K. I. and Culick, F. E. C. (2003b). Limit-cycle properties of a Rijke tube. *Electronic Journal Technical Acoustics*, 3:102–114.

McManus, K., Vandsburger, U., and Bowman, C. (1990). Combustor performance enhancement through direct shear layer excitation. *Combust. Flame*, 82(1):75–92. https://doi.org/10.1016/0010-2180(90)90079-7.

Mei, C. C. and Vernescu, B. (2010). *Homogenization Methods for Multiscale Mechanics*. World Scientific Co. Pte. Ltd.

Mensah, G. A. and Moeck, J. P. (2017). Acoustic damper placement and tuning for annular combustors: an adjoint-based optimization study. *J. Eng. Gas Turb. Power*, 139(6). https://doi.org/10.1115/1.4035201.

Merk, H. J. (1957). An analysis of unstable combustion of premixed gases. *Symposium (International) on Combustion*, 6(1):500–512. https://doi.org/10.1016/S0082-0784(57)80067-8.

Morse, P. M. and Feshbach, H. (1953). *Methods of Theoretical Physics*. McGraw-Hill Book Company, Inc., New York, NY.

Nicoud, F., Benoit, L., Sensiau, C., and Poinsot, T. (2007). Acoustic modes in combustors with complex impedances and multidimensional active flames. *AIAA J.*, 45(2):426–441. https://doi.org/10.2514/1.24933.

Nicoud, F. and Wieczorek, K. (2009). About the zero Mach number assumption in the calculation of thermoacoustic instabilities. *Int. J. Spray Comb.*, 1(1):67–111. https://doi.org/10.1260/175682709788083335.

Noiray, N. (2007). Linear and nonlinear analysis of combustion instabilities, application to multipoint injection systems and control strategies. *PhD thesis, École Centrale Paris*.

Noiray, N., Durox, D., Schuller, T., and Candel, S. (2008). A unified framework for nonlinear combustion instability analysis based on the flame describing function. *J. Fluid Mech.*, 615:139–167. https://doi.org/10.1017/S0022112008003613.

Noiray, N. and Schuermans, B. (2013). On the dynamic nature of azimuthal thermoacoustic modes in annular gas turbine combustion chambers. *P. Roy. Soc. A-Math. Phy.*, 469(2151):20120535. https://doi.org/10.1098/rspa.2012.0535.

Olny, X. and Boutin, C. (2003). Acoustic wave propagation in double porosity media. *J. Acoust. Soc. Am.*, 114(1):73–89. https://doi.org/10.1121/1.1534607.

Orchini, A., Illingworth, S., and Juniper, M. (2015). Frequency domain and time domain analysis of thermoacoustic oscillations with wave-based acoustics. *J. Fluid Mech.*, 775:387–414. https://doi.org/10.1017/jfm.2015.139.

Orchini, A. and Juniper, M. P. (2016). Linear stability and adjoint sensitivity analysis of thermoacoustic networks with premixed flames. *Combust. Flame*, 165:97–108. https://doi.org/10.1016/j.combustflame.2015.10.011.

Orchini, A., Pedergnana, T., Buschmann, P. E., Moeck, J. P., and Noiray, N. (2022). Reduced-order modelling of thermoacoustic instabilities in can-annular combustors. *J. Sound Vib.*, 526:116808. https://doi.org/10.1016/j.jsv.2022.116808.

Ozan, D. E. and Magri, L. (2024). Data-driven computation of adjoint sensitivities without adjoint solvers: An application to thermoacoustics. *Phys. Rev. Fluids*, 9:103902. https://doi.org/10.1103/PhysRevFluids.9.103902.

Peracchio, A. A. and Proscia, W. M. (1998). Nonlinear heat-release/acoustic model for thermoacoustic instability in lean premixed combustors. *Turbo Expo: Power for Land, Sea, and Air*, Volume 3: Coal, Biomass and Alternative Fuels; Combustion and Fuels; Oil and Gas Applications; Cycle Innovations:V003T06A022. https://doi.org/10.1115/98-GT-269.

Polifke, W. (2020). Modeling and analysis of premixed flame dynamics by means of distributed time delays. *Prog. Energ. Combust.*, 79. https://doi.org/10.1016/j.pecs.2020.100845.

Polifke, W., Paschereit, C. O., and Döbbeling, K. (2001). Constructive and destructive interference of acoustic and entropy waves in a premixed combustor with a choked exit. *Int. J. Acoust. Vib*, 6(3):135–146.

Pralits, J. O., Airiau, C., Hanifi, A., and Henningson, D. S. (2000). Sensitivity analysis using adjoint parabolized stability equations for compressible flows. *Flow Turbul. Combust.*, 65:321–346.

Pralits, J. O., Brandt, L., and Giannetti, F. (2010). Instability and sensitivity of the flow around a rotating circular cylinder. *J. Fluid Mech.*, 650:513–536. https://doi.org/10.1017/S0022112009993764.

Pralits, J. O., Hanifi, A., and Henningson, D. (2002). Adjoint-based optimization of steady suction for disturbance control in incompressible flows. *J. Fluid Mech.*, 467:129–161. https://doi.org/10.1017/S0022112002001301.

Putnam, A. A. and Dennis, W. R. (1954). Burner oscillations of the gauze-tone type. *J. Acoust. Soc. Am.*, 26(5):716–725. https://doi.org/10.1121/1.1907406.

Raghu, S. and Sreenivasan, K. R. (1987). Control of acoustically coupled combustion and fluid dynamic instabilities. In *11th Aeroacoustics Conference*, page 2690. https://doi.org/10.2514/6.1987-2690.

Rajaram, R. and Lieuwen, T. (2009). Acoustic radiation from turbulent premixed flames. *J. Fluid Mech.*, 637:357–385. https://doi.org/10.1017/S0022112009990681.

Rasmussen, C., Quan, L., and Alù, A. (2021). Acoustic nonreciprocity. *J. Appl. Phys.*, 129:210903. https://doi.org/10.1063/5.0050775.

Raun, R., Beckstead, M., Finlinson, J., and Brooks, K. (1993). A review of Rijke tubes, Rijke burners and related devices. *Prog. Energ. Combust.*, 19(4):313–364. https://doi.org/10.1016/0360-1285(93)90007-2.

Rayleigh, J. W. S. B. (1896). *The Theory of Sound*, volume 2. Macmillan.

Rayleigh, L. (1878). The explanation of certain acoustical phenomena. *Nature*, 8:319–321.

Rienstra, S. W. and Hirschberg, A. (2004). *An Introduction to Acoustics*. Technische Universiteit Eindhoven, The Netherlands.

Sayadi, T., Le Chenadec, V., Schmid, P., Richecoeur, F., and Massot, M. (2014). Thermoacoustic instability – a dynamical system and time domain analysis. *J. Fluid Mech.*, 753:448–471. https://doi.org/10.1017/jfm.2014.357.

Schaefer, F. and Polifke, W. (2019). Low-order network model of a duct with non-uniform cross-section and varying mean temperature in the presence of mean flow. In *AIAA Propulsion and Energy 2019 Forum*, page 4376. https://doi.org/10.2514/6.2019-4376.

Schäfer, F., Magri, L., and Polifke, W. (2022). A hybrid adjoint network model for thermoacoustic optimization. *J. Eng. Gas Turb. Power*, 144(3):031017. https://doi.org/10.1115/1.4051959.

Schmid, P. J. and Brandt, L. (2014). Analysis of fluid systems: Stability, receptivity, sensitivity. *Appl. Mech. Rev.*, 66(2):024803. https://doi.org/10.1115/1.4026375.

Schuller, T., Poinsot, T., and Candel, S. (2020). Dynamics and control of premixed combustion systems based on flame transfer and describing functions. *J. Fluid Mech.*, 894:1–95. https://doi.org/10.1017/jfm.2020.239.

Selle, L., Benoit, L., Poinsot, T., Nicoud, F., and Krebs, W. (2006). Joint use of compressible large-eddy simulation and Helmholtz solvers for the analysis of rotating modes in an industrial swirled burner. *Combust. Flame*, 145(1):194–205. https://doi.org/10.1016/j.combustflame.2005.10.017.

Shapiro, A. H. (1953). *The dynamics and thermodynamics of compressible fluid flow*. The Ronald Press Company, New York, USA.

Silva, C. F., Nicoud, F., Schuller, T., Durox, D., and Candel, S. (2013). Combining a Helmholtz solver with the flame describing function to assess combustion instability in a premixed swirled combustor. *Combust. Flame*, 160(9):1743–1754. https://doi.org/10.1016/j.combustflame.2013.03.020.

Song, B. H. and Bolton, J. S. (2000). A transfer-matrix approach for estimating the characteristic impedance and wave numbers of limp and rigid porous materials. *J. Acoust. Soc. Am.*, 107(3):1131–1152. https://doi.org/10.1121/1.428404.

Stow, S. R. and Dowling, A. P. (2001). Thermoacoustic oscillations in an annular combustor. *Turbo Expo: Power for Land, Sea, and Air*, Volume 2: Coal, Biomass and Alternative Fuels; Combustion and Fuels; Oil and Gas Applications; Cycle Innovations:V002T02A004. https://doi.org/10.1115/2001-GT-0037.

Stow, S. R., Dowling, A. P., and Hynes, T. P. (2002). Reflection of circumferential modes in a choked nozzle. *J. Fluid Mech.*, 467:215–239. https://doi.org/10.1017/S0022112002001428.

Strogatz, S. H. (2018). *Nonlinear Dynamics and Chaos with Student Solutions Manual: With Applications to Physics, Biology, Chemistry, and Engineering*. CRC Press, 2nd edition. https://doi.org/10.1201/9780429399640.

Summerfield, M. (1951). A theory of unstable combustion in liquid propellant rocket systems. *J. Am. Rocket Soc.*, 21(5):108–114. https://doi.org/10.2514/8.4374.

Watkins, D. S. (2002). *Fundamentals of Matrix Computations*. John Wiley & Sons, Inc. New York, 2nd edition.

Waugh, I. C., Geuß, M., and Juniper, M. P. (2011). Triggering, bypass transition and the effect of noise on a linearly stable thermoacoustic system. *P. Comb. Inst.*, 33(2):2945–2952. https://doi.org/10.1016/j.proci.2010.06.018.

Waugh, I. C. and Juniper, M. P. (2011). Triggering in a thermoacoustic system with stochastic noise. *Int. J. Spray Comb.*, 3(3):225–241. https://doi.org/10.1260/1756-8277.3.3.225.

Wei, J. and Arabi, S. (2025). Effects of open boundary condition, non-uniform temperature field, mean flow, and noise on nonlinear thermoacoustic instabilities. *J. Sound Vib.*, Under Review.

Wei, J., Arabi, S., Pralits, J. O., Bottaro, A., and Heckl, M. A. (2024). An adjoint Green's function approach for thermoacoustic instabilities in a duct with mean flow. *J. Sound Vib.*, 593:118673. https://doi.org/10.1016/j.jsv.2024.118673.

Wei, J. and Bottaro, A. (2025). The effective interface condition for acoustic propagation through rigid porous materials. *Ongoing*.

Wei, J., Bottaro, A., and Pralits, J. O. (2025). Adjoint-based mean-flow uncertainty and feedback-forcing analyses of a thermoacoustic model system. *Combust. Flame*, 272:113901. https://doi.org/10.1016/j.combustflame.2024.113901.

Whitaker, S. (1999). *The Method of Volume Averaging*. Springer Science & Business Media Dordrecht. https://doi.org/10.1007/978-94-017-3389-2.

Yang, D. and Morgans, A. S. (2016). A semi-analytical model for the acoustic impedance of finite length circular holes with mean flow. *J. Sound Vib.*, 384:294–311. https://doi.org/10.1016/j.jsv.2016.08.006.

Yang, D. and Morgans, A. S. (2017). The acoustics of short circular holes opening to confined and unconfined spaces. *J. Sound Vib.*, 393:41–61. https://doi.org/10.1016/j.jsv.2016.12.027.

Yang, M. and Sheng, P. (2017). Sound absorption structures: From porous media to acoustic metamaterials. *Annu. Rev. Mater. Res.*, 47(Volume 47, 2017):83–114. https://doi.org/10.1146/annurev-matsci-070616-124032.

Zhao, D. and Li, J. (2012). Feedback control of combustion instabilities using a helmholtz resonator with an oscillating volume. *Combust. Sci. Technol.*, 184(5):694–716. https://doi.org/10.1080/00102202.2012.660224.

Zhao, D. and Li, X. Y. (2015). A review of acoustic dampers applied to combustion chambers in aerospace industry. *Prog. Aerosp. Sciences*, 74:114–130. https://doi.org/10.1016/j.paerosci.2014.12.003.

Zhao, D. and Morgans, A. S. (2009). Tuned passive control of combustion instabilities using multiple Helmholtz resonators. *J. Sound Vib.*, 320(4-5):744–757. https://doi.org/10.1016/j.jsv.2008.09.006.

Zhou, H. and Meng, S. (2019). Numerical prediction of swirl burner geometry effects on nox emission and combustion instability in heavy oil-fired boiler. *Appl. Therm. Eng.*, 159:113843. https://doi.org/10.1016/j.applthermaleng.2019.113843.

Zinn, B. T. and Lores, M. E. (1971). Application of the Galerkin method in the solution of non-linear axial combustion instability problems in liquid rockets. *Combust. Sci. Technol.*, 4(1):269–278. https://doi.org/10.1080/00102207108952493.